DEVELOPMENT OF OPTIMAL CONTROL METHODS FOR UNSEEDED BATCH COOLING CRYSTALLIZATION: COMBINATION OF FIRST-PRINCIPLE AND MACHINE-LEARNING APPROACHES

A Dissertation
Presented to
The Academic Faculty

By

Youngjo Kim

In Partial Fulfillment
of the Requirements for the Degree
Doctor of Philosophy in the
School of Chemical and Biomolecular Engineering

Georgia Institute of Technology

August 2021

DEVELOPMENT OF OPTIMAL CONTROL METHODS FOR UNSEEDED BATCH COOLING CRYSTALLIZATION: COMBINATION OF FIRST-PRINCIPLE AND MACHINE-LEARNING APPROACHES

Thesis committee:

Dr. Martha A. Grover, Advisor
School of Chemical and Biomolecular
Engineering
Georgia Institute of Technology

Dr. Ronald W. Rousseau, co-Advisor
School of Chemical and Biomolecular
Engineering
Georgia Institute of Technology

Dr. Yoshiaki Kawajiri, co-Advisor
School of Chemical and Biomolecular
Engineering
Georgia Institute of Technology

Dr. Andrew J. Medford
School of Chemical and Biomolecular
Engineering
Georgia Institute of Technology

Dr. Blair K. Brettmann
School of Materials Science and
Engineering
Georgia Institute of Technology

Date approved: April 27th, 2021

Dedicated to my family with love,

Soeun, Jooha, Jungheon, and Hyunjoo

ACKNOWLEDGMENTS

LIST OF TABLES

LIST OF FIGURES

xviii

LIST OF ACRONYMS

AIC Akaike information criteria

AICc corrected Akaike information criteria

ANN artificial neural network

ATR-FTIR attenuated total reflectance-Fourier transform infrared

BCF Burton-Cabrera-Frank

BIC Bayesian information criteria

CE conservation element

CE/SE conservation element/solution element

CFL Cournat-Friedrichs-Lewy

CLD chord length distribution

CNT classical nucleation theory

CSD crystal size distribution

DNC direct nucleation control

DP dynamic programming

FBRM focused beam reflectance measurement

FDM finite-difference method

FEM finite-element method

FVM finite-volume method

MPC model predictive control

MSM Markov state model

PAT process analytical technology

PBM population balance model

PDE partial differential equation

PSD particle size distribution

SE solution element

SNN shallow neural network

SSC supersaturation control

NOMENCLATURE

English letters

$\bar{L}$ Mean crystal size

$\bar{L}_{a,b}$ Mean crystal size with a^{th} and b^{th} moments

$\hat{c}$ Measured concentration

$\hat{v}$ Measured volume density distribution

$\sqrt{d}$ Distance between current state and target position

A Surface area of crystals

B^j Matrix of the sensitivities

B_1 Primary nucleation constant

B_2 Secondary nucleation constant

c Concentration

C_0 Normalized non-weighted chord count

C_2 Normalized square-weighted chord count

c_s Solubility

D Crystal dissolution rate

D_{diff} Diffusion coefficient

G Crystal growth rate

G_s Gibbs free energy for the formation of a surface

G_v free energy change for the phase transformation

h FTIR peak height ratio between paracetamol and ethanol

K Mass transfer coefficient

k Boltzmann's constant

k_a	Area shape factor
k_g	Crystal growth constant
k_i	Parameters for FTIR conversion model
k_v	Volume shape factor
k_{b1}	Pre-exponential factor in the Arrhenius equation for primary nucleation rate
k_{b2}	Pre-exponential factor in the Arrhenius equation for secondary nucleation rate
L	characteristic length of crystals
M	Mid-point of each bin in the FBRM measurements
m_c	Crystal mass
M_T	suspension density
n	Number density of crystals
$N_{d,i}$	Number of sampled data for the ith run
$N_{d,q}$	Number of samples for each measurement
$N_{m,v}$	Number of size ranges for volume density distribution
N_r	Number of experimental runs
R	Universal gas constant
r_c	radius of a cluster
S	Relative supersaturation, c/c_s
s_1	Reduced-order state in crystallization control, $s_1 = \mu_0 \times 10^{-6}$
s_2	Reduced-order state in crystallization control, $s_2 = \mu_3 \times 10^{-12}$
T	Temperature
t	time
V	Actual volume of crystals
v	Molar volume of solute
v_s	Stirring rate
V_θ	Covariance matrix of parameter set, θ
w_c	Weight for the term of concentration

X Mole fraction of paracetamol in the ethanolic solution

E_{a_d} Activation energy of crystal dissolution

E_{a_g} Activation energy of crystal growth

Greek letters

α Exponential factor in the model for secondary nucleation rate

β Exponential factor in the model for secondary nucleation rate

δ Boundary thickness

γ Parameter to adjust running cost in 4.11

γ_d Exponential parameter on supersaturation for crystal dissolution

γ_g Exponential parameter on supersaturation for crystal growth

γ_{ls} Liquid-solid surface tension

$\hat{\theta}$ Set of estimated parameters

μ_j j^{th} moment

Φ Objective function

π State-feedback control policy

ρ Weight to input effort in 4.11

ρ_c crystal density

σ Relative supersaturation, $S - 1$

τ Time index

θ Set of parameters

Superscription

$\oplus$ Target

Subscription

$_0$ Initial value or initial condition

$_c$ Terms for crystal or crystallization

$_d$ Terms for dissolution

SUMMARY

This thesis reports a framework to control the mean volume size and mass of paracetamol crystals in ethanolic solution for batch cooling crystallization. This framework utilizes the Markov state model (MSM) and dynamic programming (DP) approaches based on simulation results by a population balance model (PBM) model to obtain the optimal control policy for crystallization.

Since the MSM is an empirical model, a training data set is required, and numerous data points are needed to improve the model accuracy. To reduce the experimental attempts to establish the MSM, PBM simulation results are employed instead of experimental data. The PBM includes kinetic models for primary nucleation, secondary nucleation, crystal growth, and crystal dissolution. Crystallization experiments were carried out with temperature cycling, and kinetic parameters of the PBM were estimated and validated using the experimental data set. Since the PBM can predict the crystallization processes, this model generates data points to train the MSM. The trained MSM and DP approach optimizes the control policy to obtain desired crystal properties. The policies are tested by the PBM simulation and open-loop control experiments. However, it is challenging to get desired crystal properties using the open-loop control scheme due to the thermal response delay in the experimental system. Also nucleation time is stochastic.

In addition, a feedback control scheme with an updated optimal control policy was employed to obtain the desired crystals. Since the process analytical technology (PAT) measurements, such as the focused beam reflectance measurement (FBRM), differ from the reduced-order states in the MSM, a model was built to convert the measurements into reduced-order states. A shallow neural network (SNN) model is developed for the data translation, and the crystallization system employs this model to monitor the solution status during the feedback control. The feedback control automatically manipulates the temperature profile to obtain crystals with the desired characteristics, and the control processes are

completed when the system condition meets the control criteria. This thesis combines the first-principle model with a machine learning approach to demonstrate a process to control the mean volume size and crystal mass in unseeded batch cooling crystallization.

CHAPTER 1

INTRODUCTION

Separation and purification are important steps to improve the product quality in chemical processes. Among various types of separation processes, crystallization has a simple method but efficient results. Batch and continuous processes can be employed to operate crystallization according to the manufacturing scale and frequency of the product change in one process for the bulk, fine chemical, pharmaceutical, and food industries [1]. Batch crystallization has several advantages such as simple facilities, low installation cost, and flexibility in a product change [2]. Crystallization processes are generally operated to produce solid crystals with desired size, crystal size distribution (CSD), and polymorphic forms. The fundamental driving force for crystallization control is the chemical potential which is represented as supersaturation. To obtain desired product characteristics from the crystallization process, operators can manipulate process variables such as system temperature, pH of the solution, and amount of anti-solvent. From various methods to adjust the supersaturation, cooling crystallization can be performed by manipulating only a single control variable, temperature, without the addition of another component [1]. However, it is challenging to obtain the optimal temperature profile to produce crystals with desired crystal characteristics. Therefore, the goal of this study is to control the mean size and mass of paracetamol crystals from ethanolic solution using Markov state model (MSM) and dynamic programming (DP), where the population balance model (PBM) simulations generate the training set for the MSM. Chapter 2 reviews the fundamentals of crystallization and experimental measurements relevant to this thesis.

Chapter 3 shows development of a PBM to describe the crystallization and dissolution of paracetamol from an ethanolic solution. Kinetic model parameters for primary nucle-

ation, secondary nucleation, growth, and dissolution of crystals are estimated to describe experimental data. The PBM considers one-dimensional crystallization and dissolution, which is solved by the space-time conservation element/solution element (CE/SE) method. This model predicts crystal size distributions during the crystallization and dissolution in a temperature cycling strategy that performs a repetition of increasing and decreasing temperature.

Even though the PBM is established, obtaining optimal control policy using only the PBM is still challenging due to the numerous potentialities of manipulating temperature profiles. Hence, Chapter 4 demonstrates open-loop control to produce crystals with the desired mean size and mass of crystals. The optimal control policies are obtained by dynamic programming with a trained MSM through training sets by the developed PBM. The MSM is implemented to describe the change of states, which consists of moments of crystal size. DP is used to find the optimal control policy to produce crystals that have the desired mean size and mass. The optimal control policies by this step are validated by simulation and experiments.

Chapter 5 describes a transformation method for measurements given by the focused beam reflectance measurement (FBRM) to obtain key properties of crystals, with the aim of performing feedback control of the system. The states used in the DP approach are modified from the simulation results, and the measurements by the FBRM capture some characteristics of crystals such as shape, size, and density. Hence, a correlation between the measurements and simulation results is required. For this purpose, stepwise linear regression determines the appropriate input for correlating the measurements, and regression via a shallow neural network is carried out using the chosen input.

The insights from the above works are extended to the feedback control of batch cooling crystallization in Chapter 6. Simulation and experiments for feedback control are carried out that generate the crystals with the target mean size and mass. The temperature profile has been updated according to the converted measurements and the learned supersaturation

values stored in the lookup table. This chapter shows results through a cascade control in the experimental system. This chapter compares the monitored control results by process analytical technology (PAT) tools and analyzed crystals by sieving and weighing, and the results show consistency.

Chapter 7 summarizes results and conclusion through this thesis. Moreover, recommendations and further works to improve this study are discussed.

CHAPTER 2

BACKGROUND

In this chapter, the fundamentals of crystallization and the control of crystallization processes are presented. Also, several analysis techniques for the crystallization process and product are described.

2.1 Mechanisms in crystallization

2.1.1 Nucleation

Nucleation is the first step of crystallization because a new phase appears from the solution. Nucleation can be classified by two kinds of phenomena: primary nucleation and secondary nucleation. Each nucleation step also has various causes as shown in Figure 2.1.

Primary nucleation

Primary nucleation has two categories: homogeneous nucleation and heterogeneous nucleation. Homogeneous nucleation means nuclei are generated from the clear supersaturated solution i.e., one without any suspended crystals. To explain primary nucleation, two theories are suggested: the classical nucleation theory (CNT) and the two-step nucleation theory.

The CNT expresses the formation of a new cluster using Gibbs free energy [3, 4] and the critical size of the crystal. This idea was described by Gibbs, and the free energy for the nucleation consists of the summation of the free energy change for the volume of the new solid phase and the free energy change for the formation of a surface. The CNT has an assumption that the cluster has a spherical shape, so the free energy change for cluster
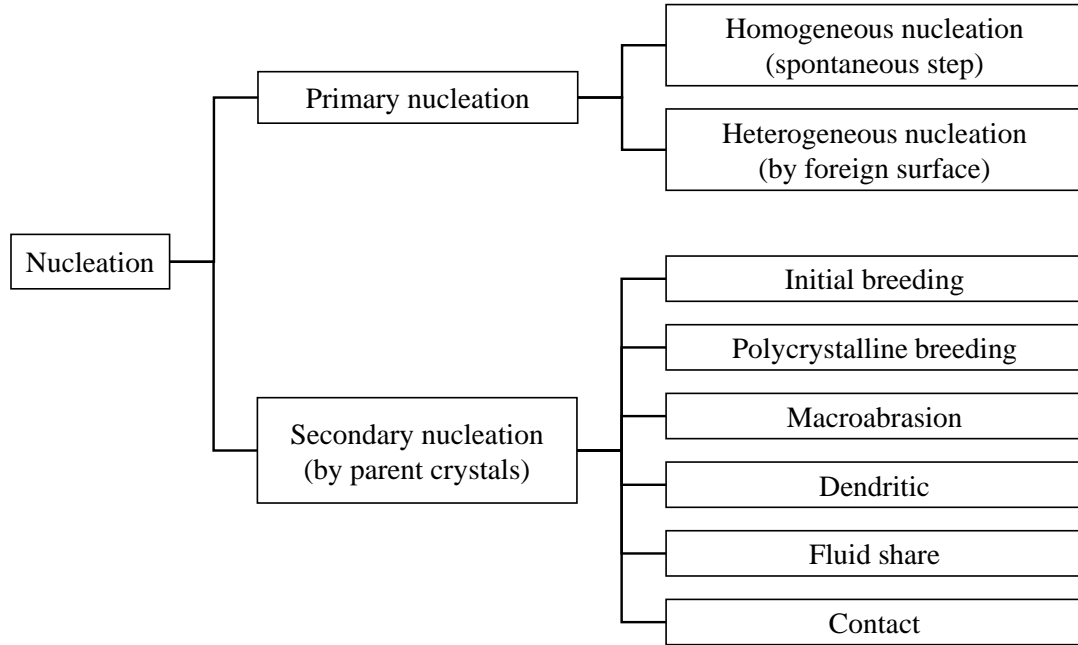
Figure 2.1: Categories of nucleation

formation is

$$\Delta G = \Delta G_s + \Delta G_v = 4\pi r^2 \gamma_{ls} + \frac{4}{3}\pi r^3 \Delta G_v \qquad (2.1)$$

where ΔG_s is free energy change for the formation of a surface, ΔG_v is free energy change for the phase transformation, r is the radius of the cluster or crystal, and γ_{ls} is the interfacial tension between solute cluster and solvent. ΔG_v has negative values because the solid state is more stable. This aspect makes ΔG decrease in the system as shown in Figure 2.2.

The cluster size with the maximum value of ΔG is the critical size of the cluster, r_c. If the cluster size reaches r_c, the cluster becomes stable, and remains in the solid phase. ΔG_{crit}, which is the maximum value of ΔG, can be obtained through $d(\Delta G)/dr = 0$, so

$$\frac{d(\Delta G)}{dr} = 8\pi r_c \gamma_{ls} + 4\pi r_c{}^2 \Delta G_v = 0 \qquad (2.2)$$

therefore,
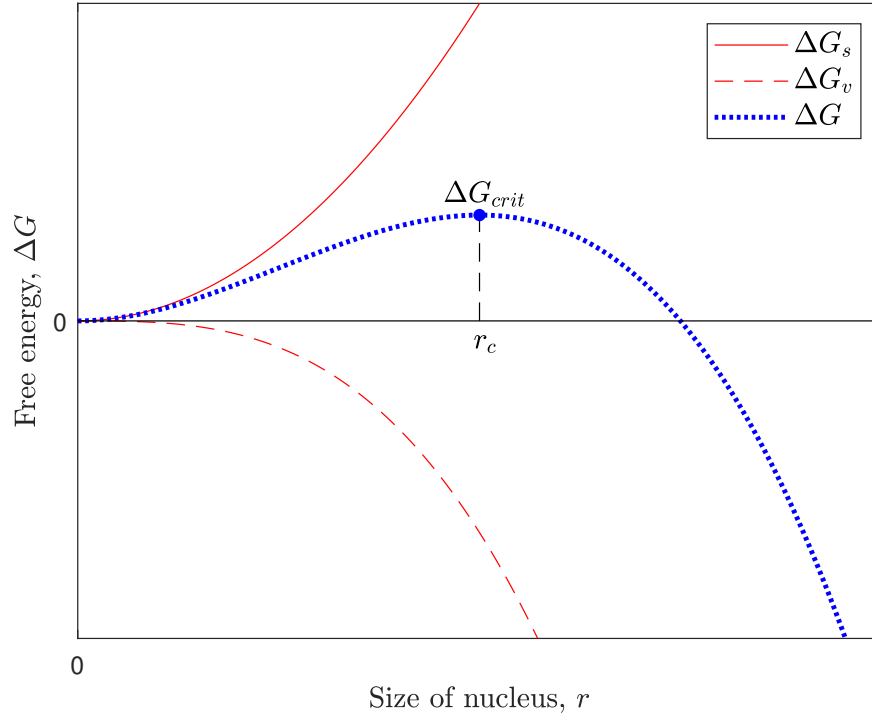
Figure 2.2: Trends of free energies to determine the critical size of the cluster

$$r_c = -\frac{2\gamma_{ls}}{\Delta G_v} \tag{2.3}$$

By substituting Equation (2.3) into Equation (2.1),

$$\Delta G_{crit} = \frac{4\pi r_c{}^2 \gamma_{ls}}{3} \tag{2.4}$$

However, ΔG_{crit} is a function of the critical size of a cluster and the surface tension. It is difficult to measure r_c and γ_{ls} directly, but supersaturation, S can be determined more easily. Therefore, supersaturation was used to evaluate ΔG_{crit} more easily. Here, the Gibbs-Thomson equation is employed to find the relationship between ΔG_{crit} and the supersaturation. The Gibbs-Thomson equation is

$$\ln \frac{c}{c_s} = \ln S = \frac{2\gamma_{ls}v}{kTr} \tag{2.5}$$

where c is the concentration of solute in solvent, c_s is solubility of solute in solvent, v is a molar volume of solute, k is Boltzmann's constant, T is absolute temperature, and r is the cluster size. Substituting Equation (2.5) with r_c into Equation (2.4), ΔG_{crit} becomes

$$\Delta G_{crit} = \frac{16\pi\gamma_{ls}^3 v^2}{3\left(kT\ln S\right)^2} \tag{2.6}$$

The nucleation rate has been expressed in the form of an Arrhenius equation [5, 6]

$$B_1 = k_{b1}\exp\left(-\frac{\Delta G_{crit}}{kT}\right) \tag{2.7}$$

where $B_{1,pre}$ is a pre-exponential factor. Substituting Equation (2.6) into Equation (2.7) provides the final equation for the primary nucleation rate by CNT as

$$B_1 = k_{b1}\exp\left[-\frac{16\pi\gamma_{ls}^3 v^2}{3k^3T^3\left(\ln S\right)^2}\right] \tag{2.8}$$

The CNT assumes that the aggregation of solute molecules and the alignment of the structure take place simultaneously. However, another theory suggests that nucleation occurs through two steps: the first step is that a dense liquid phase appears, and the second step is reorganization of the cluster into the crystalline structure. The classical nucleation and two-step theories are described in Figure 2.3. A few cases of two-step nucleation observation have been reported. Bonnet *et al.* [7] directly observed separation of solute-rich liquid phase during crystallization of a small organic molecule for the first time. The two-step nucleation of gold crystals was also observed in real-time using transmission electron microscopy (TEM) [8]. According to Jeon *et al.* [8], the atoms repeatedly transit between dense-liquid and crystalline states during the nucleation. However, the two-step nucleation theory is usually applied and validated for complex and large molecules such as proteins and polymers [9, 10].

Heterogeneous nucleation takes place on foreign bodies such as dust, the wall of crystallizers, and the stirrer. It is known that the foreign bodies have a role to reduce the required
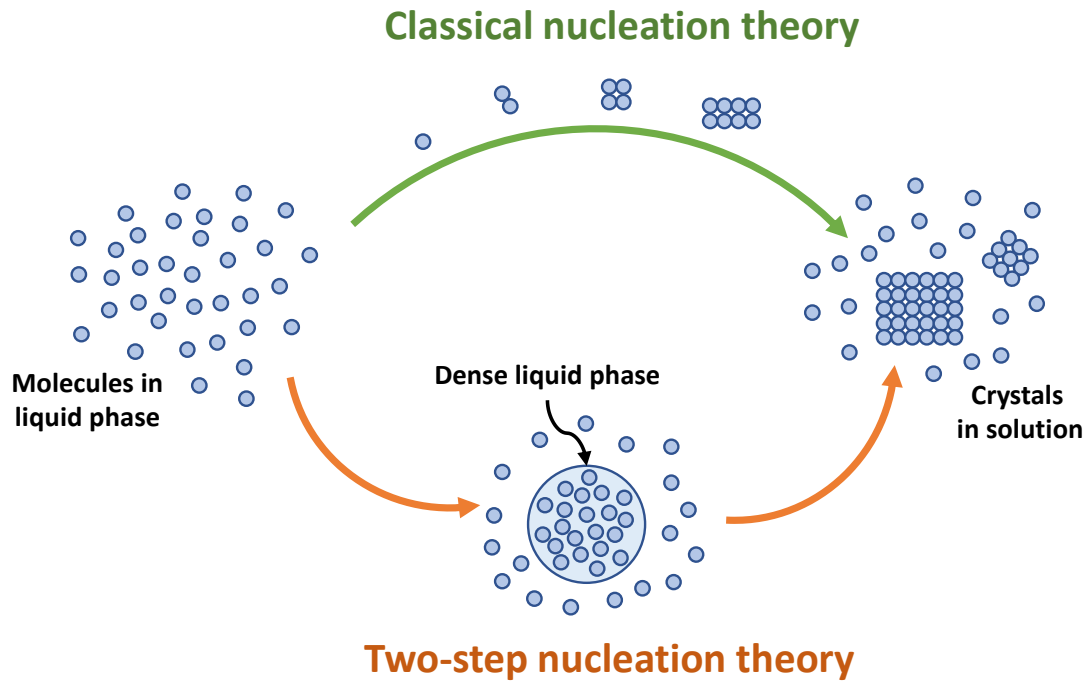
Figure 2.3: Classical nucleation theory and two-step nucleation theory

activation barrier for nucleation [11]. According to Volmer and Weber [12], the reduction of the activation barrier depends on the contact angle between the cluster and the foreign surface. If the contact angle is lower, the shape of the cluster becomes flatter. In this case, the nucleation can happen at lower supersaturation due to the reduced activation barrier.

Primary nucleation is reported to have a stochastic characteristic, which has been investigated by measuring the induction time [13–17]. The stochasticity of primary nucleation is modeled using statistical descriptions such as a Poisson distribution, the Weibull distribution, and the log-normal distribution [17]. Due to the stochastic nature of primary nucleation, seeding is often employed to control the crystallization via secondary nucleation. Another method to minimize the stochastic nature of primary nucleation is adding a temperature plateau in the temperature profile to make the crystallization system robust to the stochasticity [18, 19].

Secondary nucleation

Secondary nucleation occurs through mechanisms involving existing crystals in the solution and occurs at supersaturations lower than required for primary nucleation. Even though various mechanisms affect the secondary nucleation such as initial breeding, the formation of needle-like and polycrystalline particulates, microabrasion through contact of crystals, collision among crystals, impurity concentration gradient, and fluid shear, as shown in Figure 2.1, it is challenging to investigate which mechanism takes place in the crystallization system [1].

Factors that affect secondary nucleation are the degree of supersaturation, stirring rate or mixing intensity [20, 21], and suspension density. Therefore, an empirical model with these factors was employed to describe the secondary nucleation as below

$$B_2 = k_{b2} v_s^i M_T^j (S - 1)^n \tag{2.9}$$

where k_{b2} is the secondary nucleation rate constant, v_s is the stirring rate, M_T is the suspension density, and S is supersaturation in the solution. Δc is the difference of the concentration in the solution and the solubility, and this property can be used instead of S. If v_s is constant, it can be lumped with k_{b2}.

2.1.2 Growth and dissolution of crystals

Crystal growth is a phase change between liquid and solid phases, while supersaturation is the driving force to transport solute molecules from the solution to the crystal surface. Crystal growth occurs as a continuous process of mass transfer from the solution to the crystal face, which may be represented by diffusion of solute molecules through a boundary layer, and integration on the surface of existing crystals. Hence, when one of the two mechanisms is limiting the rate of growth, the crystal growth rate can be determined by one of the two mechanisms.

Solute integration into growing crystals has been described by three different growth models: 1) continuous growth on a rough surface, 2) birth-and-spread growth, and 3) Burton-Cabrera-Frank (BCF) growth or spiral growth [22]. The crystal surface usually has three kinds of sites such as (A) flat site, (B) step site, and (C) kink site as shown in Figure 2.4. Each site has different number of surrounding faces, and molecules tend to bond at sites with higher number of nearest neighbors.
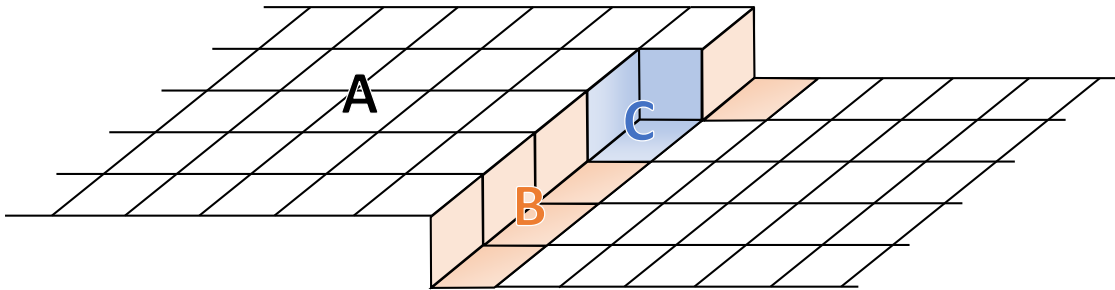
Figure 2.4: The possible sites on a surface for growing crystals: (A) flat surface, (B), step site, and (C) kink site.

The rough growth is a simple idea that occurs at a site with the lowest energy for the crystal integration on a rough surface of crystals. The birth and spread mechanism is also called two-dimensional growth. The beginning of this mechanism is nucleation on the crystal surface. Subsequently, the crystal spreads near a new cluster. Because the energy requirement of spreading is lower than nucleation, the spreading process is faster than the birth of the new cluster. However, the idea that nucleation is obligatory for crystal growth cannot describe the continuous crystal growth in lower supersaturation. The BCF model shows a self-perpetuating growth of crystal along the spiral shape, initiated by a screw dislocation. In the BCF model, the step and kink sites are generated automatically near the spiral, which can explain continuous growth.

Diffusion-controlled growth is the case where the diffusion process is the rate-limiting step. In diffusion-controlled growth, the boundary layer thickness and diffusivity between

solution and crystal affect the growth rate. The basic mass transfer principle is used to describe the crystal growth rate. If the crystallization takes place without agitation, the thickness of the boundary layer cannot be neglected. In this case, the crystal growth rate can be expressed as a simple mass transfer equation [1]:

$$\frac{dm_c}{dt} = D_{\text{diff}} A \left(\frac{c - c_s}{\delta} \right) \tag{2.10}$$

where m_c is the mass of crystals, t is time, D_{diff} is the diffusion coefficient, A is the surface area, c is concentration of the solvent, c_s is the solubility, and δ is the boundary layer thickness. The boundary layer thickness may vary, based on the system condition, such as the stirring rate, but is not measured directly. Therefore, a mass transfer coefficient, $K = D/\delta$, is employed. The mass of crystals and surface area are expressed by the following equations

$$m_c = \rho_c V = \rho_c k_v L^3 \tag{2.11}$$

$$A = k_a L^2 \tag{2.12}$$

where ρ_c is the crystal density, k_v is a volume shape factor of crystals, k_a is an area shape factor, V is the actual volume of crystals, and L is the characteristic length of crystals. Substituting Equations (2.11) and (2.12) in Equation (2.10) gives

$$\frac{dL}{dt} = \frac{K k_a}{3 k_v \rho_c} (c - c_s) = k_g \Delta c \tag{2.13}$$

In the crystallization system, diffusion and integration affect the crystal growth simultaneously. It is challenging to separate the effect of each phenomenon, so the growth rate is usually expressed as an empirical model. Since supersaturation is the driving force of growth and the growth kinetic rate is temperature-dependent, the empirical growth rate is

11

often given by

$$G = k_g \exp\left(-\frac{E_{a_g}}{RT}\right)(c - c_s)^{\gamma_g}, \qquad c \geq c_s \tag{2.14}$$

where G is the growth rate of crystals, k_g is the pre-exponential rate constant, E_{a_g} is the activation energy, γ_g is an exponential parameter on supersaturation, and R is the universal gas constant. The subscript g represents the crystal growth.

Crystal dissolution occurs when the supersaturation becomes less than 1, and it is the opposite mechanism to crystal growth. Crystal dissolution takes place in two steps: 1) detachment of a molecule from the crystal surface and 2) mass transfer of the molecule to the bulk solution through the boundary layer. Equation (2.14) expresses the crystal dissolution in this study.

$$D = k_d \exp\left(-\frac{E_{a_d}}{RT}\right)(c_s - c)^{\gamma_d}, \qquad c \leq c_s \tag{2.15}$$

where parameters with the subscript, d, indicating dissolution in Equation (2.15), have the same definition as parameters in Equation (2.14).

2.1.3 Agglomeration

Agglomeration is one of the key mechanisms in the crystallization system because it can affect the particle size distribution (PSD) and the shape of crystals [23]. According to Brunsteiner *et al.*, agglomeration takes place through a seriese of steps: 1) approaching a various number of particulates on a macroscopic scale through the flow of solution, 2) interacting among particles, solvent, impurities that are close in nanometer scale, and 3) bonding of solid particles as shown in Figure 2.5.

This agglomeration mechanism is strongly affected by collision frequency, and the collision rate is highly related to the shear rate [24]. Mumtaz *et al.* [25] reported that the agglomeration rate reaches a maximum as the shear rate increases, but decreases again
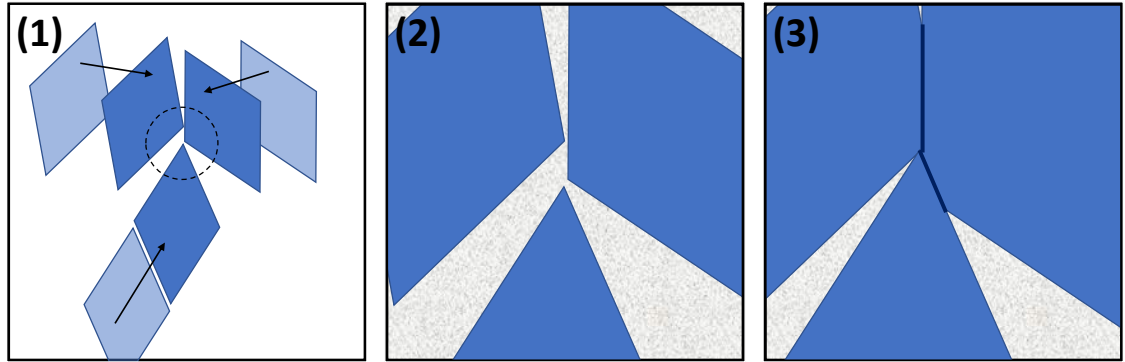
Figure 2.5: Steps of agglomeration: (1) approaching crystals, (2) interacting crystals in the microscopic scale that represents zoomed-in part of the dashed-line circle in the first figure, and (3) bonding crystals where the dark blue lines show the agglomerated surfaces on crystals.

when the shear rate becomes higher than a certain value. Because the shear rate is proportional to stirring speed, sufficiently fast enough agitation can reduce the agglomeration since a high shear rate causes frequent collisions among crystals, which can also break agglomerated crystals. Therefore, the implementation of a sufficient stirring rate can reduce the agglomeration rate.

2.1.4 Breakage

Breakage of crystals generates a larger number of small fragments from a parent crystal by collisions among crystals or collision between the crystal and impeller. The broken crystals can serve as seeds for the secondary nucleation or grow into a new crystal.

An important factor of crystal breakage is crystal shape specifically the aspect ratio. Sato *et al.* reported the breakage of needle-like potassium dihydrogen phosphate crystals that have higher aspect ratios than a threshold aspect ratio and developed a model to describe the crystal breakage using experimental data [26]. If crystals are spontaneously broken in the crystallization system, this mechanism should be considered in the modeling. However, if the crystal breakage is not observed from the experimental system, the population balance model (PBM) model does not need to include the mechanism.

2.2 Control of crystallization

2.2.1 Model-free control

The crystallization process control is challenging due to the complicated internal and external attributes of crystallization phenomena. Crystallization involves highly nonlinear dynamics, stochasticity, and complexity, and the crystallization process can be affected by unexpected external irregularities such as nonideal mixing and property changes by polymorphic transformations. In order to control crystallization processes, various methods have been developed and employed, including model-free methods and model-based methods. Representative examples of model-free control methods are supersaturation control (SSC) and direct nucleation control (DNC).

Supersaturation control

In SSC, the supersaturation, which is obtained with the measured concentration of the mother liquor, is controlled to maintain a specified value [27–34]. In this control strategy, the temperature profile is continuously moving to keep the supersaturation level at the setpoint.

Direct nucleation control

In DNC, the *in situ* measurement of the number of crystals in the system can switch between two modes, cooling and heating. When the number of crystals exceeds the setpoint, heating is triggered to dissolve crystals; conversely, when the number of crystals is smaller than the target number of crystals, the system switches to the cooling mode to grow crystals. In this manner, the fines can be removed so that the mean crystal size is increased. To estimate the number of crystals, the focused beam reflectance measurement (FBRM) can be utilized [35–39].

Moreover, SSC and DNC can be combined for optimized crystallization control [40].

For SSC and DNC methods, the measured concentration and the system temperature are used to estimate the supersaturation, and temperature or amount of anti-solvent are manipulated through a cascade PID controller. Model-free control is intuitive, but it has drawbacks such as unknown a priori batch time and the lack of optimality.

2.2.2 Model-based control

In contrast to a model-free feedback control scheme, feedback control approaches based on an objective function can be effective to minimize the process cost. System control with an objective function can estimate the optimal input policy to minimize the expected operation cost or to maximize the productivity of the crystallization system. The optimal input policy can be determined according to the *in situ* measurement and a dynamic model. Key examples of the model-based control methods are model predictive control (MPC) and dynamic programming (DP) [41–43].

Model predictive control

MPC has been widely used in chemical process control following the improvement of computers. Researchers began to use model-based optimization for crystallization control in the 1990s [43]. In this strategy, online computation is required to predict the states at the next time step based on either a first-principle model or an empirical model. The PBM is a typical first-principle model, but it is a partial differential equation that is nonlinear and computationally expensive. A reduced model with several ordinary differential equations based on the method of moments was applied for MPC to control the crystallization [44–47]. Moreover, MPC for batch crystallization has been conducted in simulations due to nonlinear characteristics of the PBM, with only a few applications of MPC in experimental crystallization processes [48, 49].

Dynamic programming

The DP approach for crystallization control also requires a model to establish the control policy, but control actions can be precalculated offline and stored in a look-up table. This approach breaks down a complicated problem into simple sub-problems and searches sub-problem solutions from the look-up table instead of repeating calculations for the same sub-problems. This approach is simple to apply to actual systems so that domain practitioners can use it intuitively. The dynamic model in this approach does not need to be a theoretical model. Griffin *et al.* utilized the concept of the Markov state model (MSM) for the dynamic model of a crystallization system, and used data points measured using the FBRM and attenuated total reflectance-Fourier transform infrared (ATR-FTIR) in real-time to train the MSM [50, 51]. The first-order MSM has an assumption that a state transition depends on the state and input only at the current time; past conditions do not affect the future states. A look-up table stores the trained MSM results, and the DP approach employed data in the look-up table to obtain optimal control policy for crystals with desired characteristics. This idea was applied in this thesis, with details described in Chapter 4.

2.3 Measurements in experiments

2.3.1 Focused beam reflectance measurement

The FBRM is an *in situ* instrument with applications that include investigating crystallization fundamentals [52], designing crystallization process [53–55], monitoring and operating crystallization processes [56, 57], optimizing crystal shape [58, 59], and managing impurities [60, 61]. This equipment shoots a laser and detects the back-scattered light on the surface of crystals. As the laser passes over the surface of a particle in a circular movement, the length and number of the arcs that reflected the laser are recorded. Figure 2.6 schematically shows how the FBRM works.

If the crystal surface is perfectly smooth, it is easy to analyze back-scattered light. How-

ever, the crystal surface is usually rough due to various reasons such as secondary nucleation, agglomeration, or breakage. Therefore, the FBRM has two different chord-selection modes depending on which phenomenon the user focuses on: 1) primary mode and 2) macro mode. The primary mode collects all reflectance signals without any treatments, so fines or needle-type particles can be detected with higher sensitivity. This mode has advantages when nucleation and breakage are the desired phenomena to observe. On the other hand, the macro mode uses a digital filter to reduce sensitivity when it is thought that the edges of the particles are nearby. If the crystal surface has steps or bumps, the primary mode might collect a number of detected chords on the same crystal surface. However, the macro mode can count this as one chord so that this mode can reduce error from the roughness of growing crystals.

The measured chord length is not perfectly translated to the particle size because the laser randomly passes on the crystal. In addition, the crystal shape affects the chord length. For example, a system with spherical crystals can provide a broad chord length distribution
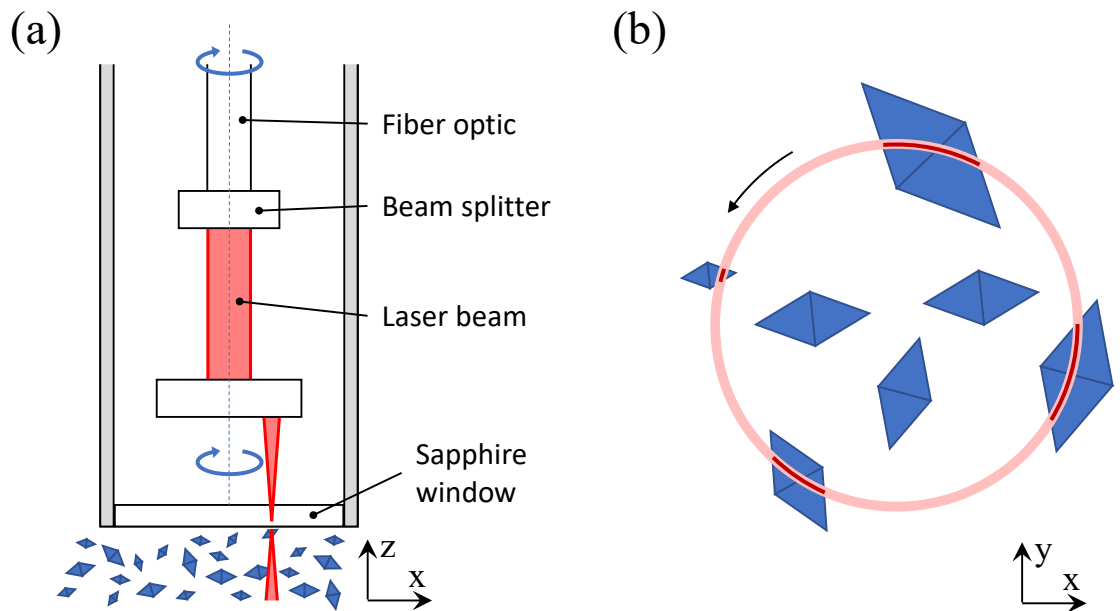
Figure 2.6: FBRM measuring principle. (a) A schematic diagram inside the FBRM probe, (b) The measuring chord lengths and counts with the rotating laser. The pink circle is the laser path from the probe, and the red arcs are the detected chords.

(CLD) [62], but needle-shape crystals show skewed distributions [63]. Therefore, many studies have been reported to convert between CLD and CSD using various methods. Even though the actual systems are in 3-dimensional space, the scanned region by the laser can be considered as a 2-dimensional plane by a projection. Hence, geometric models are developed to convert for different particle shapes [62, 64–68]. Li *et al.* instead employed a fingerprint region from CLD and a convolution form to recognize CSD [69, 70]. Irizarry *et al.* [71, 72] employed data-driven approaches to translate CLD to CSD for unimodal and multimodal size distributions. Crestani *et al.* used an artificial neural network (ANN) model to translate from CLD by the FBRM to CSD by the sieving analysis [73].

2.3.2 Attenuated Total Reflectance-Fourier Transform Infrared

Calibration for solution concentration

An ATR-FTIR instrument was employed to recognize the concentration of paracetamol in ethanolic solution in this study. The concentration of the paracetamol solution was estimated by the measured IR absorbance data and a calibration model. The mass ratio of the paracetamol to ethanol was used for consistency with previous studies [19, 74–77]. Generally, the definition of a solution concentration is the mass or mole of a solute divided by the volume of a solution. However, it is difficult to track the accurate volume of a solution because it depends on the dissolved amount of solute. Thus, the unit of g-solute/g-solvent or g-solute/kg-solvent was employed.

A univariate approach was applied to infer the characteristics of crystallization because only two species affect the concentration of the solution; univariate approaches usually use peak heights, integrated peak area, or ratio of the normalized peak heights or area [78]. In this study, the calibration model is based upon the ratio of peak heights of each material on the FTIR spectrum because the peak height of paracetamol increases, and the peak height of ethanol decreases when the paracetamol concentration increases. According to the previous research [19], the wavenumbers of ethanol and paracetamol are 1048 cm^{-1}

and 1667 cm^{-1}, respectively, as shown in Figure 2.7. However, the FTIR signals depend on various conditions such as probe alignment, contact of liquid and probe, and background absorbance [79]. To handle this problem, the peak at 1800 cm^{-1}, which is not affected by the concentration of paracetamol and ethanol, was used as a reference peak. The concentrations of ethanol and paracetamol were given by normalizing two peaks, at 1048 and 1667 cm^{-1}, by that of the reference peak. The concentration is based on the ratio between these two species, so the ratio of peak heights for paracetamol and ethanol was applied to determine the concentration in the solution.

A set of experiments was performed to relate the response of the peak-height ratio of IR absorbance to the actual concentration and temperature change. Paracetamol-ethanol solution samples ranging from pure ethanol to 0.40 g-solute/g-solvent were prepared, and the ratios of peak heights for paracetamol and ethanol of IR absorbance were measured. The
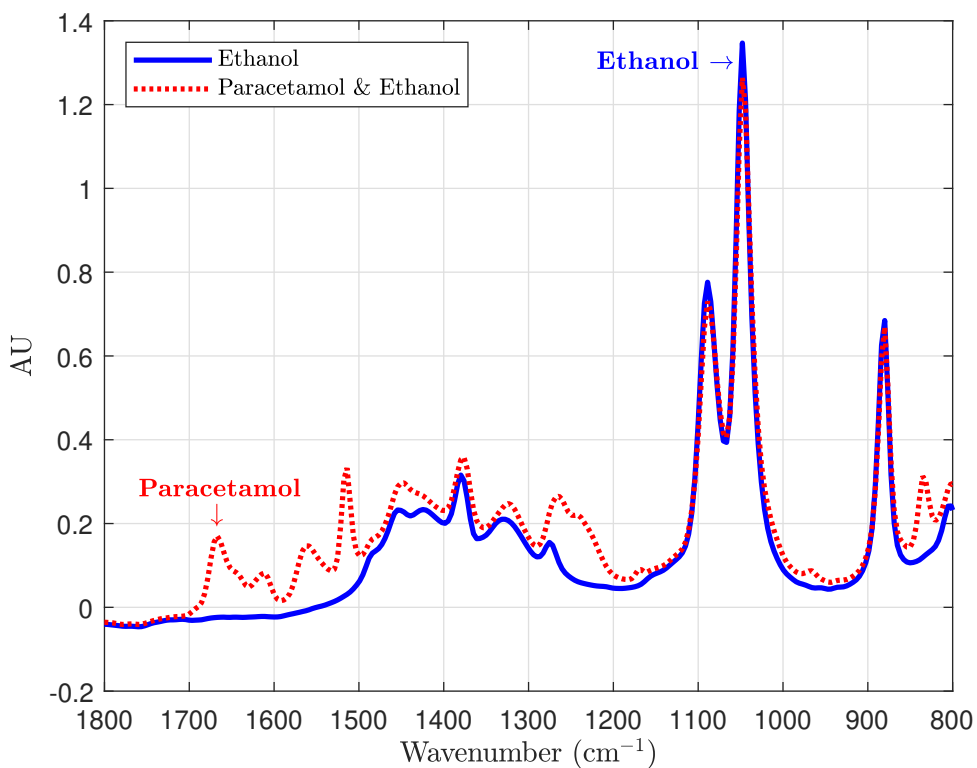
Figure 2.7: IR spectra for pure ethanol and paracetamol solution. Peaks at 1048 cm^{-1} and 1667 cm^{-1} represent ethanol and paracetamol, respectively.

range of concentration for this calibration model was determined up to 0.40 g-solute/g-solvent because the desired maximum concentration in this work was 0.35 g-solute/g-solvent. Figure 2.8 shows that the ratio of peak heights changes according to the temperature of the solution even when the concentration of the solution is constant. Hence, the influence of temperature should be considered in the calibration model between the ratio of IR peak heights and concentration. The calibration model is

$$h = k_1 X^2 + k_2 XT + k_3 X + k_4 T + k_5 T^2 + k_6 \tag{2.16}$$

where h is the FTIR peak-height ratio. Here, X is the mole fraction of paracetamol in the ethanolic solution, and T [K] represents the temperature of the system. The sensitivity of ATR-FTIR depends on the environmental conditions in the lab, so calibration is carried out
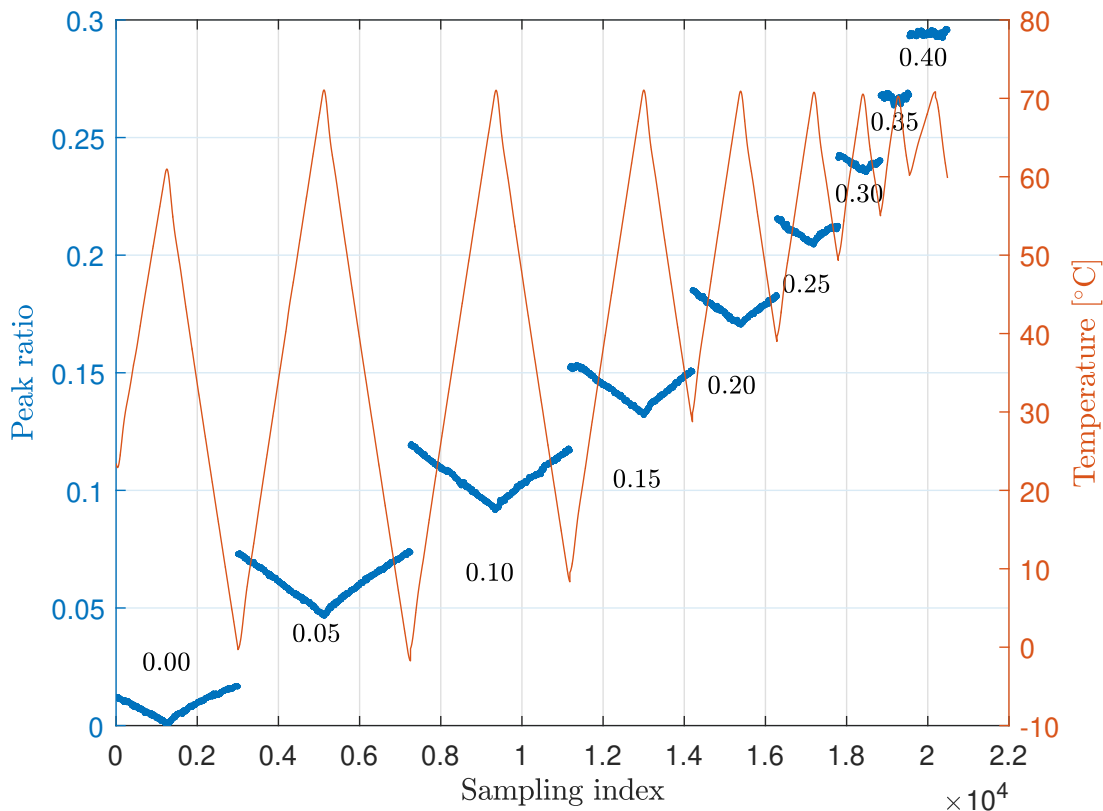
Figure 2.8: Change of IR peak-height ratio based on temperature. Values shown together with the peak ratios are the prepared concentration of the solution. Peak-height ratio has a nonlinear relationship with the solution concentration and the system temperature.

periodically to obtain accurate parameters for Equation (2.16).

Determination of solubility of paracetamol in ethanol

Solubility of paracetamol in ethanol was determined by five sets of continuous dissolution experiments by increasing temperature at the rate of 0.5 K/min. Each dissolution experiment was performed on a different day and the measured data varied slightly. Figure 2.9 shows the result of the solubility measurements. Solubility data sets have similar trends, and the average values of these data sets were used to correlate the solubility of paracetamol in ethanol, c_s [g-paracetamol/g-ethanol], as the following polynomial equation

$$c_s = -8.707 + 9.669 \times 10^{-2}T - 3.610 \times 10^{-4}T^2 + 4.590 \times 10^{-7}T^3 \qquad (2.17)$$
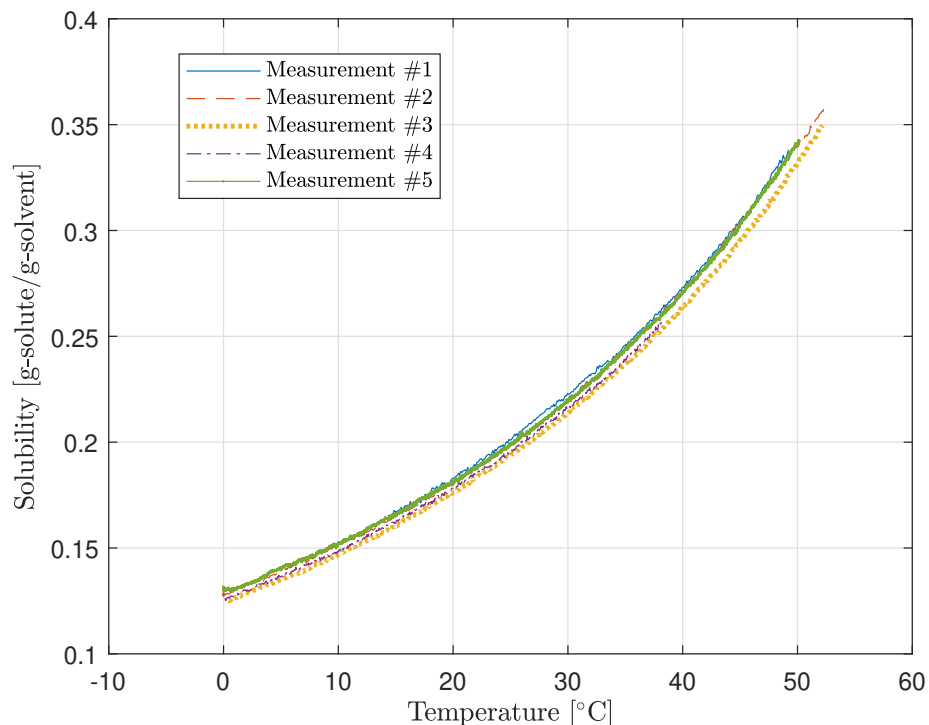
Figure 2.9: Five sets of solubility measurement data for paracetamol in the ethanol solution.

21
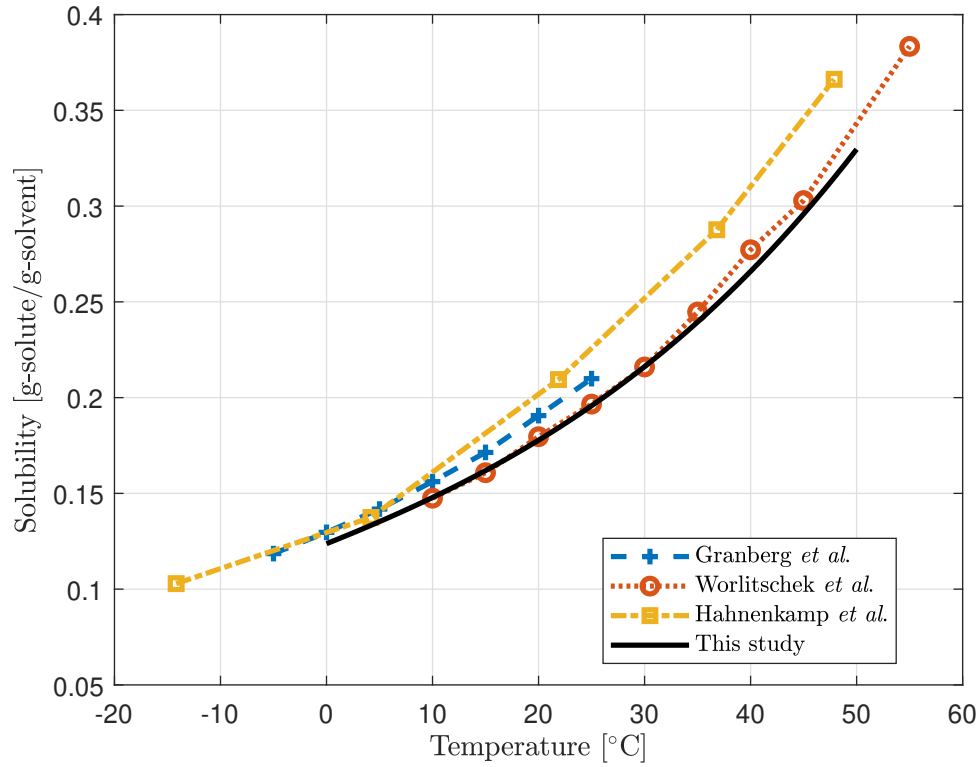
Figure 2.10: Solubility of paracetamol in ethanol.

where T is the system temperature, and the unit in Equation (2.17) is K.

The solubility of paracetamol in ethanol was reported several times [74, 80, 81], and the solubility from this study was compared to reported data in Figure 2.10. The obtained solubility curve shows similar trend to the results by Worlitschek and Mazzotti [74].

2.3.3 Characteristics of crystals

Volume shape factor of crystals

It is difficult to determine the volume of paracetamol crystals directly because of its complicated shape. Hence, a volume shape factor has been used to approximate the volume and mass of crystals [82]. Generally, the volume shape factor, k_v, is defined as follows:

$$k_v = \frac{V}{L^3} = \frac{m_c}{\rho_c L^3} \tag{2.18}$$

22

where k_v is the volume shape factor of crystals, V is the actual volume of crystals [m^3], L is the characteristic length of crystals [m], m_c is the mass of one crystal [kg], and ρ_c is the crystal density [kg/m^3]. The characteristic length was determined by the sieving and assumed to be the second-longest length of the crystal.
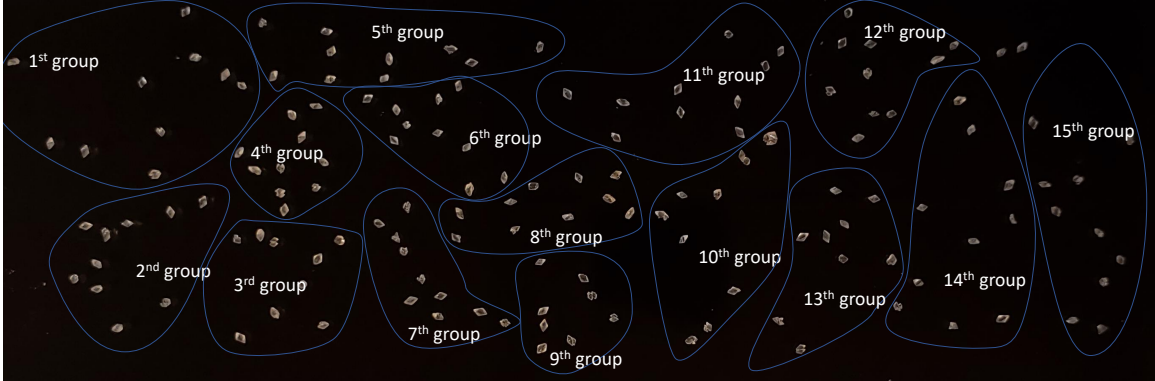
Figure 2.11: An example of the measurement of the volume shape factor of crystals. In this example, the crystal sizes are between 355 μm and 425 μm, and the geometric mean crystal size of two boundaries, 388.4 μm, represents all crystal sizes. In order to count crystals easier, crystals were grouped into bundles of ten crystal each. The mass of the 152 crystals is 7.68 mg.

The volume shape factor of paracetamol crystals was evaluated through gravimetric and geometric methods. Since the density of paracetamol crystals is already reported [70], measured crystal size and mass can provide the shape factor, via Equation (2.18). As shown in Figure 2.11, the mass and number of sieved crystals were measured to estimate the shape factors. In this work, 15 observations were carried out with crystals from seven different sieve size ranges of trays with 106 – 150, 150 – 212, 212 – 250, 355 – 420, 420 – 500, 500 – 600, and 600 – 850 μm, resulting in a shape factor of 0.778, which is close to 0.866 obtained by Worlitschek and Mazzotti [74].

In addition, geometric analysis was utilized to evaluate the volume shape factor with an assumption that the paracetamol crystal has octahedral shape, and the determined volume shape factor is 0.797. The detail steps and results for gravimetric and geometric analyses are shown in Appendix B.

Mean crystal size

Mean crystal size is defined by two different systems: 1) the moment-ratio system and 2) ISO system, but the former is usually employed since it can address particle size distributions [83]. Mean crystal size can be evaluated by various definitions, and more than 20 different methods have been reported [84–86]. A few examples of widely used mean size definitions when the crystal density is assumed constant are shown below.

$$\bar{L}_{10} = \frac{\Sigma n_i L_i}{\Sigma n_i} = \frac{\mu_1}{\mu_0} \tag{2.19}$$

$$\bar{L}_{21} = \frac{\Sigma n_i L_i^2}{\Sigma n_i L_i} = \frac{\mu_2}{\mu_1} \tag{2.20}$$

$$\bar{L}_{32} = \frac{\Sigma n_i L_i^3}{\Sigma n_i L_i^2} = \frac{\mu_3}{\mu_2} \tag{2.21}$$

$$\bar{L}_{43} = \frac{\Sigma n_i L_i^4}{\Sigma n_i L_i^3} = \frac{\mu_4}{\mu_3} \approx \frac{\Sigma (M_i L_i)}{\Sigma M_i} \tag{2.22}$$

$$\bar{L}_{30} = \left(\frac{\Sigma n_i L_i^3}{\Sigma n_i} \right)^{1/3} = \left(\frac{\mu_3}{\mu_0} \right)^{1/3} \tag{2.23}$$

where $\bar{L}_{ab}$ represents the mean crystal size with used moments, μ_a and μ_b; n, L, and M are the number density of crystals, characteristic length of crystals from each sieve tray, and mass of crystals, respectively; and subscript i is the size bin number. Among these methods, the volume-weighted mean crystal size, which is defined as Equation (2.22), is frequently used to evaluate the mean crystal size [86], and this mean size can represent the crystal size distribution by sieving analysis [85]. The volume-weighted mean crystal size and mass mean size have the same value under the assumption that the crystal density is constant. The sieving method provides crystal mass on each sieve tray as the result, so the

mean size of the sieve tray and mass from each sieve tray can be used to estimate the mass mean crystal size. The volume-weighted mean size is useful to evaluate the quality and yield of product from the process, but the fines cannot affect the volume-weighted mean size very much, due to the small mass of each fine. Therefore, a different method is needed to assess the influence of fines on the mean crystal size of the product.

The mean volume size, $\bar{L}_{30}$, uses μ_3 and μ_0, so $\bar{L}_{30}$ depends on the total number of crystals for crystals with a similar total volume. A large mean volume size for the same mass of crystals shows that the total number of crystals is low. Especially for cases of a similar volume density distribution, the larger mean volume size indicates the crystal bulk has less fines. The formation of nuclei by secondary nucleation can result in large amounts of fine particles being produced in the crystallizer. So, if the purpose of process control is to reduce the fraction of fine particles, obtaining a temperature profile that can minimize the number of fines is required for efficient process operation.

CHAPTER 3

A POPULATION BALANCE MODEL TO DESCRIBE UNSEEDED BATCH CRYSTALLIZATION WITH TEMPERATURE CYCLING

3.1   Objectives

Temperature cycling has been employed in batch crystallization processes to control many crystal properties such as crystal size and distribution [39, 50, 51, 76], shape [77, 87], polymorphic form [35, 38], and chirality of crystals [88, 89]. Cycling the temperature leads to dissolution and recrystallization, so that the system can eliminate small undesired crystals. As reported by Wu *et al.* [90], a temperature-cycling strategy can be classified into the following three categories: 1) continuous dissolution in equipment external to the crystallizer, 2) sequential heating and cooling in the crystallizer, and 3) simultaneous heating and cooling at different locations in a single crystallizer. Among these three categories, the second approach is used here because of the simplicity in the experimental setup.

Among various crystal qualities, a unimodal crystal size and narrow size distribution improve the efficiency of filtration in commercial processes [1, 74]. Mathematical modeling can reduce the experimental effort and time needed to optimize temperature profiles for obtaining a desired crystal size distribution. Such models should include nucleation and growth of crystals, and also may include agglomeration and breakage. However, the main mechanisms that affect the final crystal product qualities are nucleation and growth [1]. Moreover, the dissolution and disappearance of crystals take place as well when the temperature-cycling strategy is employed. Hence, the model must describe the disappear-

ance of crystals as well as nucleation, growth, and dissolution in order to model attributes of crystallization by temperature cycling. In this study, a population balance model (PBM) is used to describe the crystallization in a batch process. While many studies have examined primary nucleation, secondary nucleation and growth [19, 74, 91–93], fewer modeling studies involving disappearance of crystals are found in the literature [76, 94, 95].

The PBM is a partial differential equation (PDE) and most PDEs cannot be solved analytically except for very simple cases. Therefore, various techniques have been employed to solve the PBM numerically, which include method of moments [96–98], method of characteristics [99, 100], finite-element method (FEM) [101], finite-volume method (FVM) [102–104], and the space-time conservation element/solution element (CE/SE) [19, 105, 106]. Qamar *et al*. [106] compares various numerical methods to solve the PBM, and the CE/SE scheme demonstrated "much better performance" among tested approaches.

The present study aims to develop and validate a mathematical model of unseeded crystallization of paracetamol from an ethanolic solution in a batch process employing a temperature-cycling strategy. The model handles kinetics of primary and secondary nucleation, growth and dissolution of crystals, and disappearance of fines. Experiments that apply temperature-cycling strategies were carried out to estimate kinetic parameters. Each experiment employed PAT tools such as FBRM and ATR-FTIR spectroscopy to measure properties of particles and solution, respectively. The final crystal size distribution was analyzed by an *ex situ* method, sieve analysis after washing and drying crystals.

3.2 Population balance model

The one-dimensional population balance model is often used to describe a well-mixed batch crystallization system [19, 74]. If agglomeration and breakage of crystals can be ignored, the population balance equation can be expressed as

$$\frac{\partial n}{\partial t} + G\frac{\partial n}{\partial L} = 0 \qquad (3.1)$$

where *n* represents the number density of crystals [#/(μm·kg of solvent)], *G* denotes the growth rate of crystals [μm/min], *t* is the time [min], and *L* is the characteristic crystal size [μm]. Equation (3.1) is based on assumptions that the crystal shape does not depend on the crystal size and the growth rate is size-independent and without dispersion. The initial condition and the boundary condition for batch crystallization from a clear solution are

$$n(t = 0, L) = n_0(L) \tag{3.2}$$

$$n(t, L = 0) = \frac{B}{G}, \quad S \geq 1 \tag{3.3}$$

$$n(t, L = 0) = 0, \quad S < 1 \tag{3.4}$$

where *B* denotes the nucleation rate [#/(min·kg of solvent)], $n_0(L)$ is the initial number density, and *S* is the supersaturation, which is defined as $S = c/c_s$. *c* is the concentration in the solution and c_s is the solubility at the system temperature. It is assumed that new nuclei appear only in the smallest size domain. Therefore, $n_0(L)$ is zero in the entire domain in an unseeded crystallization.

The nucleation rate, *B*, in Equation (3.3), can be divided into primary and secondary nucleation. Primary nucleation is the mechanism in which crystals are formed from a clear solution (i.e. does not have any crystals). On the other hand, secondary nucleation models the mechanism where formation of new nuclei is caused by existing crystals [107].

If the concentration in the solution is lower than the solubility, crystals dissolve and some small crystals may disappear. In order to describe the disappearance of crystals, various criteria such as the critical size of crystals [94], detection limit [76], and physically minimum size of crystals, $L = 0$ [95, 108–112], have been applied to describe the disappearance of crystals. However, the critical size of crystals can change according to the system condition and it is difficult to detect the exact size. Hence, the boundary condition

in Equation (3.4) is employed in this study.

According to classical nucleation theory (CNT), the homogeneous primary nucleation rate is given by the surface free energy change of nuclei and the free energy change on the phase transformation.

$$B_1 = \begin{cases} k_{b1} \exp\left(-\frac{16\pi\nu^2\gamma_{ls}^3}{3k^3T^3(\ln S)^2}\right), & S \geq 1 \\ 0, & S < 1 \end{cases} \tag{3.5}$$

where k_{b1} is a pre-exponential rate constant [#/(min·kg solvent)], ν is the volume of one solute molecule [m^3], γ_{ls} is the interfacial energy between crystal and solution [J/m^2], k is the Boltzmann constant [m^{2}kg/s^2/K], and T is the system temperature [K]. In this chapter, k_{b1} and γ_{ls} are handled as parameters, T and S are provided by experimental measurements, and v is calculated with the molecular weight and density of the solid solute.

In this study, the secondary nucleation rate, B_2, is described by an empirical model:

$$B_2 = \begin{cases} k_{b2}\,(S-1)^\alpha\,M_T^\beta, & S \geq 1 \\ 0, & S < 1 \end{cases} \tag{3.6}$$

where k_{b2} is the pre-exponential rate constant [#/(min·kg solvent)], M_T is the suspension density [g-solute/g-solvent], and α and β are the exponential parameters for the model. In this model, secondary nucleation is determined by the supersaturation of the solution and mass of crystals in the slurry. The secondary nucleation is known to be affected by collisions among crystals in the system according to the stirring rate [113–116], and different mixing conditions cannot provide consistent collision behavior. Therefore, we used a constant stirring speed in all experiments. The total nucleation rate, B, is determined by

$$B = B_1 + B_2 \tag{3.7}$$

In this study, size-independent growth and dissolution were assumed for paracetamol

in ethanolic solution, similar to past work [19, 74]. Hence, growth and dissolution rates of crystals can be expressed similarly as functions of temperature and the absolute supersaturation.

$$G = k_g \exp\left(-\frac{E_{a_g}}{RT}\right)(c - c_s)^{\gamma_g}, \qquad c \geq c_s \qquad (3.8)$$

$$D = k_d \exp\left(-\frac{E_{a_d}}{RT}\right)(c_s - c)^{\gamma_d}, \qquad c < c_s \qquad (3.9)$$

where G and D are the growth and dissolution rates of crystals [(μm/min)], respectively, k_g and k_d are the pre-exponential rate constants for the crystal growth [(μm/min)(g-solute/g-solvent)$^{-\gamma_g}$] and dissolution [(μm/min) (g-solute/g-solvent)$^{-\gamma_d}$], respectively, E_{a_g} and E_{a_d} are the activation energies [J/mol] for growth and dissolution, γ_g and γ_d are exponential parameters on supersaturation for the growth and dissolution, respectively, and R is the universal gas constant [J/mol/K]. Crystals grow when the concentration of the solution is higher than the solubility, but crystals dissolve into the solution under the opposite condition. Therefore, $c - c_s$ and $c_s - c$ determine the growth and dissolution of crystals in the model, respectively.

3.2.1   Numerical method

In this work, the space-time CE/SE method was employed to obtain the solution of the PBM. This scheme was originally developed to solve Navier-Stokes and Euler equations [117], and it has been employed to solve many partial differential equations in fields such as magnetohydrodynamics [118], heat transfer [119, 120], adsorption [121, 122], and crystallization [19, 95, 105, 106, 108, 123, 124]. Motz *et al.* [105] showed that the CE/SE method can provide more accurate and faster solutions for the PBM than those given by the FVM, with fewer grid points. Also, Qamar *et al.* [106] reported that the CE/SE method presents faster estimation and more accurate results than all other presented schemes such

as the high resolution semi-discrete FVM and PARSIVAL. In particular, the CE/SE scheme accurately simulated the sharp peaks and discontinuities. The details of the CE/SE method are explained in Appendix A.

In order to describe the crystallization system including crystallization, dissolution, and disappearance of crystals, the CE/SE scheme was coded in MATLAB™ R2019b for a size range from 0 μm to 1000 μm with evenly spaced bins of ΔL, where ΔL is 5 μm.

3.2.2 The method of moments

The method of moments provides an alternative method for solving a PBM. The moments of the distribution are calculated, after multiplying the PBM by L^j and then integrating over the size L. The definition of the jth moment, μ_j, is

$$\mu_j(t) = \int_0^\infty L^j n(t, L) dL, \qquad j = 0, 1, 2...$$ (3.10)

The zeroth moment through the third moment μ_0, μ_1, μ_2, and μ_3, are proportional to the total number, length, surface area, and volume of crystals, respectively. For a finite number of moments, the method of moments does not provide the entire size distribution. In our study, the moments defined in Equation (3.10) are obtained both from the model and from experiments, and they are compared.

Under the assumption that the growth and dissolution rates are size-independent, the moments can be calculated by solving a set of ordinary differential equations from Equations (3.1) and (3.10) [1]:

$$\frac{d\mu_j}{dt} = jG\mu_{j-1}, \qquad j = 0, 1, 2...$$ (3.11)

When $S > 1$, the time derivative of the zeroth moment, which is the rate of change in the total number of crystals, is the nucleation rate:

$$\frac{d\mu_0}{dt} = B = B_1 + B_2 \tag{3.12}$$

Since the third moment is related to the total volume of crystals in the system, the solute concentration in the solvent is estimated using the following two equations:

$$c(t) = c_0 - k_v \rho_c \mu_3(t) \tag{3.13}$$

$$\frac{dc(t)}{dt} = -k_v \rho_c \frac{d\mu_3(t)}{dt} = -3k_v \rho_c G \mu_2(t) \tag{3.14}$$

where c_0 is the initial concentration in the system, k_v is the volume shape factor of crystals, and ρ_c is the solid density of crystal [g/cm^3]. This method was employed to estimate dissolution rate parameters in this study.

3.2.3 Parameter estimation

In this study, parameter estimations were carried out for crystallization and dissolution separately by minimizing the sum of squared absolute errors between experimental data and model predictions. Because experimental methods to obtain the crystallization and dissolution data were different, the objective functions for each parameter estimation are different. The minimization problems were solved by the `fmincon` function which is an SQP solver [125] in MATLAB™ R2019b. Parameters for the primary nucleation, secondary nucleation, crystal growth were obtained using the objective function, Equation (3.15), which includes the concentration and the final volume density distribution, and parameters for dissolution were estimated through Equation (3.16):

$$\Phi_c(\theta_c) = \sum_{i=1}^{N_r} \sum_{j=1}^{N_{d,i}} \frac{1}{N_{d,i}} \left(\hat{c}_{ij} - c_{ij}(\theta_c) \right)^2 + \sum_{i=1}^{N_r} \sum_{k=1}^{N_{m,v}} \frac{1}{N_{m,v}} \left(\frac{\hat{v}_{ik} - v_{ik}(\theta_c)}{10^{12}} \right)^2 \tag{3.15}$$

$$\Phi_d(\theta_d) = \sum_{i=1}^{N_r} \sum_{j=1}^{N_{d,i}} \frac{1}{N_{d,i}} \left(\hat{c}_{ij} - c_{ij}(\theta_d)\right)^2 \tag{3.16}$$

where $\theta_c = \{k_{b1}, \sigma, k_{b2}, \alpha, \beta, k_g, E_{a_g}, \gamma_g\}$, and $\theta_d = \{k_d, E_{a_d}, \gamma_d\}$ are the parameter sets for crystallization and dissolution kinetics, respectively, N_r is the number of experimental runs, $N_{d,i}$ is the number of sampled data for i^{th} run, $N_{m,v}$ is the number of size ranges for volume density distribution, c and v represent concentration and volume density distributions, respectively, w_c is the weight for the term of concentration, $\hat{c}_{ij}$ and c_{ij} are the measured and predicted concentrations; and $\hat{v}_{ik}$ and v_{ik} are the measured and predicted final volume density distribution from each run. Due to the different order of magnitude for each term in Equation (3.15), the volume densities were divided by 10^{12} to balance the significance of error terms.

To estimate the dissolution parameters, the method of moments was employed because the objective function uses the error of only concentration in the mother liquor. On the other hand, for the parameter estimation of crystallization, the PBM was solved by the CE/SE method, which can solve partial differential equations efficiently. However, because the time grid of the CE/SE method does not necessarily match the time points in the experimental data, the solution of the model is interpolated for calculation of Φ_c. Similarly, for the final volume density distribution, the sieving analysis has 11 unequally spaced bins while the model has equally spaced finite elements which are 5 μm. Thus, the crystal size, L, was integrated over multiple size ranges that match the size bins in the sieve analysis.

Uncertainty in the model parameters can be quantified via confidence intervals. To estimate confidence intervals accurately, uncertainty in the experimental measurement must be quantified, which requires repetition of experiments. For this problem, an alternative method given by Bard *et al.* [126], which is employed for crystallization by Li *et al.* [19] and Rawlings *et al.* [127], was used for approximation of the confidence intervals for estimated parameters:

$$(\boldsymbol{\theta} - \hat{\boldsymbol{\theta}})^{\mathrm{T}}(V_\theta)^{-1}(\boldsymbol{\theta} - \hat{\boldsymbol{\theta}}) \leq \chi^2_{N_p,\alpha} \tag{3.17}$$

The confidence intervals for each parameter, $\hat{\boldsymbol{\theta}}$, are calculated by Equation (3.17) with an assumption that the sum of squares errors follows a chi-square distribution. The degree of freedom, N_p, is the number of parameters, and α is 0.05 in 95% confidence for the chi-squared distribution:

$$(V_\theta)^{-1} = \sum_q (V_\theta^q)^{-1} = \sum_j \left(B_q^j\right)^T (V^q)^{-1} \left(B_q^j\right), \qquad q \in \{c, sv\} \tag{3.18}$$

where V_θ is a covariance matrix of parameters, $\boldsymbol{\theta}$, from different measured data for concentration and sieved results for the crystallization, which are represented by c and v, respectively, B^j is a $N_m \times N_p$ matrix of the sensitivities, $N_m = N_c + N_v$ is the total number of measured variables, $dy/d\theta$, of the nth sample, and V is the diagonal covariance matrix of the measurements. V and B_k^j can be estimated by Equations (3.19) and (3.20):

$$V^q = \frac{1}{N_{d,q}} \sum_{i=1}^{N_{d,q}} e_{i,q}^2, \qquad q \in \{c, v\} \tag{3.19}$$

where $N_{d,q}$ is the number of samples for each measurement, e_i^2 is the squared error between experimental data and predicted results using $\hat{\boldsymbol{\theta}}$, e.g. $e_{i,c}^2 = (\hat{c}_i - c_i(\hat{\theta}))^2$ for concentration. The sensitivity matrix, B_k^j is approximated by the finite difference method.

$$B_{k,q}^j = \frac{\partial y_j}{\partial \theta}\bigg|_{\theta=\hat{\theta}} \approx \frac{y_{k,q}^j(\hat{\boldsymbol{\theta}} + h_k \mathbf{e_k}) - y_{k,q}^j(\hat{\boldsymbol{\theta}})}{h_k}, \qquad k = 1, 2, \ldots, N_m, \qquad q \in \{c, v\} \tag{3.20}$$

where $y_{k,q}^j$ is the simulated result according to parameters, h_k is a perturbation to $\hat{\boldsymbol{\theta}}$, and $\mathbf{e}_k$ is a $1 \times N_p$ unit vector. In this work, $N_{m,c} = 1$ for concentration, $N_{m,v} = 11$ for sieving, and $N_p = 11$ for the number of parameters. The degree of perturbation, h_k, is 0.1% of the magnitude in each element of $\hat{\boldsymbol{\theta}}$.

3.3 Experimental methods

3.3.1 Materials and equipment

Crystallization and dissolution experiments for paracetamol (Sigma-Aldrich, $> 99\%$) were performed in ethanol (KOPTEC, 200 proof anhydrous) in a 250-ml glass crystallizer with a pitched four-blade stirrer and temperature controller. The equipment, which is shown in Figure 3.1, includes three sensors which are Attenuated Total Reflectance-Fourier Transform Infrared (ATR-FTIR), Focused-Beam Reflectance Measurements (FBRM), and a temperature sensor to measure characteristics of solutions and crystals in the crystallizer. The crystallization system, Optimax™ from Mettler-Toledo, can control the experimental conditions via a connected computer and software, iControl™ 6.0 by Mettler-Toledo. The ATR-FTIR, ReactIR iC10™ by Mettler-Toledo, measured the IR spectrum for wavenumbers from 650 to 3000 cm^{-1}, at a rate of one sample every 30 seconds. The ATR-FTIR equipment was purged by compressed air and cooled down by liquid nitrogen before every measurement. Measured IR absorbance data were collected through software, iCIR™ by Mettler-Toledo. The concentration of the solution was evaluated based on measured IR absorbance data with a calibration model; further detail is provided later in the calibration section. The FBRM equipment, ParticleTrack G400™ by Mettler-Toledo, was set in the macro mode with the laser focus distance of 0 μm and a scanning speed of 2 m/s. The FBRM measures the chord length every 30 seconds, and the computer and the software, iCFBRM™ by Mettler-Toledo, analyzed the chord length distributions (CLD). The software divides the chord size from 1 μm to 1000 μm into 100 bins via a logarithmic scale and generates the chord length histogram for each measurement. The range of experimental temperature was from 0 to 70 °C and every measurement was performed with a constant stirring rate of 400 rpm.
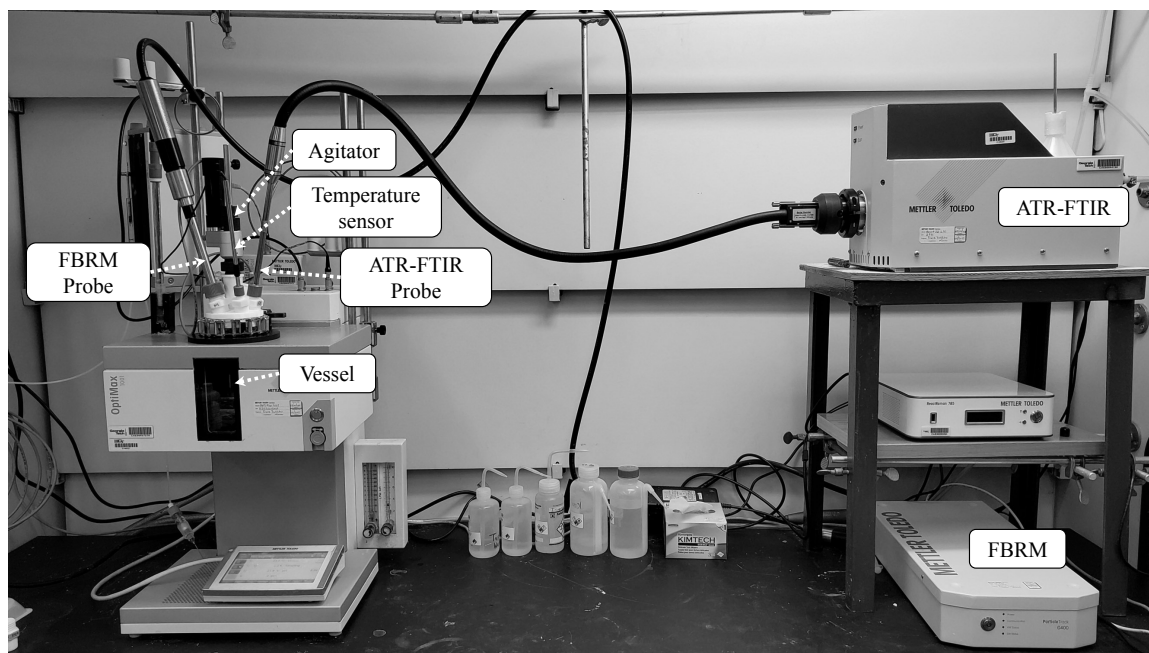
Figure 3.1: OptiMax system from Mettler Toledo equipped with probes for focused beam reflectance measurements (FBRM) and attenuated total reflectance Fourier transform infrared (ATR-FTIR) measurements.

3.3.2 Dissolution experiments

Every dissolution experiment was performed in a 250 ml-glass crystallizer with isothermal conditions. The manipulated conditions in these experiments were the system temperature and the initial crystal sizes. The paracetamol solution in ethanol with $S = 0.95$ at the desired temperature was prepared to perform these experiments. Initial solutions were based on 100 g of ethanol, and the concentration of solution has a unit of g-solute/g-solvent. For each solution, the system temperature was kept as the desired temperatures, 10, 15, 20, and 30 °C. A specific mass of crystals was introduced in the solution, having a particular size associated with one sieve tray. The introduced mass of crystals was determined based on the paracetamol solubility in ethanol to recover the desired mass of remaining crystals. The time of the introduction of crystals was set as the initial time of the experiment. The dissolution experiments were completed when the *in situ* FTIR absorbance maintained a constant value. After the experiment, the remaining crystals were filtered *in vacuo* to sep-

arate ethanol from the paracetamol crystals. Next, the recovered crystals were washed by toluene because ethanol is soluble in toluene, and paracetamol is insoluble in toluene. The remaining toluene on the surface of the crystals was evaporated, and the dried crystals were sieved with 11 size ranges from 0 to 850 μm to analyze the particle size distributions.

3.3.3 Crystallization experiments with temperature cycling

The goal of Chapter 3 is to model unseeded crystallization of paracetamol from ethanolic solution with a temperature cycling strategy. Unseeded crystallization is also called internal seeding crystallization because the crystals appear through primary nucleation initially, and these crystals can then act as seed crystals in the system. Internal seeding is usually implemented by the continuous cooling profile [35, 39, 128]. However, primary nucleation is known to have stochasticity, so a temperature plateau was applied to minimize the influence of the stochasticity in primary nucleation, on the reproducibility of the subsequent process [18, 19].

The stirring speed in this system was fixed at 400 rpm to minimize bubble formation while maintaining mass and heat transfer in the system. The initial temperature of the system was set at least 5 °C higher than the saturation temperature of the initial concentration so that the initial solution was undersaturated. The system temperature was decreased until the supersaturation reached the target value, with -1.0 °C/min as the cooling rate. The time when the decrease in temperature begins was considered as the initial time for the modeling. Next, the system was kept on the plateau temperature between 60 and 150 minutes, based on the status of crystals in the solution. The length of the temperature plateau was determined by the total chord counts using the FBRM and ATR-FTIR. If the total chord counts were kept nearly constant, we assumed that further nucleation is negligible. The first appearance and growth of crystals took place during this temperature plateau. After this step, the temperature-cycling strategy was employed to obtain crystals with different mean sizes and size distributions. Each experiment had different initial concentrations and

supersaturations on the temperature plateau. The plateau temperature was determined by the initial concentration and the target supersaturation. The concentration of paracetamol in the solution was evaluated based on the *in situ* ATR-FTIR measurement.

3.4 Experimental results

3.4.1 Observation for agglomeration and breakage

First of all, agglomeration and breakage were observed to determine whether the model should include these mechanisms. The initial part of the usual experimental procedure was carried out, and the temperature plateau was kept for 20 hours. If crystals agglomerate or break in the system, the chord counts should increase or decrease drastically, but significant changes are not observed. Even though we can see a slight increase in chord counts at the end of the observation, the chord counts are kept constant for more than 6 hours without a change. Moreover, the temperature plateau is employed only for 2 hours, illustrated between the black dotted lines. Hence, agglomeration and breakage of crystals were neglected in this work.
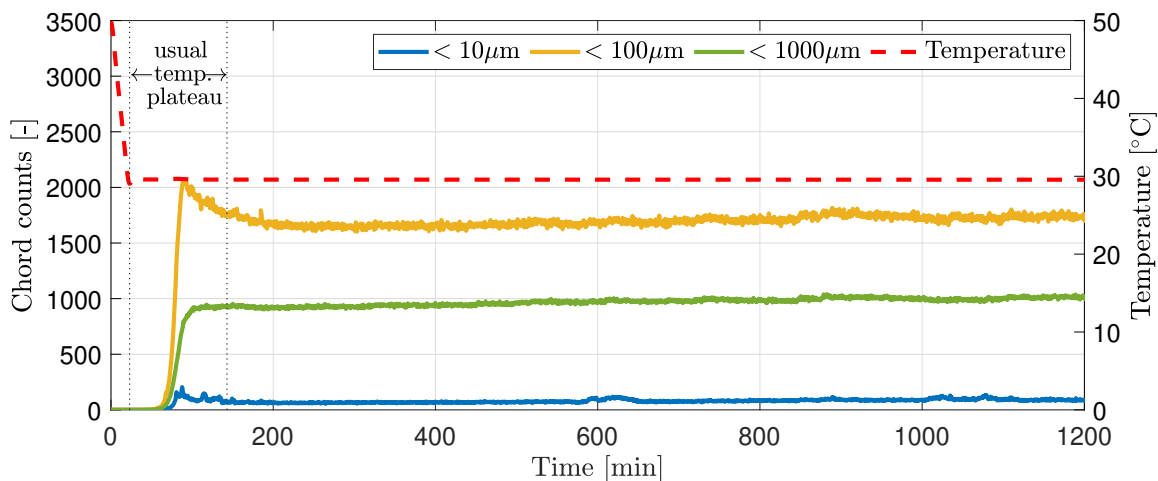
Figure 3.2: Chord counts profiles for 20-hour experiment with three divided ranges in chord length distribution

38

3.4.2 Temperature plateau and reproducibility
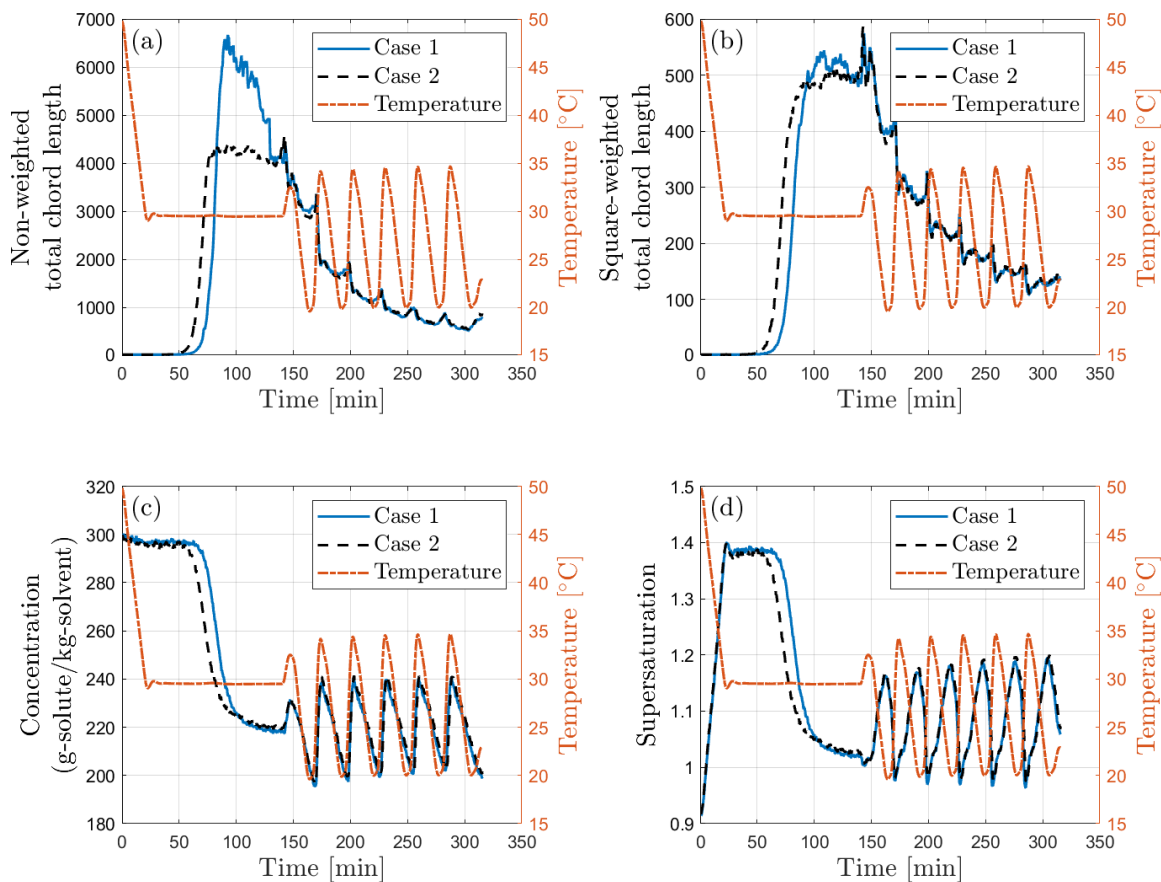
Figure 3.3: Comparison of two experimental cases with the same temperature profile. (a) non-weighted total chord counts, (b) square-weighted total chord counts, (c) concentration of paracetamol in ethanolic solution, (d) supersaturation.

As mentioned in the previous section, we employed a temperature plateau to reduce the influence of the stochasticity of primary nucleation. Two experimental cases with the same temperature profile were compared to show the effect of the temperature plateau and reproducibility of crystallization. As a result, we can see the stochasticity of primary nucleation in Figure 3.3. Case 2 shows the change sooner than Case 1 in all plots, even though the temperature plateau begins at the same time. However, we can also see that the non-weighted and square-weighted total chord counts show similar values at the end of the temperature plateau. If we manipulate the temperature without a temperature plateau after the crystals appeared, the crystallization behaviors can show different trends according to the charac-

teristics of nucleated crystals, even though the temperature profile is the same. Therefore, the temperature plateau can reduce the influence of stochastic primary nucleation.

This figure also shows the reproducibility of the crystallization process. The behaviors of chord counts, concentration, and supersaturation from both experiments have very similar trends in all crystallization processes. The non-weighted total chord counts of Case 1 have values larger than those of Case 2 immediately after the crystals appear, but this trend becomes close to Case 2 at the end of the temperature plateau. The square-weighted chord counts demonstrate similar values for both experimental cases despite the non-weighted chord counts having different values immediately after the primary nucleation. This happens because tiny crystals in the system do not affect square-weighted chord counts as much. Concentration and supersaturation also have similar trends for the same temperature profiles.

3.4.3   Results of dissolution experiments

Seven sets of experiments were carried out to investigate the dissolution of crystals. In each dissolution experiment, the initial undersaturation was fixed as 0.95, so that dissolution kinetics are observed over a slow enough time scale for quantification. Additionally, the number of crystals was assumed to be constant during the experiments since the size of the monodisperse seed crystals is significantly larger compared to the observed reduction in size during dissolution.

Two variables, temperature and mean size of seed crystals, were manipulated to design and carry out the dissolution experiments. The temperature affects the dissolution rate because the dissolution is a type of mass transfer, which depends on temperature. To observe the temperature dependence of dissolution, experiments were carried out at four different isothermal conditions—10, 15, 20, and 30 °C. Furthermore, the sizes of the seed crystals were varied since the surface area also influences the dissolution rate. Specifically, we employed the following three different size ranges—300 – 355, 425 – 500, and 600 –

Table 3.1: Experimental conditions and results of dissolution experiments

	Exp.	Temp., T, [°C]	Initial crystal size, L_{ini} [μm]	Initial conc., c_{ini} [g-solute /g-solvent]	Final conc., c_{fin} [g-solute g-solvent]	Diff. of conc., $\Delta c = c_{fin} - c_{ini}$ [g-solute g-solvent]	mass of seed crystals m_{seed}, [g]	mass of recovered crystals m_{fin}, [g]
	1	10.0	$425 - 500$	0.1425	0.1479	0.0054	4.80	4.31
	2	15.0	$425 - 500$	0.1539	0.1618	0.0079	4.85	4.00
Training sets	3	20.0	$300 - 355$	0.1672	0.1771	0.0099	4.90	3.66
	4	20.0	$600 - 700$	0.1672	0.1773	0.0101	4.90	3.71
	5	30.0	$425 - 500$	0.2018	0.2154	0.0136	5.10	3.68
Test sets	6	10.0	$600 - 700$	0.1425	0.1478	0.0053	4.80	4.27
	7	20.0	$425 - 500$	0.1672	0.1773	0.0099	4.90	3.70

710 μm—which were prepared by sieving. These larger sizes were selected to minimize disappearance of crystals.

The driving force for dissolution in Equation (3.9) is $c_s - c$, the absolute undersaturation. The initial driving force is expressed as $c_{fin} - c_{ini}$ because the measured final concentration is the solubility in these experiments. The initial and final values of concentration, c_{ini} and c_{fin}, are similar for cases at the same temperature, and thus the total mass of the final crystal products are nearly the same: In Table 3.1, the mass of remaining crystals, m_{fin}, show similar values when the temperature is the same, even though the initial size is different.

Figure 3.4 presents the result of dissolution experiments using seed crystals with different initial mean sizes at two different temperatures. Figure 3.4(a) shows the dissolution rate of crystals at 10 °C. Two experimental results are compared in this figure: the dissolution of crystals whose initial sizes are between $425 - 500$ μm and $600 - 710$ μm. We can observe that the dissolution rate of larger crystals shows a slower profile than the smaller crystals for the same experimental condition. In particular, the results at 20 °C shown in Figure 3.4(b) have different trends depending on each initial size range of seed crystals. Despite the initial and final concentrations having similar values, the dissolution for $300 - 355$ μm shows the highest rate between 0 and 10 min. On the other hand, the dissolution rates of the largest size, $600 -- 700$ μm, was the slowest in the same period. This dependence is expected since the larger crystals have a lower amount of surface area per mass.
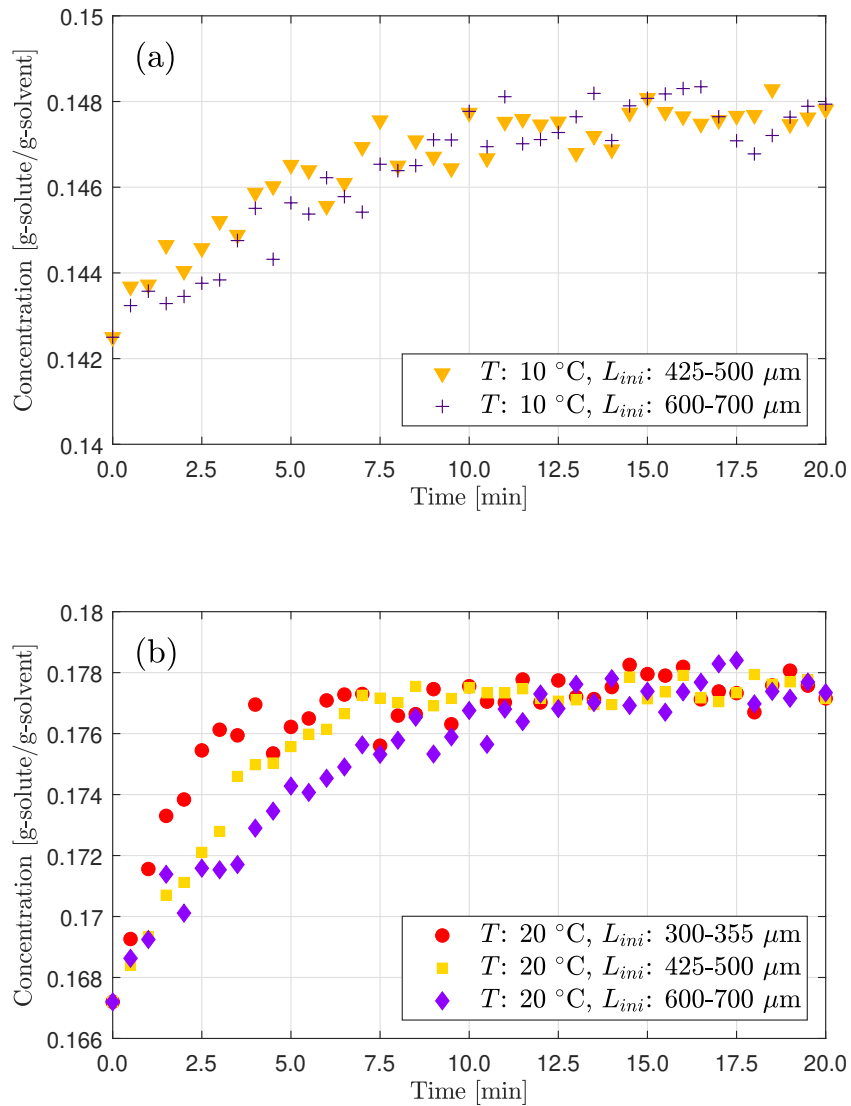
Figure 3.4: Comparisons of concentrations in dissolution experiments with different initial seed sizes. (a) 10 °C and (b) 20 °C.

3.4.4   Results of crystallization experiments with temperature cycling

In this study, six experiments were performed, and the conditions and the results are shown in Table 3.2. The initial concentrations, c_{ini}, are between 0.250 and 0.350 g-solute/g-solvent. The supersaturation values at the plateau temperatures, S_p, are chosen among

Table 3.2: Conditions and measured results of crystallization experiments

	Exp.	Desired c_{ini} [g-solute /g-solvent]	Measured c_{ini} [g-solute /g-solvent]	Desired S_p [-]	Measured S_p [-]	T_p [°C]	t_p [min]	T_{fin} [°C]	m_{fin} [g]	$\bar{L}_{4,3,\text{fin}}$ [μm]
Training sets	8	0.300	0.308	1.40	1.41	30.0	120	10.7	15.6	317.4
	9	0.250	0.245	1.30	1.27	24.0	150	19.9	7.25	259.7
	10	0.350	0.348	1.20	1.18	44.3	150	25.9	14.2	451.7
Test sets	11	0.275	0.282	1.40	1.43	25.0	120	4.8	12.6	258.7
	12	0.300	0.299	1.30	1.29	33.2	120	19.1	12.1	391.2
	13	0.300	0.300	1.40	1.39	29.6	120	22.9	10.3	309.6

Table 3.3: Comparisons of final crystal mass between by balance and by ATR-FTIR

Exp.	weighed final crystal mass [g]	final crystal mass by ATR-FTIR [g]	Error based on weighing
8	15.6	15.8	1.3%
9	7.2	7.2	0.0%
10	14.2	13.7	-3.5%
11	12.6	13.2	4.8%
12	12.1	11.9	-1.7%
13	10.3	9.8	-4.9%

1.2, 1.3, and 1.4. The plateau temperatures, T_p, were set based on the initial concentration and target supersaturation during the plateau time, t_p. The final mass of recovered crystals, m_{fin}, was measured after the washing and drying procedures and is related to the initial and final concentrations by a mass balance. The final volume-weighted mean crystal size, $\bar{L}_{\text{fin}}$, is estimated using the results of sieving analysis.

Figures 3.5 and 3.6 show the trends of mass of crystals and supersaturation, together with temperature profiles for all runs. The temporal trends of crystal mass in Figure 3.5 are estimated using the paracetamol concentration in the solution based on the ATR-FTIR measurements. Differences between values from a mass balance (based on measurements of solution concentration) and weighing product crystals differed by less than 5%, as shown in Table 3.3.
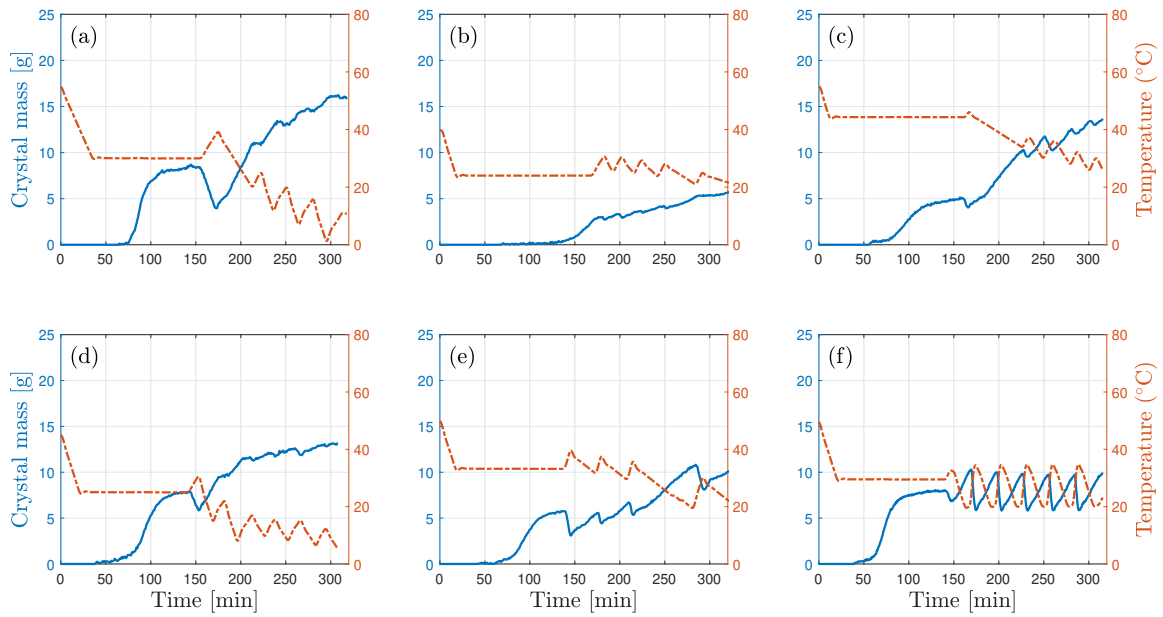
Figure 3.5: Mass of crystal and temperature profile from crystallization experiments. (a) Exp. 8, (b) Exp. 9, (c) Exp. 10, (d) Exp. 11, (e) Exp. 12, and (f) Exp. 13: blue solid line — crystal mass in the solution and red dash-dotted line — temperature profile. Ranges of axes in all figures are fixed based on the largest range among all data sets for easier comparison.
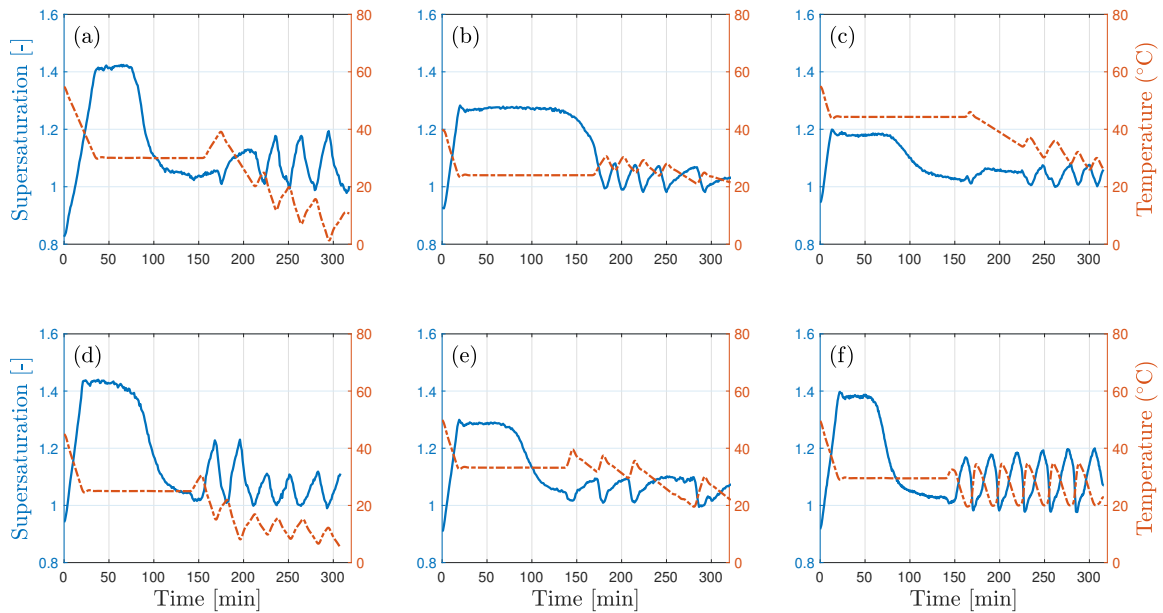
Figure 3.6: Supersaturation and temperature profile from crystallization experiments. (a) Exp. 8, (b) Exp. 9, (c) Exp. 10, (d) Exp. 11, (e) Exp. 12, and (f) Exp. 13: blue solid line — supersaturation and red dash-dotted line — temperature profile. Ranges of axes in all figures are fixed based on the largest range among all data sets for easier comparison.

3.5 Results of parameter estimation and model validation

3.5.1 Parameter estimation for crystal dissolution

The method of moments was used to estimate the parameters in the dissolution kinetics model. The initial conditions for the moments, μ_0, μ_1, μ_2, and μ_3, were evaluated by the mass, size, and volume shape factor of crystals.

Table 3.4: Estimated parameters and confidence intervals for the primary nucleation rate, secondary nucleation rate, and growth rate of crystals

	Parameter	Unit	Value	Confidence interval
Dissolution rate	k_d	$[(\mu m/min)(g/g)^{-\gamma_d}]$	-4.08×10^4	$(-4.84 - -3.47) \times 10^4$
	E_{a_d}	[J/mol]	9.80×10^3	$(9.37 - 10.2) \times 10^4$
	γ_d	[-]	0.929	$0.911 - 0.947$
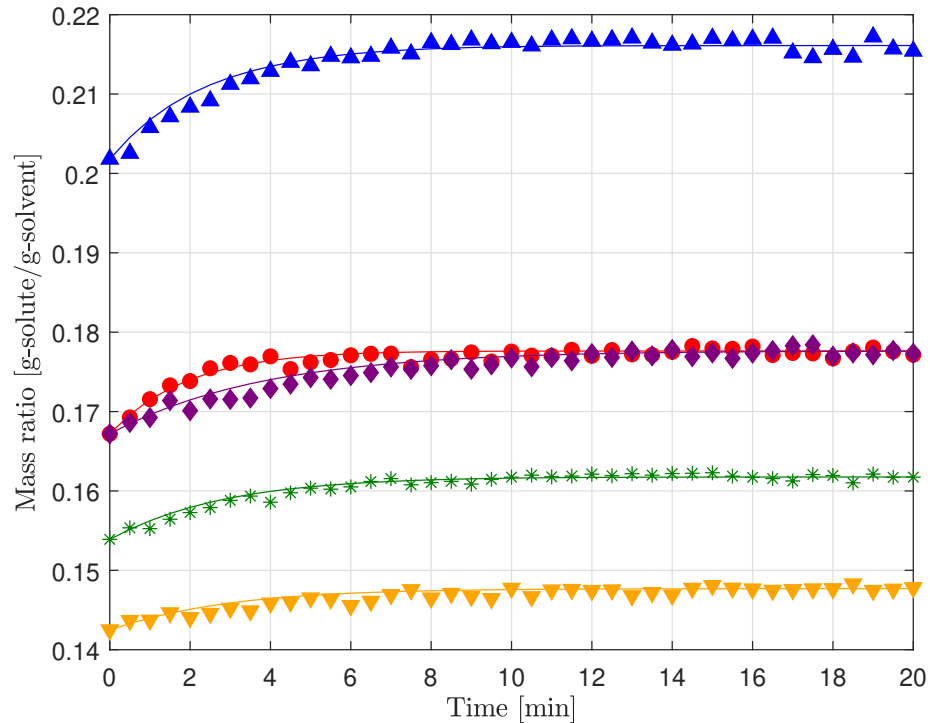
Figure 3.7: Experimental data and fitted result for training sets: blue upward triangle: 462.5 μm and 30 °C, red circle: 325.5 μm and 20 °C, purple rhombus: 655 μm and 20 °C, green asterisk: 462.5 μm and 15 °C, orange downward triangle: 462.5 μm and 10 °C, and solid lines on data points represent the fitted results by model
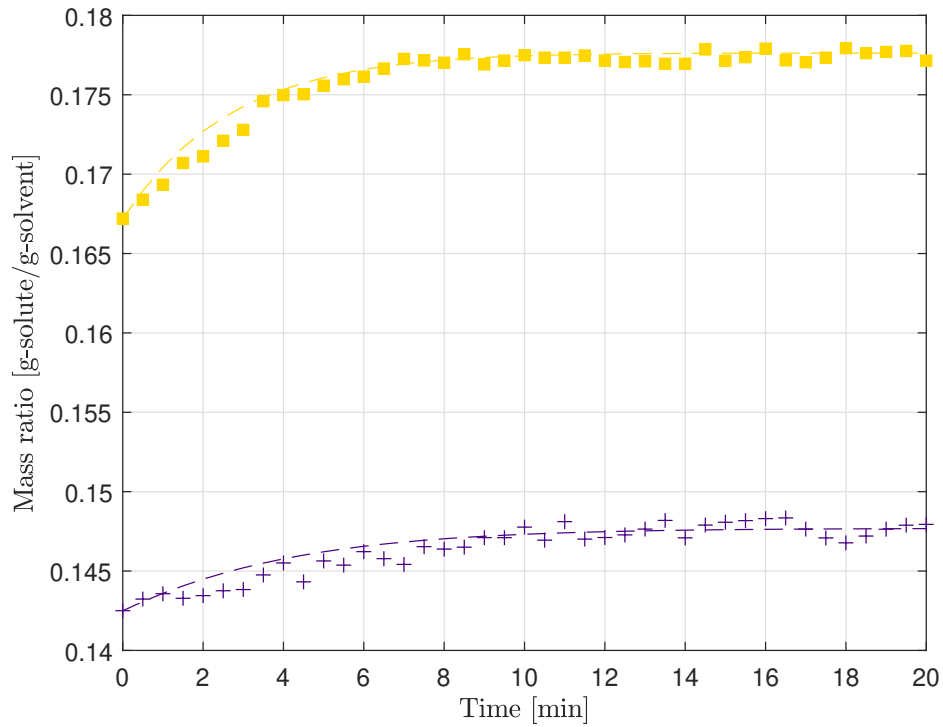
Figure 3.8: Experimental data and predicted result for test sets: yellow square: 462.5 μm and 20 °C, purple plus sign: 655 μm and 10 °C, and solid lines on data points represent the predicted results from the model

The estimated parameters for the dissolution based on five experimental data sets are shown in Table 3.4. Figure 3.7 compares the experimental training data and fitted results, and Figure 3.8 compares the experimental test data and predicted results.

The obtained kinetic model describes the dissolution of crystals very well. In particular, the model shows different initial dissolution rates depending on the seed crystal size. Additionally, this model can predict volume-weighted mean crystal size at the end of the experiment based on μ_4/μ_3 in Table 3.5. The final products were sieved to analyze the size distribution. Table 3.5 compares the volume-weighted mean crystal sizes from experiments and predictions. The estimated mean crystals show a small error of 1 — 3%.

Table 3.5: Comparison of experimental and predicted mean crystal sizes from different temperatures using the same initial crystals (425 – 500 μm)

	Temperature [°C]		
	10	20	30
Experimental crystal size [μm]	441.0	420.3	405.2
Predicted crystal size [μm]	448.3	430.4	417.8
Error based on the experimental results	1.65%	2.40%	3.11%

3.5.2 Parameter estimation for nucleation and crystal growth

Among six experimental data sets in Table 3.2, the first three experiments were used as the training set for the parameter estimation and the last three experiments were utilized as the test set. All crystallization experiments were carried out from clear solutions without any seed crystals, so the initial number density distributions are set to zero. Because training sets, Experiments 8 – 10, employed temperature cycling, the model should describe dissolution of crystals. Hence, the model used the estimated dissolution kinetic parameters from Table 3.4.

Due to the high non-linearity of the kinetic models, multiple local minima may exist in the optimization problem of parameter estimation. For this problem, `GlobalSearch` and `MultiStart` functions in MATLAB™ were applied to identify the global minimum. The logarithm with base 10 was applied to the rate constants and activation energies such as k_{b1}, k_{b2}, k_g, and E_{a_g}, to reduce the searching range of each parameter during optimization.

Table 3.6: Estimated parameters and confidence intervals for the primary nucleation rate, secondary nucleation rate, and growth rate of crystals

	Parameter	Unit	Value	Confidence interval
Primary nucleation rate	k_{b1}	[#/min/kg solvent]	10.6	9.46 – 12.0
	γ_{ls}	[mJ/m^2]	3.83	3.01 – 4.65
Secondary nucleation rate	k_{b2}	[#/min/kg solvent]	1.39×10^6	$(1.27 - 1.52) \times 10^6$
	α	[-]	2.39	2.38 – 2.40
	β	[-]	0.41	0.34 – 0.49
Growth rate	k_g	[(μm/min)(g/g)$^{-\gamma_g}$]	2.264×10^8	$(2.00 - 2.56) \times 10^8$
	E_{a_g}	[J/mol]	3.62×10^4	$(2.97 - 4.41) \times 10^4$
	γ_g	[-]	1.14	1.00 – 1.27

Table 3.6 lists the parameters obtained from the optimization, and estimated parameters were compared to previously reported parameters, especially energies and exponents. In contrast, rate constants such as k_{b1}, k_{b2}, and k_g may vary based on the experimental equipment and conditions. The estimated interfacial energy between paracetamol crystal and ethanol solution for the primary nucleation is 3.83 mJ/mol, which is 10% less than 4.25 mJ/mol reported by Li *et al* [19]. The estimated exponents in the kinetic model of the secondary nucleation, α and β, are 2.39 and 0.41, which have the same order of magnitude from reported values by Li *et al*. [19], 2.08 and 0.71. The activation energy and exponent for crystal growth rate are 36.2 kJ/mol and 1.14. Crystal growth rates of paracetamol from ethanolic solution were reported from various studies [19, 74, 129], as compared in Table 3.7.

Table 3.7: Comparisons of activation energy and exponent for crystal growth rate

Source	E_{a_g} [kJ/mol]	γ_g
Worlitschek and Mazzoti [74]	41.6	1.9
Mitchell *et al*. [129]	40.56	1.602
Li *et al*. [19]	41.3	1.24
This study	36.2	1.14

The 95% confidence intervals are also estimated in Table 3.6. Confidence interval is sometimes evaluated from repeating experiments, but this study used the quadratic approximation of Equation (3.17). Therefore, it is noted that the reported values have limitations since Equations (3.17) and (3.20) approximated the error and sensitivities for this model. Even though this method may not evaluate sensitivities accurately, it can help to determine which parameters are sensitive or insensitive in the model.

Figure 3.9 shows an example of comparisons between experimental data and fitted results from the training set such as trends of supersaturation, crystal mass, and the final volume density distributions. The fitted trends of supersaturation and mass in Figure 3.9(a) and (b) show that the estimated parameters can describe the concentration change according to the crystallization and dissolution mechanisms. When the temperature profile enters
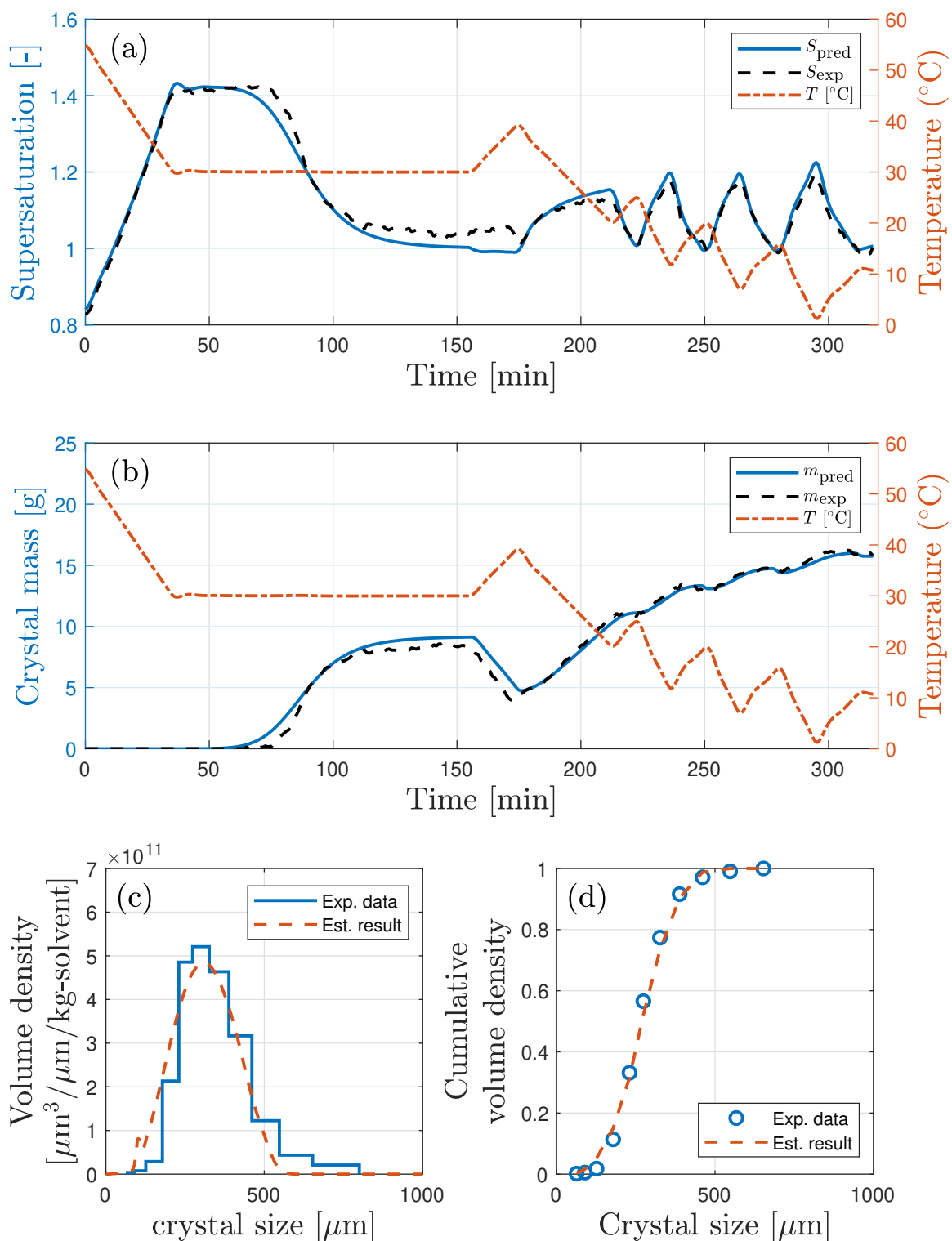
Figure 3.9: Comparisons between experimental data and fitted results for the Exp. 8 in training sets: (a) supersaturation, (b) crystal mass in the solution, (c) volume density distribution, and (d) cumulative volume density distribution.

49
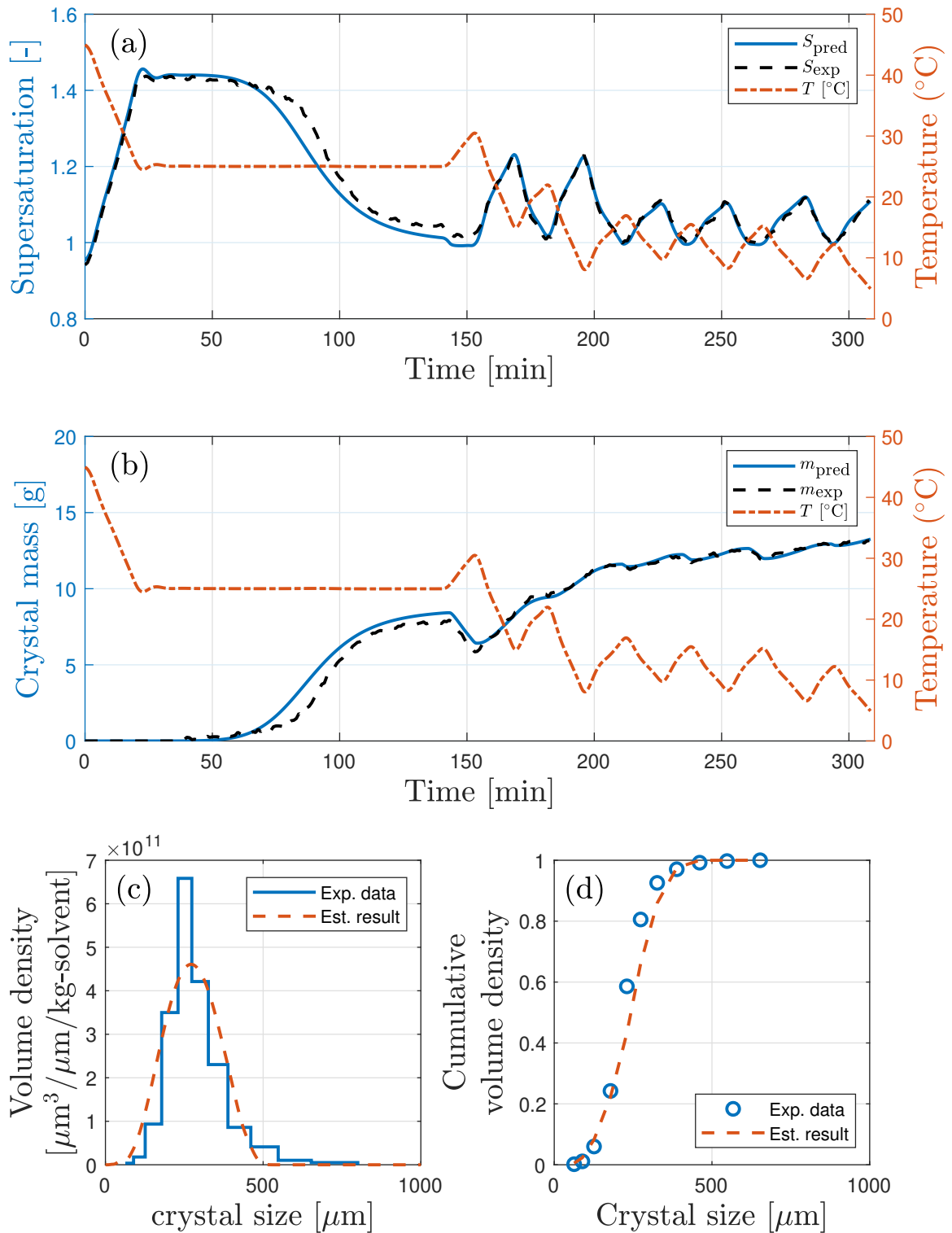
Figure 3.10: Comparisons between experimental data and fitted results for the Exp. 11 in test sets: (a) supersaturation, (b) crystal mass in the solution, (c) volume density distribution, and (d) cumulative volume density distribution.

the temperature plateau, the supersaturation shows a little variation by the temperature profile. The generation of crystals is initiated by primary nucleation and is accelerated by secondary nucleation, so the nucleation mechanisms are critical to establish the model of an unseeded batch crystallization. Appropriate parameters for nucleation mechanisms tend to predict when significant nucleation happens on the temperature plateau even though it is still challenging to describe the primary nucleation exactly due to the stochasticity. Volume densities at the final stage of the process are compared in Figure 3.9(c) and (d), and we can see that the estimated parameters depict the development of volume density distributions.

For validation of obtained kinetic models, three experimental runs, Exp. $11 - 13$ were simulated by the model with the estimated parameters, with the conditions of the test sets in Table 3.2. An example of simulated results for Experiment 11 is shown in Figure 3.10. The predicted properties regarding solution concentration, supersaturation, and crystal mass, offer a good fit to the temperature cycling stage. However, some disagreement is seen in the temperature plateau stage, due to the stochasticity of the primary nucleation; however, the temperature plateau reduces this impact on the subsequent process. Hence, the predicted final volume density distributions also show a good agreement with the experimental results. Other comparisons for training and test sets are in Appendix B.

Table 3.8: Comparisons of final mean crystal size between sieving analysis and simulation

Exp.	volume-weighted mean size by sieving [μm]	volume-weighted mean size from simulation [μm]	error based on experimental results
8	317.4	311.8	-1.8%
9	260.0	279.9	7.6%
10	452.0	507.3	12.2%
11	258.5	274.2	6.0%
12	391.2	352.2	-10.0%
13	309.6	289.3	-6.6%

Table 3.8 lists and compares the volume mean crystal sizes from experiments and predicted results. The first term in Equation (2.22), $\bar{L}_{43} = \Sigma n_i L_i^4 / \Sigma n_i L_i^3$, estimates the mean crystal size given by the model, and the second term in Equation (2.22), $\bar{L}_{43} =$

$\Sigma(M_i L_i)/\Sigma M_i$, calculates mean crystal size measured in the experiments. Errors between mean crystal sizes from experiments and simulations range from -10% to +12%, which may be partly due to inaccuracies associated with the sieving process. Some crystals may agglomerate during post-crystallization steps such as washing and drying and they may have led to measurement error in the crystal size distributions of the final product. However, the errors for the test data are similar to those for the training data, suggesting that the model is predictive.

3.6   Analyzing the crystallization system through the PBM

3.6.1   Analysis of nucleation, growth, and dissolution rates

In this section, the nucleation rates and crystal growth rate are analyzed to determine which rate is dominant under which condition, and how they affect the crystallization system. We can see that the solution concentration begins to be consumed significantly, and the supersaturation decreases drastically on the temperature plateau for all experiments in Figure 3.6. Moreover, the model and parameters can describe these phenomena. Hence, the simulated results are used to investigate the effect of nucleation, crystal growth, and dissolution rates on the crystallization system.

The total nucleation rate in this model is considered as the sum of the primary and nucleation rates. Figure 3.11 presents the primary nucleation rate, secondary nucleation rate, and crystal growth and dissolution rates of Exp. 12 as an example. From the clear solution, which does not contain any crystals, the primary nucleation is dominant, although the rate is meager. Due to the low primary nucleation rate, the concentration in the solution seems not to change at all. In this region, it is still difficult to observe crystals from the solution experimentally. However, if the initial nuclei from a clear solution grow, the grown crystals eventually provide enough area for secondary nucleation. This effect is expressed as the term regarding crystal mass in Equation (3.6). Once the secondary nucleation significantly
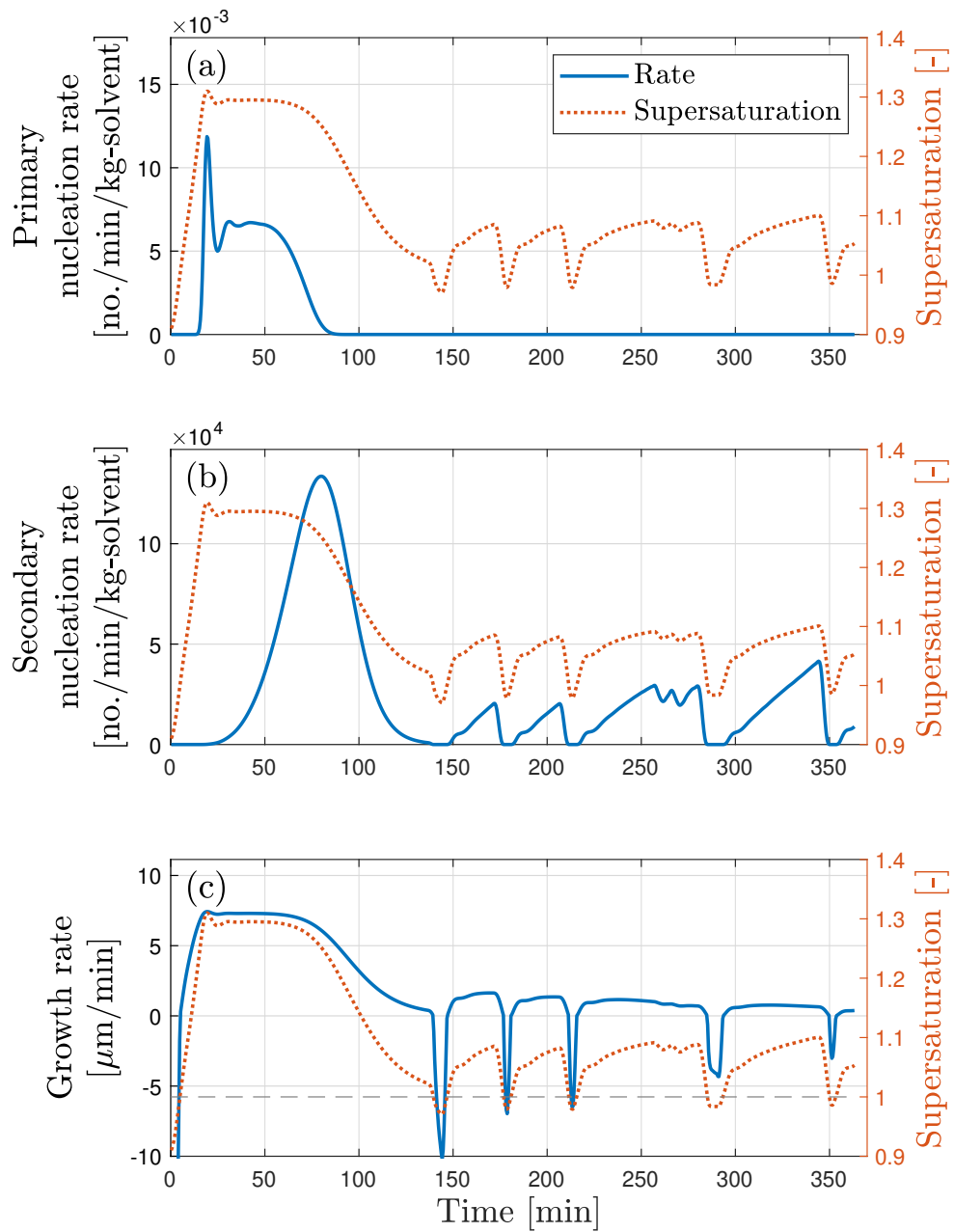
Figure 3.11: Trends of (a) the primary nucleation rate, (b) secondary nucleation rate, and (c) crystal growth and dissolution rate based on the supersaturation for Exp. 12. The grey dashed line in Figure (c) represents the saturation level is 1 to compare the saturation in the solution is supersaturated or undersaturated.

begins, the supersaturation in the solution decreases drastically due to the much higher magnitude of the secondary nucleation rate compared to the primary nucleation rate. In this step, the primary nucleation rate can be ignored due to the difference in magnitudes. As the supersaturation decreases and approaches 1, the nucleation rates come to near zero, but the crystal growth rate has values that cannot be ignored even though it becomes lower than the initial stage of the temperature plateau, where supersaturation has the highest value in the whole process.
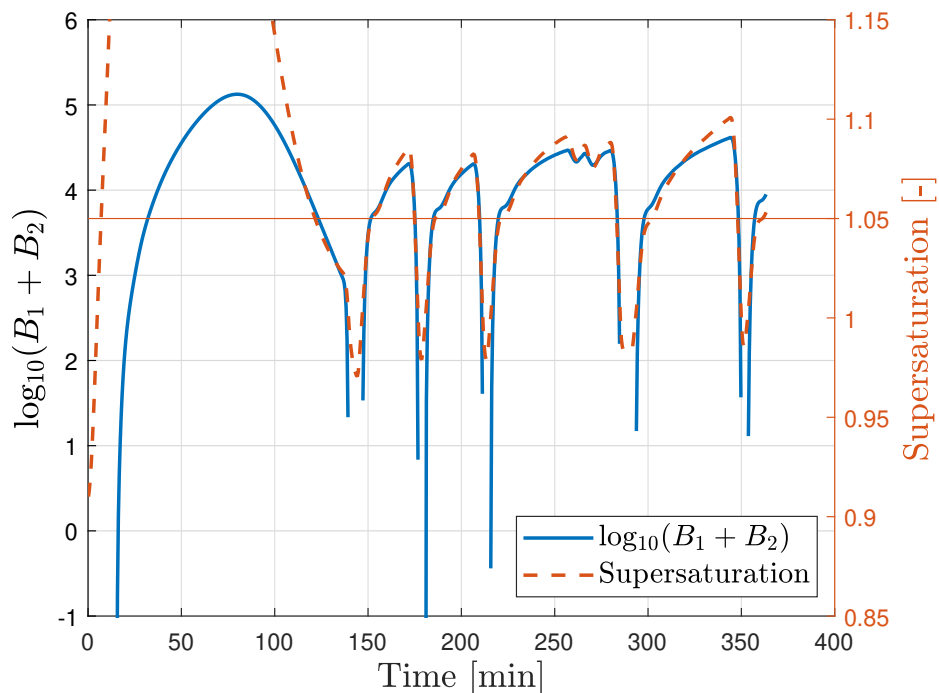
Figure 3.12: Trends of total nucleation rate according to supersaturation for Exp. 12. The total nucleation rate is plotted as the logarithm in this figure. The solid orange line represents the supersaturation of 1.05.

When the solution is undersaturated, there is no more nucleation, and crystals begin dissolving. While the temperature cycles are employed, the system repeatedly enters the supersaturated and undersaturated regions. This makes the crystals grow and dissolve. Secondary nucleation also occurs. The supersaturation level depends on the temperature rate of change in the crystallizer. If the temperature decreases quickly, supersaturation reaches a level higher than 1.05, so many new nuclei are generated, depending on the

supersaturation, although the growth rate also becomes higher. Figure 3.12 shows that a lower supersaturation than 1.05 can cause nucleation. However, the number of newly generated nuclei is not significant based on a comparison between the total nucleation rate with the logarithm with base 10 and the supersaturation in the solution.

This interpretation using the model shows the effect of supersaturation on the nucleation, growth, and dissolution rates. In particular, this analysis shows that supersaturation greater than 1.05 provides meaningful nucleation rate to generate new crystals for the system of paracetamol in ethanolic solution as shown in Figures 3.11(b) and 3.12. Hence, the model can help to find the optimized temperature profiles to reach the target crystal attributes in the unseeded batch cooling crystallization.

3.6.2 Effect of temperature cycling on crystal size distribution

Temperature cycling strategies cause changes in crystal size distribution due to repeating temperature increase and decrease. However, the volume-weighted mean crystal size does not become larger conspicuously when the temperature cycles in a fixed range as shown in Figure 3.13 (Exp. 13). In Figure 3.14, the volume-weighted average size reaches a similar value if the final temperature is the same despite the different temperature paths. As a result, the final temperature affects the final volume-weighted mean crystal size because small powders do not influence the total volume or mass of the crystal.

Nonetheless, the small powder makes problems on the industrial processes, especially for transportation processes and safety. Small particles and fines generate larger Van der Waals forces of attraction that create adhesion among particles [130], and greater specific surface area by smaller crystal size causes larger surface resistance [131]. Moreover, crystals with larger mean size and narrower distribution have higher flowability than crystals with smaller mean size and wider distribution [132]. From the viewpoint of safety, particles smaller than 500 μm are more likely to generate powder explosion, and the probability of the accident increases as particulates become smaller [133]. Hence, the trend of mean
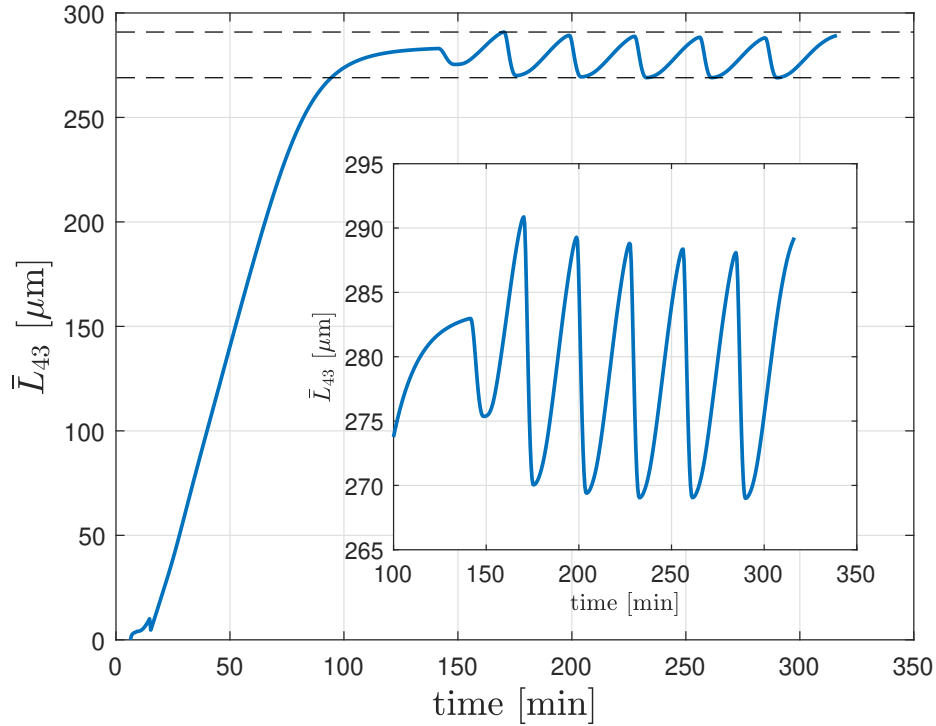
Figure 3.13: Trend of volume-weighted mean crystal size for Exp 13. Dashed black lines are to compare $\bar{L}_{43}$ for each temperature cycle. *Inset*: Zoomed-in profile of oscillation of trend.

crystal size using number density such as volume mean size [83], $\bar{L}_{30} = (\mu_3/\mu_0)^{1/3}$, could be used instead even though fine particles do not affect the total volume of crystals very much. However, it is challenging to measure the number of powders using sieve trays since the powder less than 53 μm. If we assume the mean crystal size between the smallest sieve trays as 26.5 μm, the mass of one particle with crystal density, 1.263×10^{-12} g/μm, and volume shape factor, 0.797, is only 1.87×10^{-2} μg. Therefore, it can be impractical to detect the mass of crystals in this tray range according to the resolution of the measurement.

To figure out the influence of temperature cycling on crystal attributes, a case study was carried out as shown in Figure 3.14. This simulation compares the supersaturation, mean volume crystal size, volume-weighted mean crystal size, and the number of crystals for small and entire size ranges. The small size range is from 0 to 55 μm and the entire size range is from 0 to 1000 μm. The reason that the number of crystals is analyzed for two size ranges is to determine the impact of the small crystals on the total number of

56
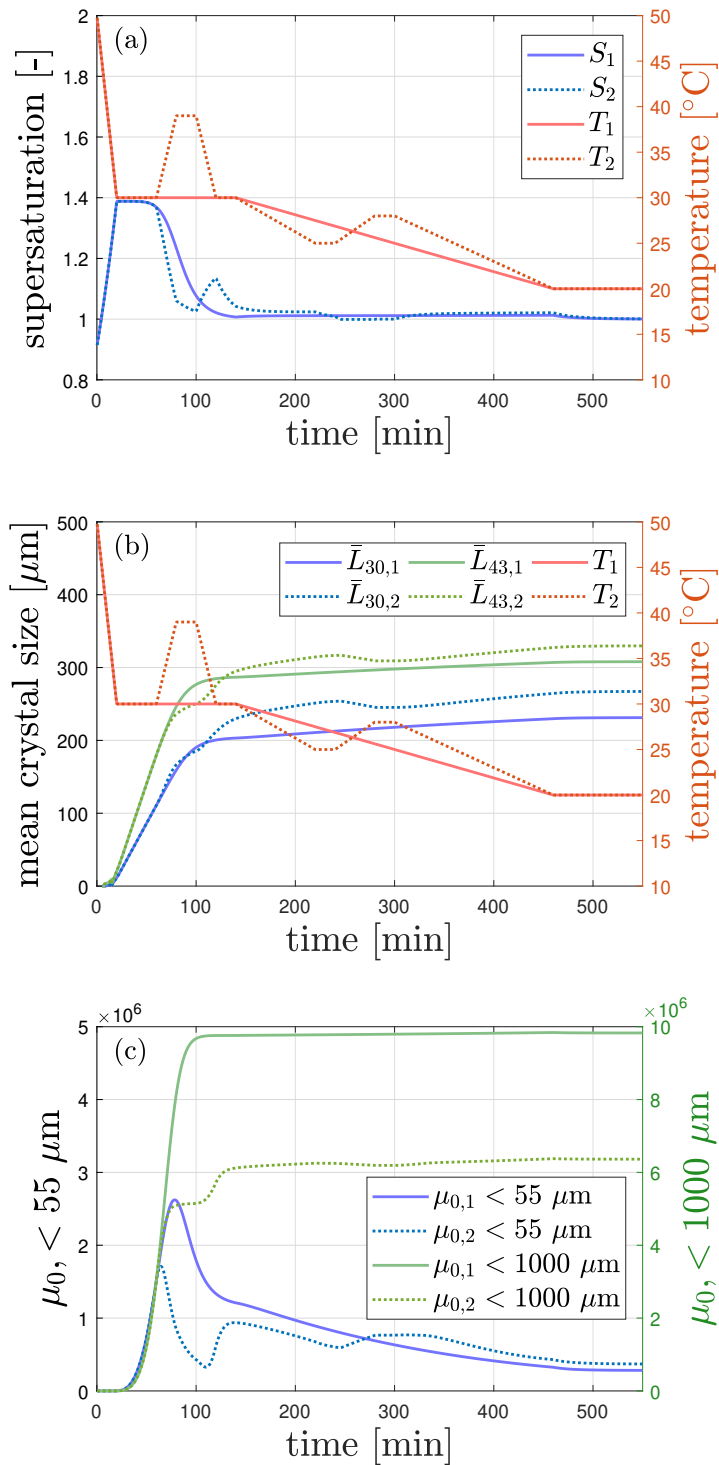
Figure 3.14: Crystal characteristics according to temperature profiles with and without temperature cycling: (a) Supersaturation, (b) mean volume crystal size ($\bar{L}_{30}$) and volume-weighted mean crystal size ($\bar{L}_{43}$), and (c) numbers of crystals less than 55 μm and all ranges for each case. The numbers, 1 and 2, as subscript represent the case of simulation.

crystals at the final time step. Case 1 is a reference case, so the temperature profile does not ever have increasing temperature. In Case 1, the temperature profile begins from 50 °C and the temperature decreases to the temperature plateau, 30 °C, with the decreasing rate of -1 °C/min. The second temperature decreasing begins at 140 min, and temperature of the second cooling stage decreases to 10 °C for 320 min in Case 1. Case 2 employs an additional heat/cool phase during the plateau period of Case 1. In addition, the temperature changing was employed once again on the second cooling stage.

In Figure 3.14(a), the maximum supersaturation values at the temperature plateau are 1.4 for both cases, but increasing temperature in Case 2 reduced the supersaturation level more quickly than Case 1. This operation restrains the development of small particles is less than 55 μm as shown in Figure 3.14(c); this criterion was chosen because the smallest sieve tray in this study has pores of 53 μm. Due to this operation, the total number of crystals in the solution is kept much lower than Case 1 as shown in Figure 3.14(c). As a result, the mean crystal sizes, $\bar{L}_{30}$ and $\bar{L}_{43}$ of Case 2 show larger values than those of Case 1 (Figure 3.14(b)). This simulation can show that temperature cycling promotes fines removal and that a well-designed temperature profile can optimize the operation of the crystallization process.

3.7 Summary

A mathematical model for unseeded batch crystallization of paracetamol in ethanol solutions was developed that includes primary and secondary nucleation, growth, and dissolution of crystals. Parameters for crystallization and dissolution were obtained separately. Seven dissolution experiments and six unseeded batch crystallization experiments were carried out to estimate and validate model parameters.

This model can account for the dissolution and disappearance of crystals when the temperature rises. Therefore, this model can be used to explain and analyze the evolution of a crystal population density distribution when heating and cooling are part of the crystal-

lization protocol. In addition, this model analyzed the influence of supersaturation on each nucleation rate and growth rate. This analysis can provide the temperature profiles that can be employed to minimize the number of fines during the process and maximize the mean crystal size through the model.

CHAPTER 4

OPEN-LOOP CONTROL OF BATCH COOLING CRYSTALLIZATION THROUGH MACHINE LEARNING APPROACH UTILIZING TRAINING DATA FROM THE PBM

4.1 Objectives

In this chapter, the PBM was employed to obtain optimal control policies through the Markov state model (MSM) and dynamic programming (DP), and the obtained control policies were validated through simulation and experiment in an open-loop manner. In past studies, MSM and DP based on experimental measurement have been employed to control the batch crystallization [50, 51], but these control approaches are sensitive to the quantity and quality of data sets for the training. To address this problem, collecting an abundant number of samples is important in this method because more data can provide a better control policy. Nonetheless, collecting samples takes time and effort. If there exists an accurate theoretical model, the crystallization dynamics can be simulated instead of performing experiments. The same idea has been employed for other systems [134–136] so that the PBM was used to generate training sets for empirical models based on the MSM.

4.2 Exploration for the optimal control policy

4.2.1 Determination of reduced order states

Crystallization processes are highly nonlinear, and various states exist. If the number of states that are handled by the MSM increases, the size of the transition matrix expands exponentially so that it takes a longer time to calculate the control policy. In order to make the MSM more economical, appropriate reduced-order states are required.

Various manipulating factors, such as temperature, pH in the solution, and amount of introduced anti-solvent, can be employed to operate the crystallization process. However, the purpose of manipulating variables is to adjust the level of supersaturation or undersaturation in the solution to produce or dissolve crystals. To describe the effect of supersaturation on the crystallization and dissolution, in this study, relative supersaturation is chosen as the input of the MSM. The relative supersaturation is,

$$\sigma(T) = \frac{c - c_s}{c_s} = S(T) - 1 \tag{4.1}$$

where c is the current solute concentration [g-solute/kg-solvent], and c_s is the solubility of solute in a unit mass of solvent [g-solute/kg-solvent]. Relative supersaturation has positive values for the supersaturated condition and negative values for the undersaturated condition. This attribute can make the MSM has change in the positive direction for nucleation and growth, change in the negative direction for dissolution and disappearance on the state space. This is an important constraint for the optimization to determine coefficients of the MSM.

In this study, the desired control targets are set with the crystal mass and the mean volume crystal size, $\bar{L}_{30}$, which can be estimated by Equation (2.23), at the end of crystallization runs. Griffin *et al.* employed the crystal mass and non-weighted total chord counts for reduced-order states to estimate the mean crystal size, because mean crystal size cannot

be measured directly [50, 51]. They constructed an empirical correlation between the mean crystal size and measurable data, the chord counts and solute concentration, to control desired properties. However, the mean volume crystal size can be estimated by the calculated zeroth and third moments utilizing the PBM. Therefore, the zeroth and the third moments were selected as reduced-order states for this study.

According to a study about relationships between moments and chord couts [137], the total number of crystals in a unit volume can be related to chord counts by the FBRM. Because the total number of crystals can be shown in μ_0, using moments for the reduced-order states can be conducive to link PBM simulation results with experiments. This work is necessary to conduct the feedback control based on the measurements, which will be described in Chapter 5. The third moment, μ_3, represents the total volume of crystals in a unit volume so that the mass of crystals in the system can be determined by μ_3, assuming the crystal density and the volume shape factor are known. The orders of μ_0 and μ_3 from the developed PBM are generally larger than 10^6 and 10^{12}, respectively, and the relative supersaturation, σ, as the input is smaller than 1. This large differences lead to poor scaling in the MSM. To avoid this problem, we use scaled moments, $\mu_0 \times 10^{-6}$ and $\mu_3 \times 10^{-12}$, which have similar magnitudes. The reduced-order states are expressed as s_1 and s_2. The dynamic state, $\mathbf{s}$, is shown as

$$\mathbf{s} \equiv \begin{bmatrix} \mu_0 \times 10^{-6} \\ \mu_3 \times 10^{-12} \end{bmatrix} = \begin{bmatrix} s_1 \\ s_2 \end{bmatrix} \tag{4.2}$$

and this relationship converts Equation (2.23) as

$$\bar{L}_{30} = \left(\frac{\mu_3}{\mu_0} \right)^{1/3} = 100 \left(\frac{s_2}{s_1} \right)^{1/3} \tag{4.3}$$

4.2.2 Markov state model to describe the crystallization dynamics

A key assumption for this step is that the MSM is *memoryless*, where the future states at the next time step depend only on the current states. In former studies [50, 51], a machine-learning strategy was applied to identify the MSM for the crystallization dynamics based on measured PAT data, and the obtained model was utilized for the crystallization control.

The MSM for the crystallization dynamics is expressed in discrete-time as

$$\Delta \mathbf{s}_\tau = \mathbf{s}_{\tau+1} - \mathbf{s}_\tau = F\left(\mathbf{s}_\tau, \sigma_\tau\right) \Delta t \tag{4.4}$$

where τ is the time index, so $\mathbf{s}_\tau$ and $\mathbf{s}_{\tau+1}$ are states at time, t_τ and $t_{\tau+1}$, respectively, σ_τ is the relative supersaturation at t_τ as the input, and Δt is the time interval between t_τ and $t_{\tau+1}$. For the function, $F\left(\text{ś}, \sigma\right)$, at each position, ś, a sixth-order polynomial of σ with zero constant was employed to give enough flexibility as below

$$\begin{aligned}
\left.\frac{\Delta \mathbf{s_1}}{\Delta t}\right|_{\text{ś}} &= \mathbf{F}_1(\text{ś}, u) = \beta_{1,1}^{[\text{ś}]} u + \beta_{1,2}^{[\text{ś}]} u^2 + \cdots + \beta_{1,6}^{[\text{ś}]} u^6. \\
\left.\frac{\Delta \mathbf{s_2}}{\Delta t}\right|_{\text{ś}} &= \mathbf{F}_2(\text{ś}, u) = \beta_{2,1}^{[\text{ś}]} u + \beta_{2,2}^{[\text{ś}]} u^2 + \cdots + \beta_{2,6}^{[\text{ś}]} u^6.
\end{aligned} \tag{4.5}$$

where $\beta_{i,j}^{[\text{ś}]}$ denotes the jth coefficient for the ith state at each position, ś. This model has three constraints below:

1. the saturated condition cannot make any change in the system,

2. supersaturation makes increasing change, and undersaturation makes decreasing change on the state space, and

3. state change by supersaturation level is monotonic.

The mathematical expression of these constraints on the function, $F(\mathbf{s}_\tau, u_\tau)$ are:

1. $F(\mathbf{s}, u) = \mathbf{0}$ if $u = 0$ $\forall \mathbf{s}$;

2. $u F(\mathbf{s}, u) \geq \mathbf{0}$ $\forall \mathbf{s}$; and

3. $\partial F/\partial u \geq \mathbf{0}$ for a fixed s.

Coefficients for each state, $\beta^{[\acute{s}]}$, were regressed by the locally weighted least-square scheme following an algorithm in Equation (4.6).

for a given position, $\acute{s}$

$$\beta^{[\acute{s}]} = \underset{\beta \in \mathbb{R}^{2 \times 6}}{\operatorname{argmin}} \left(\sum_{j=1}^{N_{\text{train}}} w(\acute{s}, \hat{s}_j; \kappa) ||[\hat{u}_j, \hat{u}_j^2, \dots, \hat{u}_j^6]\beta \Delta t - \Delta \hat{s}_j||_2^2 \right)$$

$$\text{subject to} \quad u[u \ u^2 \dots u^6]\beta \geq \mathbf{0}, \qquad \forall u; \tag{4.6}$$

$$[2u \ 3u^2 \ 4u^3 \ 5u^4 \ 6u^5] \begin{bmatrix} \beta_{2,1} & \beta_{2,2} \\ \beta_{3,1} & \beta_{3,2} \\ \beta_{4,1} & \beta_{4,2} \\ \beta_{5,1} & \beta_{5,2} \\ \beta_{6,1} & \beta_{6,2} \end{bmatrix} \geq \mathbf{0}, \qquad \forall u.$$

where N_{train} denotes the number of samples in the training data set, κ is a bandwidth for determining the size of neighborhood, $w(\acute{s}, \hat{s}_j; \kappa)$ is a weight function with κ, and $\Delta \hat{s}_j$ means the measured following change in state over the time interval Δt for the jth training data set. The coefficient of obtained empirical model from the model training process changes based on each inquired state of the system. The set of coefficients can be composed as a matrix and the coefficients are queried to find the change to the next time step to identify the crystallization dynamics. Even though this model cannot be expressed as a global model, we can use vector fields to visualize the trained MSM as shown in Figure 4.1.

The optimization problem with constraints as shown in Equation (4.6) was solved using CVX: a MATLAB package to specify and solve convex optimization [138, 139].

$$\Delta\mathbf{s}_\tau = \mathbf{s}_{\tau+1} - \mathbf{s}_\tau = F(\mathbf{s}_\tau, u_\tau)\Delta t$$
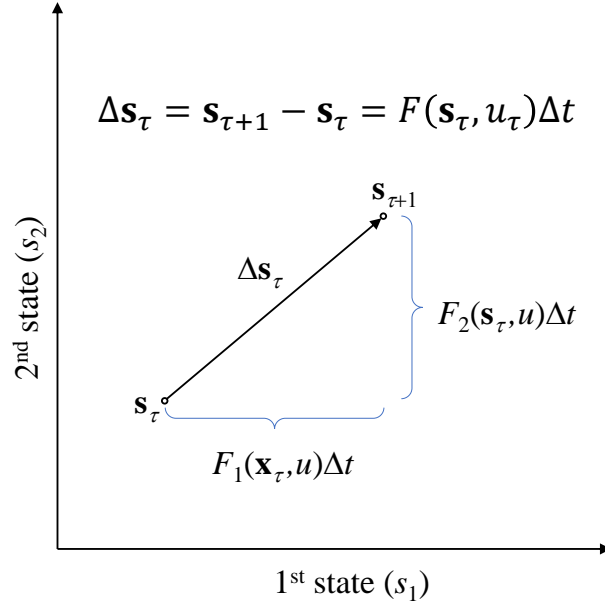
Figure 4.1: Schematic diagram of the MSM on the state space. The state change from current state, s_τ, moves to the state at the next time step according to the current state and current supersaturation level, u_τ, through the function, $F(s_\tau, u_\tau)$.

4.2.3 Finding the optimal control strategy via dynamic programming

Once the empirical model is established through the MSM, we can find the optimal control policy by solving a dynamic optimization problem as below:

$$
\begin{aligned}
&\underset{u_\tau = \pi(\mathbf{s}_\tau)}{\text{minimize}} && \Phi\left(\mathbf{s}_{\tau=1,\dots,N}, u_{\tau=1,\dots,N}\right) \\
&\text{subject to} && \mathbf{s}_{\tau+1} = F\left(\mathbf{s}_\tau, u_\tau = \pi(\mathbf{s}_\tau)\right)\Delta t + \mathbf{s}_\tau, \ \tau = 0,\dots,N-1; \\
&&& \mathbf{s}_0 = \mathbf{s}^{\text{init}};
\end{aligned}
\tag{4.7}
$$

where Φ is the objective function, π is the state-feedback control policy, N is the desired batch time, and F is the discrete-time dynamic model, that is the MSM in this study.

The purpose of this control is to produce crystals with specific mean crystal size and mass. The target mean size in this thesis is defined as mean volume crystal size, $\bar{L}_{30}$, that can be evaluated by the two states, s_1 and s_2. The target crystal mass can be estimated by the second state (s_2), volume shape factor (k_v), and crystal density (ρ_c). The objective of

this control is making the current states reach the target position on the state space, which is the desired crystal properties. This objective is achieved by minimizing the distance between the current state and the target position. The *distance-to-target* can be estimated by Equation (4.8):

$$d(\mathbf{s}_\tau, \mathbf{s}^\oplus) \equiv (\mathbf{s}_\tau - \mathbf{s}^\oplus)^\top Q(\mathbf{s}_\tau - \mathbf{s}^\oplus), \text{ where } Q = \begin{bmatrix} 1 & 0 \\ 0 & \lambda^2 \end{bmatrix} \tag{4.8}$$

where $\mathbf{s}^\oplus$ is the target position on the state space, and λ is a scaling factor to normalize the values of states when they have large differences in the magnitude of values. The range of s_1 is between 0 and 100, and that of s_2 is between 0 and 200. Because the ranges for each state are similar, the λ in this study was set as 1.

Another key point of the control is minimizing the operating cost. Even if the controller can control the system perfectly, the cost and time must be within a reasonable limit. It is assumed that the cost is dominated by the effort to heat and cool the crystallizer to bring the supersaturation and undersaturation to the desired values. Thus, the *input-effort* function is defined by the square of supersaturation at each time step to evaluate the absolute value of σ:

$$\varepsilon(u_\tau) \equiv \sigma_\tau^2 \tag{4.9}$$

Here, a straightforward formulation of the objective function could consist of the distance to the target at the final time step and weighted input effort:

$$\Phi\left(\mathbf{s}_{\tau=1,\dots,N}, u_{\tau=1,\dots,N}\right) = \rho \sum_{\tau=0}^{N-1} \varepsilon(u_\tau) + d(\mathbf{s}_N, \mathbf{s}^\oplus) \tag{4.10}$$

However, Equation (4.10) does not enforce the system to settle down at the end of the operation. To resolve the problem, we distinguished the *distance-to-target* function with running and terminal costs: $(t_\tau/t_N)^\gamma d(\mathbf{s}_\tau, \mathbf{s}^\oplus)$ is the running cost term and $d(\mathbf{s}_N, \mathbf{s}^\oplus)$ is the

terminal cost term. Based on this idea, the objective function is formulated as:

$$\Phi\left(\mathbf{s}_{\tau=1,\dots,N}, u_{\tau=1,\dots,N}\right) = \sum_{\tau=0}^{N-1} \left\{(t_\tau/t_N)^\gamma d(\mathbf{s}_\tau, \mathbf{s}^\oplus) + \rho\varepsilon(u_\tau)\right\} + d(\mathbf{s}_N, \mathbf{s}^\oplus) \tag{4.11}$$

where γ is a parameter to adjust the final approach of the control. If the time-varying term has a small value of γ, the value of $(t_\tau/t_N)^\gamma$ is enforced to reduce quickly, which approaches the target from the beginning. In contrast, a large γ leads to a mild controller action where more deviation from the target is allowed at the beginning of the run. Finally, the optimization problem is formulated as follows:

$$\begin{aligned} \underset{u_\tau = \pi(\mathbf{s})}{\text{minimize}} \quad & \sum_{\tau=0}^{N-1} \left\{(t_\tau/t_N)^\gamma d(\mathbf{s}_\tau, \mathbf{s}^\oplus) + \rho\varepsilon(u_\tau)\right\} + d(\mathbf{s}_N, \mathbf{s}^\oplus) \\ \text{subject to} \quad & \mathbf{s}_{\tau+1} = F\big(\mathbf{s}_\tau, u_\tau = \pi(\mathbf{s}_\tau)\big)\Delta t + \mathbf{s}_\tau, \ \tau = 0,\dots,N-1, \\ & \mathbf{s}_0 = \mathbf{s}^{\text{init}}. \end{aligned} \tag{4.12}$$

To apply dynamic programming to solve the optimization problem given by Equation (4.12), the state space and input variables are discretized, and the function, F, is converted into the cell-to-cell mapping from point-to-point mapping [140, 141]. If the state values are in a discretized area, all values are represented by the center point of the grid. Figure 4.2 illustrates the difference between two mapping approaches. Any values in a square in Figure 4.2(b) are represented by the center point of the square. $\mathcal{S}$ is as set of the center points of the discretized state space, and $\mathcal{U}$ is a set of discretized inputs. The states in the cell-to-cell mapping are

$$\mathbf{s}_{\tau+1} = \mathcal{C}(\mathbf{s}_\tau, u_\tau, \Delta t) \equiv \underset{\mathbf{s}_{\tau+1} \in \mathcal{S}}{\text{argmin}} \quad ||\mathbf{s}_{\tau+1} - \big(F(\mathbf{s}_\tau, u_\tau)\Delta t + \mathbf{s}_\tau\big)||_2^2 \ , \tag{4.13}$$

where $\mathcal{C}$ represents the current position in the grid, $\mathbf{s}_\tau \in \mathcal{S}$, with the input, $\mathbf{u}_\tau \in \mathcal{U}$, over

the time step Δt.

(a)

$$\Delta \mathbf{s}_\tau = \mathbf{s}_{\tau+1} - \mathbf{s}_\tau$$
$$= F(\mathbf{s}_\tau, u_\tau)\Delta t$$

$\mathbf{s}_{\tau+1}$

$F_2(\mathbf{s}_\tau, u)\Delta t$

$\mathbf{s}_\tau$

$F_1(\mathbf{x}_\tau, u)\Delta t$

s_2

s_1

(b)

$$\Delta \mathbf{s}_\tau = \mathbf{s}_{\tau+1} - \mathbf{s}_\tau$$
$$= C(\mathbf{s}_\tau, u_\tau, \Delta t)$$

$\mathbf{s}_{\tau+1}$

$\mathbf{s}_\tau$

s_2

s_1
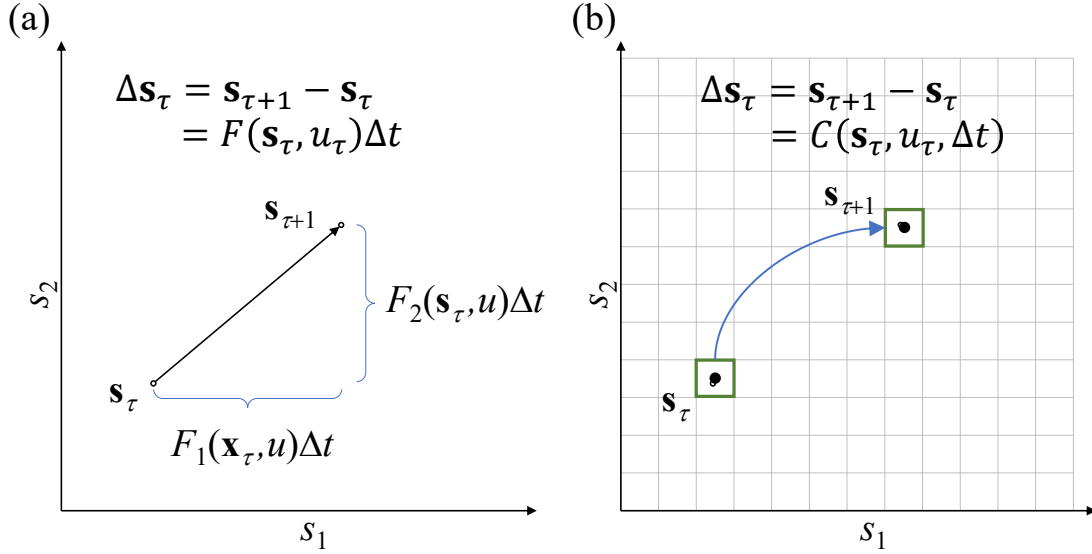
Figure 4.2: Comparison between (a) point-to-point dynamics and (b) cell-to-cell mapping.

Table 4.1: Dynamic programming algorithm for solving optimization problem using Equations (4.12) and (4.13)

Dynamic Programming Algorithm   *Optimal Control Policy*

set $V_N(\mathbf{s}_N) = d(\mathbf{s}_N, \mathbf{s}^\oplus)$ for each $\mathbf{s}_N \in \mathcal{S}$

for $\tau = N - 1, \ldots, 0$

    for each $\mathbf{s} \in \mathcal{S}$

$$\phi_\tau^*(\mathbf{s}) \equiv u_\tau^* \mid_\mathbf{s} \;=\; \underset{u_\tau \in \mathcal{U}}{\arg\min} \quad \{(t_\tau/t_N)^\gamma d(\mathbf{s}, \mathbf{s}^\oplus) + \rho\varepsilon(u_\tau) + V_{\tau+1}(\mathbf{s}_{\tau+1})\}$$

$$\text{subject to} \quad \mathbf{s}_{\tau+1} = C(\mathbf{s}, u_\tau, \Delta t);$$

    and

$$V_\tau(\mathbf{s}) = (t_\tau/t_N)^\gamma d(\mathbf{s}, \mathbf{s}^\oplus) + \rho\varepsilon\left(u_\tau^* \mid_\mathbf{s}\right) + V_{\tau+1}\left(C\left(\mathbf{s}, u_\tau^* \mid_\mathbf{s}, \Delta t\right)\right).$$

combine to construct the optimal control policy

$$\pi^* = \{\phi_0(\mathbf{s}), \ldots, \phi_{N-1}(\mathbf{s})\}$$

Note: the optimization problem posed at each step and state can be solved using the look-up table obtained by the cell-to-cell mapping.

The Bellman equation solves the optimization problem given by Equation (4.12) for the discretized input and state variables, as well as for the discretized time steps according to the dynamic programming algorithm in Table 4.1. Each reduced-order state has 101 grids of the same size, so the state space contains 10,201 squares in Figure 4.2(b). The set of inputs, $\mathbf{u}_\tau \in \mathcal{U}$, is from -0.05 to 0.50 with a spacing of 0.025, and Δt is 30 seconds. The solutions, which are the supersaturation setpoints for each state at a given time, are stored in a look-up table, where the dimension of the look-up table depends on the numbers of discretized grids of states and time steps. Temperature, which is the manipulated variable in the crystallization system, is determined by the chosen supersaturation found from the look-up table and the solubility of the system.

4.3 Training set generation using the PBM

To collect the data points for the training set, 6,000 simulations were conducted for the crystallization with the initial concentrations of 300 g-solute/kg-solvent. Half of the simulation cases were for unseeded and the other were for seeded crystallization. For unseeded crystallization simulations, the range of supersaturation at the temperature plateau in each run is set between 1.20 and 1.40, as verified experimentally in the previous chapter. In order to develop the mean volume crystal size, the temperature cycling strategy was applied. In this strategy, the minimum and maximum temperature in temperature cycles, which use $T_{\max}, T_{\min}, \Delta T_{\text{heat}}$, and ΔT_{cool}, temperature changing rates, R_{heat} and R_{cool}, and the number of cycles, N_{cycle}, were randomly determined in each simulation run. The randomly generated temperature profiles follows profile structures shown in Figure 4.3 for unseeded crystallization and Figure 4.4 for seeded crystallization. Table 4.2 shows ranges of values for each parameter to determine the temperature profile for the simulations.

The initial temperature for unseeded crystallization was set to keep the solution undersaturated. On the other hand, the initial temperature for seeded crystallization was determined lower than the saturation temperature of the solution to prevent the dissolution of
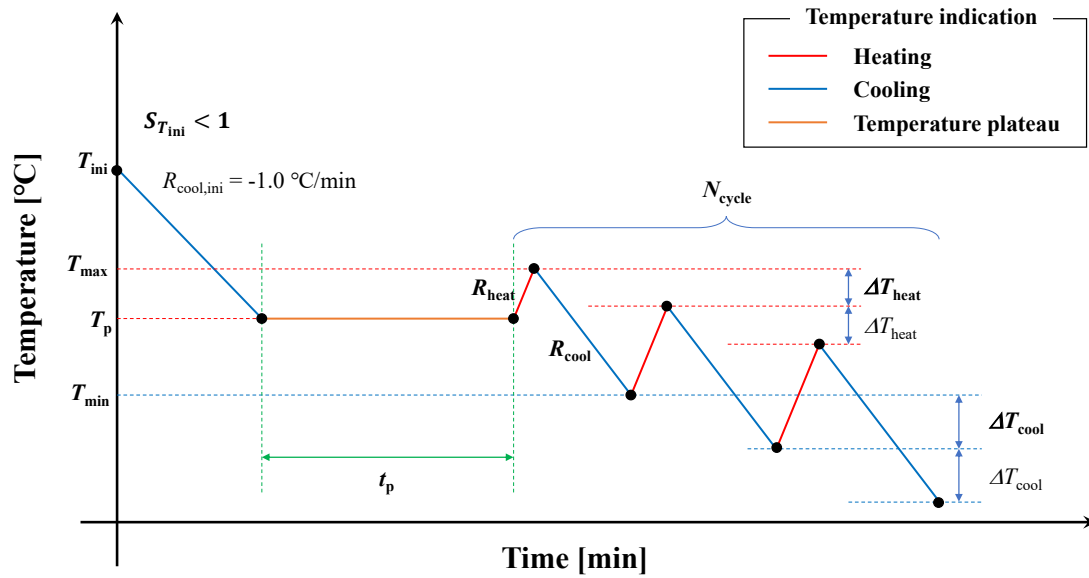
Figure 4.3: Randomly generated temperature profile scheme for unseeded crystallization simulation for the training set
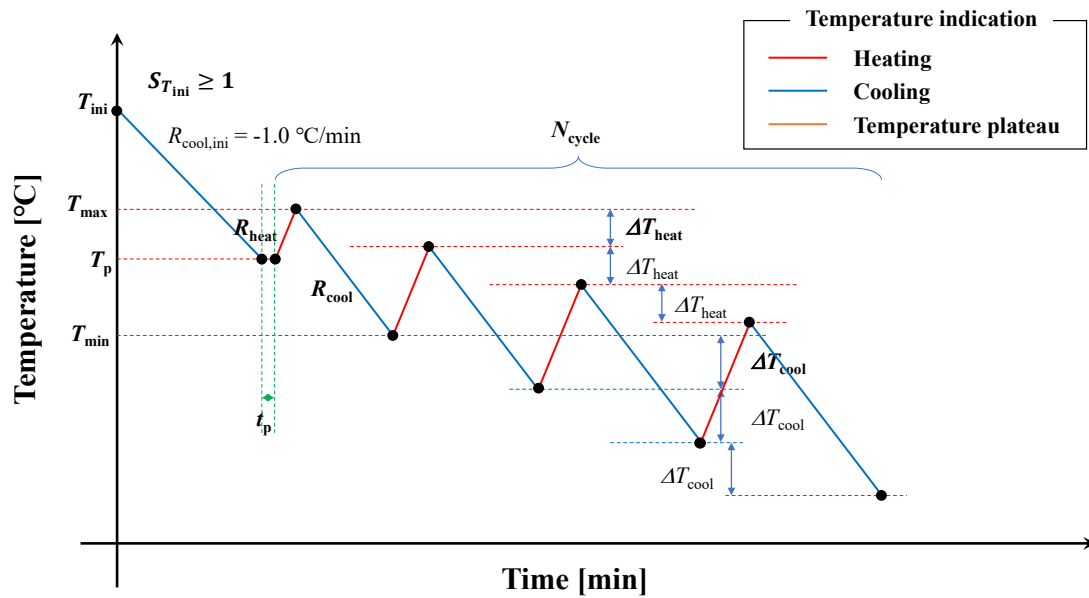
Figure 4.4: Randomly generated temperature profile scheme for seeded crystallization simulation for the training set

seed crystals at the initial stage. In the seeded crystallization simulations, the seed crystal size distribution can affect the final attributes of the crystallization process so that seed crystal distributions, which follow log-normal distributions, were randomly generated for each simulation case.

Table 4.2: Ranges of condition for random simulation to obtain training data set

Symbol	Unit	Meaning	Range
c_0	g/kg	initial concentration	300
T_0	°C	initial temperature	$T_0 = 50$
T_p	°C	temperature at the plateau	$25 < T_p < 44$
t_p	min	time of the plateau	$t_p = 120$
$T_{\max}$	°C	maximum temperature of the first cycle	$T_p + 1 < T_{\max} < T_p + 4$
$T_{\min}$	°C	minimum temperature of the first cycle	$T_p - 4 < T_{\min} < T_p - 1$
R_{heat}	°C/min	heating rates in cycle (constant for all cycles)	$0.2 < R_{\text{heat}} < 1.0$
R_{cool}	°C/min	cooling rates in cycle (constant for all cycles)	$0.1 < R_{\text{cool}} < 1.5$
$R_{\text{cool},0}$	°C/min	cooling rates to the temperature plateau	$R_{\text{cool},0} = -1.0$ (constant for all cases)
ΔT_{heat}	°C	variation of maximum temperature on each cycle (constant for all cycles)	$0.5 < \Delta T_{\text{heat}} < 1.5$
ΔT_{cool}	°C	variation of minimum temperature on each cycle (constant for all cycles)	$0.5 < \Delta T_{\text{cool}} < 2.5$
N_{cycle}	-	number of temperature cycles	$1 < N_{\text{cycle}} < 15$

Around 2 million data points were collected from the 6,000 simulations in total. Estimated data were screened by criteria for entire data points to remove meaningless data points on the MSM training. In cases of unseeded crystallization, data points at the initial stage of the temperature plateau prior to significant nucleation and growth have state values are zero due to the lack of crystals, and these points were rejected. After the screening, 50,000 data points from the unseeded crystallization cases and 50,000 points from the seeded crystallization cases were randomly extracted for the current states, $\mathbf{s}_\tau$, the state changes, $\Delta \mathbf{s} = \mathbf{s}_{\tau+1} - \mathbf{s}_\tau$, and the supersaturation, σ. The time interval, Δt, is fixed as 30 seconds in the simulation.

Figure 4.5 shows the randomly selected data points for the training set. Each plot in Figure 4.5 illustrates crystallization and dissolution data points from unseeded and seeded simulations. Data points in Figure 4.5(a) are dense between 0 and 30 for s_1 because the unseeded crystallization begins from a clear solution where $s_1 = 0$ and $s_2 = 0$. The most data points for unseeded crystallization in Figure 4.5(a) and (b) are concentrated in a specific range of the state space, especially between 0 and 40 for s_1, since the initial development

of crystals occurs at the temperature plateau with narrow ranges of reduced-order states. If only data points in Figure 4.5(a) and (b) are used in the MSM training, the reduced-order states at the region without data points in the state space should be extrapolated, and the model prediction may be inaccurate. To resolve this issue, the seeded crystallization was simulated using randomly generated seed crystal distributions, and these points fill the empty space in the state space. The data points from seeded crystallization simulations are shown in Figure 4.5(c) and (d).
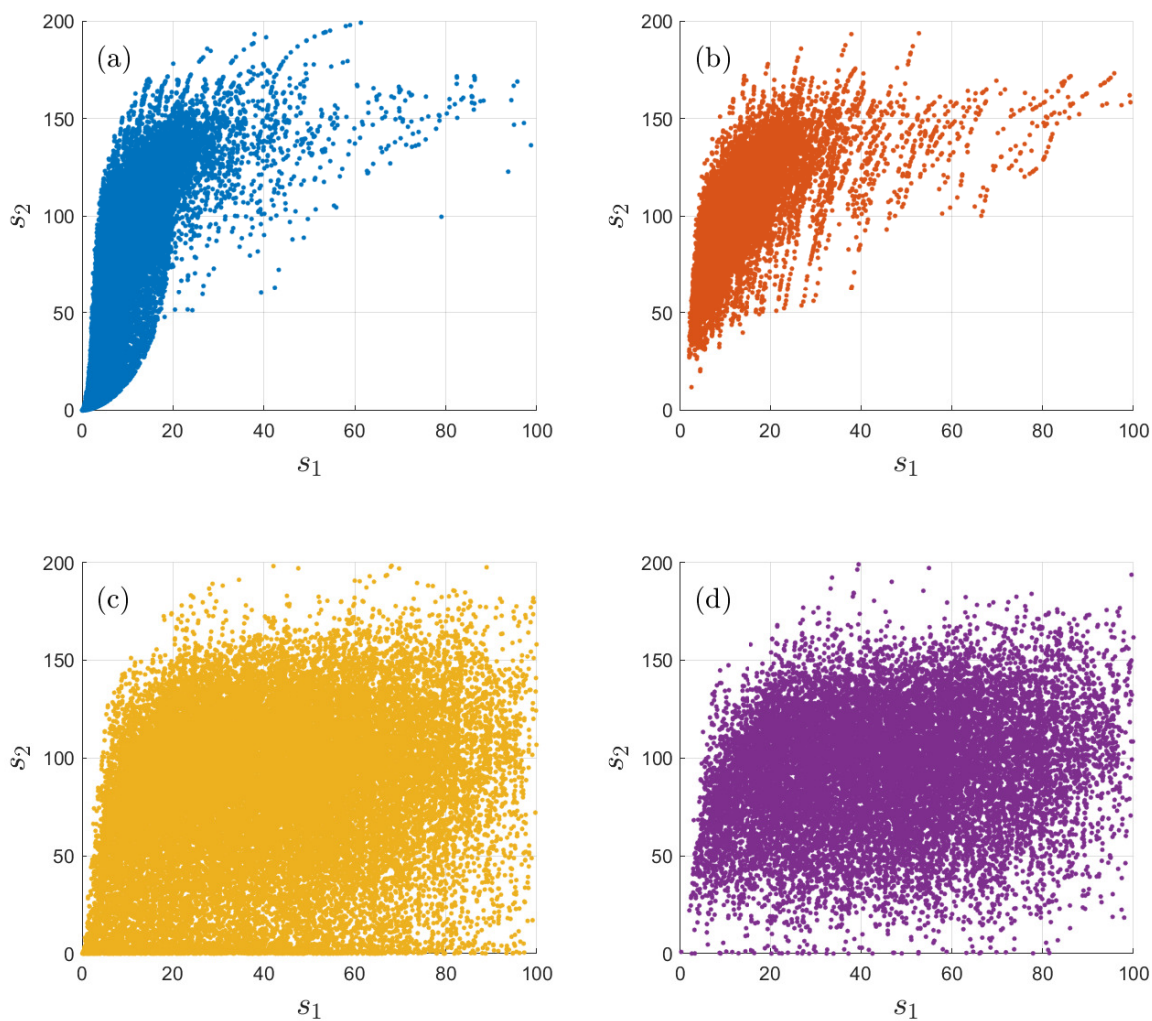
Figure 4.5: Distributions of chosen sample points for the MSM training set: (a) crystallization data points from unseeded cases, (b) dissolution data points from unseeded cases, (c) crystallization data points from seeded cases, and (d) dissolution data points from seeded cases.

4.4 Investigation and validation of optimal control policies

4.4.1 Validation of obtained control policy using the PBM simulation

The MSM was trained with 100,000 training data points in Figure 4.5 to describe the crystallization and dissolution of paracetamol in ethanolic solution. Figure 4.6 visualizes the change from each state, depending on combinations of states and the input level. The vertical and horizontal directions of arrow represent the changes of the mass and the total number of crystals, respectively. In Figure 4.6(a) – (d) that have positive supersaturation, it can be seen that the arrows point up and to the right, and the lengths of arrows become longer at higher supersaturation. This is because existing crystals lead to secondary nucleation and crystal growth, which are faster at higher supersaturation. In the undersaturated conditions of σ = -0.05 and -0.025, on the other hand, the arrows point to the downward and left-hand side which indicate dissolution and disappearance of crystals as shown in Figure 4.6(e) and (f). By changing σ, the trajectory can be manipulated for crystallization control.

The target mean volume size, $\bar{L}_{30}$, and the target crystal mass for the control can be indicated on the state space as a point according to Equation (4.3), $\bar{L}_{30} = 100 \times (s_2/s_1)^{1/3}$. The estimated mean volume crystal size from the simulation is defined by Equation (2.23), which can be obtained using the reduced-order states. The mass of crystals in the crystallization system is defined as Equation (2.11). The values of k_v and ρ_c in this study of paracetamol are 0.797 and 1.263×10^{-15} g/μm^3. The target μ_3 and μ_0 were calculated by inverting the Equations (2.11) and (2.23), respectively, based on the target mass and target mean volume size.

To acquire optimal control policies employing the MSM and DP in the unseeded batch crystallization employing a temperature plateau, the policy obtaining process did not start at the origin representing the clear solution but at a specific point in the state space. The main reason for this approach is reducing the stochasticity of primary nucleation that happens in the crystallization experiment. Even though the control approach using the MSM
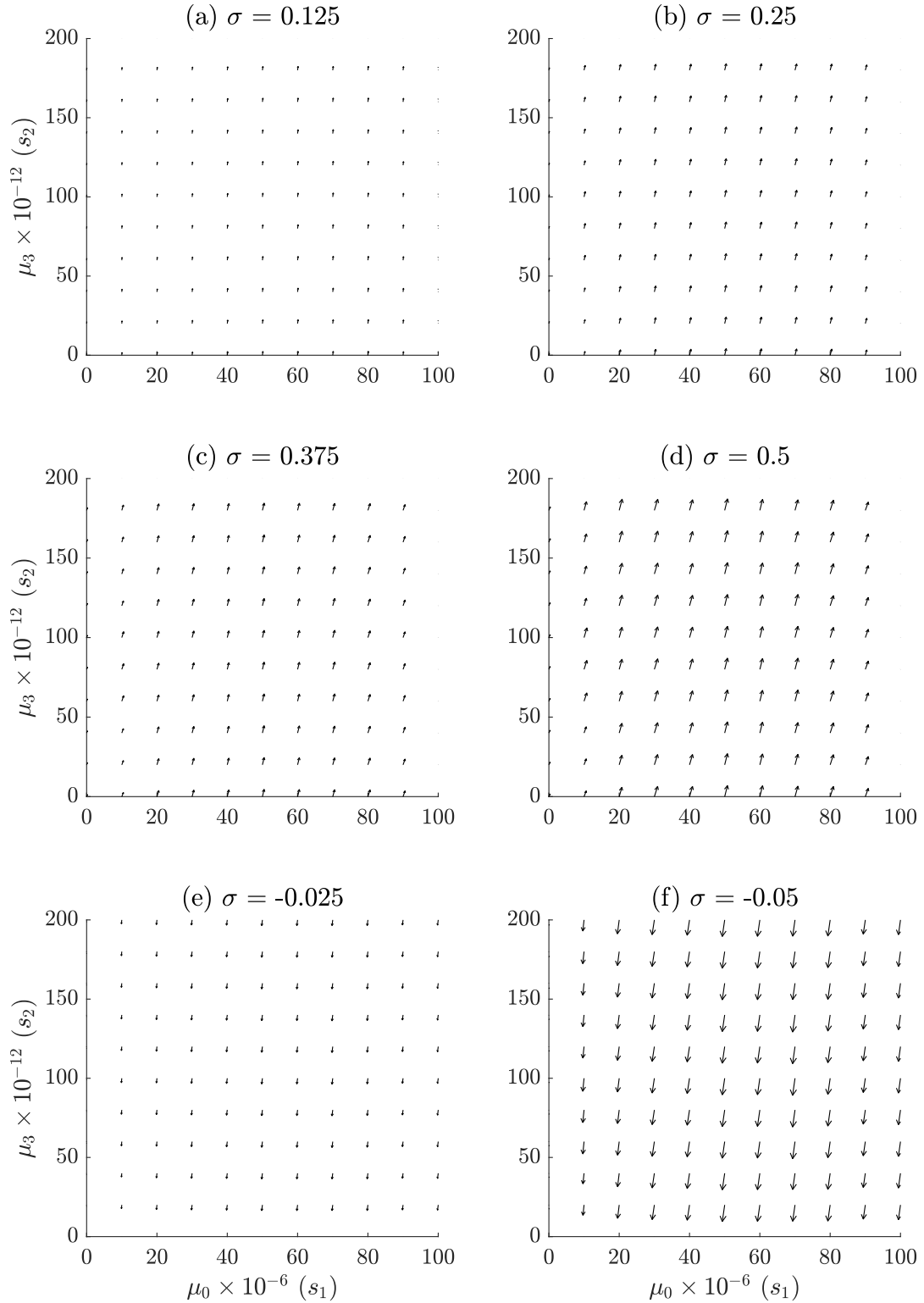
Figure 4.6: Visualization of the MSM, $F(\mathbf{s}, \sigma)$, at different supersaturation conditions. Arrows represent the change of crystals over a 30-second interval predicted by the MSM. Subplots from (a) to (d) show changes in the state space when crystallization happens, and subplots (e) and (f) illustrate changes while dissolution occurs.

74

and DP can provide the temperature profile to produce crystals with desired properties, the obtained control policy cannot reflect the stochasticity since the training set for the MSM was from the simulation by the PBM that has deterministic characteristics. In Chapter 3, a temperature plateau was implemented to reduce the effect of the stochastic characteristics, and the experimental data showed the measurements by PAT tools at the end of the temperature plateau have similar values for repetitive experiments. However, because the MSM and DP approach cannot implement the temperature plateau naturally, the initial states for control were defined by the PBM simulation. The simulated states employing a temperature plateau by the PBM were used as the beginning point to obtain optimal control policy through the MSM and DP in this study. An example of the internal seeding application
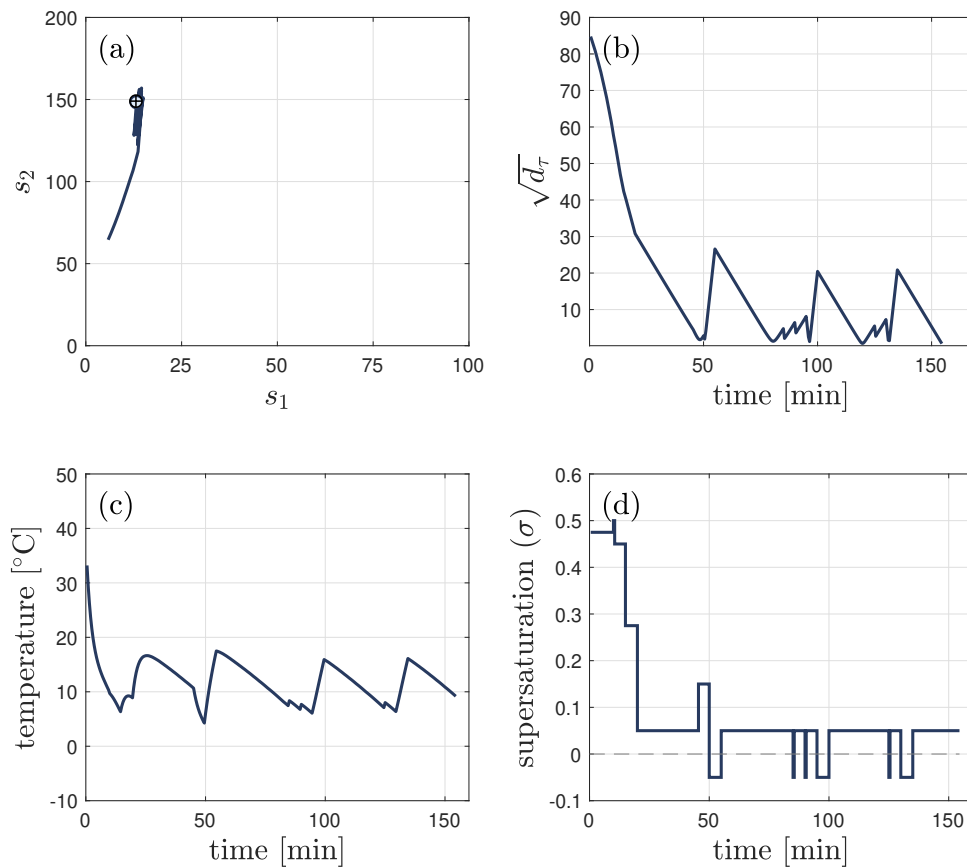
Figure 4.7: States and control profiles obtained by the MSM and DP for target mean volume size of 225 μm and target mass of 15 g: (a) predicted trajectory of states for optimal open-loop control toward the target, (b) predicted distance to the target, (c) optimal temperature profile, and (d) profiles of optimal supersaturation set point

Table 4.3: Comparison among targets, predicted results by the obtained optimal policies, and the PBM simulation results

		$\bar{L}_{30}$ [μm]	m [g]	s_1	s_2	$\sqrt{d_{\mathrm{fin}}}$
	Targets	225.0	9.0	7.8	89.4	-
Case 1	Final results by MSM and DP	220.7	9.0	8.3	89.1	0.080
	Final results by PBM	199.5	8.4	10.5	83.4	6.5
	Targets	200.0	9.0	11.2	89.4	-
Case 2	Final results by MSM and DP	202.9	9.0	10.7	89.3	0.064
	Final results by PBM	208.3	9.5	10.6	95.5	6.1
	Targets	175.0	7.0	13.0	69.5	-
Case 3	Final results by MSM and DP	178.0	7.0	12.4	69.8	0.18
	Final results by PBM	163.2	7.5	17.1	74.5	6.5
	Targets	160.0	8.0	19.4	79.5	-
Case 4	Final results by MSM and DP	162.0	8.0	18.8	79.7	0.21
	Final results by PBM	100.2	8.8	86.4	86.9	67

is shown in Figure 4.7. In Figure 4.7(a), the trajectory begins from a point, $s_1 = 5.83$ and $s_2 = 64.6$, that is the reduced-order state at the end of a temperature plateau for 120 minutes. The control policy was obtained through the dynamic programming algorithm in Table 4.1 from this point. Therefore, the time axis in Figure 4.7(b) – (d) represents the time after the temperature plateau finished. Optimal supersaturation profiles were explored by the MSM and DP and Figure 4.7(d) shows the optimal supersaturation profiles to reach target. The states trajectory and the distances between current state at each time step, τ, and target state were evaluated and illustrated in and Figure 4.7(a) and (b), respectively. The temperature profile was estimated by the optimal supersaturation and state at each time step, and it is shown in Figure 4.7(c).

Using the MSM and DP method which were confirmed to provide the optimal control policy to produce crystals with desired states, four control cases were considered to test whether the PBM can simulate the crystallization processes using the temperature profiles from DP. Table 4.3 shows the four target mean volume size and the mass of crystals. The target reduced-order states that are estimated by the target size and mass are also in Table 4.3. Furthermore, Table 4.3 compares the results by the MSM and DP and results of the PBM simulation.

76
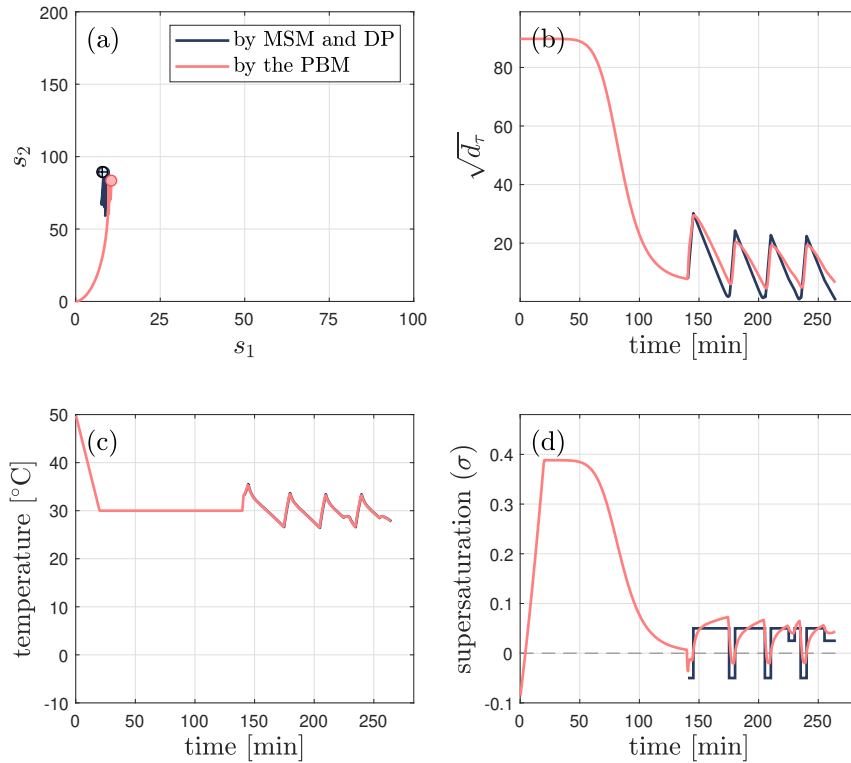
Figure 4.8: States and control profiles obtained by the MSM and DP for Case 1: target $\bar{L}_{30} = 225\ \mu$m and $m = 9$ g, (a) predicted trajectory of states for optimal open-loop control toward the target, (b) predicted distance to the target, (c) optimal temperature profile, and (d) profiles of optimal supersaturation set point. Lines and markers in dark blue color are results using the MSM and DP approach, and lines in light red color are from the PBM simulation, respectively.
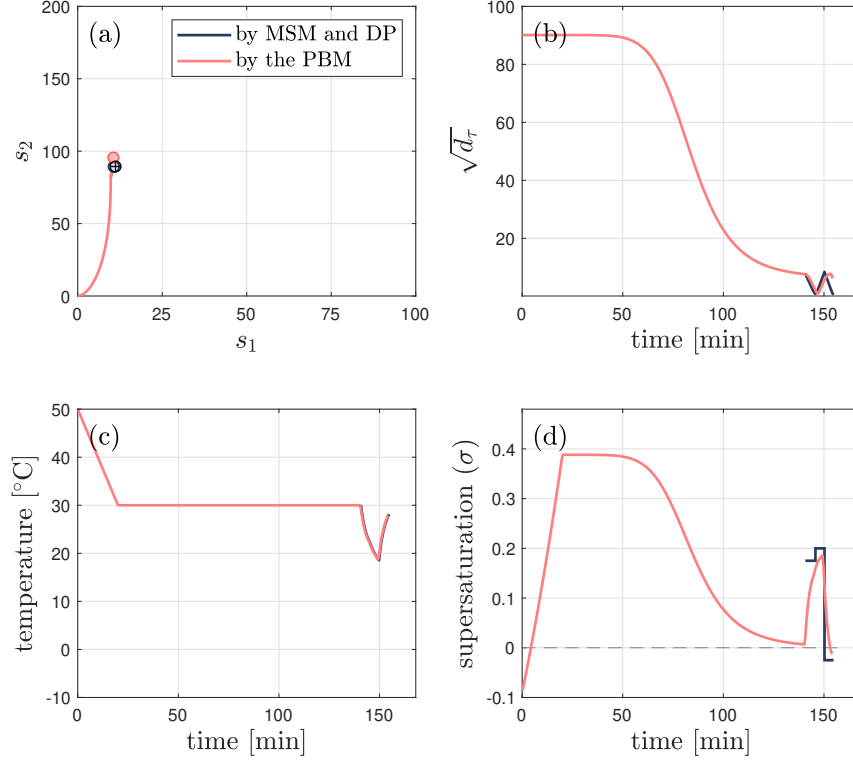
Figure 4.9: States and control profiles obtained by the MSM and DP for Case 2: target $\bar{L}_{30} = 200 \ \mu$m and $m = 9$ g, (a) predicted trajectory of states for optimal open-loop control toward the target, (b) predicted distance to the target, (c) optimal temperature profile, and (d) profiles of optimal supersaturation set point. Lines and markers in dark blue color are results using the MSM and DP approach, and lines in light red color are from the PBM simulation, respectively.

The final reduced-order states given by the MSM and DP are close to target values. The square root of the final distances-to-target, $\sqrt{d_{\text{fin}}}$, in Table 4.3, by the MSM and DP are less than 0.5. However, the final results from the PBM simulation show longer distances between the final and target positions. In particular, Case 4 shows the distance of 67, which is very far from the target states. In Case 4, the final s_2 by the PBM has around 10% error, but the final s_1 shows a value longer than the target.

Figures 4.8 – 4.11 compare the profiles of states, $\sqrt{d_{\text{fin}}}$, temperature, and supersaturation between the MSM and DP approach and the PBM for test cases. In each figure, panel (a) presents the trajectories of reduced-order states on the state space, panel (b) shows the trend of $\sqrt{d_{\text{fin}}}$ from the current state, panel (c) shows temperature profiles, and panel (d)
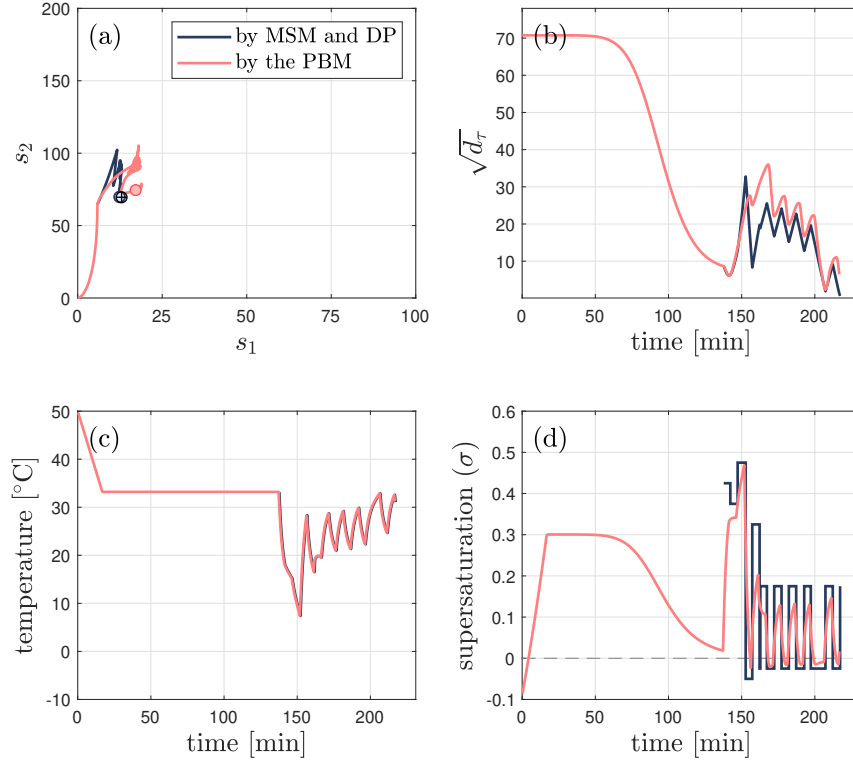
Figure 4.10: States and control profiles obtained by the MSM and DP for Case 3: target $\bar{L}_{30} = 175\ \mu$m and $m = 7$ g, (a) predicted trajectory of states for optimal open-loop control toward the target, (b) predicted distance to the target, (c) optimal temperature profile, and (d) profiles of optimal supersaturation set point. Lines and markers in dark blue color are results using the MSM and DP approach, and lines in light red color are from the PBM simulation, respectively.

compares the supersaturation profiles from DP and the PBM. In these figures, the dark blue lines and marks represent the results from the MSM and DP approach, and the light red lines and marks show the results by the PBM. The DP approach in Table 4.1 employed the estimated reduced-order states at the end of the temperature plateau using PBM simulation results as the initial reduced-order states; thus, the dark blue trajectories in panel (a) begin from specific positions on the state space. However, the light red trajectories in panel (a) start from the origin because the PBM simulations implemented the temperature plateau. The PBM simulations implemented the temperature profiles from the DP approach, so the temperature profiles in each case perfectly overlapped, as shown in each figure (c). Simulated supersaturation profiles by the PBM are also compared to the obtained optimal
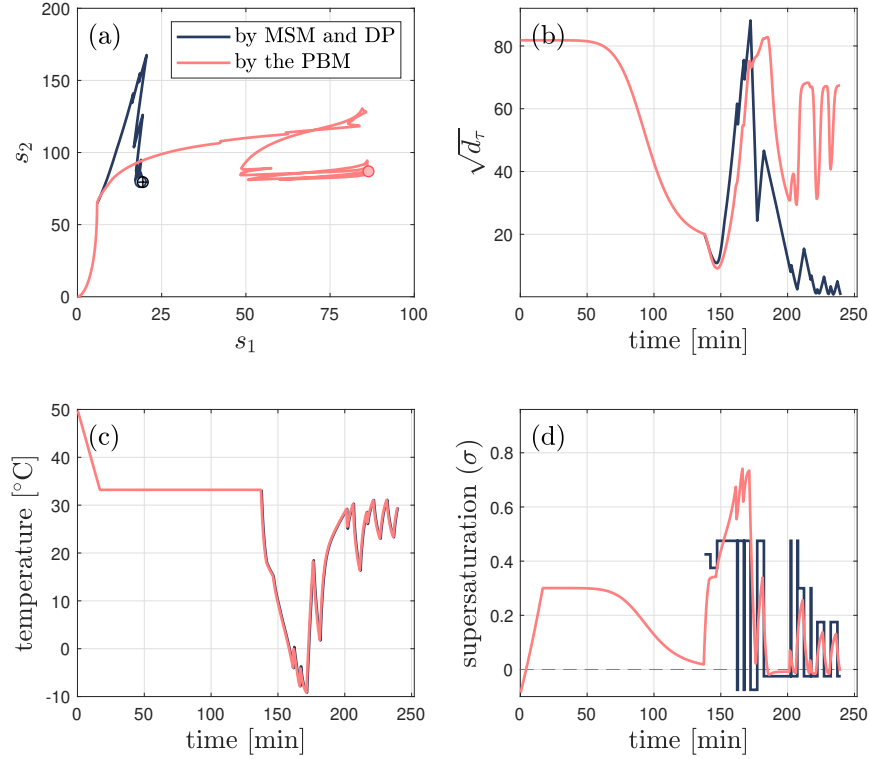
Figure 4.11: States and control profiles obtained by the MSM and DP for Case 4: target $\bar{L}_{30} = 160\ \mu$m and $m = 8$ g, (a) predicted trajectory of states for optimal open-loop control toward the target, (b) predicted distance to the target, (c) optimal temperature profile, and (d) profiles of optimal supersaturation set point. Lines and markers in dark blue color are results using the MSM and DP approach, and lines in light red color are from the PBM simulation, respectively.

supersaturation profiles in panel (d) of each figure.

Among four cases in Table 4.3, PBM simulations for three cases excluding Case 4 reach near the target states. However, even PBM simulations for all cases cannot reduce the distance-to-target to less than 1 at the end of the simulation due to the deviation from the predicted behaviors given by the MSM and the PBM. The MSM used predicted results by the PBM for the training set, but the MSM simplified the input and output in the model using a six-order polynomial function. Furthermore, the predicted movements on the state space by both models can be similar but may not be the same because the MSM uses reduced-order states to explain the crystallization process. Even though the mean crystal sizes by the PBM simulation have errors from the target sizes, the results of the crystal

mass show good predictions. The predicted mean volume crystal size and mass have errors less than 10% from the target for Cases 1, 2, and 3. Moreover, the profiles of optimal supersaturation by the MSM and DP and simulated supersaturation profiles for these three cases show very similar behaviors as shown in panel (d) of Figures 4.8 – 4.10.

However, the PBM does not predict crystallization of Case 4 as shown in Figure 4.11. In Figure 4.11(a), s_1 increases rapidly, where the trajectory goes to right-hand side on the state space. This means that nucleation is more significant than crystal growth in this condition. The supersaturation level lower than 1.05 (here, $\sigma < 0.05$) affects the growth rate more than the secondary nucleation rate, but as the supersaturation level becomes higher, the secondary nucleation rate increases, as mentioned in Section 3.6.1. In Figure 4.11(d), we can see the predicted supersaturation level by the PBM increases higher than 0.7, even though the optimal supersaturation is less than 0.5. After the temperature plateau ended, the suddenly increased supersaturation level produces numerous nuclei, which makes increasing s_1 in Figure 4.11(a). This mismatching of supersaturation prediction between the MSM and the PBM led to farther than 65 of the square root of the final distances-to-target, $\sqrt{d_{\text{fin}}}$, at the end of the process.

4.4.2   Experimental validation of obtained control policy

The obtained optimal control policies in this chapter tend to be predicted by the PBM excluding examples with specific conditions, but which is expected because the MSM is trained using the PBM simulation results. Therefore, the experimental validations are necessary through the open-loop control. Four crystallization experiments with the obtained temperature profiles from previous simulations were carried out. The temperature profiles presented as red lines in Figures 4.8 – 4.11 were implemented in the experimental equipment.

set $V_N(\mathbf{x}_N) = d(\mathbf{x}_N, \mathbf{x}^\oplus)$ for each $\mathbf{x}_N \in \mathcal{X}$.

for $\tau = N-1, \ldots, 0$

    for each $\mathbf{x}_\tau \in \mathcal{X}$

$$\phi^\star_{\mathrm{dp},\tau}(\mathbf{x}_\tau) \equiv u^\star_\tau \mid_{\mathbf{x}_\tau} = \underset{u_\tau \in \mathcal{U}}{\mathrm{argmin}} \quad \{(t_\tau/t_N)^\gamma d(\mathbf{x}_\tau, \mathbf{x}^\oplus) + \rho\varepsilon(u_\tau) + V_{\tau+1}(\mathbf{x}_{\tau+1})\}$$

$$\text{subject to} \quad \mathbf{x}_{\tau+1} = \mathcal{C}(\mathbf{x}_\tau, u_\tau, \Delta t);$$

$$V_\tau(\mathbf{x}_i) = (t_\tau/t_N)^\gamma d(\mathbf{x}_\tau, \mathbf{x}^\oplus) + \rho\varepsilon(u^\star_\tau \mid_{\mathbf{x}_\tau}) + V_{\tau+1}\big(\mathcal{C}(\mathbf{x}_\tau, u^\star_\tau \mid_{\mathbf{x}_\tau}, \Delta t)\big).$$

construct the optimal feedback control policy from the optimal input for each time step and state:

$$\pi_{\mathrm{dp}} = \big\{\phi^\star_{\mathrm{dp},0}(\mathbf{x}_0), \ldots, \phi^\star_{\mathrm{dp},N-1}(\mathbf{x}_{N-1})\big\}$$

Note: the simple optimization problem posed at each step and state can be solved by enumeration.

1. Obtaining control policies using DP

2. Implementing temperature profile

Control computer

Thermocouple

FBRM   ATR-FTIR

Thermocouple
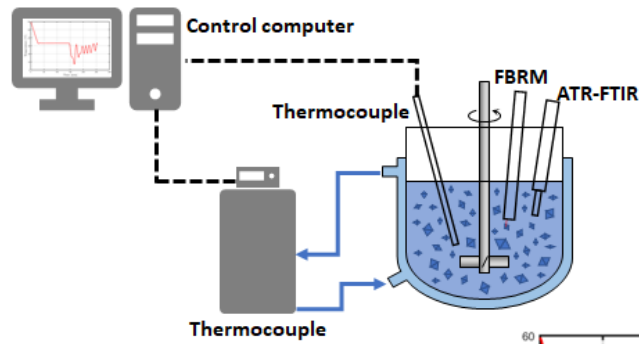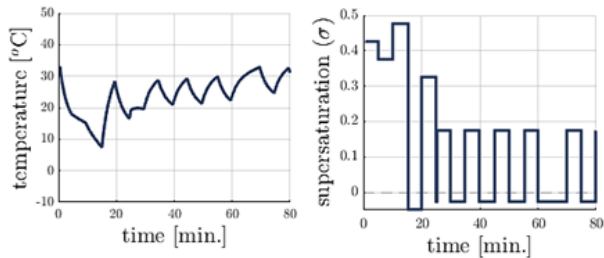
3. Running open-loop controlled experiments according to the determined temperature
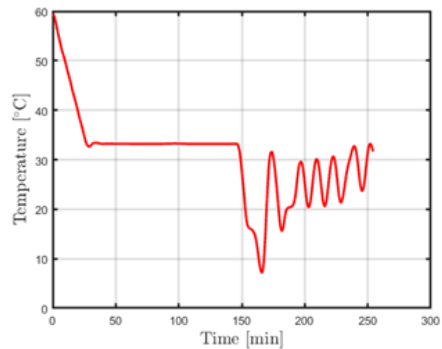
Figure 4.12: Flowchart to show the experimental implementation of the obtained temperature profile for the open-loop control

Experimental method: The open-loop control experiments were carried out by follow-
ing the steps indicated in Figure 4.12. The experiments are prepared according to the
method described in Chapter 3, and the determination and implementation of the temper-
ature profile are explained here. In the first step, the desired targets, including the mean
volume crystal size and crystal mass, are chosen. Next, dynamic programming determines
the optimal temperature profile to generate crystals that satisfy the target at the end of the
process. The obtained temperature profile was input to the control software, iControl™,
manually since the open-loop control does not take any feedback signal during the pro-
cess. After finishing all steps, the crystallization experiment is carried out. The post-run
procedures such as washing and drying of the crystals are described in Chapter 3.

The recovered crystals were sieved and weighed. The number densities in each sieve
tray were approximated based on the measured mass of crystals and the mean size of crys-
tals. The crystal mean sizes were assumed to the geometric average of pore sizes of upper
and lower sieve trays. Finally, the mean volume size, $\bar{L}_{30}$, was obtained by Equation (2.23).

Experimental results. Experimental results for the four cases are presented in Table 4.4.
This table compares the targets, experimental results through sieving and weighing recov-
ered crystals, and the PBM simulation results using the measured temperature profiles from
experiments; thus, the PBM simulations in Table 4.3 and Table 4.4 shows different results.
To compare the experimental results and targets, final states and distance-to-target of re-
covered crystals were evaluated from the sieved mean volume size and weighed crystal
mass.

In Table 4.4, the weighed masses of recovered crystals are near the target within errors
of 10%. However, the mean volume sizes by sieving analysis tend to be smaller than the
target size. The smaller obtained mean volume crystal sizes than target $\bar{L}_{30}$ values make
s_1 values much larger from the targets according to Equation (4.3), so values of $\sqrt{d_{\text{fin}}}$ in
Table 4.4 are larger than 4, which is larger than criteria, for all experimental results. On
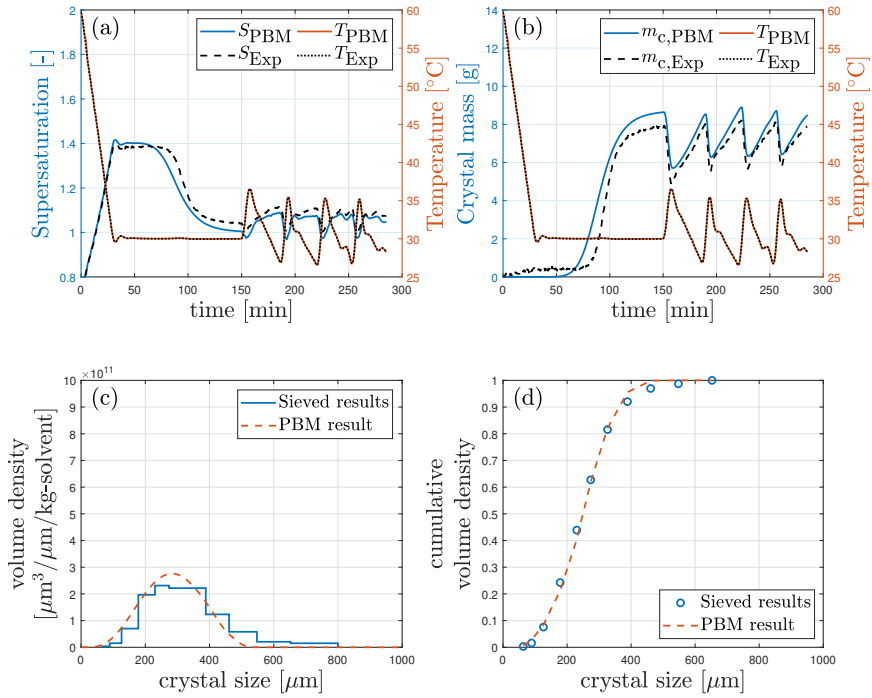
Figure 4.13: Comparison of open-loop control results for Case 1: (a) supersaturation, (b) crystal mass in the solution, (c) volume density distribution, and (d) cumulative volume density distribution.
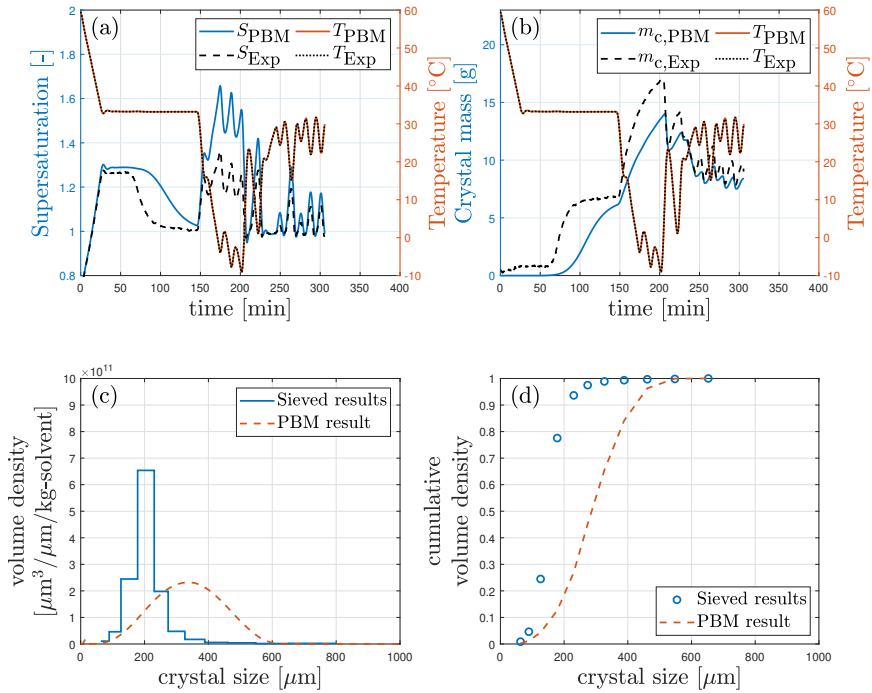
Figure 4.14: Comparison of open-loop control results for Case 4: (a) supersaturation, (b) crystal mass in the solution, (c) volume density distribution, and (d) cumulative volume density distribution.

the other hand, the PBM simulation results have closer values of $\sqrt{d_{\text{fin}}}$ than experimental values excluding Case 4. In Cases 1, 2, and 3, the predicted mean volume sizes have errors of smaller than 15%, and these results are similar to the simulation results in Table 4.3. However, the simulation result for Case 4 have values of $\sqrt{d_{\text{fin}}}$ longer than 90 which means the control is not effective.

To analyze what happened during open-loop controls, two examples, Cases 1 and 4, are compared in Figures 4.13 and 4.14 for trends of the supersaturation (Figure (a)), mass of crystals (Figures (b)), and volume density distribution of crystals in two different ways as shown in Figures (c) and (d). Figure 4.13 shows that PBM can predict the experimental results very well. In particular, the simulated bulk density distribution results agree well with the sieve analysis data. On the other hand, trends of simulated supersaturation and crystal mass of Case 4 in Figure 4.14 do not follow experimental data. Especially, the

Table 4.4: Results comparison among targets, experimentally sieved and weighed recovered crystals, and the PBM simulation using measured temperature profiles from open-loop experiments

		$\bar{L}_{30}$ [μm]	m [g]	$s_1{}^*$	$s_2{}^*$	$\sqrt{d_{\text{fin}}}{}^*$
Case 1	Targets	225.0	9.0	7.8	89.4	-
	Sieved and weighed results	168.6	8.2	16.9	81.2	13
	The PBM results with experimental temperature profile	193.0	8.5	11.7	84.3	7.4
Case 2	Targets	200.0	9.0	11.2	89.4	-
	Sieved and weighed results	127.8	9.3	44.0	91.9	33
	The PBM results with experimental temperature profile	209.2	10.0	10.9	99.9	9.3
Case 3	Targets	175.0	7.0	13.0	69.5	-
	Sieved and weighed results	132.0	7.4	31.8	73.2	19
	The PBM results with experimental temperature profile	165.3	7.4	16.2	73.2	4.2
Case 4	Targets	160.0	8.0	19.4	79.5	-
	Sieved and weighed results	136.2	8.2	32.3	81.6	13
	The PBM results with experimental temperature profile	91.3	8.4	109.6	83.3	90

* Note: Final states and square root of distances, s_1, s_2, and $\sqrt{d_{\text{fin}}}$, in this table are evaluated based on the measured and simulated $\bar{L}_{30}$ and m.

85

predicted supersaturation between 150 and 200 minutes is much higher than the measured supersaturation as shown in Figure 4.14(a). This result is very similar to the supersaturation trends in Figure 4.11(d). The unpredictable supersaturation and crystal mass profiles seem to be caused by the steep temperature change rate and low temperature near -10 °C that is not experimentally validated in Chapter 3.

Limitation of open-loop control experiments. The reduced-order state, s_1, cannot be calculated directly from FBRM and ATR-FTIR measurements. Even though the crystal mass can be estimated by *in situ* measurement of the IR spectrum, the number of crystals cannot be determined by any PAT tools. It is a limitation that s_1 of the open-loop control experiments could not be monitored in real-time. If the *in situ* mean volume size can be measured directly, s_1 can be evaluated, but that is also not possible. Therefore, the real-time trends of s_1 and d were not observed.

For open-loop experiments, the experimental system used the temperature profile obtained with the MSM and DP approaches, but the temperature control system has a response delay; thus, the experimental system could not control the temperature equal to the obtained optimal temperature profile. Figure 4.15 compares temperature profiles from the MSM and DP approaches and experimentally measured temperature profiles for all cases. In all cases, we can see the manipulated temperature profiles in the experimental equipment takes longer times than the optimal temperature profiles. Moreover, cases with more rapid temperature change rates and many cycles, such as Cases 3 and 4, show longer delays. Also, due to the open-loop control nature, the control variables cannot be adjusted because the control system does not have any feedback response according to the monitored results.

4.5 Summary

The PBM simulation generated data points for the training set to obtain optimal control policy through the MSM and DP. The obtained control policies were stored, and the optimal
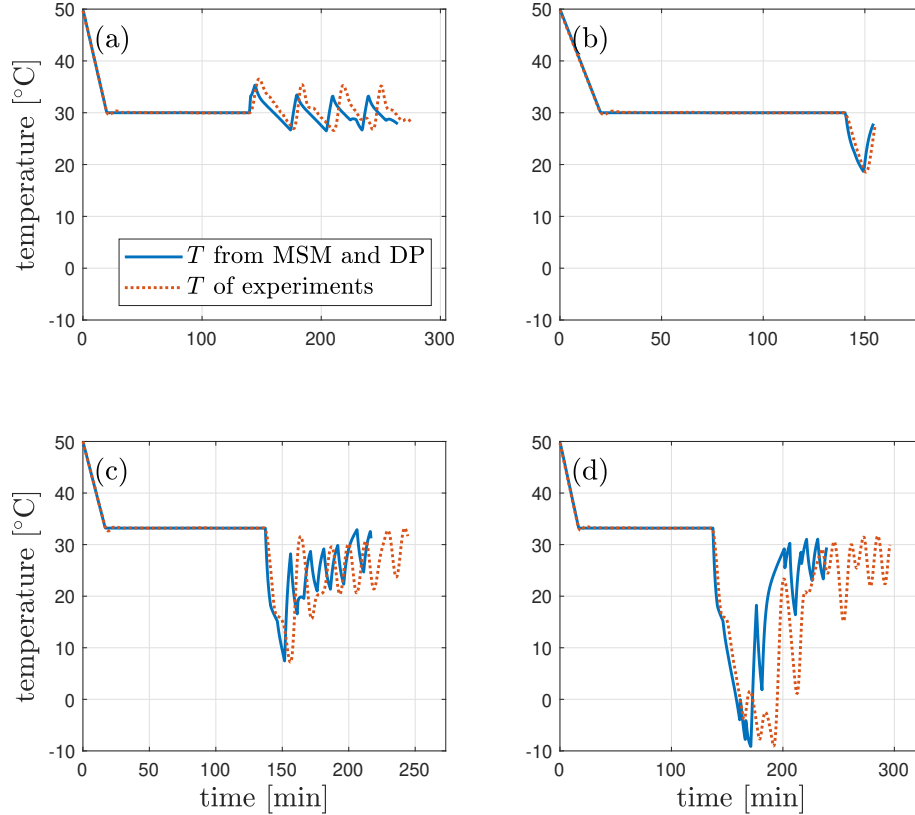
Figure 4.15: Comparison of temperature profiles for (a) Case 1, (b) Case 2, (c) Case 3, and (d) Case 4. Blue solid lines and red dotted lines represent temperature profiles from the MSM and DP and experimentally measured temperature profiles, respectively.

supersaturation trend to produce desired crystals was chosen by an optimization procedure. Since the supersaturation is controlled by the temperature manipulation in this project, the obtained supersaturation trends and the solution concentration estimate the optimal temperature profile to control the crystallization. The optimization procedure by DP provides selected test cases in Table 4.3, where the obtained temperature profiles were tested by the PBM simulations and experimental open-loop control.

The PBM simulations for Cases 1, 2, and 3 predicted good mean volume crystal sizes and crystal masses, but the simulation for Case 4 predicted a value of s_1 that is four times larger. For the simulation using the measured temperature profile for Case 4, the mismatch result on s_1 is also shown. The results of open-loop control experiments have errors less than 10% for crystal masses, but the mean volume sizes are smaller than the target sizes for

all cases. However, the implemented temperature profiles into the experimental equipment have response delays, where the length of processing time in experiments is longer than the operation time by the optimization. This limitation of inaccurate open-loop control results concludes that a feedback control scheme is required to obtain crystal properties close to the target. However, s_1 should be determined for the feedback control utilizing the approach that is introduced in this chapter, so an *in-situ* monitoring technique for s_1 is necessary to realize the feedback control.

CHAPTER 5

CORRELATION BETWEEN MEASUREMENTS AND PBM SIMULATION TO REALIZE THE FEEDBACK CONTROL

5.1 Objectives

In this chapter, a shallow neural network (SNN) model was developed to convert the measurement by the FBRM to the first reduced-order state ($s_1 = \mu_0 \times 10^{-6}$) for crystal size control. Chapter 4 demonstrates that obtaining a control policy for the crystallization control was made possible by the training data set using the PBM simulation, but it also shows limitation of the open-loop control. Feedback control can be employed to overcome the weakness of the open-loop control. The crystallization control in this thesis uses the reduced-order states from the PBM simulation, but the reduced-order states cannot be measured by PAT tools directly. Because the only measurable data available from experiments are chord length distribution given by the FBRM and the concentration information given by the ATR-FTIR, a model is required to convert the measured data to reduced-order states. This chapter shows the steps to determine the correlation between the measured data and simulated results by the PBM using statistical and machine learning approaches.

5.2 Investigation into relationships between crystal size and chords

The crystallization control through MSM and DP uses two states that are defined by $s_1 = \mu_0 \times 10^{-6}$ and $s_2 = \mu_3 \times 10^{-12}$. The zeroth and third moments are from the PBM prediction.

The third moment can be directly estimated from the crystal mass in the solution with assumptions that the volume shape factor and density of crystal are constant, so s_2 can be converted from the measured concentration by the ATR-FTIR. However, the zeroth moment cannot be evaluated using the measured data directly, and thus the conversion model in this chapter is necessary to determine the reduced-order state, s_1, which relates to the zeroth moment that represents the total number of crystals in a unit volume.

The FBRM measures *in situ* characteristics of particulates in the solution, but the collected data do not perfectly represent the crystal attributes. As explained in Chapter 2, measured data by the FBRM are chord counts of various lengths. Even though a small crystal can generate short chords, a large crystal can simultaneously make long and short chords. In particular, the measured CLD is highly dependent on the crystal shape, so conversion methods are necessary to determine the particle properties. The chord lengths and counts are assumed to be related to particle size, shape, and numbers, respectively. Hence, the relationship between measured data and predicted attributes of particles must be found to control the crystallization system based on the model prediction.

The measured CLD data can be processed as weighted chord length distributions. Weighted chord length distribution and weighted chord count emphasize the measured CLD in the bin of longer chords due to the multiplication of chord lengths to the raw counts. Higher-order weighted chord counts reduce the effect of shorter chords and amplify the impact of longer chords. The weighted chord count defined by the manufacturer, Mettler-Toledo, is shown below.

$$C_\gamma = \sum_{i=1}^{N} C_{0,i} \frac{M_i^\gamma}{\sum_{j=1}^{N} M_j^\gamma} N \tag{5.1}$$

where C_0 and C_2 are non-weighted and square-weighted chord counts, respectively. M is the mid-point of each bin in the FBRM measurements, i is the index of each bin, γ is the weight for the attribute, and N is the number of bins in the FBRM measurements. For

example, the square-weighted chord count is given by $\gamma = 2$ in Equation (5.1).

At the initial stage of this project, a model to convert moments to chord counts was investigated to confirm the chord counts are related to the moments. For this study, the estimated moments by the PBM were used as input, and the non-weighted and square-weighted chord counts were used as the output of the relationship. Experimental data by Li *et al.* [19] were adapted for this work. The square-weighted chord count in this study shown below has a slightly different definition from Equation (5.1).

The difference between Equations (5.1) and (5.2) is only the presence or absence of the term for the sum of the number of bins and the weighted bin size. However, those values are constant for all measurements in this paper, so the values calculated in both equations are proportional.

$$C_2^+ = \sum_{i=1}^{N} C_{0,i} M_i^2 \tag{5.2}$$

The non-weighted and square-weighted chord counts were modeled using the zeroth, first, second, and third moments as given below:

$$C_\gamma^+ = \sum_{i=0}^{3} a_{i,\gamma} \mu_i^{\alpha_{i,\gamma}}, \qquad \gamma = 0, 2 \tag{5.3}$$

where subscript i is the ith moments, and a and α are the proportional and exponential coefficients for each moment, respectively. The parameters, $a_{i,k}$ and $\alpha_{i,k}$, were estimated with minimizing by the least square method.

As a result of the parameter estimation, the parameters, $a_{i,\gamma}$ and $\alpha_{i,\gamma}$, that appear only in the zeroth moment have non-zero values in both cases. This result indicates that the total chord count is strongly correlated to the number of crystals in the system as calculated by the PBM. The R^2 values for both cases are 0.869 and 0.943, respectively, and Figure 5.1 compares the experimental data and fitted results. In Figure 5.1(a), the non-weighted chord counts have a large difference among experimental measurements for the same zeroth
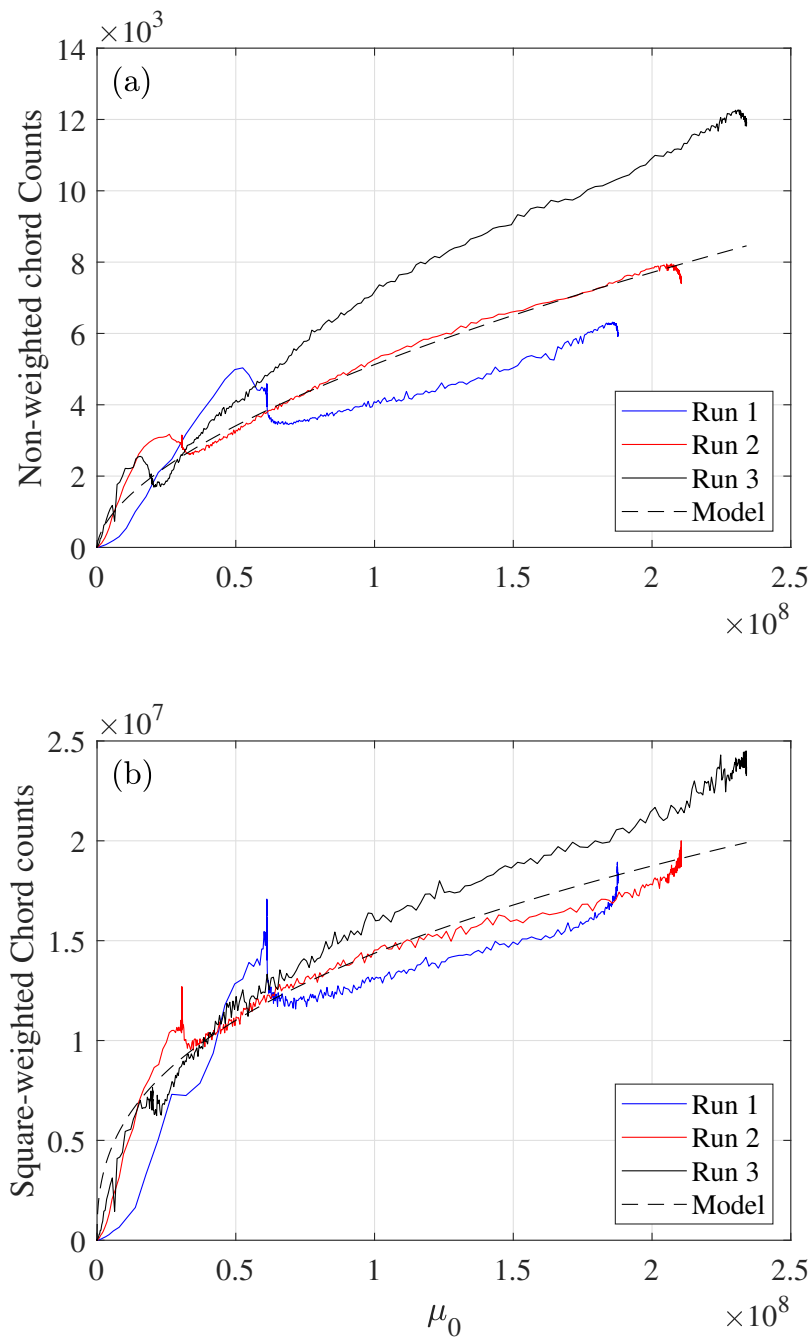
Figure 5.1: Plots for total chord counts versus the zeroth moment, (a) for non-weighted total chord counts, and (b) for square-weighted total chord counts. Solid lines represent experimental data and the dashed line shows the model prediction.

moment by the PBM model. On the other hand, the square-weighted total chord counts show smaller variations for the zeroth moment among the three experimental data as shown in Figure 5.1(b). This result shows the zeroth moment has a stronger relationship with the square-weight total chord count than the non-weighted chord count, and it is likely to provide a more reliable prediction of the zeroth moment.

Even though the result gives a clue for a conversion model between measurements and prediction, this model has two limitations: 1) The inputs and outputs of the correlation are the opposite of the desired model, and 2) higher accuracy is necessary for the feedback control. For the feedback control, the measured data by the PAT tools should be converted to the reduced-order state, s_1, but this model's input is the zeroth moment and output is the chord count. Hence, this correlation cannot be used directly for the feedback control of the crystallization. Moreover, the conversion model requires higher accuracy to evaluate the reduced-order state, s_1, for more effective and efficient feedback control, so the next section shows the steps to select predictors for a better model.

5.3   Selection of predictors

In the previous section, the result shows that the moments of crystals are related to the chord counts measured by the FBRM, but the model has limitations for the feedback control. In addition, non-weighted and square-weighted total chord counts dilute the properties of measured CLD. The same non-weighted or square-weighted chord count may correspond to different CLD because total chord count is a merged attribute, regardless of the chord length. Figure 5.2 shows an example of this case. The red circle in Figure 5.2(a) covers two monitored data points. One point is for crystallization period (at 63 min) and the other point is for dissolution region (at 85 min). Even though these data points have very close crystal mass and square-weighted total chord counts each, non-weighted CLD (Figure 5.2(b)) and square-weighted CLD (Figure 5.2(c)) of these two data points are obviously different. This example shows that using only the total chord counts for neither the non-weighted nor the
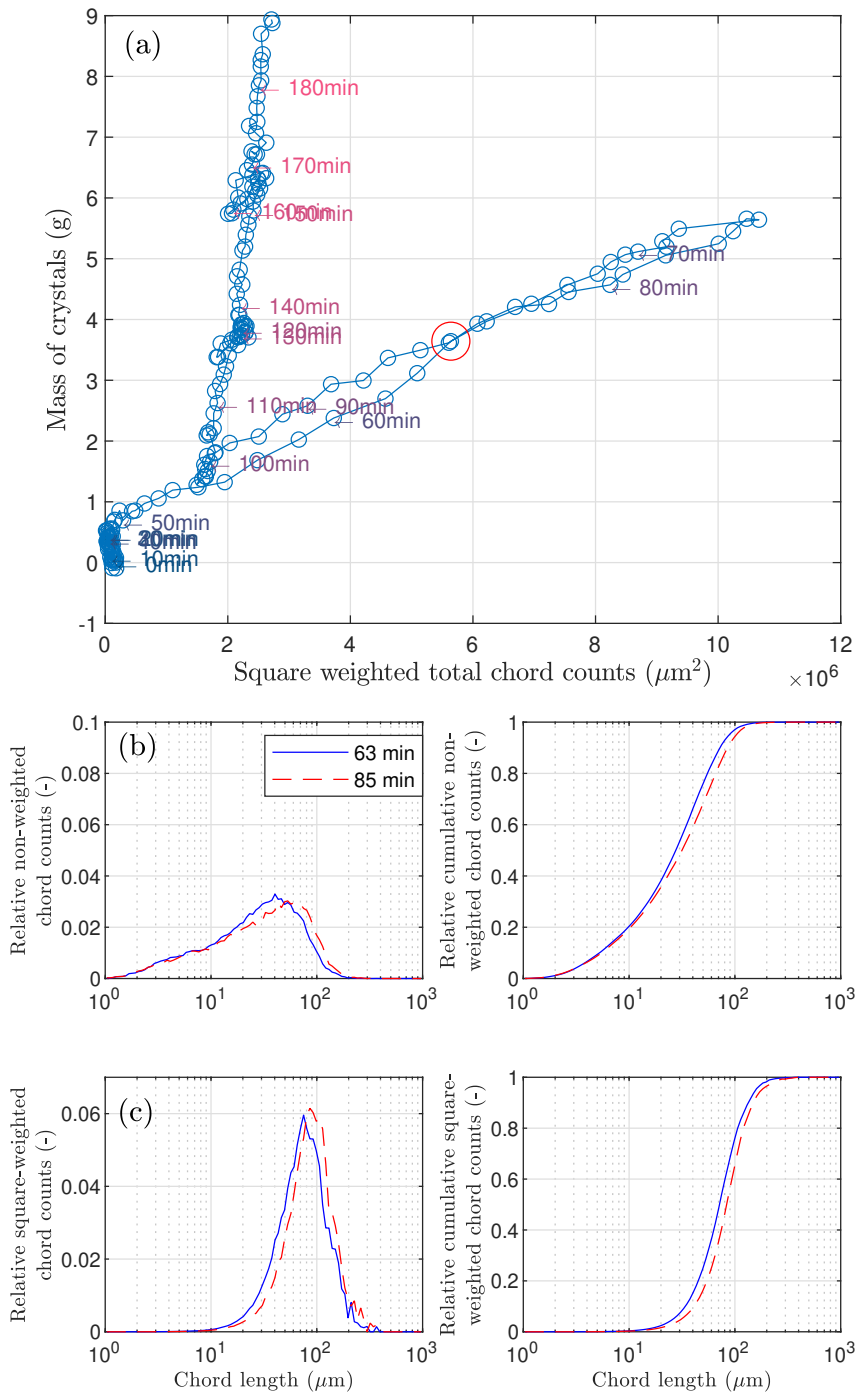
Figure 5.2: Comparison of chord length distributions for very close experimental data points on the mass-count space: (a) trajectory of an experiment on a mass-count space, the chord count is square-weighted, (b) comparison of non-weighted chord length distributions for the data points at 63 min and 85 min, and (c) comparison of square-weighted chord length distributions for the data points at 63 min and 85 min. For (b) and (c), left figures show original distributions and right figures show cumulative distributions.

squared-weighted approach cannot give a good prediction for the zeroth moment due to the property of non-unique correspondence. Therefore, total chord counts are divided by three ranges (1 μm – 10 μm, 10 μm – 100 μm, and 100 μm – 1,000 μm) and used as inputs of the conversion model to correlate between measurements and s_1.

Figures 5.3 and 5.4 compare trends of non-weighted total chord counts, square-weighted total chord counts, divided non-weighted chord counts in three ranges, crystal mass, and zeroth moments from the PBM simulation for 9 experimental cases. All experiments were performed independently, but they are shown in one plot for easier comparisons. The black dotted lines in both figures represent the simulated zeroth moment. The crystal mass trend was added as the yellow dash-dot line in Figure 5.3, and only its trend has the same direction as the zeroth moment's behavior. All other trends, which are for total or divided chord counts, show opposite directions to the zeroth moment. When the zeroth moment increases, the chord counts decrease generally.

Based on this analysis, the measured properties such as non-weighted total chord counts, divided non-weighted chord counts, square-weighted chord counts, the mass of crystals, and interactions among mass and each kind of chord counts were chosen to predict the zeroth moment of crystals through an empirical model. As shown in the previous section, the zeroth moments and square-weighted chord counts have a relationship with each other, but using only square-weight chord counts is not enough for a more accurate correlation. Hence, additional testing is required for more measurable attributes. A linear model was assumed as the first step to determine variables for the correlation between the reduced-order state and measurements by the FBRM.

Even though a model using more variables, such as all possible variables and their derivatives, can fit and predict the desired characteristics, it is inappropriate because unnecessary predictors can provide overfitted results and generate noise to the predictions. According to the principle of Occam's Razor, the simplest one is the best, so it is necessary to pick up the essential variables to describe phenomena. In this process, therefore,
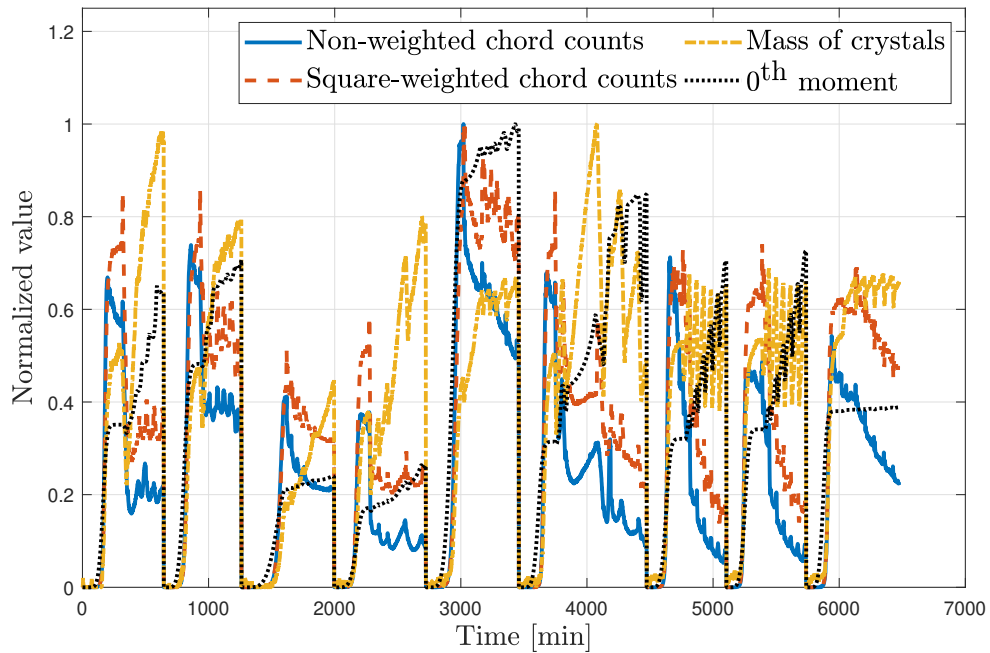
Figure 5.3: Comparison of normalized total chord counts, crystal mass, and the zeroth moments from 9 experiments to figure out the tendency of each property during the crystallization.
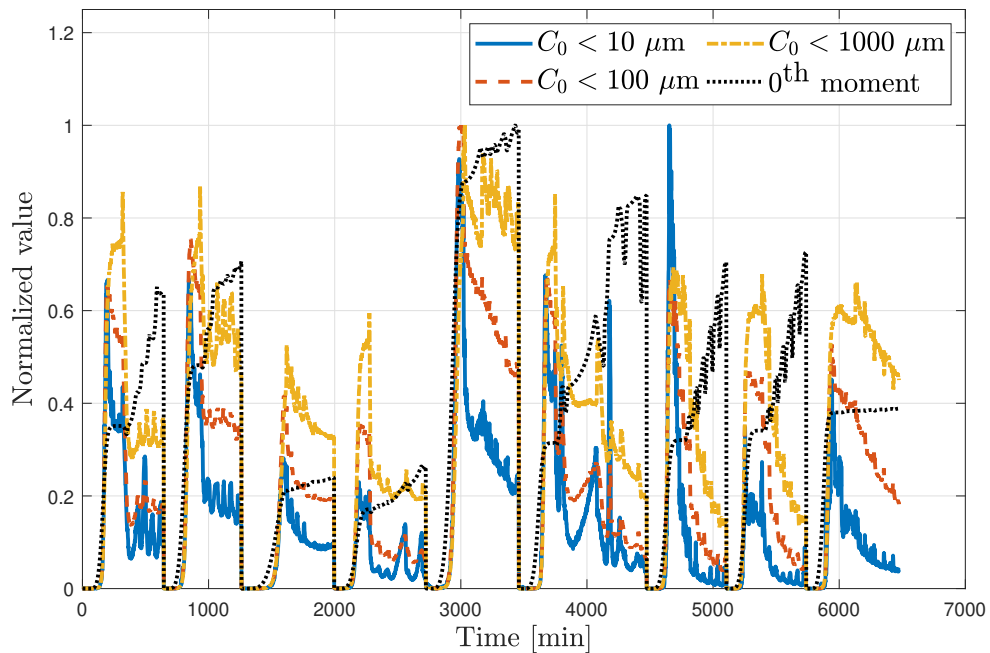
Figure 5.4: Comparison of normalized non-weighted chord counts that are divided into three ranges and the zeroth moments from 9 experiments to figure out the tendency of each property during the crystallization.

appropriate variables were chosen through the stepwise regression.

The stepwise linear regression, which was proposed in 1960 [142], begins regressing the data points with an initial linear model. The p-value of F-statistics of the regressed model is evaluated, and the result determined if predictor terms need to be added or removed. The stepwise regression has two main approaches: forward selection and backward elimination. The two approaches have opposed concepts. The forward selection begins with no variables in the model, and variables are added sequentially based on a model fit criterion. If the model does not improve statistical significance during the repeat of variable addition process, the forward selection stops. The backward elimination has the opposite process from the forward selection. The procedure begins with all candidate predictors, and each predictor is removed repeatably based on the model fit criterion. If the statistically significant deterioration happens by removing predictors in the model, the elimination process is terminated. However, the stepwise regression conducts a forward selection and backward elimination simultaneously [143].

Selection of predictors using the stepwise linear regression   In this section, the predictors were made from the FBRM measurements of 9 experimental cases, and the reduced-order state, s_1, was simulated by the PBM simulation. The stepwise linear regression was carried out using `stepwisefit` function in Matlab™ 2019b. The total number of data points is 6476, where 70% of all data points were selected as the training set. The validation

Table 5.1: Steps of stepwise linear regression to choose appropriate predictors for s_1

Case	m	C_0	$C_0^{<10}$	$C_0^{<100}$	$C_0^{<1000}$	C_2	mC_0	mC_2	$mC_0^{<10}$	$mC_0^{<100}$	$mC_0^{<1000}$	p-value
1	IN	OUT	OUT	OUT	OUT	OUT	OUT	OUT	OUT	OUT	OUT	0
2	IN	OUT	OUT	OUT	OUT	OUT	OUT	OUT	OUT	IN	OUT	3.59E-254
3	IN	OUT	OUT	IN	OUT	OUT	OUT	OUT	OUT	IN	OUT	1.27E-10
4	IN	OUT	OUT	IN	OUT	OUT	OUT	OUT	IN	IN	OUT	1.18E-06
5	IN	OUT	OUT	IN	OUT	IN	OUT	OUT	IN	IN	OUT	6.19E-13
6	IN	OUT	OUT	IN	IN	IN	OUT	OUT	IN	IN	OUT	3.58E-36
7	IN	OUT	OUT	IN	IN	IN	OUT	OUT	IN	IN	IN	2.16E-17
8	IN	OUT	OUT	IN	IN	IN	IN	OUT	IN	IN	IN	3.67E-195
9	IN	OUT	OUT	IN	IN	IN	IN	IN	IN	IN	IN	6.12E-156
10	IN	OUT	OUT	OUT	IN	IN	IN	IN	IN	IN	IN	0.595
Final coefficient	1.289	0	0	0	-0.154	0.355	-0.632	-0.0511	0.632	0.632	0.654	

97
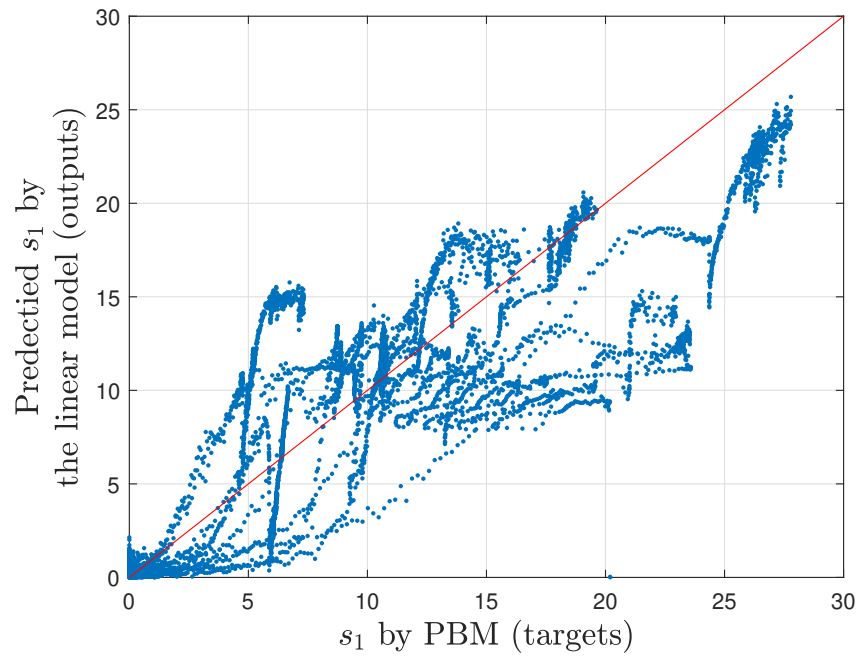
Figure 5.5: Comparison between the target and fitted s_1 for the training set.
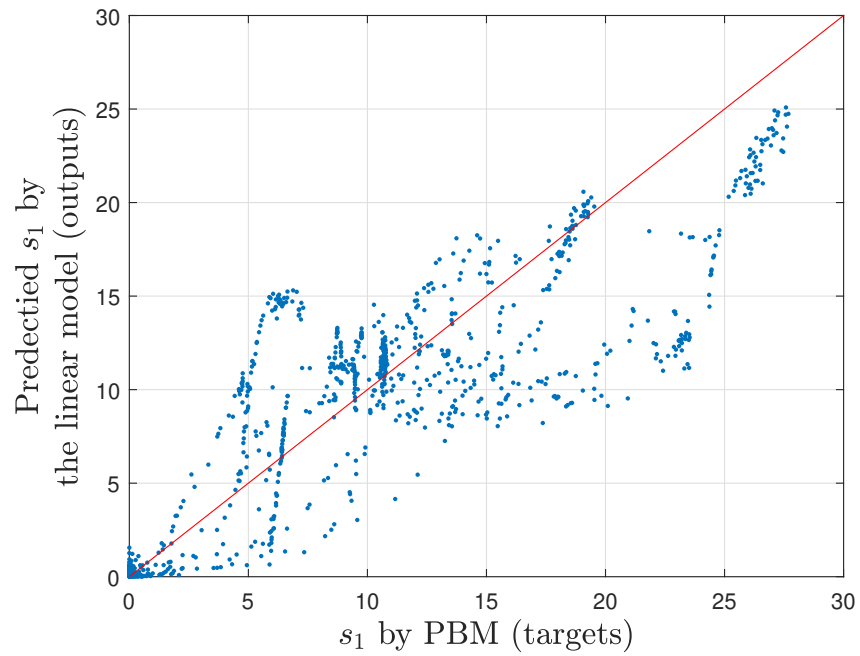
Figure 5.6: Comparison between the target and predicted s_1 for the test set.

set and test set have 15% of the total data points, respectively.

Table 5.1 reports the steps of regression. Each predictor was added and removed, and the p-values were evaluated at each step. The criterion of the p-value was set as 0.05; so when the p-value became larger than the criteria, the stepwise regression stopped and the final model was selected. As a result, three predictors that are related to non-weighted chord counts were rejected for the final regressed model. Figures 5.5 and 5.6 present the fitted and predicted results by the final linear model, respectively. Even though the comparison of s_1 follows the red diagonal lines in the figures, the comparisons have large variation from the diagonal lines, $R^2 = 0.724$. This result means a linear model is not enough to convert the measured data to s_1 for the feedback process control.

5.4   Shallow neural network

ANN, which have been gaining attention to the machine learning field in recent years, are composed of three parts: the input layer, hidden layer, and output layer as shown in Figure 5.7. Input and output layers literally deal with the input and output of the model while the key part of ANN is the hidden layer. Each layer is connected to preceding and succeeding layers, and the number of connections depends on the number of neurons in each layer.

Among the three kinds of layers, the hidden layers determine the performance of the model. Since constructing hidden layers is critical, various ideas, such as the combinations of connections among nodes and layers and types of transfer functions (or activation functions), have been suggested to improve the prediction results. Each node has a mathematical function, which is called a transfer function. Several types of functions are employed for the transfer function, and a few common and new examples are shown in Table 5.2 [144, 145].

The input values from the input layer or nodes of the previous layers are put given into the transfer function in the form below which is schematically illustrated in Figure 5.8.

Table 5.2: Examples of transfer functions for the neural network

Name	Equation, $f(x)$	Derivative, $f'(x)$	Range	Order of Continuity	Monotonic derivative
Linear	$f(x) = x$	1	$(-\infty, +\infty)$	C^∞	Yes
Binary step	$\begin{cases} -1, x < 0 \\ 1, x \geq 0 \end{cases}$	$\begin{cases} 1, x \neq 0 \\ \text{unidentified}, x = 0 \end{cases}$	$(-1,1)$	C^1	No
Logistic	$\dfrac{1}{1+e^{-x}}$	$f(x)(1 - f(x))$	$(0,1)$	C^∞	No
tanh	$\dfrac{e^x - e^{-x}}{e^x + e^{-x}}$	$1 - f(x)^2$	$(-1,1)$	C^∞	No
ReLU (Rectified Linear Unit)	$\begin{cases} 0, x < 0 \\ x, x \geq 0 \end{cases}$	$\begin{cases} 0, x < 0 \\ 1, x > 0 \\ \text{unidentified}, x = 0 \end{cases}$	$[0, +\infty)$	C^0	Yes
PReLU (Parametric Rectified Linear Unit)	$\begin{cases} \alpha x, x < 0 \\ x, x \geq 0 \end{cases}$	$\begin{cases} \alpha, x < 0 \\ 1, x > 0 \\ \text{unidentified}, x = 0 \end{cases}$	$(-\infty, +\infty)$	C^0	Yes
Swish	$\dfrac{x}{1+e^{-x}}$	$\dfrac{e^x(x+e^x+1)}{(e^x+1)^2}$	$(\approx -0.2784, +\infty)$	C^∞	No
Mish	$x\tanh(\log(1 + e^x))$	$\dfrac{e^x\left(4e^x x + 4x + 6e^x + 4e^{2x} + e^{3x} + 4\right)}{(2e^x + e^{2x} + 2)^2}$	$(\approx -0.3088, +\infty)$	C^∞	No

$$\mathbf{a} = f(\mathbf{x}) = f(\mathbf{Wp} + \mathbf{b}) \tag{5.4}$$

In this study, an SNN, which has only one hidden layer, is employed to generate a model to convert the PAT measurements to s_1. The neural network model can be trained through several training algorithms such as Levenberg-Marquardt backpropagation, resilient backpropagation, scaled conjugate gradient, and so on. Mathworks® tested various training algorithms according to the purpose of training with six different datasets [146]. According to Ref. [146], the Levenberg-Marquardt backpropagation algorithm and scaled conjugate gradient show the best performance, for supervised training for function approximation. However, the Levenberg-Marquardt backpropagation algorithm demonstrates faster convergence for cases with a few hundreds weights [147] and more accurate fitting result so
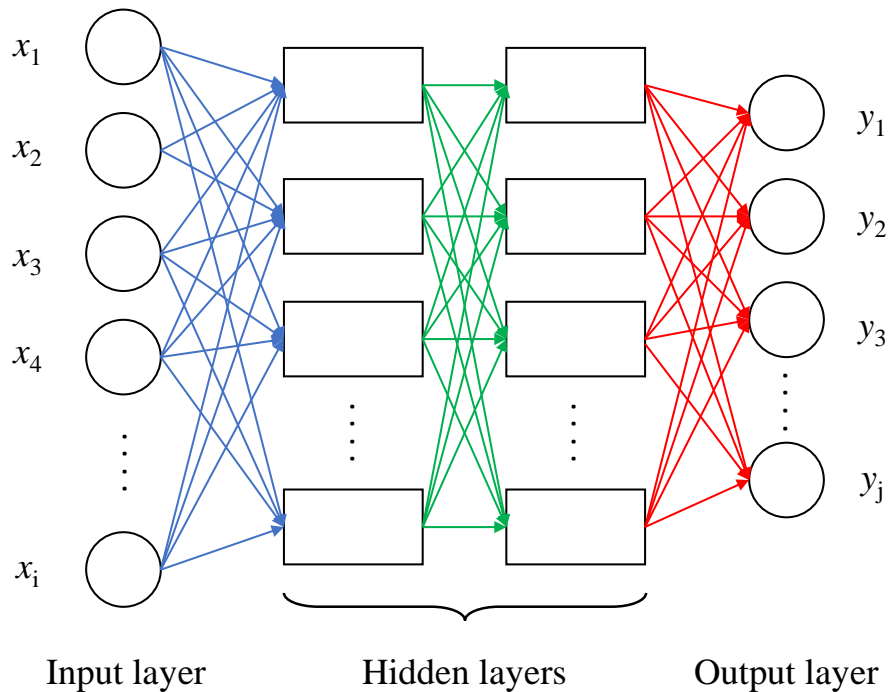
Figure 5.7: Schematic figure of the artificial neural network
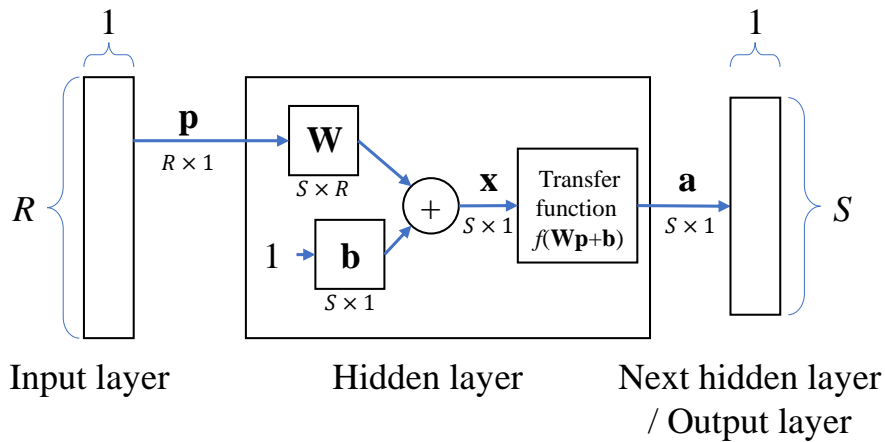
Figure 5.8: Layer diagram of the artificial neural network. R is the number of elements in the input layer and S is the number of nodes in the hidden layer.

that this algorithm was chosen for the training of the conversion model [146].

5.4.1 Information criteria

Selecting the number of parameters is also an important part of the model selection. In the research area of deep learning, it is still challenging to decide the number of hidden layers and nodes for each layer, but the SNN architecture has only one hidden layer. The number of parameters in a SNN model depends on the number of neurons (or nodes) in the hidden layer, so the number of neurons determines the performance of the SNN model if other conditions are constant. A model with too few nodes cannot convert measurements to particle attributes well. On the other hand, in a model with a superfluous number of nodes, overfitting may occur. An overfitted model shows that the training set can be converted well, but the test set or actual data show incorrect predictions. Therefore, it is important to determine the optimal number of neurons in the SNN.

Information criteria are statistical methodologies to evaluate model performance. Akaike information criteria (AIC) [148] and Bayesian information criteria (BIC) [149] are most widely used to evaluate the model efficiency using the number of parameters in the model and maximum likelihood of the data set. If the training set has a small sample size, mod-

102

ified information criteria, corrected Akaike information criteria (AICc) [150] or adjusted R^2, are employed. In particular, it is reported that the use of AICc is possible when the ratio between the number of data points and the number of parameters is less than 40; i.e. $n/p < 40$ [151]. Because the SNN is a statistical model, information criteria have been employed to determine the number of neurons in the hidden layer for ANN of various areas [151–154]. These four types of information criteria are shown below:

$$\text{AIC} = 2p - 2\ln \hat{L} = 2p + n\ln(\text{RSS}/n) \tag{5.5}$$

$$\text{BIC} = p\ln n - 2\ln \hat{L} = p\ln n + n\ln(\text{RSS}/n) \tag{5.6}$$

$$\text{AICc} = \text{AIC} + \frac{2p^2 + 2p}{n - p - 1} \tag{5.7}$$

$$R_a^2 = 1 - (1 - R^2)\frac{n - 1}{n - p - 1} \tag{5.8}$$

where p is the number of parameter in the model, n is the number of data points, $\hat{L}$ is the maximum likelihood of the training data, and RSS is the residual sum of squares for the training data. The prediction is considered better if the values of AIC and BIC are small, while R^2 and R_a^2 are large. In this chapter, information criteria introduced above were used to choose the number of neurons for three cases with different transfer functions.

5.4.2 Determination of the transfer function and the number of neurons

Three different transfer functions, tanh, ReLU, and logistic, were employed to train the conversion model. Figure 5.9 depicts the implemented transfer functions for this test. Hyperbolic tangent function, tanh, returns values between -1 and 1 for all inputs. Rectified linear unit function, ReLU, gives outputs zero or positive values, and the logistic function

outputs between 0 and 1. The SNN training was performed using the same data points that divided for samples of training, validation, and test used in the stepwise linear regression study.
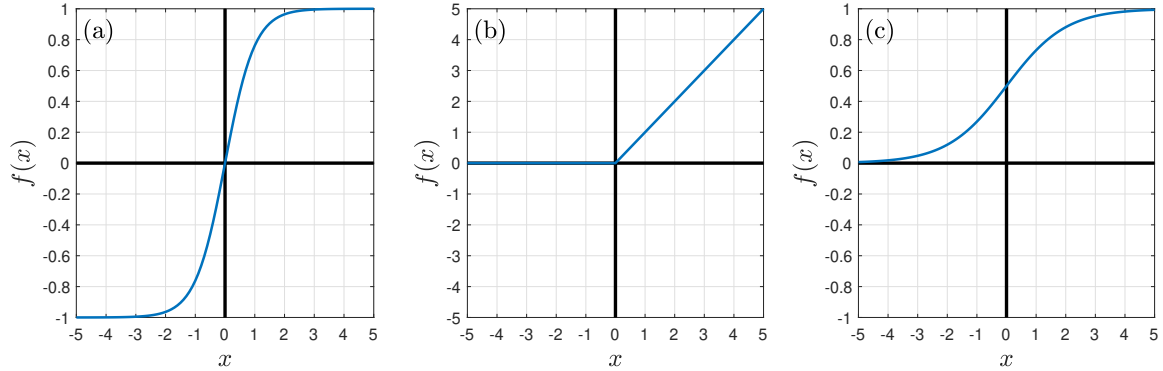
Figure 5.9: Three transfer functions chosen for testing the SNN model. (a) hyperbolic tangent, (b) rectified linear unit, and (c) logistic function.

In this test, the number of neurons ranges from 10 to 150 with an increment of 10. The number of data points in the training set is 4533, so if the number of neurons is greater than 110, n/p is less than 40. Therefore, AICc was also implemented to compare cases where there were more than 110 neurons.

From Figure 5.10 to Figure 5.12 and Table 5.3 compare the information criteria of the models with each function and the number of neurons. The selected models are highlighted for each transfer function based on the comparison of information criteria in Table 5.3. Among three cases, the SNN models using the ReLU function show smaller value of R^2 values than models with other transfer functions, which indicats that ReLU may not be a suitable function for the model. Hyperbolic tangent and logistic functions provide similar results, while the optimal number of neurons that give the lowest AIC and BIC varies depending on the choice of transfer function. The optimal number of neurons is 80 and 50 for the hyperbolic tangent and logistic function models, respectively. We also note that the optimal number of neurons that give the smallest value of BIC is different from that of AIC. The model with the lowest BIC has fewer neurons than the selected model by AIC, but the model based on BIC does not have the largest R^2 and R_a^2 values. Figure 5.13 compares

104

Table 5.3: Comparison of information criteria values depending on the neuron numbers for each transfer function.

Transfer function	Neuron No.	AIC	BIC	AICc	R^2	R_a^2
	10	6036.0	6684.3	10574.7	0.937	0.936
	20	910.8	2201.0	5463.8	0.980	0.979
	30	3373.2	5305.3	7950.5	0.967	0.964
	40	2073.8	4647.8	6686.3	0.974	0.972
	50	1848.6	5064.5	6507.9	0.977	0.975
	60	2003.9	5861.7	6722.7	0.978	0.975
	70	1788.0	6287.7	6579.8	0.979	0.975
tanh	**80**	**-1051.2**	**4090.3**	**3828.2**	**0.990**	**0.988**
	90	1209.2	6992.7	6192.1	0.984	0.980
	100	1950.8	8376.2	7054.4	0.982	0.977
	110	1421.4	8488.6	6664.3	0.984	0.979
	120	1299.6	9008.7	6702.4	0.985	0.979
	130	2114.3	10465.3	7699.1	0.983	0.976
	140	2812.1	11805.0	8603.4	0.980	0.972
	150	1125.7	10760.5	7150.3	0.987	0.980
	10	9489.6	10137.9	14028.4	0.866	0.863
	20	5897.7	7187.9	10450.6	0.941	0.939
	30	9325.6	11257.7	13902.8	0.881	0.873
	40	7352.9	9926.8	11965.3	0.925	0.918
	50	6956.4	10172.2	11615.7	0.933	0.925
	60	5826.6	9684.4	10545.4	0.951	0.943
	70	6229.8	10729.4	11021.5	0.949	0.939
ReLU	80	6247.1	11388.6	11126.5	0.949	0.939
	90	5598.0	11381.4	10580.8	0.959	0.949
	100	**5289.6**	**11714.9**	**10393.1**	**0.962**	**0.951**
	110	6681.1	13748.3	11924.0	0.953	0.937
	120	7531.9	15241.0	12934.6	0.945	0.925
	130	7225.6	15576.6	12810.4	0.950	0.930
	140	6271.8	15264.7	12063.0	0.962	0.945
	150	7467.2	17102.0	13491.8	0.953	0.930
	10	3957.0	4605.3	8495.7	0.961	0.960
	20	2243.3	3533.5	6796.2	0.974	0.973
	30	414.7	2346.8	4992.0	0.983	0.982
	40	2043.4	4617.3	6655.8	0.976	0.974
	50	**-580.0**	**2635.8**	**4079.3**	**0.988**	**0.986**
	60	642.5	4500.3	5361.3	0.984	0.982
	70	1220.9	5720.5	6012.6	0.982	0.979
logistic	80	1876.4	7017.9	6755.8	0.980	0.976
	90	866.0	6649.5	5848.9	0.985	0.981
	100	1187.5	7612.8	6291.0	0.984	0.979
	110	4007.0	11074.2	9249.9	0.973	0.964
	120	286.0	7995.2	5688.8	0.986	0.981
	130	1776.6	10127.6	7361.4	0.984	0.978
	140	3227.5	12220.4	9018.8	0.979	0.970
	150	1355.4	10990.2	7380.0	0.986	0.979

the predicted and targeted s_1 using the selected model with each transfer function for the test set. Red triangles lie farther from the diagonal line than blue dots and yellow squares, which indicates that the SNN model with the ReLU function shows worse performance. Models using hyperbolic tangent and logistic functions present similar prediction results, but fewer neurons were used for the case using the logistic function. Therefore, the SNN model using the logistic function is selected as the final conversion model for the feedback control.

5.5 Summary

The conversion model to translate the measurements using FBRM and ATR-FTIR to the reduced-order state, s_1, was generated through several steps. It was found that the desired reduced-order state depends on the zeroth moment. Hence, the relationship between the zeroth moment from the PBM and chord counts by the FBRM was investigated. The result
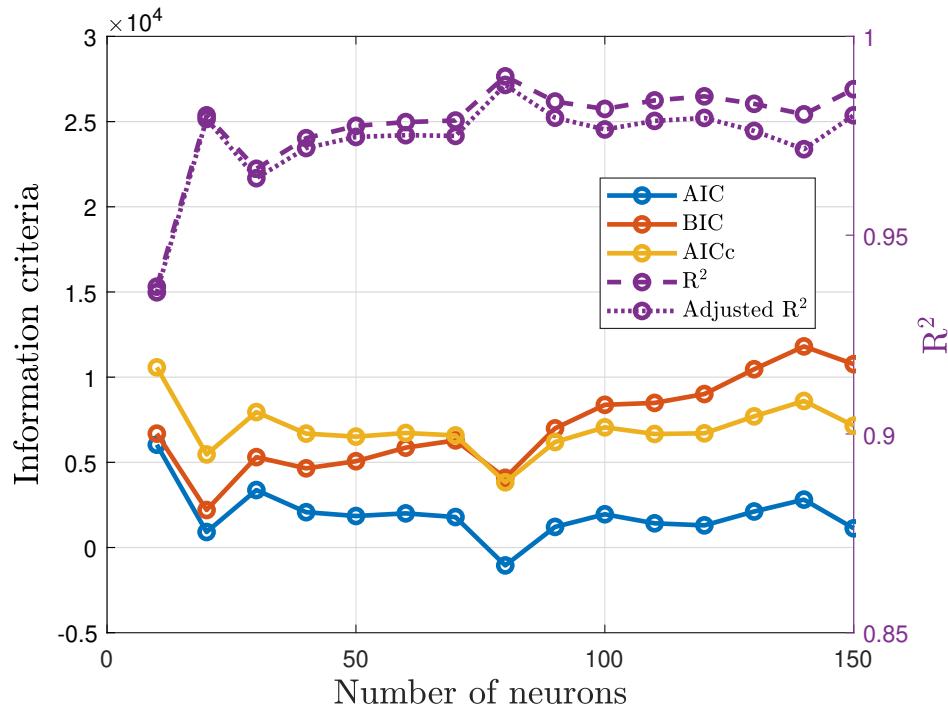
Figure 5.10: Result of model selection according to the number of neurons with tanh function.

106
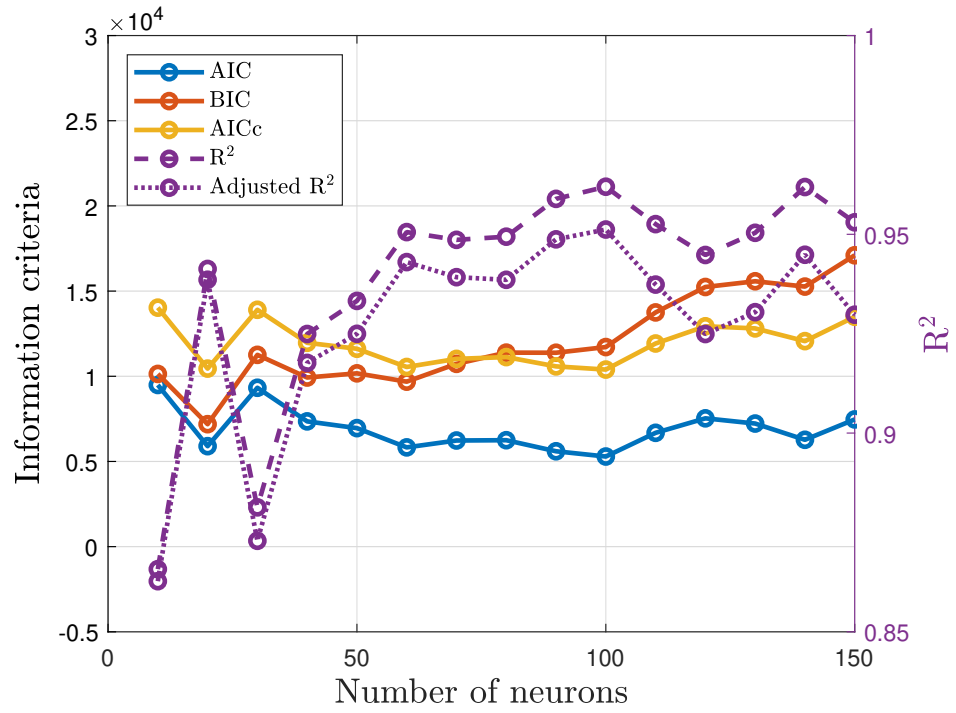
Figure 5.11: Result of model selection according to the number of neurons with ReLU function.
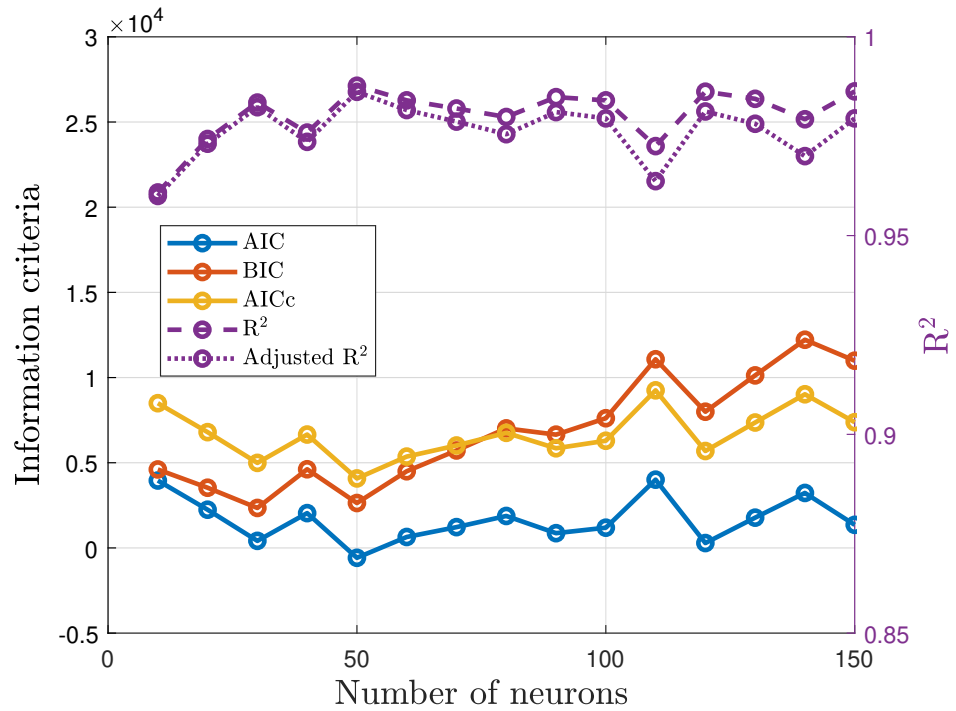
Figure 5.12: Result of model selection according to the number of neurons with logistic function.

shows that the non-weighted and square-weighted chord counts show relationships with the zeroth moment, but the accuracy of relationships was not enough to be employed in feedback control. An analysis shows that the data points with the same chord count and crystal mass can have different chord length distribution, and the trend of crystal mass only follows the same direction with the zeroth moment, but chord counts have opposite trends with the zeroth moment. Under this observation, it was concluded that the potential predictors should include crystal mass, non-weighted and square-weighted chord counts, non-weighted chord counts divided by chord lengths, and interactions of mass and chord counts.

A stepwise linear regression scheme was implemented to select predictors to prevent the model's overfitting, and 9 predictors and coefficients for the linear model were finally obtained. The linear regression model had an R^2 value of 0.72, indicating that the relationship can not be described with a simple linear model. To overcome this problem, a
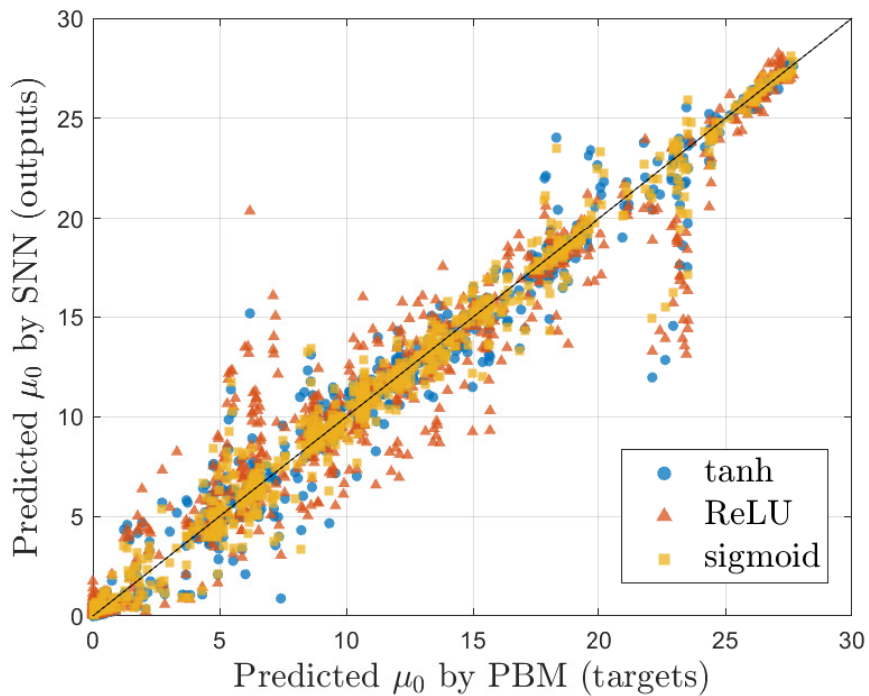
Figure 5.13: Comparison of predicted s_1 against targets using selected SNN models for each transfer function.

SNN model was employed to account for the complex relationship between the PAT measurements and s_1. Choosing the number of neurons is critical for accurate prediction while avoiding overfitting. For this challenge, four kinds of information criteria were used to find the optimal number of neurons. Moreover, three different transfer functions, such as hyperbolic tangent, rectified linear unit, and logistic functions, were tested for the SNN model. The comparison of information criteria selected the final model that uses 50 neurons and the logistic function. This final conversion model, which has an R^2 value of 0.99, was selected for the feedback control experiment of unseeded batch crystallization.

CHAPTER 6

FEEDBACK CONTROL OF MEAN VOLUME CRYSTAL SIZE AND CRYSTAL MASS THROUGH OPTIMAL FEEDBACK POLICY

6.1 Objectives

This chapter presents the feedback control for unseeded batch crystallization to obtain desired mean volume size and yield utilizing results from previous chapters. Even though Chapter 4 shows the Markov state model (MSM) and dynamic programming (DP) optimization derived the optimal control policy to produce desired crystals using training sets from the population balance model simulations, some experimental results have disagreements on mean volume crystal size due to limitations such as response delay on employing temperature profile, model errors, stochastic phenomena, and the lack of monitoring reduced-order state, s_1. Chapter 4 shows that the open-loop control alone could not evaluate whether the current state is correctly heading toward the target state in real-time and adjust control policies to obtain desired products. The process may not produce the desired result through only the open-loop control scheme because the control system can face unexpected disturbances during the control process. Therefore, the feedback control scheme was employed to operate processes in this chapter. To monitor the current state, a shallow neural network (SNN) model was developed to convert the measured data by process analytical technology (PAT) tools to s_1 in Chapter 5.
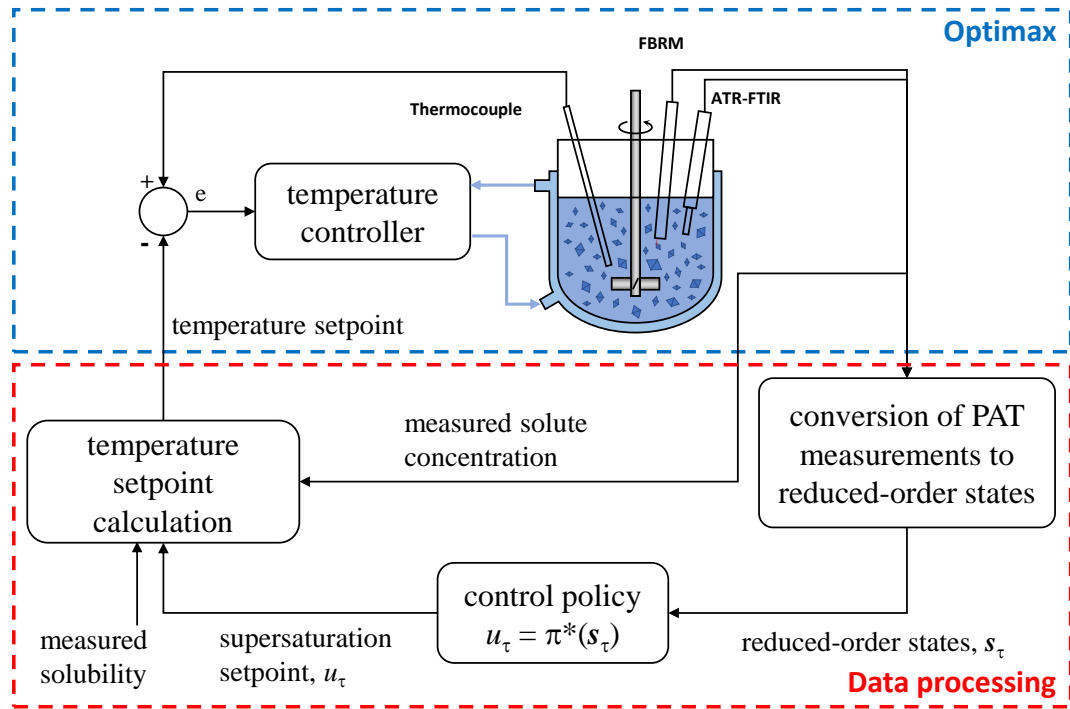
Figure 6.1: The flow of data in the feedback control process.

6.2 *Optimal feedback control of crystallization*

Feedback control requires monitoring current states and providing feedback signals to the control system. The second state, s_2, can be estimated using the measured IR spectrum, and the first state, s_1, can be monitored through the SNN model using data from the FBRM and ATR-FTIR. The distance-to-target was evaluated based on monitored reduced-order states, and the optimal control policies were updated according to the measured s_1 and s_2 to minimize the distance-to-target at each time step.

The experimental system was operated according to the logic in Figure 6.1. PAT measurements were updated once every 30 seconds, but the temperature setpoint was updated every single minute using the obtained optimal control policy. Even if the temperature setpoint was updated every 30 seconds, the system temperature takes a longer time than 30 seconds to respond to the setpoint change due to the thermal response delay. The optimal control policy was also constantly explored every 10 minutes again to reflect the current
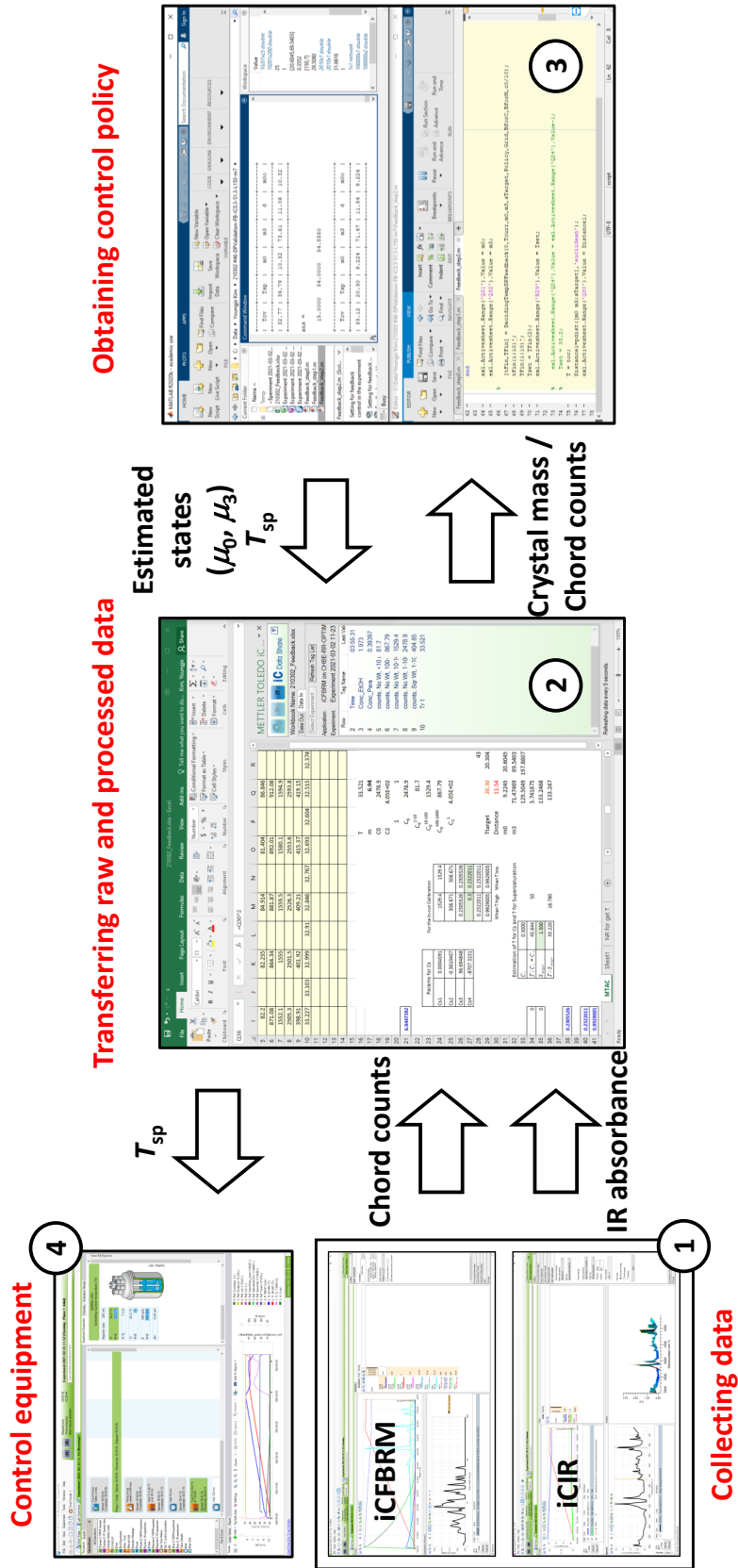
Figure 6.2: The flow of data in the feedback control process.

reduced-order states because the optimal control policy should be searched again if the controlled states do not follow the states by the previous optimal control policy. In the open-loop control, the optimal control policy was searched only once at the beginning of the control process and never searched again. If the system temperature follows the temperature setpoint without response delay, this step of continuous exploration for the optimal control policy may not be necessary. However, the optimal control policy was constantly investigated because the crystallizer temperature cannot be controlled perfectly, as shown in Chapter 4.

6.2.1   Experimental implementation of the feedback control

The implementation of the feedback control follows the steps in Figure 6.2. Five different software programs participate in the feedback control: two programs (iCFBRM and iCIR) to collect raw data (1), Microsoft Office Excel for the communication between Matlab and programs by the manufacturer, such as iCFBRM, iCIR, and iControl (2), Matlab to evaluate current states and calculate optimal control action (3), and a program (iControl) to control the experimental equipment (4). Because control software programs from the manufacturer cannot communicate to Matlab directly, MS Excel handles data between Matlab and programs by the manufacturer.

Four feedback control experiments were conducted for the same target points in Table 4.3 to verify that the feedback scheme can control the crystallization process based on the optimal control policies.

6.2.2   Results of the feedback control

Comparison of experimental results   Figure 6.3 presents trends of the controlled temperature in the crystallizer and temperature setpoints for all experimental runs. This figure compares the system temperature profiles and temperature setpoints under the optimal control, and the temperature was well-controlled based on the setpoint change at each time
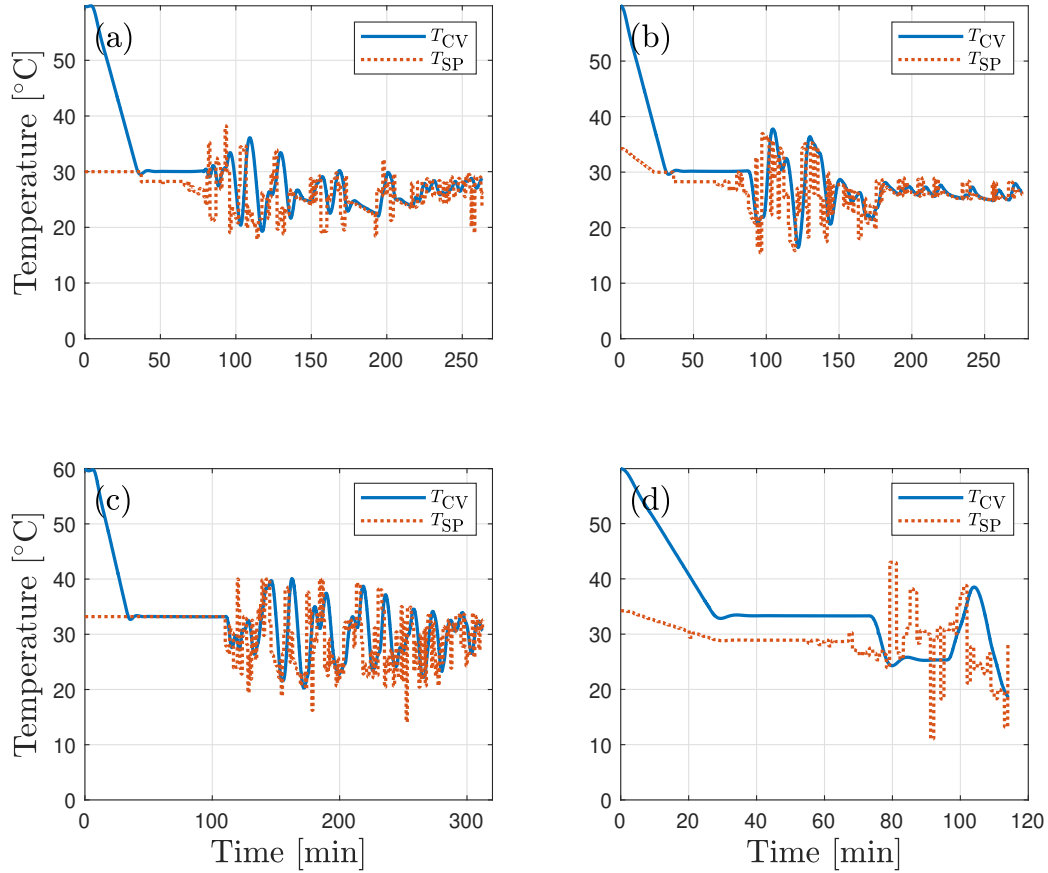
Figure 6.3: Comparison of temperature profiles for all cases: (a) Case 1, (b) Case 2, (c) Case 3, and (d) Case 4. Blue solid lines represent controlled system temperature, and red dotted lines show setpoint at each time step.

step. In some cases, the temperature setpoint profile shows spikes, but they were not realized due to the thermal response delay. The spikes on the temperature setpoint seems to be caused by incorrect conversion between PAT measurements and reduced-order states. As a result, the system temperature profiles follow the temperature setpoint profile as shown in Figure 6.3.

In Figure 6.3(a), (b), and (d), profiles of temperature setpoints at the temperature plateaus have differences from the measured temperature. However, the actual temperature control was carried out only after the temperature plateau ended, even though the temperature setpoints were updated during the temperature plateau was kept. For Case 3, the temperature setpoint was fixed as the plateau temperature (33.4 °C) as shown in Figure 6.3(c). Thus,

the control system tried to change the temperature during the temperature plateau. In the iControl software, the plateau temperature was set as a constant value, although Matlab and Excel tried to change the temperature. This is the reason that the process temperature and temperature setpoint have differences in Cases 1, 2, and 4.

Table 6.1 compares entire simulated and experimental results at the final time step for all control methods including open-loop and closed-loop. In this table, s_1, s_2, and $\sqrt{d_{\text{fin}}}$ for experimental cases by sieving and weighing analyses were estimated using measured results, Equations (2.18), and (4.3). Figure 6.4 visualized the comparisons in Table 6.1. s_1, s_2, and $\sqrt{d_{\text{fin}}}$ cannot be recognized directly by sieving and weighing crystals, but these values can be estimated by $\bar{L}_{0,3}$ and m of crystals. The mass of crystals relates to the third moments, crystals density, and volume shape factor. The mean volume crystal size can be obtained using the zeroth and third moments. Because $s_1 = \mu_0 \times 10^{-6}$ and $s_2 = \mu_3 \times 10^{-12}$, these values at the final step can be calculated using recalled Equations (2.18) and (4.3).

$$k_v = \frac{V}{L^3} = \frac{m_c}{\rho_c L^3} \tag{2.18}$$

$$\bar{L}_{30} = \left(\frac{\mu_3}{\mu_0}\right)^{1/3} = 100 \left(\frac{s_2}{s_1}\right)^{1/3} \tag{4.3}$$

Feedback experimental operations for Case 1, 3, and 4 were terminated when the system met the termination criterion, $\sqrt{d_\tau} \leq 0.5$, but Case 2 was manually finished by the operator. The estimated mean volume crystal sizes and crystal masses based on monitored reduced-order states for three automatically terminated cases show values near the target values. However, measured mean volume crystal sizes and crystal mass by sieving and weighing analyses show some deviation, which is discussed below. Figures 6.5 – 6.8 present (a) trajectories of reduced-order states to the target points on state space plots, (b) profiles of $\sqrt{d_\tau}$, (c) crystal mass, and (d) supersaturation.

The monitored results by PAT tools for Case 1 show reasonable trends in Figure 6.5.

Table 6.1: Results comparison among targets, simulation results, open-loop experimental results, and feedback experimental results. This table also compares results from feedback control experiments by the PAT monitoring and by sieving and weighing.

	Operation	Method	$\bar{L}_{30}$ [μm]	m [g]	s_1^*	s_2^*	$\sqrt{d_{\text{fin}}}^*$
	Targets		225.0	9.0	7.85	89.4	-
Case 1	Simulation**	using MSM and DP	220.7	9.0	8.30	89.1	0.080
	Simulation	using PBM	199.5	8.4	10.5	83.4	6.5
	Open-loop Exp.	sieving and weighing	168.6	8.2	16.9	81.2	13
	Feedback Exp.	Monitored by PAT	224.7	9.0	7.90	89.6	0.21
	Feedback Exp.	sieving and weighing	138.9	9.3	34.3	92.0	26
	Targets		200.0	9.0	11.2	89.4	-
Case 2	Simulation**	using MSM and DP	202.9	9.0	10.7	89.3	0.064
	Simulation	using PBM	208.3	9.5	10.6	95.5	6.1
	Open-loop Exp.	sieving and weighing	127.8	9.3	44.0	91.9	33
	Feedback Exp.	Monitored by PAT	187.4	9.0	13.8	90.5	2.8***
	Feedback Exp.	sieving and weighing	179.6	9.5	16.3	94.6	6.4
	Targets		175.0	7.0	13.0	69.5	-
Case 3	Simulation**	using MSM and DP	178.0	7.0	12.4	69.8	0.18
	Simulation	using PBM	163.2	7.5	17.1	74.5	6.5
	Open-loop Exp.	sieving and weighing	132.0	7.4	31.8	73.2	19
	Feedback Exp.	Monitored by PAT	174.1	6.9	13.2	69.7	0.3
	Feedback Exp.	sieving and weighing	164.4	7.5	16.8	74.7	5.6
	Targets		160.0	8.0	19.4	79.5	-
Case 4	Simulation**	using MSM and DP	162.0	8.0	18.8	79.7	0.21
	Simulation	using PBM	100.2	8.8	86.4	86.9	67
	Open-loop Exp.	sieving and weighing	136.2	8.2	32.3	81.6	13
	Feedback Exp.	Monitored by PAT	160.1	8.0	19.4	79.7	0.24
	Feedback Exp.	sieving and weighing	125.7	8.3	41.4	82.2	22

* Final states and square root of distances, s_1, s_2, and $\sqrt{d_{\text{fin}}}$, for all cases excluding values monitored by PAT tools in feedback control in this table are evaluated from the measured and simulated $\bar{L}_{30}$ and m. s_1 and s_2 are scaled moments, which are $\mu_0/10^6$ and $\mu_3/10^{12}$, respectively.
** Simulations and open-loop experimental results are from Table 4.4.
*** This experiment was manually terminated by the operator.
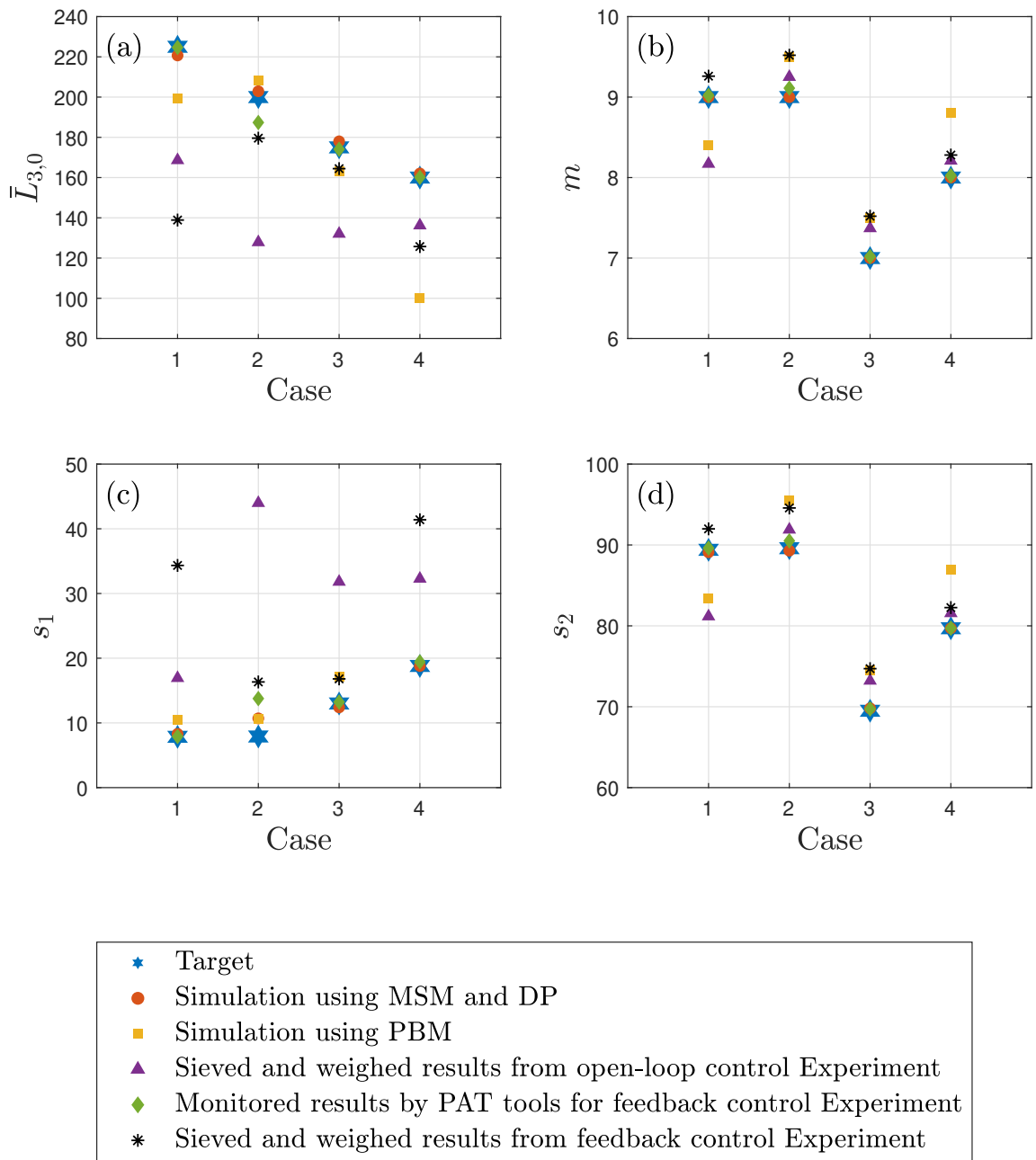
Figure 6.4: Comparisons of final status for each control case in Table 6.1.

117
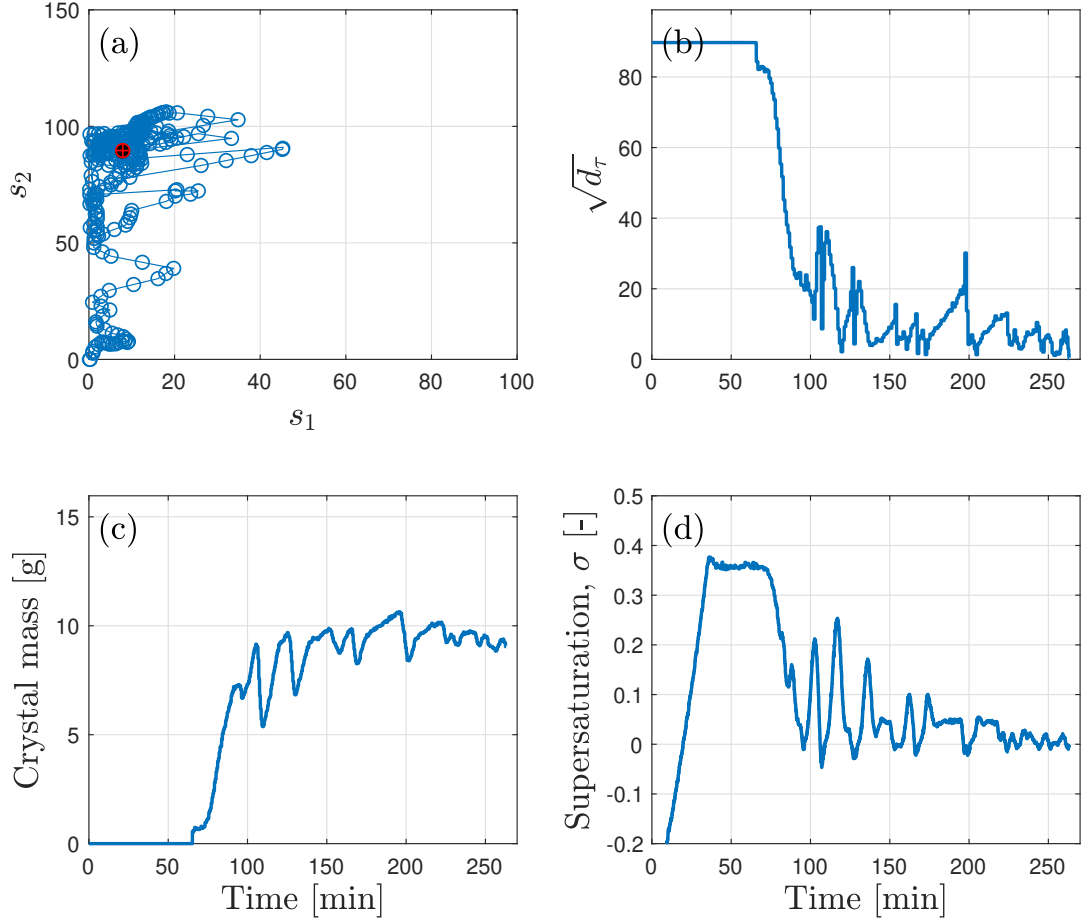
Figure 6.5: Feedback control results for Case 1: (a) trajectory of reduced-order states, (b) $\sqrt{d_\tau}$ profile, (c) monitored crystal mass profile, and (d) measured supersaturation profile. In panel (a), blue circles and line represent measured states, black dot is the target, and the red $\oplus$ shows the final measured state. Crystal mass and supersaturation are measured by ATR-FTIR.

In Figure 6.5(a), the trajectory of reduced-order states explores the state space to reach the target, and the final state lands on the target. While the controller tries to minimize $\sqrt{d_\tau}$, the supersaturation stabilizes and converges on 0, as shown in Figure 6.5(d), so the status in the crystallizer stops changing. When $\sqrt{d_\tau}$ became less than 0.5, the feedback control process was finished automatically. Because s_1 and s_2 are near the target, the estimated $\bar{L}_{30}$ and m are close to the target values as shown in Table 6.1. However, the recovered crystal has different characteristics from the monitored results. Even though the recovered crystal mass has a 3% higher mass than the target, the mean volume crystal size is 38%

less size than the target. Because the temperature and supersaturation profiles at the end of the control do not have steep changes, it is difficult to assume additional crystallization or dissolution happened between periods when the control was terminated and crystals were sampled. The remaining possible issue, in this case, is the incorrect conversion using the SNN model from Chapter 5 between the measured attributes by PAT tools and s_1. The spike on the temperature setpoints as shown in Figure 6.3(a) can be caused by the incorrect conversion of PAT measurements to the reduced-order states. The supersaturation in the look-up table and the current state determines the optimal temperature setpoint, but
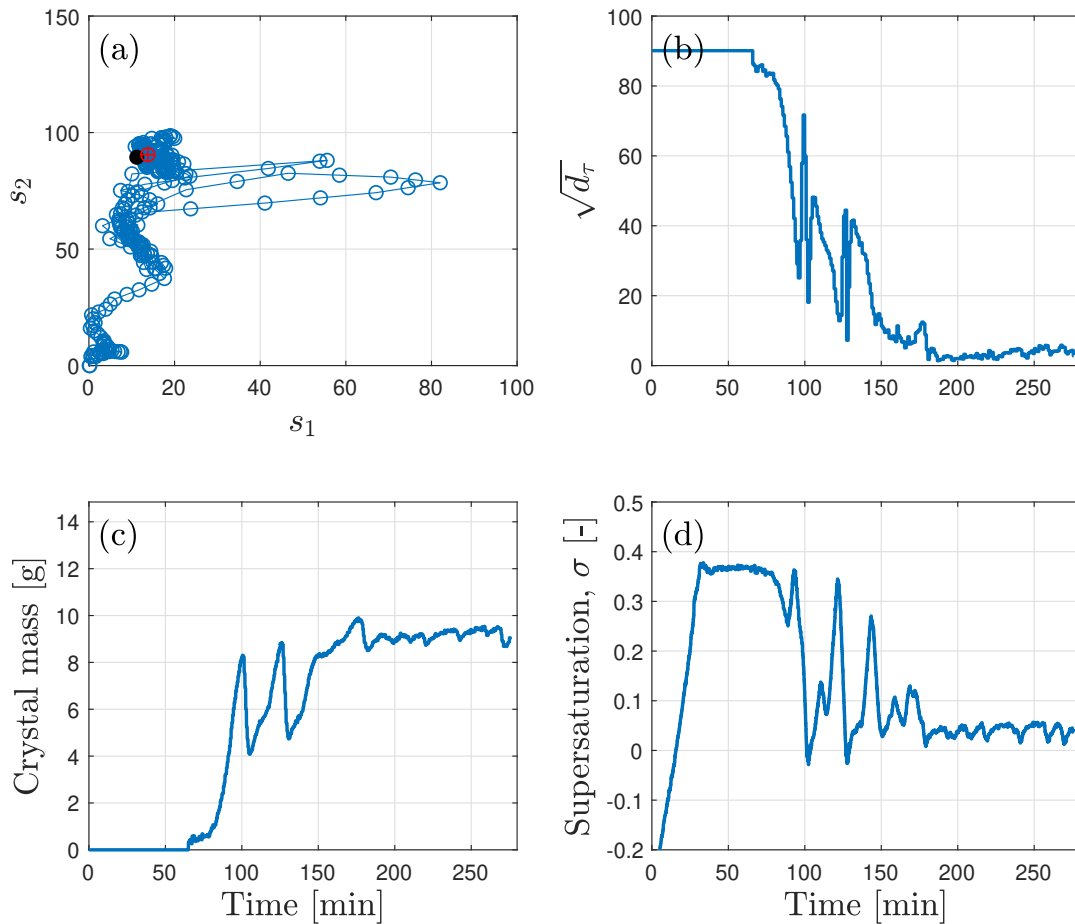
Figure 6.6: Feedback control results for Case 2: (a) trajectory of reduced-order states, (b) $\sqrt{d_\tau}$ profile, (c) monitored crystal mass profile, and (d) measured supersaturation profile. In panel (a), blue circles and line represent measured states, black dot is the target, and the red $\oplus$ shows the final measured state. Crystal mass and supersaturation are measured by ATR-FTIR.

if the converted current states are not accurate, the temperature setpoint can make unstable profiles. This issue about the conversion model will be further discussed at the end of this section.

The feedback control for Case 2 was ended manually by the operator since the reduced-order states approached the vicinity of target point but did not meet the tolerance of 0.5, as shown in Figure 6.6(a). In Figure 6.6(b), $\sqrt{d_\tau}$ had the minimum value of 1.4 at 180 minute. However, the distance-to-target slightly increased again after 180 minute, so the experiment was ended manually. Even though the final states did not quite reach the target point, the analyzed $\bar{L}_{30}$ by sieving has 10% less result than the target value. The difference of $\bar{L}_{30}$ between by sieving and monitored by PAT tools has the smallest value among four cases. The temperature profile in Figure 6.3(b) and thus the supersaturation profile in Figure 6.6(d) show small jitter. It seems that the change of the state inside the crystallizer before crystal recovery was stable, and the sieved crystals may have similar characteristics to the monitored results by PAT tools.

In Case 3, the analyzed mass and $\bar{L}_{30}$ obtained by sieving also have close results to the target among the four cases. In particular, $\bar{L}_{30}$ of this case is about 6% less than the target mean volume size, and this is the closest value to the target among the four cases. This result may happen because the amplitude of the temperature profile becomes smaller and the temperature converges on 31 °C, and the final supersaturation is near 0. As a result, the change of crystal characteristics according to further nucleation and dissolution is minimized, so the physically analyzed mean volume crystal size and mass are close to the target.

In Case 4, the feedback control experiment was terminated after 40 minutes from the beginning of the control (after the temperature plateau finished). The recovered crystal has a 21.4% smaller mean volume crystal size and a 4% greater weighed crystal mass than the target values. The control was over while the temperature was rapidly decreasing as shown in Figure 6.3(d), so the supersaturation in Figure 6.8(d) sharply increased up to near 0.3.
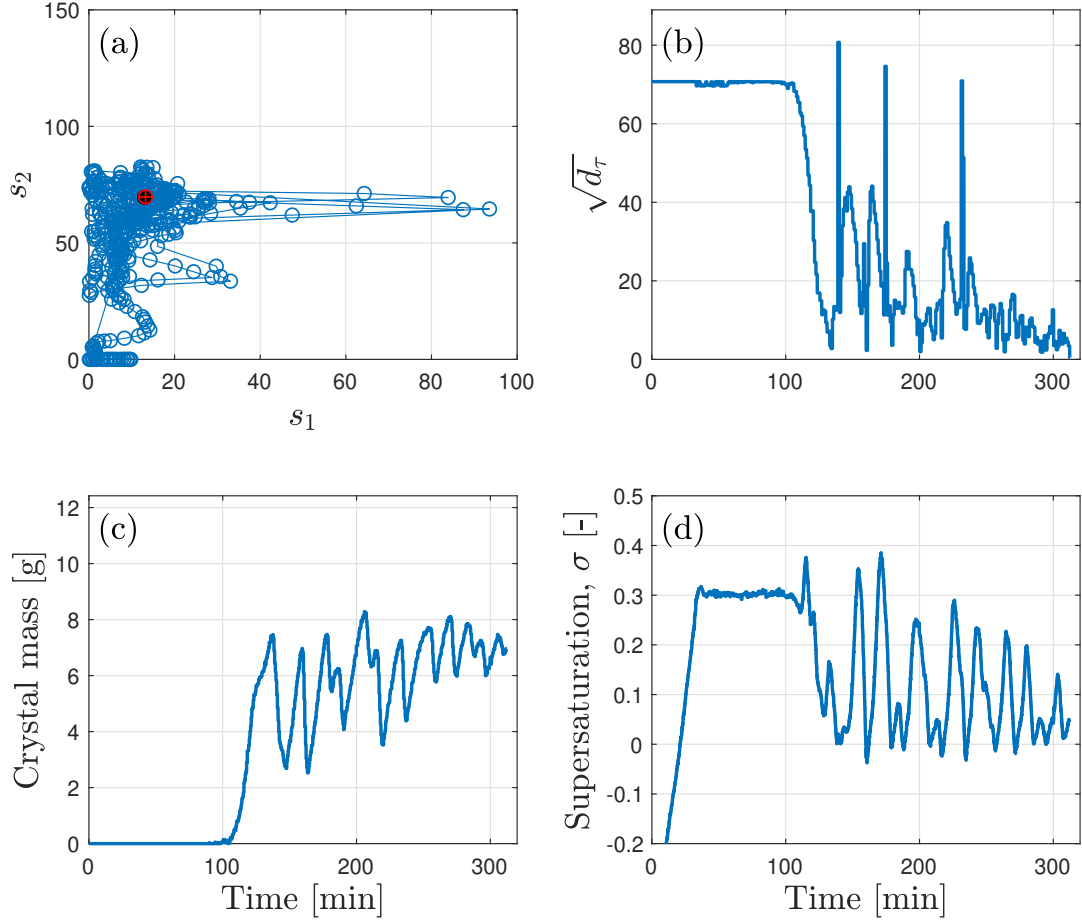
Figure 6.7: Feedback control results for Case 3: (a) trajectory of reduced-order states, (b) $\sqrt{d_\tau}$ profile, (c) monitored crystal mass profile, and (d) measured supersaturation profile. In panel (a), blue circles and line represent measured states, black dot is the target, and the red $\oplus$ shows the final measured state. Crystal mass and supersaturation are measured by ATR-FTIR.

This change makes $\sqrt{d_\tau}$ quickly decrease, and we can see the distance profile approach to zero in Figure 6.8(b). With this condition, the secondary nucleation rate raises due to this high supersaturation level as interpreted in Chapter 3 so that the total number of crystals in the system can increase significantly. The temperature in the crystallizer might become lower continuously until the crystals were sampled even though the control procedure was ended due to the thermal response delay. As a result, s_1 might have increased explosively. Despite the increase in the number of fine particles, the effect of this increase on the volume of the total crystal is not significant. Therefore, even after the end of the control procedure,
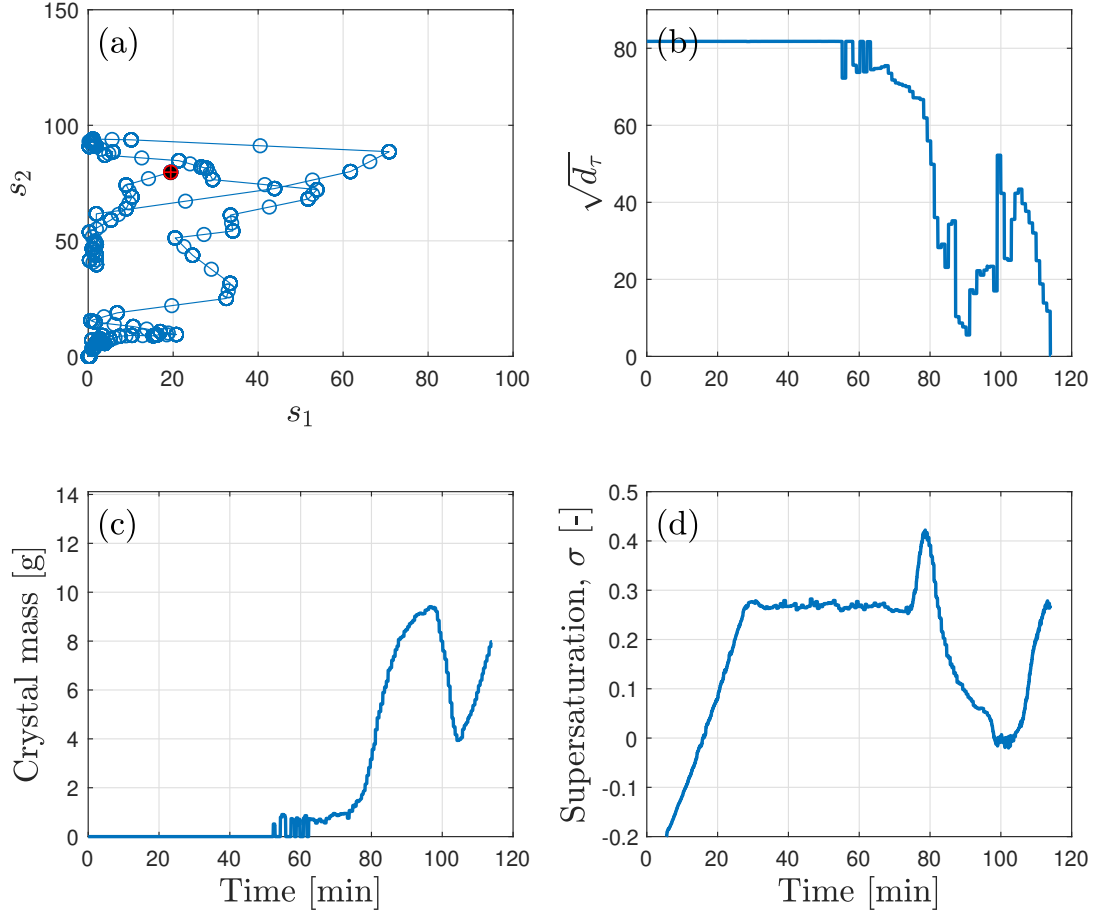
Figure 6.8: Feedback control results for Case 4: (a) trajectory of reduced-order states, (b) $\sqrt{d_\tau}$ profile, (c) monitored crystal mass profile, and (d) measured supersaturation profile. In panel (a), blue circles and line represent measured states, black dot is the target, and the red $\oplus$ shows the final measured state. Crystal mass and supersaturation are measured by ATR-FTIR.

it is expected that the actual $\bar{L}_{30}$ will decrease significantly compared to the target as s_1 increases significantly compared to the increase in s_2.

Limitations. In all cases, the mean volume crystal sizes by sieving (*ex situ*) analyses show smaller values than the targets. This result is caused by the definition of the mean volume size and the sensitivity of the total crystal number. The mean volume size is susceptible to the mass of crystals in the smallest bin size range, $0~\mu m - 53~\mu m$. Even if the crystal mass in this range is only 0.01 g, the number of crystals is approximated as 534,000 with the volume shape factor, solid density, and the characteristic size of 26.5 μm, which is the

arithmetic mean size of 0 μm and 53 μm based on Equation (2.18). In contrast, the same mass of the crystals in the range between 600 μm and 710 μm has only 36 crystals. This drastic difference in the number of crystals influences the mean volume size. The weighing balance precision employed for these experiments is 0.01 g, so even a slight change of the mass of tiny crystals can change the final mean volume size. The mass balance with the precision of 0.01 g can show the mass between 0.005 g and 0.0149 g as 0.01 g, and the possible number of crystals in the smallest sieve tray range can be around between 267,000 and 790,000. However, this crystal mass does not significantly affect the mass of total crystals, so the range of $\bar{L}_{30}$ that can be approximated becomes very wide. As a result, feedback control cases with a much higher supersaturation level, σ, than 0.1 can generate numerous nuclei, and it can make $\bar{L}_{30}$ smaller than expected results.

This feedback control approach employed an SNN model, which was developed in Chapter 5. However, it is difficult to say that the model can translate the measured data using PAT tools to the desired states perfectly, and the model never occurs errors. Additionally, data-driven models may return incorrect results for inputs present in parts not involved in the training session. Therefore, data-driven models should be constantly updated using new data points to improve the predictive ability of the model. In Chapter 5, the driven model shows a high R^2 values of 0.988, but the training data set cannot reflect all possible system states. This is a limitation of the developed SNN model, so additional training is required to improve the model accuracy.

6.3 Summary

In this chapter, feedback control experiments were carried out to produce crystals with desired mean volume size and mass. All experiments were controlled by optimal control policy and the SNN model to convert PAT measurements and reduced-order states for updating system states.

This chapter shows that the feedback control approach adjusts the temperature to re-

duce the distance-to-target, $\sqrt{d_\tau}$, and the final states were able to meet the criteria. The final state of Case 1 reached the target according to the *in situ* monitored results, but the recovered crystals have smaller $\bar{L}_{30}$ than the target values. However, the temperature and supersaturation show stable profiles at the end of the control, the status in the crystallizer may not change; therefore, it is assumed that the monitored attributes by the PAT tools may not be included in the training set of the SNN model, and the translated s_1 had incorrect values. Case 2 showed that s_1 did not land on the target value, even though the temperature profile repeatedly increased and decreased with a narrow range. Also, the distance-to-target slightly enlarged while the temperature cycled; this control was ended manually. However, the results by sieving and weighing provided the closest results to the analyzed results using the PAT tools among all cases. Case 3 completed the feedback control since the distance-to-target met the criterion, and $\bar{L}_{30}$ and m from sieving and weighing analysis also show the shortest distance-to-target. Case 4 was terminated while the temperature was rapidly decreasing, even though the control terminating condition was satisfied. The temperature control has a response delay, and the sudden termination of control kept the temperature decreasing; this phenomenon caused smaller $\bar{L}_{30}$ and larger mass of recovered crystals than the target.

Two main limitations on the feedback control were observed from control experiments: 1) Fines highly affect the value of $\bar{L}_{30}$, and 2) the data-driven model requires continuous training using new data points. However, the feedback control scheme was experimentally validated that the final crystal masses showed similar values to the target for all experimental data. Moreover, it is expected that the mean volume sizes can be improved since the reasons for the mismatch in the results were also identified.

CHAPTER 7

CONCLUSION AND RECOMMENDATION

7.1   Conclusion

This thesis presents the crystallization control to obtain paracetamol from the ethanolic solution utilizing a dynamic programming approach. The system temperature was manipulated to control the process. This approach has 4 steps to achieve the final purpose: 1) developing a population balance model to provide training sets for a Markov state model with less effort to save time and cost for conducting experiments, 2) training the Markov state model to find the optimal control policy through dynamic programming, and implementing the optimal control policy on the open-loop control approach, 3) developing a data-driven model to convert the monitored properties by PAT tools to reduced-order states, and 4) conducting feedback control to produce crystals with desired attributes utilizing previous results.

In the first step of this process, a population balance model was developed to predict the crystallization processes utilizing temperature cycling. The parameters for nucleation, growth, and dissolution kinetics were estimated based on experimental results, and the predictive ability of the model was validated using test experimental sets. Moreover, the developed model was utilized to analyze the nature of nucleation, growth, and dissolution during the crystallization and the effect of temperature cycling on controlling the mean volume size. The PBM model was also used to generate the data sets to train the Markov state model to save cost and time for experiments.

To obtain the desired crystals, crystallization processes should be controlled. In this thesis, a dynamic programming approach was implemented to find the optimal control policy

for the crystallization process. The dynamic programming approach requires a model to describe the crystallization system, but the PBM has challenges to simplify the crystallization behavior. Because the PBM is a partial differential equation, it requires much information to solve the PBM, such as information on neighbor temporal and spatial grids. However, the first-order Markov state model, which assumes only the current state can affect the state at the next time step, can simply describe the crystallization. The PBM can generate data points to train the MSM without experiments, and two reduced-order states, $s_1 = \mu_0 \times 10^{-6}$ and $s_2 = \mu_3 \times 10^{-12}$, were employed to control the crystallization. The trained MSM and DP to search the optimal control policy were employed to obtain desired crystals. The DP approach showed that it could provide the optimal control policy based on the MSM utilizing the PBM, and the temperature profiles for desired crystals were validated through PBM simulations and open-loop control experiments. However, the open-loop control presents some limitations: 1) this method cannot respond to the disturbances during the process operation, and 2) the temperature control system has response delay so that the recovered crystals had differences from the target attributes, especially the mean volume size.

To overcome these limitations, the feedback control scheme is required, but a conversion model from the measured data by PAT tools to the reduced-order states is needed. In particular, the first reduced-order state, s_1, is related to the total number of crystals, and this attribute is significant to evaluate the mean volume crystal size. Therefore, three steps were carried out to determine the conversion model: 1) validating s_1 is relating to the FBRM measurements, 2) determining which measurements from PAT tools affect s_1 through stepwise linear regression, and 3) making a shallow neural network model using inputs from the previous step. In the third step of the model development, techniques to evaluate information criteria were employed to determine the transfer function and the number of neurons for the SNN model. This model shows a good agreement with $R^2 = 0.986$ so that this model was employed in the system for the monitoring system status and making decisions in the feedback control process.

The feedback control of the crystallization employed the procedure to optimize the control policy and the SNN model to translate the PAT measurements to the reduced-order states. The conducted feedback controls were generally ended by the termination criteria, $\sqrt{d_\tau} \leq 0.5$; therefore, the monitored $\bar{L}_{30}$ and m are close to the target characteristics. Sieved and weighed attributes of recovered crystals from two experimental cases showed the similar values to the targets. For two remaining cases, measured results by sieving and weighing have smaller $\bar{L}_{30}$, but masses of sampled crystals are close to the target. The mismatching results were analyzed and possible reasons were drawn: 1) the PAT measurements for Case 1 were not included in the training set of the SNN model, which was developed in Chapter 5, and 2) numerous nuclei were generated by the rapidly increased supersaturation at the end of the control for Case 4, so the increased s_1 resulted in a reduced $\bar{L}_{30}$ than the target.

Through this thesis, we validated that the optimal control policy can be obtained by reducing the number of experiments. It is expected this framework will be utilized for crystallization control of other material systems.

7.2 Recommendations

7.2.1 Development of a digital twin of the crystallizer

A digital twin is a concept of a represented physical system using digital models or data, and the simulations by the digital system can provide the improved operation method or expected results to the physical objects. The initial application of the concept of twin is the rescue project for Apollo 13 by NASA, and they tested the optimal condition to rescue astronauts who met distress on the way to the Moon using the physically duplicated space module on the ground [155]. As the computing technique has improved, the concept of the twin was extended to the digital/virtual space. An early example of the digital twin of a chemical process is monitoring safety issues from the chemical process by Tennessee East-

man [156], and the developed digital twin is continuously improved and applied to under-stand the chemical process [157, 158]. The digital twin concept is continuously spreading in the chemical engineering and bioengineering area [159–162].

The framework through the entire work shown in this thesis can be improved as a digital twin of the batch cooling crystallization. This framework requires experimental data points to train the PBM. However, once the PBM model parameters are determined, the PBM can generate data sets to train the MSM. The trained MSM and DP approach can be utilized to obtain the optimal control policy to produce the desired crystals. Also, the conversion model between PAT measurements and reduced-order states can be trained by the provided experimental data for the PBM parameter estimation step. In this study, however, the PBM was trained for specific conditions such as supersaturation range at the temperature plateau and initial solution concentration. The conversion model also requires more data points to improve the performance.

Despite numerous works that have been reported about the PBM modeling and process control for crystallization, the cases that mentioned the digital twin concept for the crys-tallization process are rare. If the PBM model and the approach for the process control will be unified and continuously trained using experimental data points, the digital twin can provide the optimal control policy with higher accuracy and test effects of disturbance in the process operation. Digital twins can be established using any models, including em-pirical and fundamental models if the models can describe the physical system. The only limitation of the digital twin is that the quality of the digital twin depends on the number of training data set. However, if the experimental data points will be continuously added to the training set, the accuracy of the digital twin will be improved to represent the physical system. As a result, establishing a digital twin for batch cooling crystallization is expected to reduce the probability of failure and accidents in actual operation.

7.2.2 Possible attempts for better crystallization control using dynamic programming.

Variable selection in the reduced-order state space. In this thesis, the reduced-order states, s_1 and s_2, were used to represent desired crystal attributes: the mean volume crystal size, $\bar{L}_{30}$, and crystal mass, m. The training set of the MSM model was generated using the PBM simulation results, not actual experimental results. However, the developed PBM can estimate any crystal characteristics related to the crystal size distribution, so the state space can directly employ any desired attributes from the PBM simulation. For example, the PBM can provide any kind of mean size of crystals, crystal mass, and even the span of the crystal size distribution to evaluate the size distribution. Therefore, once it is confirmed that the relationship between the chosen input variable and the desired outputs is clear, the desired properties can be used directly in the state space.

Extension of the number of axes in the state space. In this thesis, a 2-D state space was utilized to control the mean volume crystal size and the mass of crystals. However, if more than two attributes should be controlled in the system, and they cannot be expressed in the 2-D state space, additional axes are needed to describe the dynamic behavior of the crystals during the control process. For instance, if three attributes, such as the crystal mass, volume-weighted mean size, and the width of the size distribution, should be controlled simultaneously, these three attributes can be illustrated in the 3-D state space. Otherwise, μ_3, μ_4, and μ_5, can be shown in the 3-D state space according to the following relationships: 1) the crystal mass is directly related to μ_3, 2) the volume-weighted mean size is μ_4/μ_3, and 3) the volume-weighted coefficient of variation is $(\mu_3\mu_5/\mu_4^2 - 1)^{1/2}$ if the size distribution follows a normal distribution [107]. However, the addition of axes in the state space may increase the time for the model training. Moreover, more data points may be required to cover the region in the state space for the control.

Correlation between particle size distribution and chord length distribution. In this thesis, a shallow network model was developed to convert the PAT measurements and the first reduced-order state, s_1, for the feedback control. The developed model shows good conversion abilities so that the feedback control experiments were successful. From this result, a neural network model was constructed to convert the FBRM measurements to the particle size distributions. Crestani *et al.* made a neural network model utilizing the measured chord length distributions and particle size distributions by sieving analysis [73]. Due to the complexity of the neural network model, the number of training data is significant. Moreover, the sieving analysis can provide only one data set per experiment. However, the PBM can supply as many data points as the FBRM generates during experiments. Therefore, the measured chord length distribution data and simulated particle size distribution results can be utilized as a training data set for the conversion model. If this model is reliable, more direct data transfer will be available during the crystallization feedback control.

7.2.3   Determination of particle size distribution using other methods

Sieving analysis was used in this study to determine the crystal size distribution. However, this method has a limitation for accurate analysis. If too many crystals exist on a sieve tray with small pores, we cannot be sure every crystal can meet the surface of the sieve during the process. Moreover, static electricity can make crystals attach to the wall of a sieve tray. Figure 7.1 presents problems that can happen while the sieving analysis is conducted.

Many other *in situ* and *ex situ* methods can be employed to investigate the crystal size distribution such as microscopic analysis, laser diffraction, *in situ* camera, ultrasound extinction, and dynamic light scattering [83]. Among various techniques, microscopic analysis can be additionally selected due to its simple operation process. Moreover, if the microscope supports taking pictures, the image analysis tools can analyze crystal size distribution. The microscopic analysis was attempted for paracetamol crystals, and the process is shown in Appendix D. Even though the image analysis showed possibility to investigate
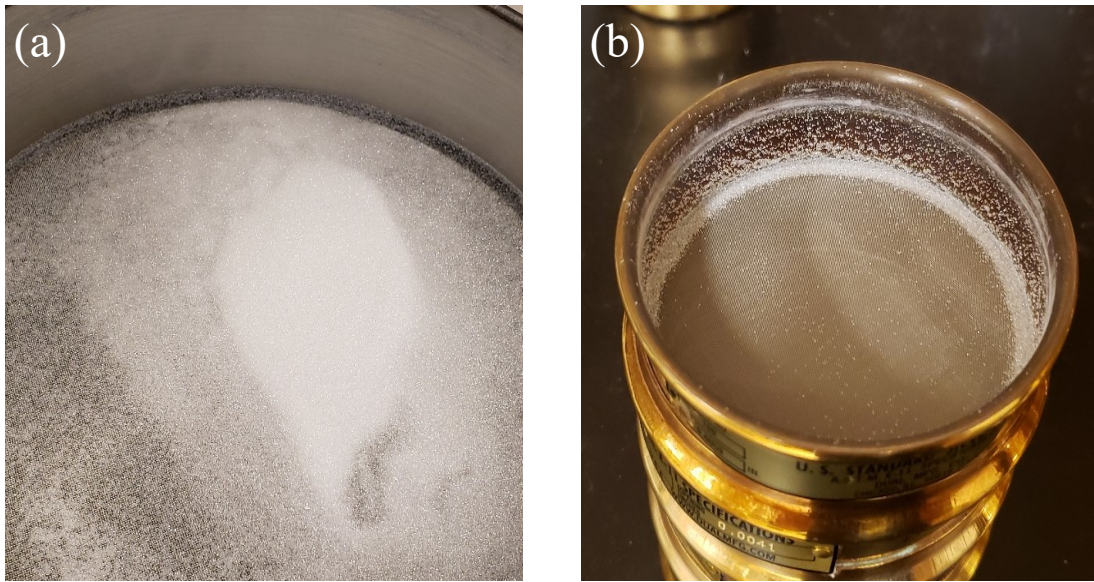
Figure 7.1: Possible issues during the sieving analysis. (a) The case with a large volume of crystals in a sieve tray, and (b) sticking crystals on the wall of the tray due to the static electricity.

crystal size distributions, the process was not establish perfectly. Additional works are necessary to implement the microscopic image analysis for the crystal size distribution.

Appendices

APPENDIX A

SPACE-TIME CONSERVATION ELEMENT/SOLUTION ELEMENT (CE/SE) METHOD

To describe the dynamics of a system that changes according to time and space, partial differential equation (PDE) is very useful. To solve the PDE, many numerical methods have been developed and employed to approximate solutions of PDEs. Representative examples are finite-difference method (FDM), finite-element method (FEM), and finite-volume method (FVM). The space-time CE/SE method developed and improved by Chang [117, 163] is an example of FVM, and this scheme was employed to obtain the characteristics of crystals from the PBM.

A.1 Definition of conservation element and solution element

Consider the one-dimensional PBM to describe crystallization in a simple Euler equation.

$$\frac{\partial u}{\partial t} + \frac{\partial f}{\partial x} = 0 \tag{A.1}$$

Suppose $\mathbf{h} = (f, u)$, Equation (A.1) becomes

$$\nabla \cdot \mathbf{h} = 0 \tag{A.2}$$

$$\iint_A \nabla \cdot dA = 0 \tag{A.3}$$

where $dA = dxdt$ and $\nabla = (\partial/\partial x, \partial/\partial t)$. The divergence theorem makes Equation (A.3) as

$$\oint_C \mathbf{h} \cdot d\mathbf{C} = 0 \tag{A.4}$$

where $\mathbf{C}$ is a closed curve that cover the target region and $d\mathbf{C}$ is a line segment perpendicular to outward directions of $\mathbf{C}$. Here, $d\mathbf{C} = (-dt, dx)$, so Equation (A.4) becomes

$$\oint_C (f)dt + (-u)dx = 0 \tag{A.5}$$

$\mathbf{C}$ is a closed curve in the domain of (x, t), and the integral in $\mathbf{C}$ is zero. Therefore, there is a scalar function ϕ whose derivative $\nabla\phi = (-u, f)$.

A.1 indicates the grid structure in the space-time domain, and the information flow of solution points that are used to estimate u_j^n and $(u_x)_j^n$ at the node of (j, n). Here, u_j^n and $(u_x)_j^n$ means

$$u_j^n \equiv u(x_j, t^n), \quad (u_x)_j^n \equiv \frac{\partial u}{\partial x}(x_j, t^n) \tag{A.6}$$
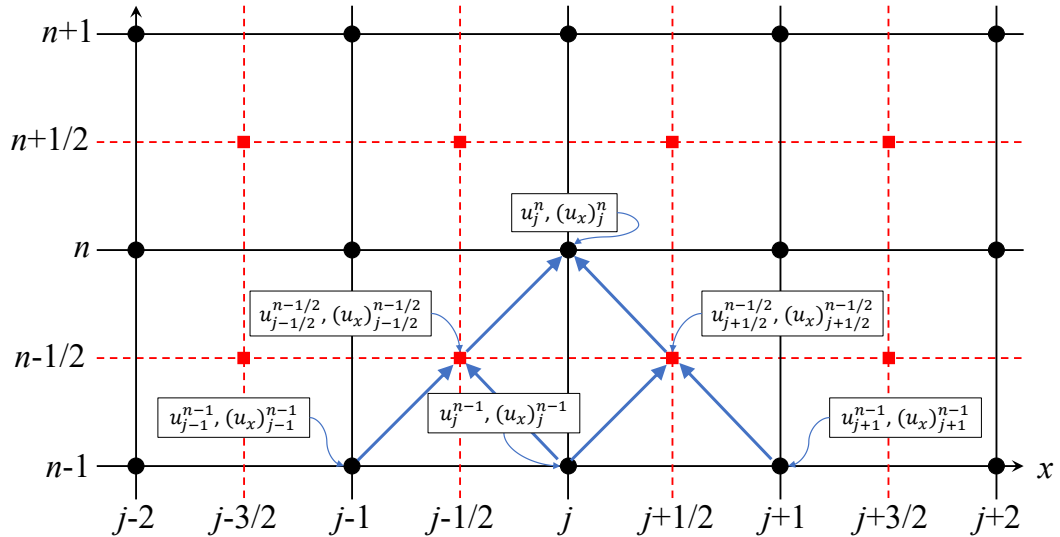
Figure A.1: Organization of grid mesh in the CE/SE scheme, and time-marching variables and the information flow to estimate one CE/SE time step.
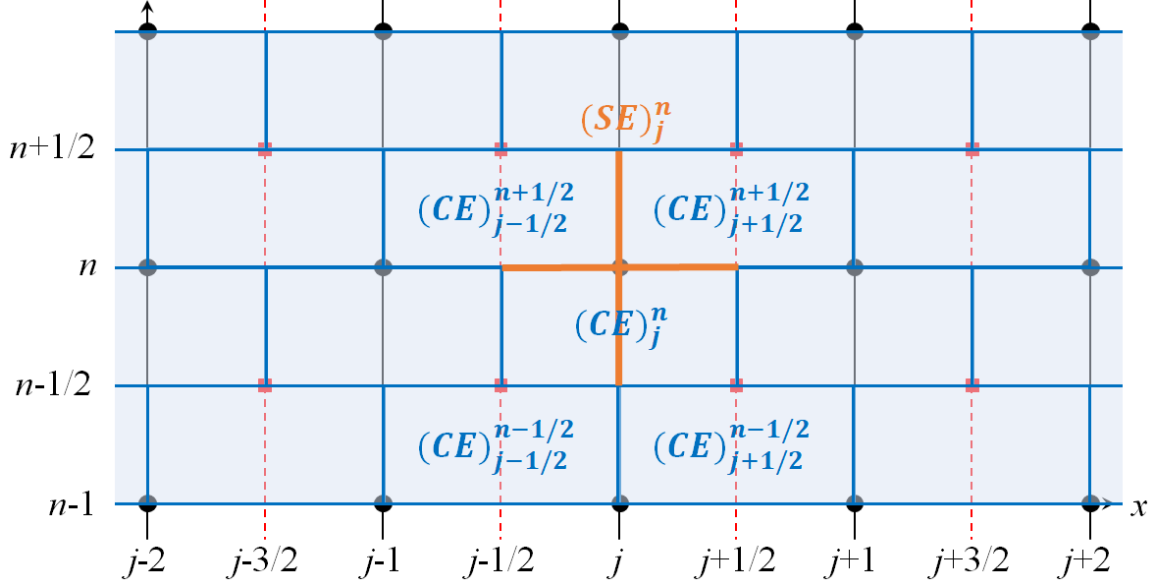
Figure A.2: Definition of conservation element (CE) and solution element (SE)

A.2 shows the definitions of conservation element (CE), and solution element (SE) of the CE/SE scheme. The CEs are the closed rectangle by blue lines, and an example of SE is shown as the cross orange lines. The $(SE)_j^n$ has a solution point at the cross point of two lines at (j, n), and it has four end points of $(j - 1/2, n)$, $(j + 1/2, n)$, $(j, n - 1/2)$, and $(j, n + 1/2)$. The solution points in the structure are shown as black dots and red squares in A.2. The CE is bounded by three SEs without overlaps; for example, $(CE)_j^n$ is covered by $(SE)_j^n$, $(SE)_{j-1/2}^{n-1/2}$, and $(SE)_{j+1/2}^{n-1/2}$. The functions $u(x, t)$ and $f(x, t)$ can be approximated by first-order Taylor expansions about the center of SE as Equations (A.7) and (A.8).

$$u(x, t) = u_j^n + u_x(x - x_j) + u_t(t - t^n) \tag{A.7}$$

$$f(x, t) = f_j^n + f_x(x - x_j) + f_t(t - t^n) \tag{A.8}$$

where $u_t = \partial u / \partial t$, $u_x = \partial u / \partial x$, $f_t = \partial f / \partial t$, and $f_x = \partial u / \partial x$.

From Equation (A.1),

$$u_t = -f_x \tag{A.9}$$

The $(SE)_j^n$ is a part of the boundary of $(CE)_j^n$, so $\nabla \phi = (-u, f)$ at (j, n). This ϕ can be

135

second-order approximated using u, u_x, u_t, f, f_x, and f_t as shown from Equation (A.10) to Equation (A.14).

$$\frac{\partial \phi}{\partial x} = -u \tag{A.10}$$

$$\frac{\partial \phi}{\partial t} = f \tag{A.11}$$

$$\frac{\partial^2 \phi}{\partial t^2} = f_t \tag{A.12}$$

$$\frac{\partial^2 \phi}{\partial x^2} = -u_x \tag{A.13}$$

$$\frac{\partial^2 \phi}{\partial x \partial t} = f_x \tag{A.14}$$

Substituting Equations (A.7) and (A.8) into Equations (A.10) and (A.11), and using Equation (A.9), ϕ_j^n becomes

$$\phi_j^n = f_j^n(t-t^n) - u_j^n(x-x_j) + \frac{1}{2}(f_t)_j^n(t-t^n)^2 - \frac{1}{2}(u_x)_j^n(x-x_j)^2 + (f_x)_j^n(x-x_j)(t-t^n) + C \tag{A.15}$$

To estimate of CEs, the flux conservation law by the neighboring SEs is considered. One CE is surrounded by three SEs, as mentioned above, and the relationship among three segments is shown in Figure A.3. The inputs of the case in Figure A.3 to estimate each ϕ are shown in Table A.1. In Figure A.3, ϕ_1 and ϕ_6 are on the same position, but they can be expressed different with Equation (A.15)
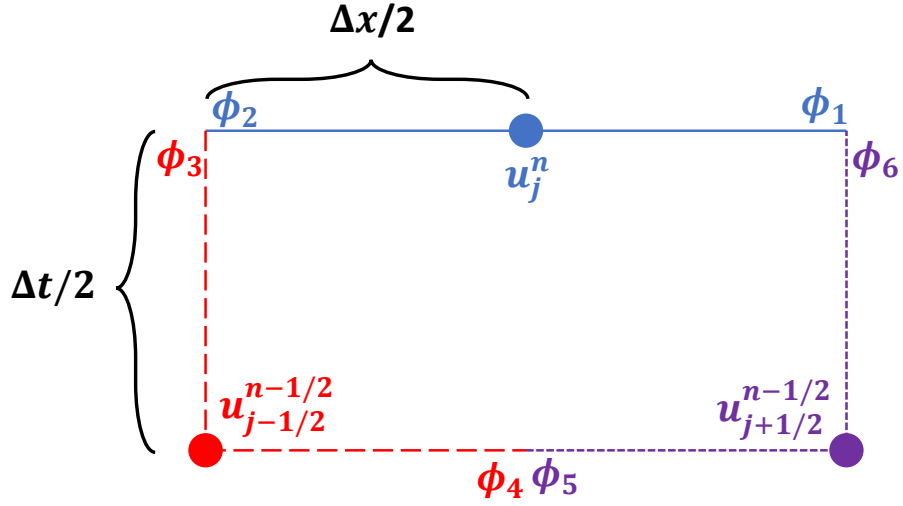
Figure A.3: Conservation law by the neighboring SEs. Each SE is illustrated by different color and line.

Table A.1: Inputs to estimation each ϕ using Equation (A.15)

	x	t	j	n
ϕ_1	$x_j + \dfrac{\Delta x}{2}$	t^n	j	n
ϕ_2	$x_j - \dfrac{\Delta x}{2}$	t^n	j	n
ϕ_3	$x_{j-1/2}$	$t^{n-1/2} + \dfrac{\Delta t}{2}$	$j - 1/2$	$n - 1/2$
ϕ_4	$x_{j-1/2} + \dfrac{\Delta x}{2}$	$t^{n-1/2}$	$j - 1/2$	$n - 1/2$
ϕ_5	$x_{j-1/2} - \dfrac{\Delta x}{2}$	$t^{n-1/2}$	$j + 1/2$	$n - 1/2$
ϕ_6	$x_{j-1/2}$	$t^{n-1/2} + \dfrac{\Delta t}{2}$	$j + 1/2$	$n - 1/2$

$$
\begin{aligned}
\phi_1 =& f_j^n \left(t^n - t^n\right) - u_j^n \left(\left(x_j + \frac{\Delta x}{2}\right) - x_j\right) \\
&+ \frac{1}{2} (f_t)_j^n \left(t^n - t^n\right)^2 - \frac{1}{2} (u_x)_j^n \left(\left(x_j + \frac{\Delta x}{2}\right) - x_j\right)^2 \\
&+ (f_x)_j^n \left(\left(x_j + \frac{\Delta x}{2}\right) - x_j\right) \left(t^n - t^n\right) + C \\
=& -u_j^n \left(\frac{\Delta x}{2}\right) - \frac{1}{2} (u_x)_j^n \left(\frac{\Delta x}{2}\right)^2 + C
\end{aligned}
\tag{A.16}
$$

and

$$\phi_6 = f_{j+1/2}^{n-1/2} \left(\left(t^{n-1/2} + \frac{\Delta t}{2} \right) - t^{n-1/2} \right) - u_{j+1/2}^{n-1/2} \left(x_{j+1/2} - x_{j+1/2} \right)$$
$$+ \frac{1}{2} (f_t)_{j+1/2}^{n-1/2} \left(\left(t^{n-1/2} + \frac{\Delta t}{2} \right) - t^{n-1/2} \right)^2 - \frac{1}{2} (u_x)_{j+1/2}^{n-1/2} \left(x_{j+1/2} - x_{j+1/2} \right)^2$$
$$+ (f_x)_{j+1/2}^{n-1/2} \left(x_{j+1/2} - x_{j+1/2} \right) \left(\left(t^{n-1/2} + \frac{\Delta t}{2} \right) - t^{n-1/2} \right) + C$$
$$= f_{j+1/2}^{n-1/2} \left(\frac{\Delta x}{2} \right) + \frac{1}{2} (f_t)_{j+1/2}^{n-1/2} \left(\frac{\Delta x}{2} \right)^2 + C$$

(A.17)

remaining ϕ are

$$\phi_2 = -u_{j+1/2}^{n-1/2} \left(-\frac{\Delta x}{2} \right) - \frac{1}{2} (u_x)_{j+1/2}^{n-1/2} \left(-\frac{\Delta x}{2} \right)^2 + C \qquad (A.18)$$

$$\phi_3 = f_{j-1/2}^{n-1/2} \left(\frac{\Delta t}{2} \right) + \frac{1}{2} (f_t)_{j-1/2}^{n-1/2} \left(\frac{\Delta t}{2} \right)^2 + C \qquad (A.19)$$

$$\phi_4 = -u_{j-1/2}^{n-1/2} \left(-\frac{\Delta x}{2} \right) - \frac{1}{2} (u_x)_{j-1/2}^{n-1/2} \left(-\frac{\Delta x}{2} \right)^2 + C \qquad (A.20)$$

$$\phi_5 = -u_{j+1/2}^{n-1/2} \left(-\frac{\Delta x}{2} \right) - \frac{1}{2} (u_x)_{j+1/2}^{n-1/2} \left(-\frac{\Delta x}{2} \right)^2 + C \qquad (A.21)$$

Because the integral of closed curve is zero,

$$(\phi_1 - \phi_2) + (\phi_3 - \phi_4) + (\phi_5 - \phi_6) = 0 \qquad (A.22)$$

Substituting all ϕ using into Equation (A.22),

$$u_j^n = \frac{1}{2} \left(u_{j-1/2}^{n-1/2} + u_{j+1/2}^{n-1/2} + s_{j-1/2}^{n-1/2} + s_{j+1/2}^{n-1/2} \right) \qquad (A.23)$$

where

138

$$s_j^n = \frac{\Delta x}{4}(u_x)_j^n + \frac{\Delta t}{\Delta x}f_j^n + \frac{\Delta t^2}{4\Delta x}(f_t)_j^n \tag{A.24}$$

If u_j^n can determine $(u_x)_j^n$, f_j^n, and $(f_t)_j^n$, iteration can be carried out through the temporal domain by this marching scheme. Suppose $f(u) = au$ in Equation (A.1), the Cournat-Friedrichs-Lewy (CFL) number, $\nu^2 < 1$, is used to attain the stability condition for the marching process, where $\nu = a\Delta t/\Delta x$. Terms in Equations (A.23) and (A.24) should be calculated to solve the PBM using this scheme. If we assume u_j^n is known, f_j^n can be calculated because f is a function of u. f_t can be obtained using equations, $f_t = f_u u_t$ and $u_t = -f_x$, so $f_t = -f_u f_x$. Finally, u_x is the only term unknown in Equations (A.23) and (A.24), so this term should be estimated from known values.

A.2   *Approximation of u_x*

Figure A.4 shows the terms that are used to approximate u_x. Suppose that values of $u_{j-1/2}^{n-1/2}$, $u_{j+1/2}^{n-1/2}$, $(u_x)_{j-1/2}^{n-1/2}$, $(u_x)_{j+1/2}^{n-1/2}$ are known, then the values of $(u_t)_{j-1/2}^{n-1/2}$ and $(u_t)_{j+1/2}^{n-1/2}$ can be
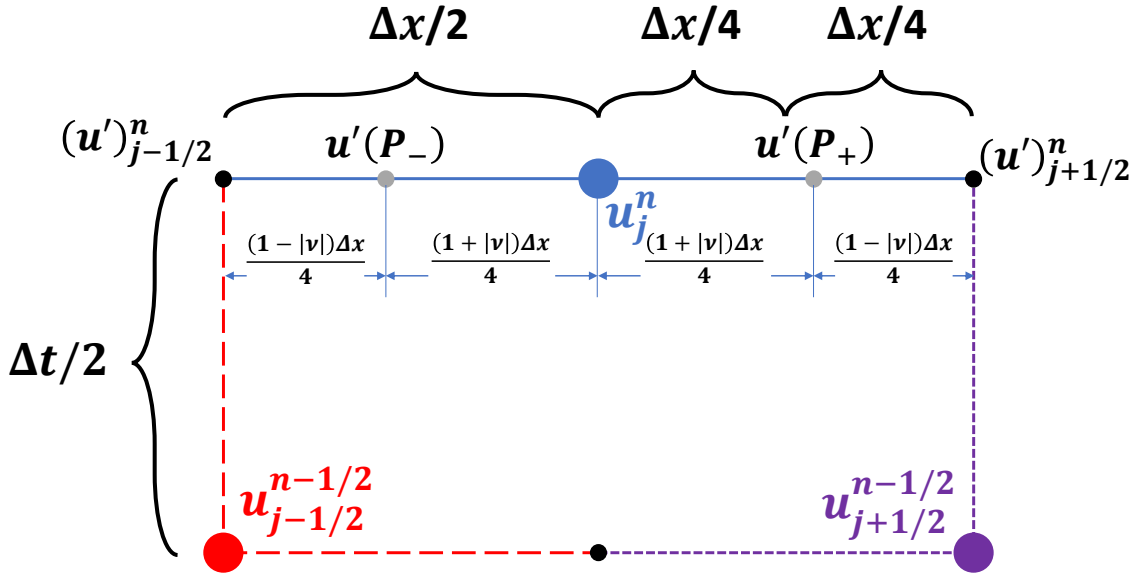
Figure A.4: Definitions of each term to estimate $(u_x)_j^n$

estimated by $u_t = -f_u u_x = -a(u_x)$. One easy way to approximate $(u_x)_j^n$ is the central-difference approach,

$$(u_x^c)_j^n = \frac{(u')_{j+1/2}^n - (u')_{j-1/2}^n)}{\Delta t} \tag{A.25}$$

where the superscription "c" represents the value is obtained by the central-difference, and $(u')_{j\pm1/2}^n = u_{j\pm1/2}^{n-1/2} + (u_t)_{j\pm1/2}^{n-1/2}\Delta t$. If discontinuities are present in numerical solutions, the central-difference cannot be employed because this method causes numerical dissipation during the approximation.

To minimize the effect of the discontinuity of the solution and to estimate u_x more accurately, Courant number insensitive scheme was introduced in this approximation [163]. For this method, two points, $P_\pm$, that can be approximated by information at $(j \pm 1/2)$,

$$u'(P_+) \equiv u_{j+1/2}^{n-1/2} + \frac{\Delta t}{2}(u_t)_{j+1/2}^{n-1/2} - \frac{(1-|\nu|)\Delta t}{4}(u_x)_{j+1/2}^{n-1/2} \tag{A.26}$$

$$u'(P_-) \equiv u_{j-1/2}^{n-1/2} + \frac{\Delta t}{2}(u_t)_{j-1/2}^{n-1/2} - \frac{(1-|\nu|)\Delta t}{4}(u_x)_{j-1/2}^{n-1/2} \tag{A.27}$$

where $u'(P_\pm)$ are first-order Taylor's approximation of u at points $P_\pm$ in Figure A.4. With the definitions of CFL number, $\nu = a\Delta t/\Delta x$, and the normalized u_x, $u_x^+ = \frac{\Delta x}{4}u_x$, Equations (A.26) and (A.27) become,

$$u'(P_+) = [u - (1 + 2\nu - |\nu|)(u_x^+)]_{j+1/2}^{n-1/2} \tag{A.28}$$

$$u'(P_-) = [u + (1 - 2\nu - |\nu|)(u_x^+)]_{j-1/2}^{n-1/2} \tag{A.29}$$

From the geometric definitions in Figure A.4, $(\hat{u}_x^+)_j^n$, $(\hat{u}_{x+}^+)_j^n$, $(\hat{u}_{x+}^+)_j^n$, and $(\hat{u}_x^{w+})_j^n$ can be defined,

$$(\hat{u}_x^+)_j^n \equiv \frac{u'(P_+) - u'(P_-)}{2(1 + |\nu|)} = \frac{\Delta x}{4}\left(\frac{u'(P_+) - u'(P_-)}{(1 + |\nu|)\Delta x/2}\right) \tag{A.30}$$

$$(\hat{u}_{x+}^+) \equiv \frac{u'(P_+) - u_j^n}{1 + |\nu|} = \frac{\Delta x}{4}\left(\frac{u'(P_+) - u_j^n}{(1 + |\nu|)\Delta x/4}\right) \tag{A.31}$$

$$(\hat{u}_{x-}^+) \equiv \frac{u_j^n - u'(P_-)}{1 + |\nu|} = \frac{\Delta x}{4}\left(\frac{u_j^n - u'(P_-)}{(1 + |\nu|)\Delta x/4}\right) \tag{A.32}$$

$$(\hat{u}_x^{w+})_j^n \equiv W_o((\hat{u}_{x+}^+), (\hat{u}_{x-}^+); \alpha) = \frac{|(\hat{u}_{x-}^+)|^\alpha(\hat{u}_{x+}^+) + |(\hat{u}_{x+}^+)|^\alpha(\hat{u}_{x-}^+)}{|(\hat{u}_{x-}^+)|^\alpha + |(\hat{u}_{x+}^+)|^\alpha} \tag{A.33}$$

where W_o is a weight averaging function, and $\alpha \geq 0$. For the equation to determine $(u_x)_j^n$,

let

$$(s_\pm)_j^n = \frac{|(\hat{u}_{x\pm}^+)_j^n|}{\min(|(\hat{u}_{x+}^+)_j^n|, |(\hat{u}_{x-}^+)_j^n|)} - 1 \geq 0 \tag{A.34}$$

Using Equations (A.33) and (A.34),

$$(\hat{u}_x^{w+})_j^n = \frac{[1 + (s_-)_j^n]^\alpha(\hat{u}_{x+}^+) + [1 + (s_+)_j^n]^\alpha(\hat{u}_{x-}^+)}{[1 + (s_-)_j^n]^\alpha + [1 + (s_+)_j^n]^\alpha} \tag{A.35}$$

For the case that $(s_\pm)_j^n \ll 1$, Equation (A.35) becomes

$$(\hat{u}_x^{w+})_j^n \approx \frac{[1 + \alpha \cdot (s_-)_j^n](\hat{u}_{x+}^+) + [1 + \alpha \cdot (s_+)_j^n](\hat{u}_{x-}^+)}{2 + \alpha[(s_-)_j^n + (s_+)_j^n]} \tag{A.36}$$

$(u_x)_j^n$ can be approximated using $\alpha = f|\nu|$ in Equation (A.36) as,

$$(u_x)_j^n = \frac{4}{\Delta x}\frac{[1 + f(|\nu|)(s_-)_j^n](\hat{u}_{x+}^+)_j^n + [1 + f(|\nu|)(s_+)_j^n](\hat{u}_{x-}^+)_j^n}{2 + f(|\nu|)[(s_-)_j^n + (s_+)_j^n]} \tag{A.37}$$

where

$$f(|\nu|) = 0.5/|\nu| \tag{A.38}$$

APPENDIX B

THE DETERMINATION OF VOLUME SHAPE

FACTOR FOR PARACETAMOL CRYSTALS

The volume shape factor of paracetamol crystals, which was mentioned in Chapter 2, was determined by two methods: 1) gravimetric observation, and 2) geometrical estimation.

B.1 Gravimetric observation

Gravimetric observations were carried out through the following steps: 1) measuring the mass of empty microscope slide, 2) sampling crystals from specific sieves, 3) putting sam-

Table B.1: The observed volume mean size by gravimetric method

lower tray size (μm)	upper tray size (μm)	geometric mean size (μm)	count	mass (mg)	k_v
106	150	126.1	830	1.84	0.875
106	150	126.1	296	0.67	0.894
106	150	126.1	1128	2.17	0.760
150	212	178.3	228	1.06	0.649
150	212	178.3	242	1.03	0.594
212	250	230.2	75	0.72	0.623
212	250	230.2	469	4.50	0.623
212	250	230.2	424	4.46	0.683
355	425	388.4	133	7.68	0.780
355	425	388.4	152	8.28	0.736
425	500	461.0	115	9.85	0.692
500	600	547.7	95	17.00	0.862
600	850	714.1	60	26.76	0.970
600	850	714.1	10	4.44	0.965
600	850	714.1	20	8.86	0.963
				average k_v	0.778
				standard deviation	0.174
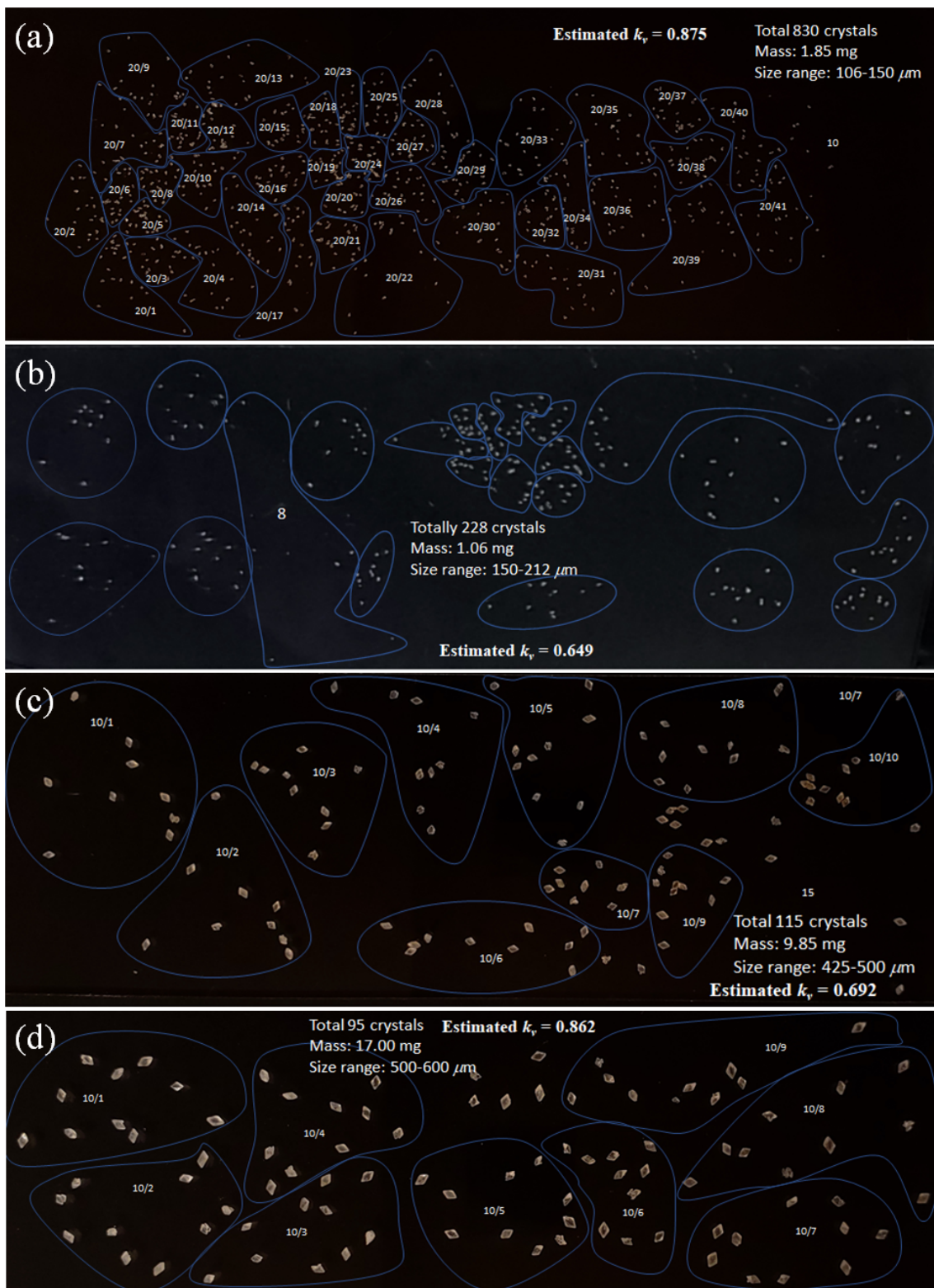
Figure B.1: Four examples of gravimetric observation of the volume shape factor for paracetamol crystals: crystals from sieve tray (a) between 106 and 150 μm, (b) between 150 and 212 μm, (c) between 425 and 500 μm, and (d) between 500 and 600 μm.

pled crystals on a microscope slide, 4) taking a picture of the crystals on the microscopic slide to count the number of crystals, 5) weighing the mass of the microscopic slide and crystals, and 6) calculating the volume shape factor with known crystal density and Equation (2.18). All observed volume shape factors using the gravimetric method are listed in Table B.1, and four examples of the crystal mass and number from taken images are shown in Figure B.1. From gravimetric observations, the mean volume shape factor is obtained as 0.778, and the standard deviation is 0.174.

B.2 Geometrical estimation

It has been assumed that the shape of paracetamol crystals has octahedral shape [19, 74]. In this study, the shape factor was evaluated using this assumption and the microscopic observation. Figure B.2 shows this assumption and the side projection of the laid crystals on the microscope slide. To evaluate the volume shape factor, each dimension in Figure B.2 and volume shape factor, k_v, are calculated by following equations.
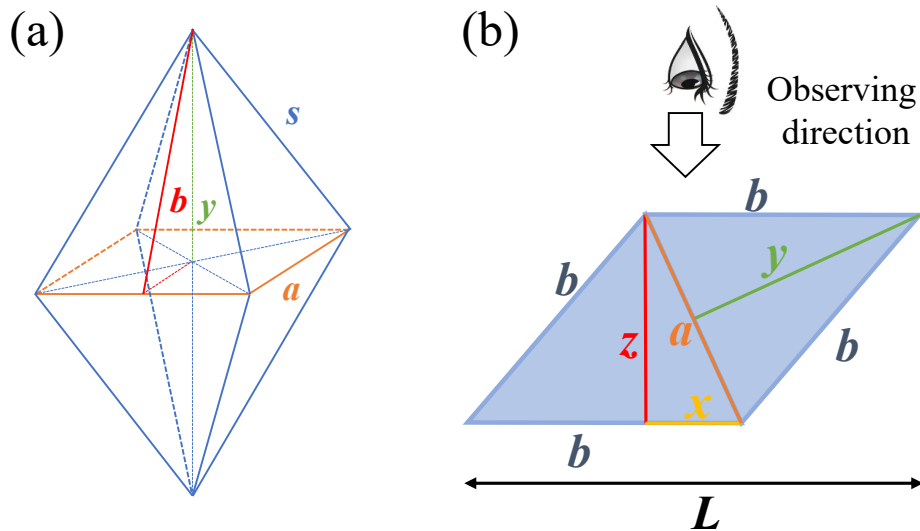
Figure B.2: Shape and dimension of an octahedral crystal: (a) 3D shape of the crystals, and (b) a side view of a laid crystal on the surface and microscopic observing
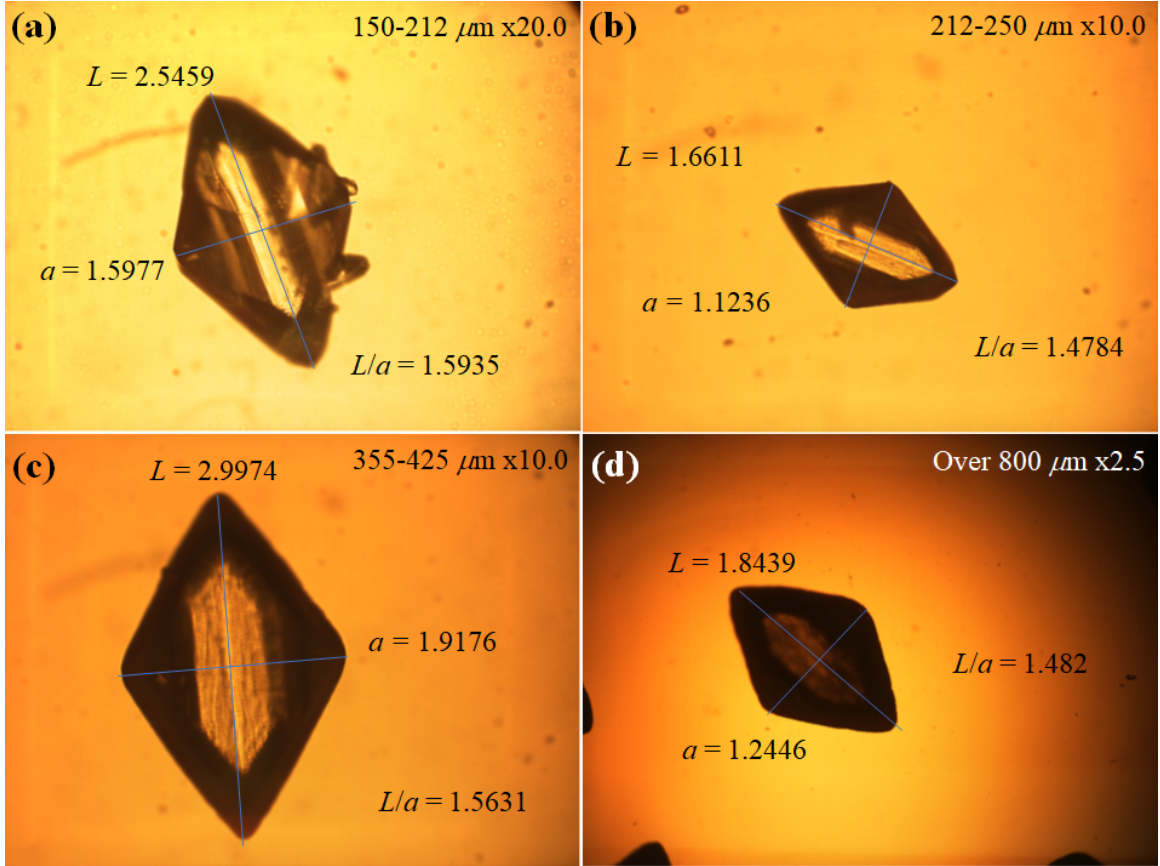
Figure B.3: Examples of aspect ratios for microscopically observed crystals from different sizes of sieve trays: (a) a crystal in $150 - 212 \ \mu$m, (b) a crystal in $212 - 250 \ \mu$m, (a) a crystal in $355 - 425 \ \mu$m, and (a) a crystal larger than $800 \ \mu$m.

$$x = \sqrt{a^2 - z^2} \tag{B.1}$$

$$L = 2b - x \tag{B.2}$$

$$y = \sqrt{b^2 - \frac{a^2}{4}} \tag{B.3}$$

$$ay = bz \tag{B.4}$$

$$k_v = \frac{1}{3}\frac{2ya^2}{a^3} = \frac{2y}{3a} \tag{B.5}$$

Relative lengths of crystals were determined from the taken microscopic images because the ratio of relative lengths can be used to estimate the volume shape factor. Four

Table B.2: The observed volume mean size by geometric method

lower tray size (μm)	upper tray size (μm)	geometric mean size (μm)	a	L	L/a	b	x	y	z	k_v
150	212	178.3	0.834	1.308	1.569	1.071	0.740	0.987	0.768	0.789
150	212	178.3	0.825	1.359	1.646	1.092	0.732	1.011	0.764	0.817
150	212	178.3	0.799	1.273	1.593	1.036	0.709	0.956	0.737	0.798
212	250	230.2	1.124	1.661	1.478	1.392	0.999	1.274	1.028	0.756
212	250	230.2	1.103	1.805	1.637	1.454	0.978	1.345	1.020	0.813
250	300	273.9	1.157	2.233	1.929	1.695	1.022	1.593	1.088	0.918
250	300	273.9	1.240	2.087	1.683	1.664	1.099	1.544	1.151	0.830
300	355	326.3	1.605	2.511	1.565	2.058	1.424	1.895	1.478	0.787
300	355	326.3	1.741	2.659	1.528	2.200	1.547	2.021	1.599	0.774
300	355	326.3	1.695	2.609	1.539	2.152	1.506	1.978	1.558	0.778
355	425	388.4	2.182	3.327	1.525	2.755	1.939	2.529	2.004	0.773
355	425	388.4	2.028	3.120	1.539	2.574	1.801	2.366	1.864	0.778
355	425	388.4	1.918	2.997	1.563	2.458	1.702	2.263	1.766	0.787
425	500	461.0	2.330	3.804	1.632	3.067	2.066	2.837	2.155	0.812
425	500	461.0	2.357	3.553	1.508	2.955	2.094	2.710	2.161	0.767
425	500	461.0	2.209	3.788	1.715	2.999	1.956	2.788	2.054	0.841
425	500	461.0	2.213	3.584	1.620	2.898	1.962	2.679	2.045	0.807
500	600	547.7	3.154	4.837	1.534	3.996	2.802	3.671	2.898	0.776
500	600	547.7	2.846	4.491	1.578	3.668	2.525	3.381	2.623	0.792
500	600	547.7	2.682	4.453	1.660	3.568	2.377	3.306	2.485	0.822
500	600	547.7	2.926	4.638	1.585	3.782	2.596	3.487	2.698	0.795
600	800	692.8	3.482	5.432	1.560	4.457	3.091	4.103	3.205	0.786
600	800	692.8	3.354	5.782	1.724	4.568	2.970	4.249	3.120	0.844
600	800	692.8	4.165	6.362	1.528	5.263	3.700	4.834	3.825	0.774
800	1000	894.4	4.978	7.376	1.482	6.177	4.427	5.653	4.556	0.757
800	1000	894.4	5.101	7.553	1.481	6.327	4.536	5.790	4.668	0.757
								average k_v		0.797
								standard deviation		0.0349

example cases are shown in Figure B.3. The microscopic images can show only two lengths for a and L in Figure B.2. Table B.2 lists the measured dimensions, estimated dimensions in Figure B.2, and volume shape factors by the geometric analysis. From geometric observations, the mean volume shape factor is obtained as 0.797, and the standard deviation is 0.0349. The volume shape factors from two different analyzes show close to each other, 0.778 and 0.797.

APPENDIX C

COMPARISON OF CRYSTAL DISSOLUTION RATE BETWEEN THE LITERATURE MODEL AND THIS WORK

This section compares the dissolution rate given by the PBM in Chapter 3 to the one in Worlitschek and Mazzotti [74]. In Worlitschek and Mazzotti's work, they applied the PBM to explain crystallization and dissolution. Their work included secondary nucleation, growth and dissolution, while our model also includes primary nucleation.

In the model given by Worklitschek and Mazzotti, the secondary nucleation rate is 0 when S is equal to or less than 1. However, the "growth rate" becomes the dissolution rate at the condition with S less than 1 and it follows a correlation as below:

$$G = \frac{2k_d \Delta c}{c_c}, \qquad S < 1 \tag{C.1}$$

where k_d is the mass transfer coefficient [m/s], Δ_c is the absolute supersaturation [kmol/m^3] which is $c_s - c$, and c_c is the molar density of solid solute [kmol/m^3]. Here, the mass transfer coefficient k_d can be obtained with Equations from (C.2) to (C.6).

$$k_d = \frac{D_{\text{diff}}}{L} \left(2 + 0.8 \left(\frac{\epsilon \bar{L}^4 \rho_l^3}{\eta_l^3} \right)^{\frac{1}{5}} Sc^{\frac{1}{3}} \right) \tag{C.2}$$

where ϵ is the mean specific power input [W/kg], $\bar{L}$ is the particle size applied for calculation of k_d and is 10^{-4} in their work, and Sc is Schmidt number as

$$Sc = \frac{\eta_l}{D \rho_l} \tag{C.3}$$

$$\epsilon = \frac{N_e v_s^3 d_s^5}{V_r} \tag{C.4}$$

where N_e is Power number or Newton number, v_s is stirring speed [rps], d_s is the impeller diameter [m], and V_r is total liquid phase volume [m^3].

$$D_{\text{diff}} = \frac{kT}{2\pi\eta_l d_m} \tag{C.5}$$

$$d_m = \sqrt[3]{\frac{1}{c_c N_A}} \tag{C.6}$$

In the above equations, we need to estimate the Power number Ne to calculate the dissolution rate. Worlitschek and Mazzotti assumed the power number as 0.5 which is the intermediate value from 0.3 to 0.7 for propellers. However, our apparatus may have the different power number than propellers, which has a pitched four-blade impeller which. Thus, we identified a correlation to obtain the power number according to the blade shape, angles, and numbers, to enable comparison with their model.

In this study, we employed the estimation method given by Hiraoka *et al.* [164] Their study produced a correlation to obtain power number for the pitched blade paddle impeller in agitated vessels. The power number becomes constant as the flow regime moves into the turbulent region and the stable power number in the turbulent region depends on type of impeller. If the flow regime is in transitional region ($100 < Re < 10000$), the power number of the agitator changes slightly as shown in Figure C.1 [165].

To employ the method by Hiraoka *et al.*, Reynolds number is necessary. The Reynolds number, Re for the impeller is defined by [165]:

$$Re = \frac{\rho_l v_s d_s^2}{\eta_l} \tag{C.7}$$

The dimension of the impeller and values of each characteristic of our system is in
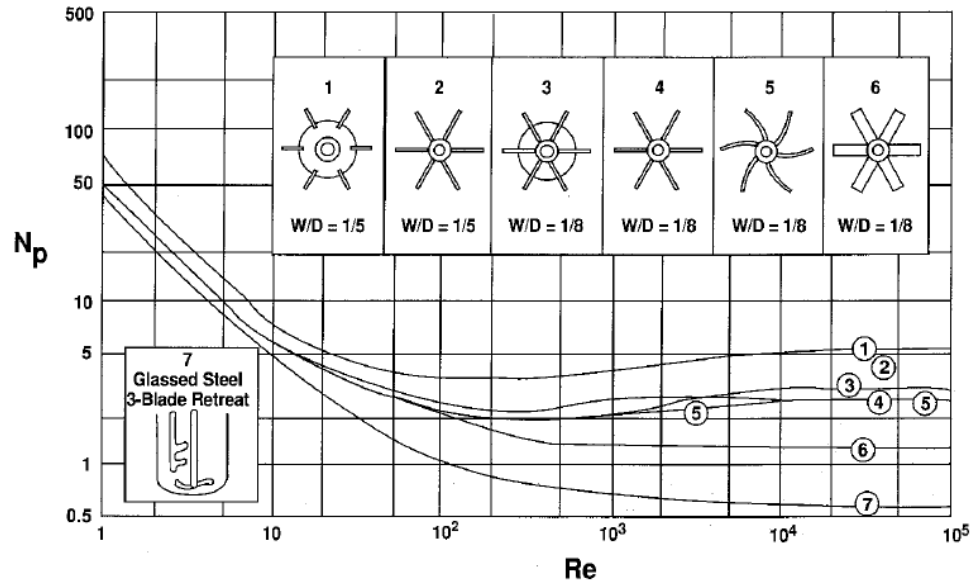
Figure C.1: Power number versus impeller Reynolds number for seven different impellers. [Reprinted with permission for Figure 6-14 from Paul *et al.*[165] Copyright Wiley Books]

Figure C.2. In our system, $d = 3.81$ cm, $b = 0.87$ cm, and θ is 34°. The angle of the pitched blade is estimated based on the trigonometrical as Figure C.1 and the unit of the angle for the calculation is converted to radians. Using these numbers, we found the Reynolds number in our system at 20 °C is 6,448 and it is in the transition regime. Because the Reynolds number is in the transition regime, the power number, N_e (N_p in Figure C.1), may not be constant.
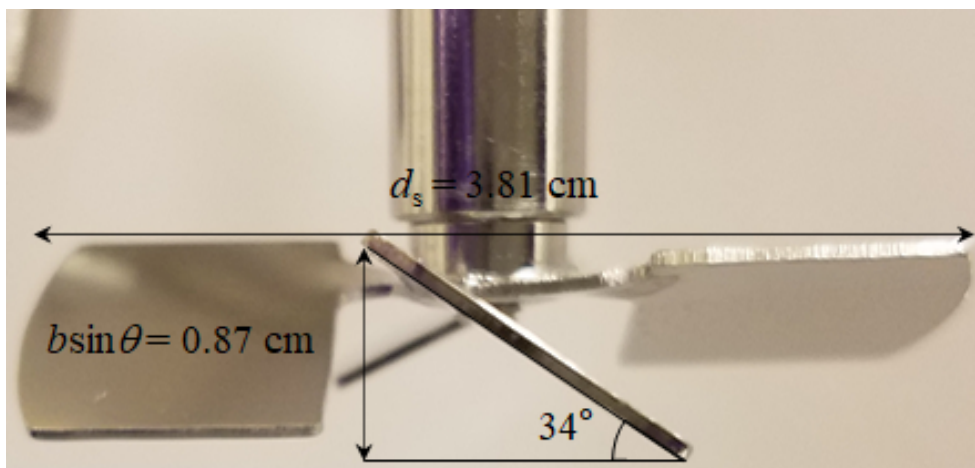
Figure C.2: The angle and dimensions of the pitched blade in our system

The power number given by Figure C.1 is not for the pitched blade, which is used in our experiments. For this type of impeller, Hiraoka *et al.* suggested the correlation of the maximum power number of a pitched blade impeller as

$$N_{e,max,\theta} = 8.3 \left(\frac{2\theta}{\pi}\right)^{0.9} \left(\frac{n_p^{0.7} b \sin^{1.6}\theta}{d}\right) \tag{C.8}$$

where n_p is the number of blades, and other variables are in Figure C.2. After we obtain the power number, then we can calculate the mean specific power input, the mass transfer coefficient, and finally the dissolution rate in Equation (C.1).

Table C.1: Comparison of dissolution rate based on kinetics between the literature and this work.

Conditions		Dissolution rate				
Temperature [°C]	Δc [g/kg]	by literature model (Np = 0.003)	by literature model (Np = 0.5)	by literature model (Np = 5)	by this model (with initial guesses in SI)	by this model (with final parameters in Chapter 3)
10	5	3.281	6.730	9.898	4.614	5.443
20	3	2.024	4.142	6.087	3.308	3.966
30	10	6.932	14.15	20.78	11.56	13.35

The estimated power number through Equation (C.8) for our system was 0.003 which is significantly lower than the literature. To validate this number, we calculated the dissolution rates at this value of 0.003, as well as at higher values of 0.5 and 5. We chose the latter two numbers as follows: the first power number, 0.5, is the value from the literature and the other, 5, is the possible maximum value near 6,000 of the Reynolds number in Figure C.1. The parameters to estimate the dissolution rates using the literature model were taken from the Worlitschek and Mazzotti[1], while different values were employed for equipment-specific parameters such as the dimension of the stirrer. The comparison of dissolution rates for given conditions are shown in Table C.1. In this table, dissolution rates given by our model is always between values by Worlitschek and Mazzotti model[1] with the two power numbers, $N_e = 0.003$ and $N_e = 5$.

APPENDIX D

DETERMINATION OF PARTICLE SIZE

DISTRIBUTION USING THE MICROSCOPIC

METHOD

In this work, I tried to employ microscopic image analysis to determine the final crystal size distributions. The filtered and dried crystals were microscopically observed before the sieving analysis. At the first step of the observation, a picture of the one-millimeter-ruler with a tick of 10 μm was taken to scale images as shown in Figure D.1.

The crystal size in images can be counted as pixel, so a conversion factor from pixel to length is necessary. One millimeter is shown as 273 pixels in the resolution of the image
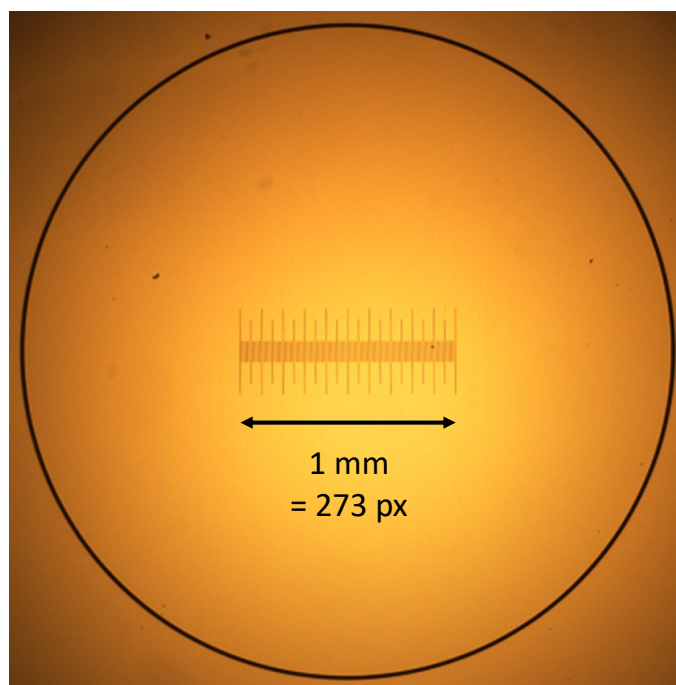
Figure D.1: The one-millimeter-ruler with 10 μm ticks for the reference
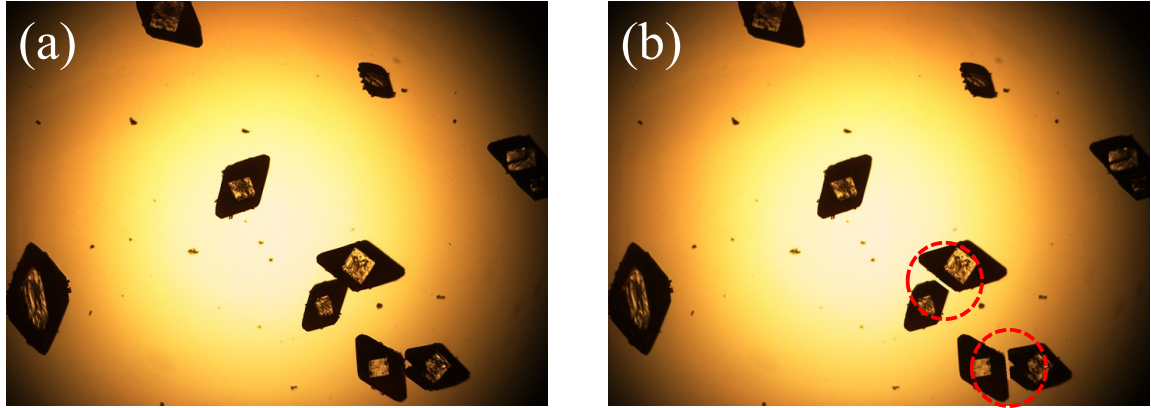
Figure D.2: Image pre-processing for cases that crystals are located too close. (a) Original image, and (b) pre-processed image. The red dashed circles in right and lower of figure (b) present the processed crystal images.

sensor, so this was used to convert the pixel of crystal diameter with a length unit.

Pre-processing all images was necessary to distinguish crystals that were too close or to eliminate crystals that were likely to be detected incorrectly. Figure D.2 shows an example of pre-processing of raw images. A code read the pre-treated images to evaluate the crystal size. Figure D.3 presents image processing steps to analyze the crystal size distribution. The code calls a pre-handled image and makes it a monochrome image. In this step, crystals
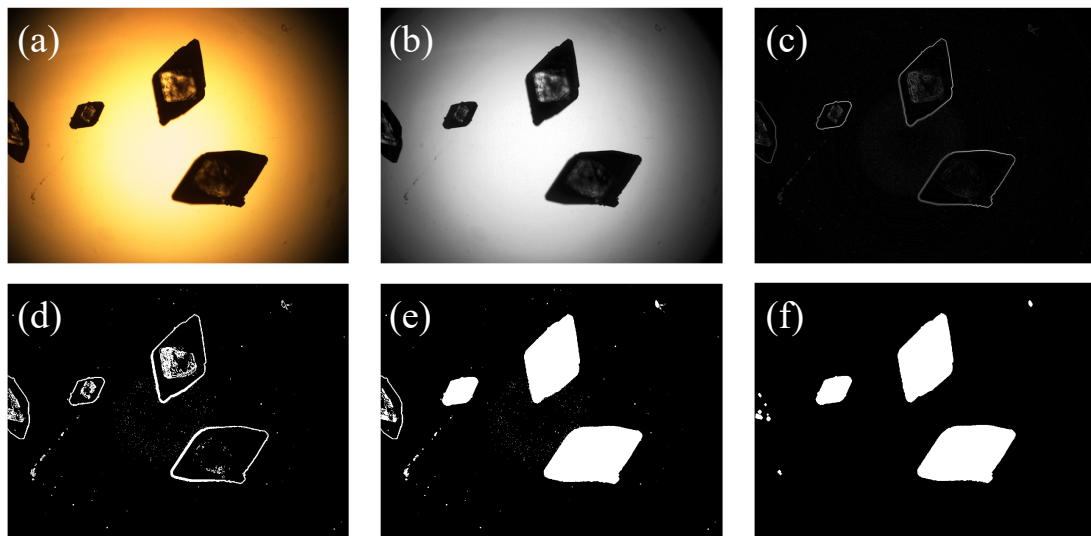
Figure D.3: Image processing steps: (a) Calling the original image, (b) making a B/W image, (c) finding the edges of the objects, (d) detecting clear edges, (e) filling the holes in each object to make a crystal object, and (f) removing small artifacts.

that are cut by the image border are ignored. Next, the code finds and detects the apparent edge of crystals. After this process, the code fills the hole of crystals in the image. As the final step, small dots that is less than the criteria are removed to clear the analysis.

Image analysis was carried out for an experimental case. I took 180 microscopic images before the sieving analysis, and all images were processed through the steps in Figure D.3. The image analysis is conducting statistically for sampled crystals, so the number of microscopic images can affect the quality of the investigation. However, the image analysis does not waste the sample crystals, but sieving analysis cannot recover analyzed crystals perfectly.

Figure D.4(a) compares the mass distribution from sieving results and image analysis using the scale factor for 273 px/μm. However, the mass distribution by image analysis is skewed more to the right than sieve analysis provides, which means that the sample has more large crystals. Therefore, other scale factors were tried to be found that can make the image analysis results similar to the sieving analysis results. The new scale factor was 350 px/μm, and the result is shown in Figure D.4(b). However, it has no theoretical basis.

Even though an image analysis process was set up, it requires more improvement. If the image analysis procedure will be accomplished, we can obtain crystal size distribution that quality is improved. Also, if we take numerous images, we can randomly choose sample images to analyze the size distribution and repeat this step, so we can make sure the size distribution is reliable statistically.
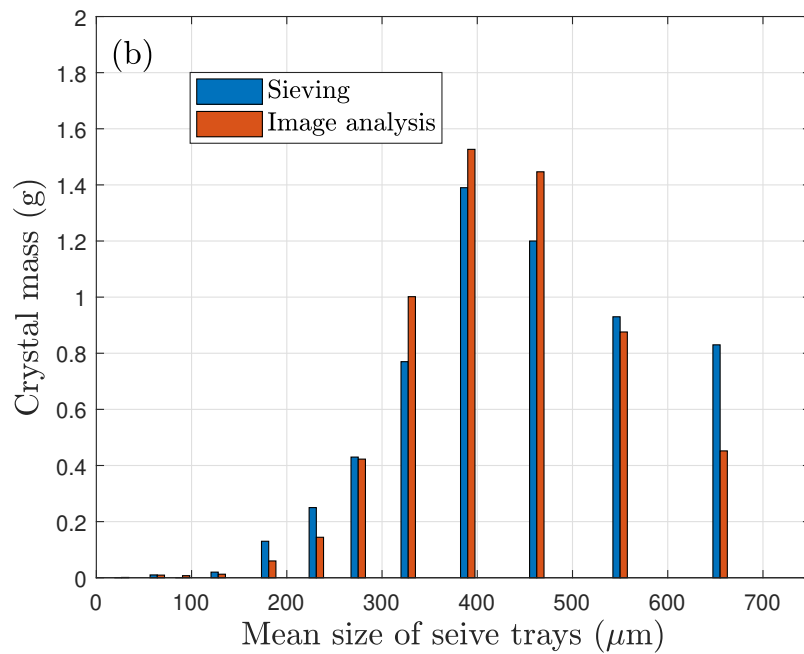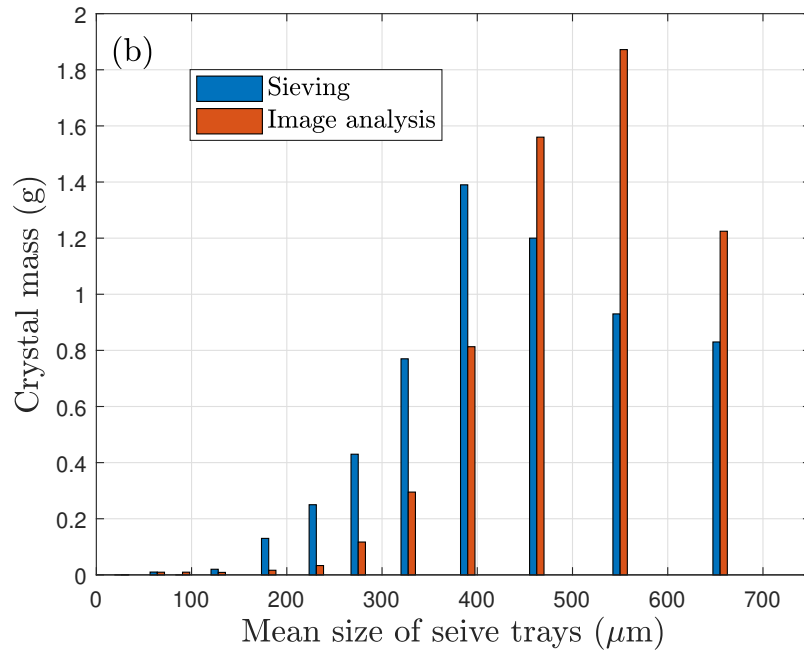
Figure D.4: Comparison between sieving and image analysis: (a)with a scale factor 273 px/μm, and (b)with a scale factor 350 px/μm

154

APPENDIX E

ADDITIONAL RESULTS

E.1   Comparisons between experimental data and PBM results

In Chapter 3, the kinetic parameters of a PBM were determined by three training sets, and the model was validated using three test sets. Because only one case from training and test sets is shown in Chapter 3, the comparisons of Exp. 9 and 10 from the training set (Figures E.1 and E.2) and Exp. 12 and 13 from the test set (Figures E.3 and E.4) are shown in this section.

For all comparison, the trends of supersaturation and crystal mass in the solution by the PBM follows the experimental data. In particular, the supersaturation and crystal mass trends, while the temperature cycling is applied, fit and predict the experimental data with high accuracy. However, the trends at the end of the temperature plateau in Exp. 9 (Figure E.1), the fitted supersaturation and crystal mass show slight discrepancies from the experimental data. This discrepancy seems to be due to the stochastic nature of primary nucleation and subsequent supersaturation consumption by secondary nucleation and crystal growth.

For the volume density distribution of crystals, the fitted and predicted distribution is similar to the sieved results. Therefore, the volume-weighted mean crystal sizes in Table 3.8 show errors less than $\pm 12\%$.
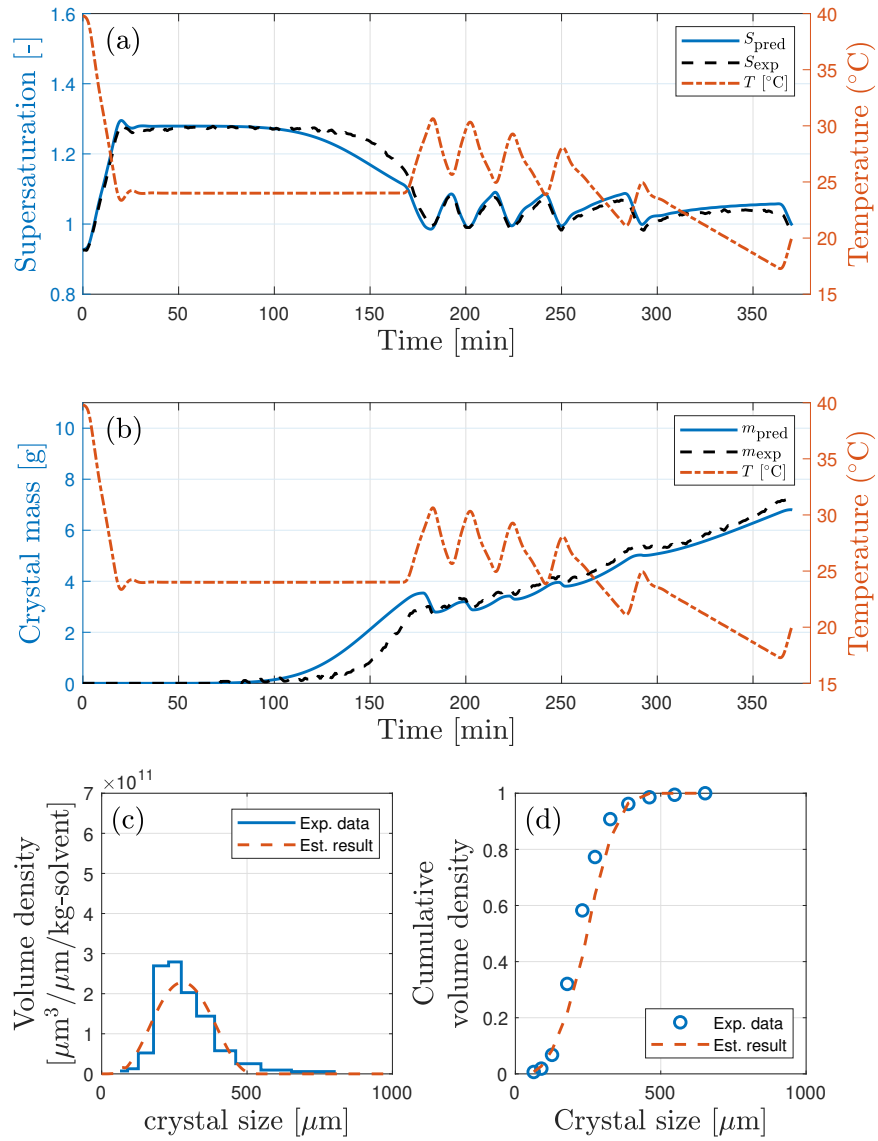
Figure E.1: Comparisons between experimental data and fitted results for the Exp. 9 in training sets: (a) supersaturation, (b) crystal mass in the solution, (c) volume density distribution, and (d) cumulative volume density distribution.
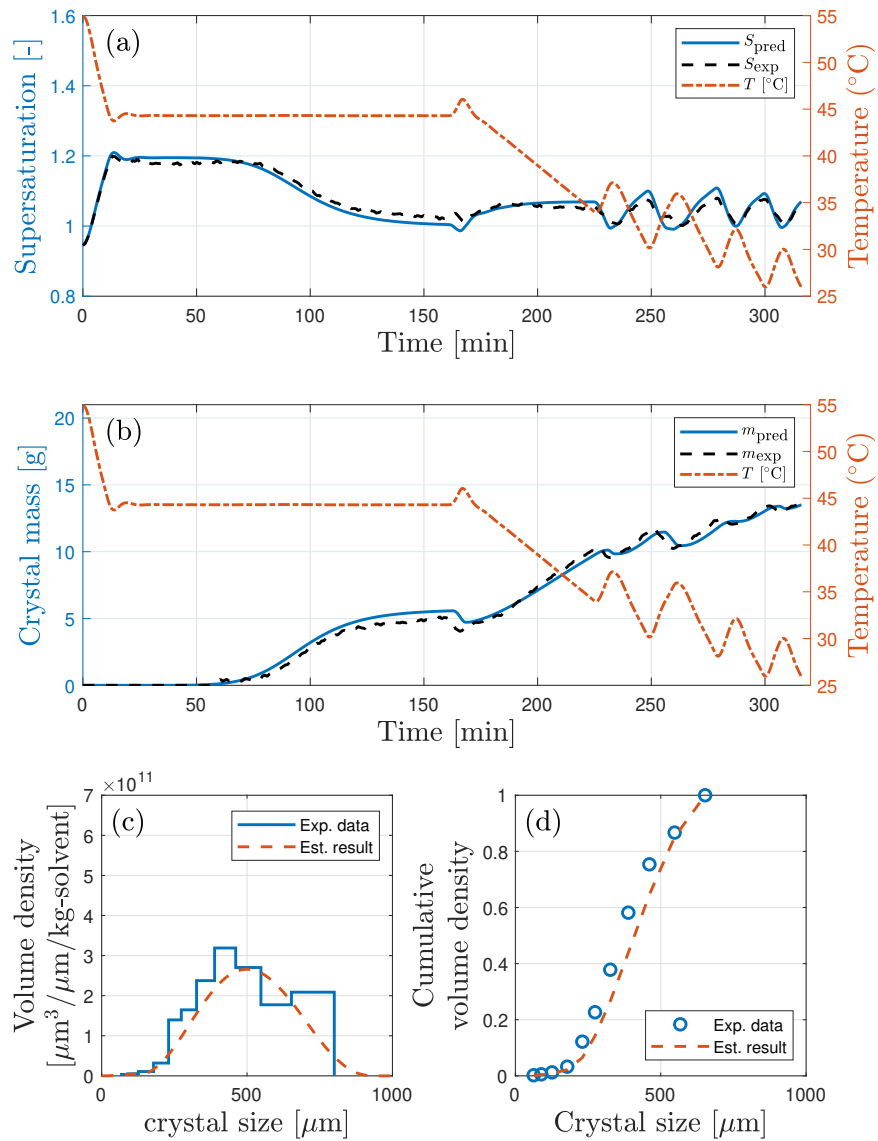
Figure E.2: Comparisons between experimental data and fitted results for the Exp. 10 in training sets: (a) supersaturation, (b) crystal mass in the solution, (c) volume density distribution, and (d) cumulative volume density distribution.
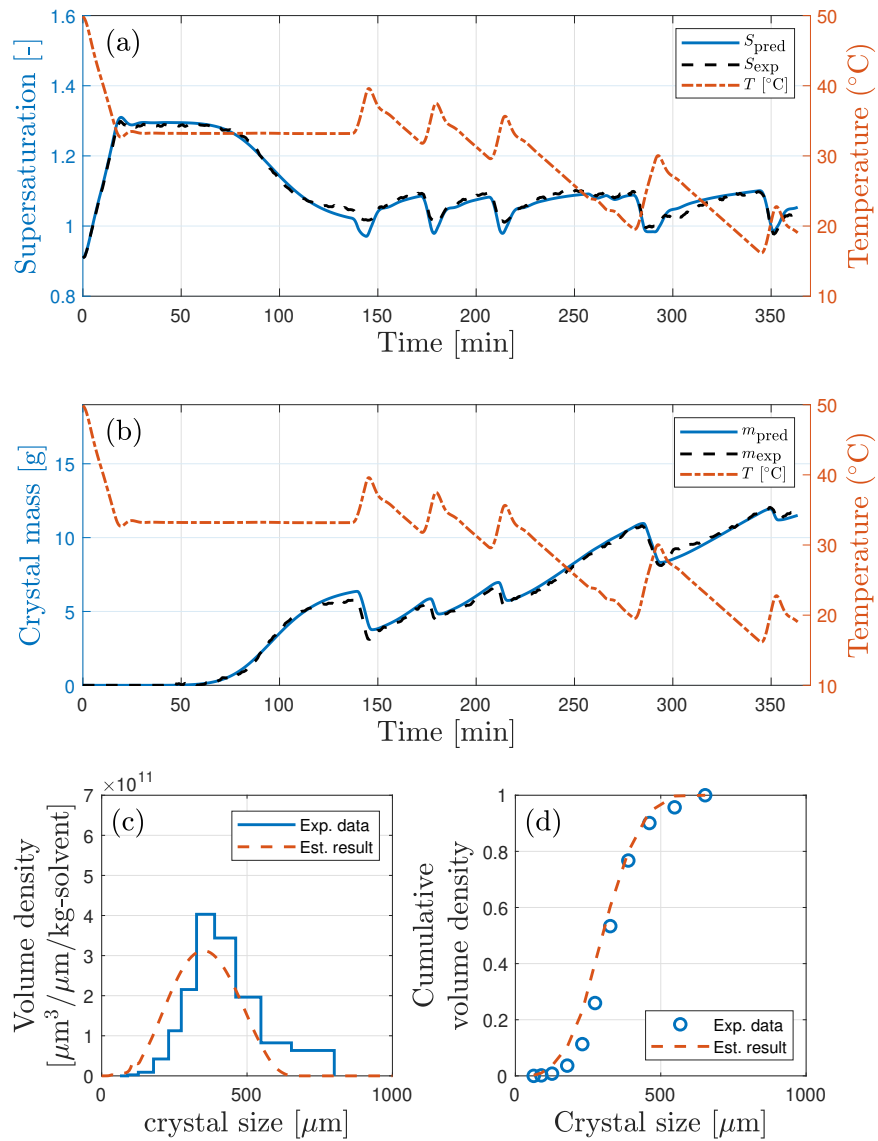
Figure E.3: Comparisons between experimental data and fitted results for the Exp. 12 in test sets: (a) supersaturation, (b) crystal mass in the solution, (c) volume density distribution, and (d) cumulative volume density distribution.
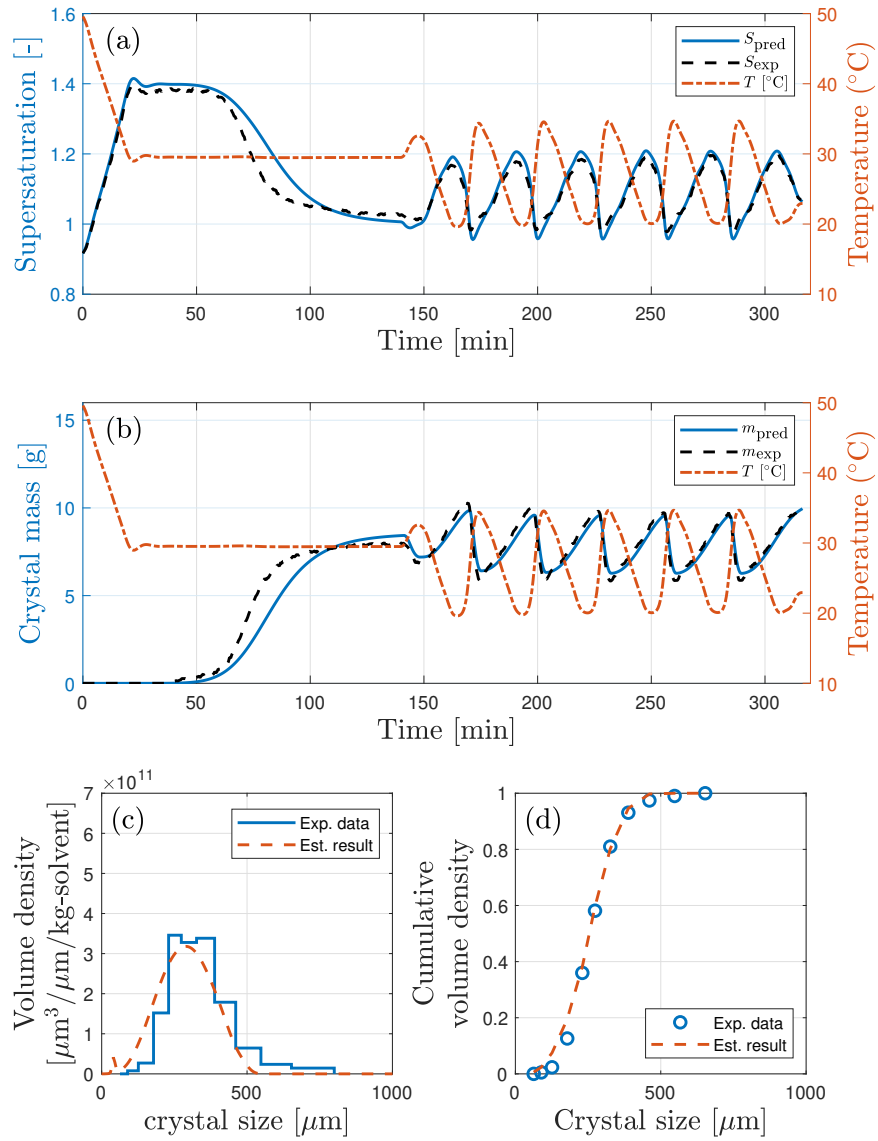
Figure E.4: Comparisons between experimental data and fitted results for the Exp. 13 in test sets: (a) supersaturation, (b) crystal mass in the solution, (c) volume density distribution, and (d) cumulative volume density distribution.

E.2 Open-loop control results using the obtained optimal temperature profiles

In Chapter 4, two comparisons (Cases 1 and 4) were presented from four cases, so the remaining comparison is shown in this section. The temperature profiles from the open-loop control experiments were implemented in the PBM and the simulated results for Case 2 and 3 are shown in Figures E.5 and E.6. The trends of the supersaturation and crystal mass are following the experimental data with slight discrepancies, but the simulated volume density distributions results show left-skewed distributions largely than experimental data. These results makes the smaller mean volume crystal sizes as shown in Table 4.4. These results imply the PBM kinetic models require additional parameter estimations using experimental data for wider condition ranges for more accurate predictions.
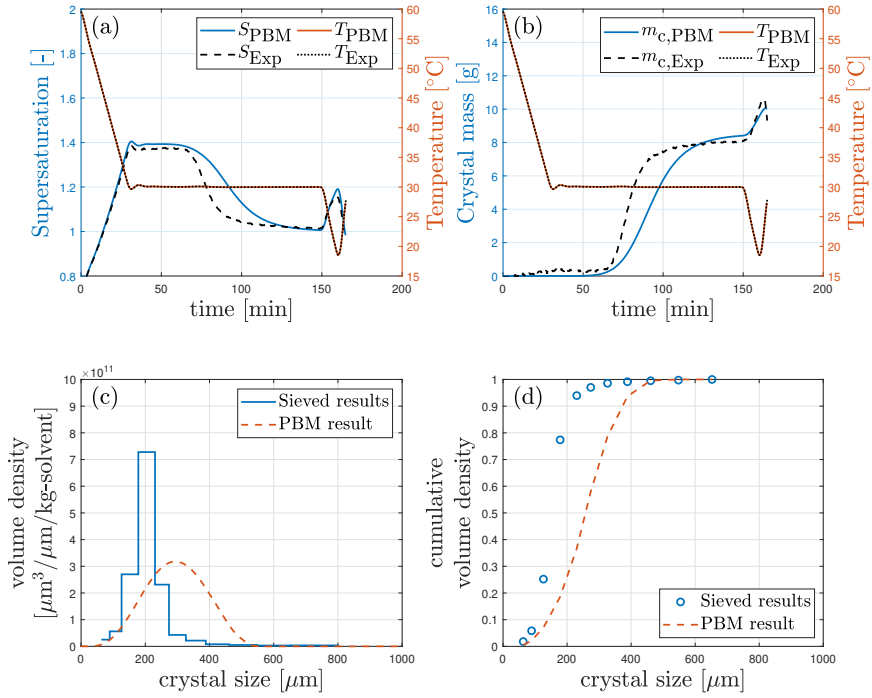
Figure E.5: Comparison of open-loop control results for Case 2: (a) supersaturation, (b) crystal mass in the solution, (c) volume density distribution, and (d) cumulative volume density distribution.
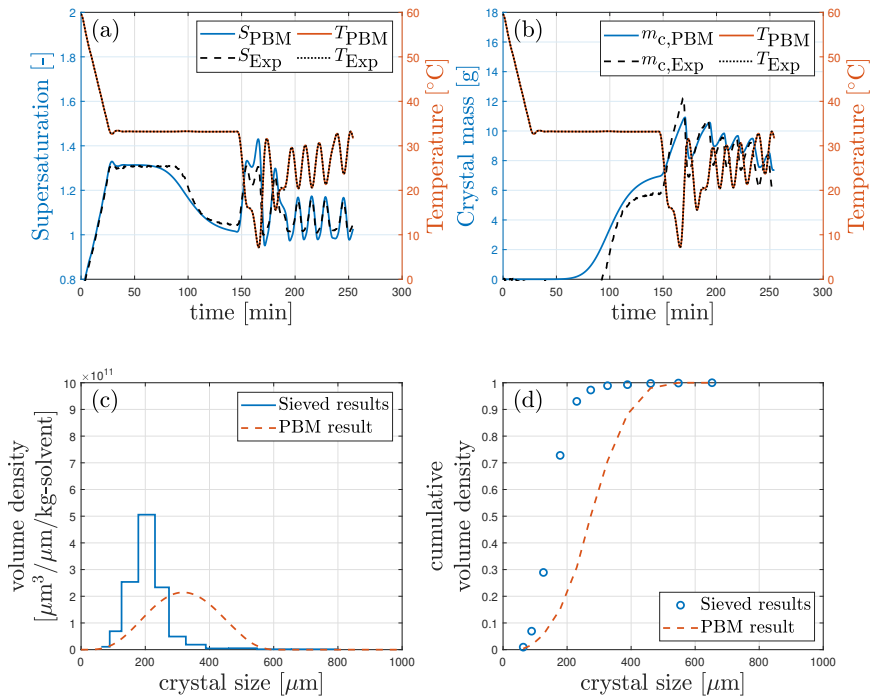
Figure E.6: Comparison of open-loop control results for Case 3: (a) supersaturation, (b) crystal mass in the solution, (c) volume density distribution, and (d) cumulative volume density distribution.

REFERENCES

(1)   Myerson, A. S.; Erdemir, D.; Lee, A. Y., *Handbook of Industrial Crystallization*, 3rd ed.; Cambridge University Press: 2019.

(2)   Tavare, N. S., *Industrial Crystallization: Process Simulation Analysis and Design*; The Plenum Chemical Engineering Series; Springer US: 1995.

(3)   Gibbs, J. W. On the Equilibrium of Heterogeneous Substances. *Transactions of the Connecticut Academy of Arts and Sciences* **1876**, *3*, 108–248.

(4)   Gibbs, J. W. On the Equilibrium of Heterogeneous Substances. *Transactions of the Connecticut Academy of Arts and Sciences* **1878**, *16*, 343–524.

(5)   Becker, R.; Döring, W. Kinetische Behandlung der Keimbildung in übersättigten Dämpfen. *Annalen der Physik* **1935**, *416*, 719–752.

(6)   Turnbull, D.; Fisher, J. C. Rate of nucleation in condensed systems. *The Journal of Chemical Physics* **1949**, *17*, 71–73.

(7)   Bonnett, P. E.; Carpenter, K. J.; Dawson, S.; Davey, R. J. Solution crystallisation via a submerged liquid-liquid phase boundary: Oiling out. *Chemical Communications* **2003**, *3*, 698–699.

(8)   Jeon, S. et al. Reversible disorder-order transitions in atomic crystal nucleation. *Science* **2021**, *371*, 498–503.

(9)   Savage, J. R.; Dinsmore, A. D. Experimental evidence for two-step nucleation in colloidal crystallization. *Physical Review Letters* **2009**, *102*, 15–18.

(10)   Hsieh, M. C.; Lynn, D. G.; Grover, M. A. Kinetic Model for Two-Step Nucleation of Peptide Assembly. *Journal of Physical Chemistry B* **2017**, *121*, 7401–7411.

(11)   Erdemir, D.; Lee, A. Y.; Myerson, A. S. Nucleation of crystals from solution: Classical and two-step models. *Accounts of Chemical Research* **2009**, *42*, 621–629.

(12)   Volmer, M.; Weber, A. Keimbildung in übersättigten Gebilden. *Zeitschrift für Physikalische Chemie* **1926**, *119*, 277–301.

(13)   Izmailov, A. F.; Myerson, A. S.; Arnold, S. A statistical understanding of nucleation. *Journal of Crystal Growth* **1999**, *196*, 234–242.

(14) Pino-García, O.; Rasmuson, Å. C. Primary nucleation of vanillin explored by a novel multicell device. *Industrial & Engineering Chemistry Research* **2003**, *42*, 4899–4909.

(15) Goh, L.; Chen, K.; Bhamidi, V.; He, G.; Kee, N. C. S.; Kenis, P. J. A.; Zukoski, C. F.; Braatz, R. D. A stochastic model for nucleation kinetics determination in droplet-based microfluidic systems. *Crystal Growth & Design* **2010**, *10*, 2515–2521.

(16) Maggioni, G. M.; Mazzotti, M. Modelling the stochastic behaviour of primary nucleation. *Faraday Discussions* **2015**, *179*, 359–382.

(17) Maggioni, G. M.; Mazzotti, M. Stochasticity in primary nucleation: measuring and modeling detection times. *Crystal Growth & Design* **2017**, *17*, 3625–3635.

(18) King, J. C.; Li, H.; Grover, M. A.; Kawajiri, Y.; Rousseau, R. W. Optimization of two-stage cooling profile in unseeded batch crystallization. *IFAC-PapersOnLine* **2015**, *48*, 9th IFAC Symposium on Advanced Control of Chemical Processes AD-CHEM 2015, 297–302.

(19) Li, H.; Kawajiri, Y.; Grover, M. A.; Rousseau, R. W. Modeling of nucleation and growth kinetics for unseeded batch cooling crystallization. *Industrial & Engineering Chemistry Research* **2017**, *56*, 4060–4073.

(20) Melia, T. P.; Moffitt, W. P. Secondary nucleation from aqueous solution. *Industrial & Engineering Chemistry Fundamentals* **1964**, *3*, 313–317.

(21) Sikdar, S. K.; Randolph, A. D. Secondary nucleation of two fast growth systems in a mixed suspension crystallizer: Magnesium sulfate and citric acid water systems. *AIChE Journal* **1976**, *22*, 110–117.

(22) Burton, W. K.; Cabrera, N.; Frank, F. C. The growth of crystals and the equilibrium structure of their surfaces. *Philosophical Transactions of the Royal Society of London. Series A, Mathematical and Physical Sciences* **1951**, *243*, 299–358.

(23) Brunsteiner, M.; Jones, A. G.; Pratola, F.; Price, S. L.; Simons, S. J. R. Toward a molecular understanding of crystal agglomeration. *Crystal Growth & Design* **2005**, *5*, 3–16.

(24) Hollander, E. D.; Derksen, J. J.; Portela, L. M.; Van den Akker, H. E. Numerical scale-up study for orthokinetic agglomeration in stirred vessels. *AIChE Journal* **2001**, *47*, 2425–2440.

(25) Mumtaz, H. S.; Hounslow, M. J.; Seaton, N. A.; Paterson, W. R. Orthokinetic Aggregation During Precipitation. *Chemical Engineering Research and Design* **1997**, *75*, 152–159.

(26) Sato, K.; Nagai, H.; Hasegawa, K.; Tomori, K.; Kramer, H. J. M.; Jansens, P. J. Two-dimensional population balance model with breakage of high aspect ratio crystals for batch crystallization. *Chemical Engineering Science* **2008**, *63*, 3271–3278.

(27) Fujiwara, M.; Chow, P. S.; Ma, D. L.; Braatz, R. D. Paracetamol Crystallization Using Laser Backscattering and ATR-FTIR Spectroscopy: Metastability, Agglomeration, and Control. *Crystal Growth & Design* **2002**, *2*, 363–370.

(28) Feng, L.; Berglund, K. A. ATR-FTIR for Determining Optimal Cooling Curves for Batch Crystallization of Succinic Acid. *Crystal Growth & Design* **2002**, *2*, 449–452.

(29) Grön, H.; Borissova, A.; Roberts, K. J. K. In-process ATR-FTIR spectroscopy for closed-loop supersaturation control of a batch crystallizer producing monosodium glutamate crystals of defined size. *Industrial & Engineering Chemistry Research* **2003**, *42*, 198–206.

(30) Liotta, V.; Sabesan, V. Monitoring and feedback control of supersaturation using ATR-FTIR to produce an active pharmaceutical ingredient of a desired crystal size. *Organic Process Research & Development* **2004**, *8*, 488–494.

(31) Zhou, G. X.; Fujiwara, M.; Woo, X. Y.; Rusli, E.; Tung, H. H.; Starbuck, C.; Davidson, O.; Ge, Z.; Braatz, R. D. Direct design of pharmaceutical antisolvent crystallization through concentration control. *Crystal Growth & Design* **2006**, *6*, 892–898.

(32) Gutwald, T.; Mersmann, A. Batch cooling crystallization at constant supersaturation: Technique and experimental results. *Chemical Engineering & Technology* **1990**, *13*, 229–237.

(33) Matthews, H. B.; Rawlings, J. B.; Rawlings, J. B. Batch crystallization of a photochemical: modeling, control, and filtration. *AIChE Journal* **1998**, *44*, 1119–1127.

(34) Kee, N. C. S.; Tan, R. B. H.; Braatz, R. D. Selective crystallization of the metastable α-form of L-glutamic acid using concentration feedback control. *Crystal Growth & Design* **2009**, *9*, 3044–3051.

(35) Doki, N.; Seki, H.; Takano, K.; Asatani, H.; Yokota, M.; Kubota, N. Process control of seeded batch cooling crystallization of the metastable α-form glycine using

an in-situ ATR-FTIR spectrometer and an in-situ FBRM particle counter. *Crystal Growth & Design* **2004**, *4*, 949–953.

(36)   Chew, J. W.; Chow, P. S.; Tan, R. B. H. Automated in-line technique using FBRM to achieve consistent product quality in cooling crystallization. *Crystal Growth & Design* **2007**, *7*, 1416–1422.

(37)   Woo, X. Y.; Nagy, Z. K.; Tan, R. B. H.; Braatz, R. D. Crystallization with Laser Backscattering Measurement. *Crystal Growth & Design* **2009**, *9*, 182–191.

(38)   Abu Bakar, M. R.; Nagy, Z. K.; Rielly, C. D. Seeded batch cooling crystallization with temperature cycling for the control of size uniformity and polymorphic purity of sulfathiazole crystals. *Organic Process Research & Development* **2009**, *13*, 1343–1356.

(39)   Saleemi, A.; Rielly, C.; Nagy, Z. K. Automated direct nucleation control for in situ dynamic fines removal in batch cooling crystallization. *CrystEngComm* **2012**, *14*, 2196–2203.

(40)   Griffin, D. J.; Grover, M. A.; Kawajiri, Y.; Rousseau, R. W. Mass-count plots for crystal size control. *Chemical Engineering Science* **2015**, *137*, 338–351.

(41)   Lee, J. H. Model predictive control and dynamic programming. *2011 11th International Conference on Control, Automation and Systems* **2011**, 1807–1809.

(42)   Görges, D. Relations between model predictive control and reinforcement learning. *IFAC-PapersOnLine* **2017**, *50*, 4920–4928.

(43)   Miller, S. M.; Rawlings, J. B. Model identification and control strategies for batch cooling crystallizers. *AIChE Journal* **1994**, *40*, 1312–1327.

(44)   Shi, D.; Mhaskar, P.; El-Farra, N. H.; Christofides, P. D. Predictive control of crystal size distribution in protein crystallization. *Nanotechnology* **2005**, *16*.

(45)   Mesbah, A.; Huesman, A. E. M.; Kramer, H. J. M.; Van Den Hof, P. M. J. A comparison of nonlinear observers for output feedback model-based control of seeded batch crystallization processes. *Journal of Process Control* **2011**, *21*, 652–666.

(46)   Cao, Y.; Kang, J.; Nagy, Z. K.; Laird, C. D. Parallel solution of robust nonlinear model predictive control problems in batch crystallization. *Processes* **2016**, *4*, 1–14.

(47)   Bötschi, S.; Rajagopalan, A. K.; Morari, M.; Mazzotti, M. Feedback control for the size and shape evolution of needle-like crystals in suspension. I . Concepts and simulation studies. *Crystal Growth & Design* **2018**, *18*, 4470–4483.

(48) Mesbah, A.; Nagy, Z. K.; Huesman, A. E. M.; Kramer, H. J. M.; Van Den Hof, P. M. J. Nonlinear model-based control of a semi-industrial batch crystallizer using a population balance modeling framework. *IEEE Transactions on Control Systems Technology* **2012**, *20*, 1188–1201.

(49) De Moraes, M. G. F.; de Souza, M. B.; Secchi, A. R., *Dynamics and MPC of an evaporative continuous crystallization process*; 2005, 2018; Vol. 43, pp 997–1002.

(50) Griffin, D. J.; Grover, M. A.; Kawajiri, Y.; Rousseau, R. W. Data-driven modeling and dynamic programming applied to batch cooling crystallization. *Industrial & Engineering Chemistry Research* **2016**, *55*, 1361–1372.

(51) Griffin, D. J.; Kawajiri, Y.; Rousseau, R. W.; Grover, M. A. Using MC plots for control of paracetamol crystallization. *Chemical Engineering Science* **2017**, *164*, 344–360.

(52) McDonald, M. A.; Marshall, G. D.; Bommarius, A. S.; Grover, M. A.; Rousseau, R. W. Crystallization Kinetics of Cephalexin Monohydrate in the Presence of Cephalexin Precursors. *Crystal Growth & Design* **2019**, *19*, 5065–5074.

(53) Saleemi, A. N.; Steele, G.; Pedge, N. I.; Freeman, A.; Nagy, Z. K. Enhancing crystalline properties of a cardiovascular active pharmaceutical ingredient using a process analytical technology based crystallization feedback control strategy. *International Journal of Pharmaceutics* **2012**, *430*, 56–64.

(54) Zhou, G.; Moment, A.; Yaung, S.; Cote, A.; Hu, T. E. Evolution and application of an automated platform for the development of crystallization processes. *Organic Process Research and Development* **2013**, *17*, 1320–1329.

(55) Duffy, D.; Barrett, M.; Glennon, B. Novel, calibration-free strategies for supersaturation control in antisolvent crystallization processes. *Crystal Growth & Design* **2013**, *13*, 3321–3332.

(56) Aamir, E.; Nagy, Z. K.; Rielly, C. D. Optimal seed recipe design for crystal size distribution control for batch cooling crystallisation processes. *Chemical Engineering Science* **2010**, *65*, 3602–3614.

(57) Yu, Z. Q.; Chow, P. S.; Tan, R. B. H.; Ang, W. H. PAT-enabled determination of design space for seeded cooling crystallization. *Organic Process Research and Development* **2013**, *17*, 549–556.

(58) Peña, R.; Nagy, Z. K. Process Intensification through Continuous Spherical Crystallization Using a Two-Stage Mixed Suspension Mixed Product Removal (MSMPR) System. *Crystal Growth & Design* **2015**, *15*, 4225–4236.

(59)   Dufour, F.; Stichel, B.; Grayson, J. I. Control of crystal modification and crystal shape by control of solid-solid transitions during crystallization and drying: Two industrial case studies. *Organic Process Research and Development* **2013**, *17*, 568–577.

(60)   Markande, A.; Nezzal, A.; Fitzpatrick, J.; Aerts, L.; Redl, A. Influence of impurities on the crystallization of dextrose monohydrate. *Journal of Crystal Growth* **2012**, *353*, 145–151.

(61)   Ferguson, S. T.; Ortner, F.; Quon, J.; Peeva, L. G.; Trout, B. L.; Livingston, A.; Myerson, A. S. Use of continuous MSMPR crystallization with integrated nanofiltration membrane recycle for enhanced yield and purity in API crystallization. *Crystal Growth & Design* **2013**, *14*, 617–627.

(62)   Pandit, A. V.; Ranade, V. V. Chord length distribution to particle size distribution. *AIChE Journal* **2016**, *62*, 4215–4228.

(63)   Agimelen, O. S.; Hamilton, P.; Haley, I.; Nordon, A.; Vasile, M.; Sefcik, J.; Mulholland, A. J. Estimation of particle size distribution and aspect ratio of non-spherical particles from chord length distribution. *Chemical Engineering Science* **2015**, *123*, 629–640.

(64)   Ruf, A.; Worlitschek, J.; Mazzotti, M. Modeling and experimental analysis of PSD measurements through FBRM. *Particle & Particle Systems Characterization* **2000**, *17*, 167–179.

(65)   Li, M.; Wilkinson, D. Determination of non-spherical particle size distribution from chord length measurements. Part 1: Theoretical analysis. *Chemical Engineering Science* **2005**, *60*, 3251–3265.

(66)   Li, M.; Wilkinson, D.; Patchigolla, K. Determination of non-spherical particle size distribution from chord length measurements. Part 2: Experimental validation. *Chemical Engineering Science* **2005**, *60*, 4992–5003.

(67)   Pons, M. N.; Milferstedt, K.; Morgenroth, E. Modeling of chord length distributions. *Chemical Engineering Science* **2006**, *61*, 3962–3973.

(68)   Kempkes, M.; Eggers, J.; Mazzotti, M. Measurement of particle size and shape by FBRM and in situ microscopy. *Chemical Engineering Science* **2008**, *63*, 4656–4675.

(69)   Li, H.; Grover, M. A.; Kawajiri, Y.; Rousseau, R. W. Development of an empirical method relating crystal size distributions and FBRM measurements. *Chemical Engineering Science* **2013**, *89*, 142–151.

(70) Li, H.; Kawajiri, Y.; Grover, M. A.; Rousseau, R. W. Application of an empirical FBRM model to estimate crystal size distributions in batch crystallization. *Crystal Growth & Design* **2014**, *14*, 607–616.

(71) Irizarry, R.; Chen, A.; Crawford, R.; Codan, L.; Schoell, J. Data-driven model and model paradigm to predict 1D and 2D particle size distribution from measured chord-length distribution. *Chemical Engineering Science* **2017**, *164*, 202–218.

(72) Irizarry, R.; Nataraj, A.; Schoell, J. CLD-to-PSD model to predict bimodal distributions and changes in modality and particle morphology. *Chemical Engineering Science* **2021**, *232*, 116332.

(73) Crestani, C. E.; Bernardo, A.; Costa, C. B. B.; Giulietti, M. An artificial neural network model applied to convert sucrose chord length distributions into particle size distributions. *Powder Technology* **2021**, *384*, 186–194.

(74) Worlitschek, J.; Mazzotti, M. Model-based optimization of particle size distribution in batch-cooling crystallization of paracetamol. *Crystal Growth & Design* **2004**, *4*, 891–903.

(75) Cornel, J.; Lindenberg, C.; Mazzotti, M. Quantitative application of in-situ ATR-FTIR and Raman spectroscopy in crystallization processes. *Industrial & Engineering Chemistry Research* **2008**, *47*, 4870–4882.

(76) Nagy, Z. K.; Aamir, E.; Rielly, C. D. Internal fines removal using population balance model based control of crystal size distribution under dissolution, growth and nucleation mechanisms. *Crystal Growth & Design* **2011**, *11*, 2205–2219.

(77) Jiang, M.; Zhu, X.; Molaro, M. C.; Rasche, M. L.; Zhang, H.; Chadwick, K.; Raimondo, D. M.; Kim, K. K.; Zhou, L.; Zhu, Z.; Wong, M. H.; O'Grady, D.; Hebrault, D.; Tedesco, J.; Braatz, R. D. Modification of crystal shape through deep temperature cycling. *Industrial & Engineering Chemistry Research* **2014**, *53*, 5325–5336.

(78) Nikolic, G., *Fourier transforms: New analytical approaches and FTIR strategies*; Intech: 2011.

(79) Griffin, D. J.; Grover, M. A.; Kawajiri, Y.; Rousseau, R. W. Robust multicomponent IR-to-concentration model regression. *Chemical Engineering Science* **2014**, *116*, 77–90.

(80) Granberg, R. A.; Rasmuson, Å. C. Solubility of paracetamol in pure solvents. *Journal of Chemical & Engineering Data* **1999**, *44*, 1391–1395.

(81)   Hahnenkamp, I.; Graubner, G.; Gmehling, J. Measurement and prediction of solubilities of active pharmaceutical ingredients. *International Journal of Pharmaceutics* **2010**, *388*, 73–81.

(82)   Chianese, A.; Kramer, H. J., *Industrial crystallization process monitoring and control*; Wiley-VCH: 2012.

(83)   Merkus, H. G., *Particle Size Measurements: Fundamentals, Practice, Quality*; Particle Technology Series; Springer Netherlands: 2009.

(84)   Alderliesten, M. Mean Particle Diameters. Part I: Evaluation of definition systems. *Particle & Particle Systems Characterization* **1990**, *7*, 233–241.

(85)   Alderliesten, M. Mean Particle Diameters. Part II: Standardization of nomenclature. *Particle & Particle Systems Characterization* **1991**, *8*, 237–241.

(86)   Mullin, J. W., *Crystallization*, 4th ed.; Butterworth-Heinemann: 2001, pp 1–594.

(87)   Lovette, M. A.; Muratore, M.; Doherty, M. F. Crystal shape modification through cycles of dissolution and growth: Attainable regions and experimental validation. *AIChE Journal* **2011**, *58*, 1465–1474.

(88)   Suwannasang, K.; Flood, A. E.; Rougeot, C.; Coquerel, G. Using programmed heating–cooling cycles with racemization in solution for complete symmetry breaking of a conglomerate forming system. *Crystal Growth & Design* **2013**, *13*, 3498–3504.

(89)   Breveglieri, F.; Maggioni, G. M.; Mazzotti, M. Deracemization of NMPA via temperature cycles. *Crystal Growth & Design* **2018**, *18*, 1873–1881.

(90)   Wu, Z.; Yang, S.; Wu, W. Application of temperature cycling for crystal quality control during crystallization. *CrystEngComm* **2016**, *18*, 2222–2238.

(91)   Gherras, N.; Fevotte, G. On the use of process analytical technologies and population balance equations for the estimation of crystallization kinetics. A case study. *AIChE Journal* **2012**, *58*, 2650–2664.

(92)   Ó'Ciardhá, C. T.; Hutton, K. W.; Mitchell, N. A.; Frawley, P. J. Simultaneous parameter estimation and optimization of a seeded antisolvent crystallization. *Crystal Growth & Design* **2012**, *12*, 5247–5261.

(93)   Trampuž, M.; Teslić, D.; Likozar, B. Crystallization of fesoterodine fumarate active pharmaceutical ingredient: Modelling of thermodynamic equilibrium, nucleation, growth, agglomeration and dissolution kinetics and temperature cycling. *Chemical Engineering Science* **2019**, *201*, 97–111.

(94) Shoji, M.; Eto, T.; Takiyama, H. A kinetic study of the influence of modulated undersaturation operation on crystal size distribution in cooling-type batch crystallization. *Journal of Chemical Engineering of Japan* **2011**, *44*, 191–196.

(95) Seki, H.; Furuya, N.; Hoshino, S. Evaluation of controlled cooling for seeded batch crystallization incorporating dissolution. *Chemical Engineering Science* **2012**, *77*, 10–17.

(96) Mao, S.; Zhang, Y.; Rohani, S.; Ray, A. K. Kinetics of (R,S)- and (R)-mandelic acid in an unseeded cooling batch crystallizer. *Journal of Crystal Growth* **2010**, *312*, 3340–3348.

(97) Frawley, P. J.; Mitchell, N. A.; Ó'Ciardhá, C. T.; Hutton, K. W. The effects of supersaturation, temperature, agitation and seed surface area on the secondary nucleation of paracetamol in ethanol solutions. *Chemical Engineering Science* **2012**, *75*, 183–197.

(98) Yang, Y.; Nagy, Z. K. Advanced control approaches for combined cooling/antisolvent crystallization in continuous mixed suspension mixed product removal cascade crystallizers. *Chemical Engineering Science* **2015**, *127*, 362–373.

(99) Kumar, S.; Ramkrishna, D. On the solution of population balance equations by discretization — III. Nucleation, growth and aggregation of particles. *Chemical Engineering Science* **1997**, *52*, 4659–4679.

(100) Porru, M.; Özkan, L. Monitoring of batch industrial crystallization with growth, nucleation, and agglomeration. Part 1: Modeling with method of characteristics. *Industrial & Engineering Chemistry Research* **2017**, *56*, 5980–5992.

(101) Wulkow, M.; Gerstlauer, A.; Nieken, U. Modeling and simulation of crystallization processes using parsival. *Chemical Engineering Science* **2001**, *56*, 2575–2588.

(102) Gunawan, R.; Fusman, I.; Braatz, R. D. High resolution algorithms for multidimensional population balance equations. *AIChE Journal* **2004**, *50*, 2738–2749.

(103) Gunawan, R.; Fusman, I.; Braatz, R. D. Parallel high-resolution finite volume simulation of particulate processes. *AIChE Journal* **2008**, *54*, 1449–1458.

(104) Sulttan, S.; Rohani, S. Coupling of CFD and population balance modelling for a continuously seeded helical tubular crystallizer. *Journal of Crystal Growth* **2019**, *505*, 19–25.

(105) Motz, S.; Mitrović, A.; Gilles, E. Comparison of numerical methods for the simulation of dispersed phase systems. *Chemical Engineering Science* **2002**, *57*, 4329–4344.

(106) Qamar, S.; Elsner, M. P.; Angelov, I. A.; Warnecke, G.; Seidel-Morgenstern, A. A comparative study of high resolution schemes for solving population balances in crystallization. *Computers & Chemical Engineering* **2006**, *30*, 1119–1131.

(107) Randolph, A. D.; Larson, M. A., *Theory of particulate processes: Analysis and techniques of continuous crystallization*; Elsevier Science: 2012.

(108) Seki, H.; Su, Y. Robust optimal temperature swing operations for size control of seeded batch cooling crystallization. *Chemical Engineering Science* **2015**, *133*, 16–23.

(109) Salvatori, F.; Mazzotti, M. Manipulation of Particle Morphology by Crystallization, Milling, and Heating Cycles—A Mathematical Modeling Approach. *Industrial & Engineering Chemistry Research* **2017**, *56*, 9188–9201.

(110) Salvatori, F.; Binel, P.; Mazzotti, M. Efficient assessment of combined crystallization, milling, and dissolution cycles for crystal size and shape manipulation. *Chemical Engineering Science: X* **2019**, *1*, 100004.

(111) Bodák, B.; Maggioni, G. M.; Mazzotti, M. Population-Based Mathematical Model of Solid-State Deracemization via Temperature Cycles. *Crystal Growth & Design* **2018**, *18*, 7122–7131.

(112) Szilagyi, B.; Nagy, Z. K. Model-based analysis and quality-by-design framework for high aspect ratio crystals in crystallizer-wet mill systems using GPU acceleration enabled optimization. *Computers & Chemical Engineering* **2019**, *126*, 421–433.

(113) Ottens, E. P. K.; Janse, A. H.; De Jong, E. J. Secondary nucleation in a stirred vessel cooling crystallizer. *Journal of Crystal Growth* **1972**, *13-14*, 500–505.

(114) Evans, T. W.; Sarofim, A. F. Models of secondary nucleation attributable. *AIChE Journal* **1974**, *20*, 959–966.

(115) Liiri, M.; Koiranen, T.; Aittamaa, J. Secondary nucleation due to crystal-impeller and crystal-vessel collisions by population balances in CFD-modelling. *Journal of Crystal Growth* **2002**, *237-239*, 2188–2193.

(116) Agrawal, S. G.; Paterson, A. H. J. Secondary nucleation: Mechanisms and models. *Chemical Engineering Communications* **2015**, *202*, 698–706.

(117) Chang, S.-C. The method of space-time conservation element and solution element —— A new approach for solving the Navier-Stokes and Euler equations. *Journal of Computational Physics* **1995**, *119*, 295–324.

(118)   Jiang, C.; Feng, X.; Zhang, J.; Zhong, D. AMR simulations of magnetohydrody-namic problems by the CESE method in curvilinear coordinates. *Solar Physics* **2010**, *267*, 463–491.

(119)   Ayasoufi, A.; Keith, T. G.; Rahmani, R. K. Application of the conservation element and solution element method in numerical modeling of three-dimensional heat conduction with melting and/or freezing. *Journal of Heat Transfer* **2004**, *126*, 937–945.

(120)   Chou, Y.; Yang, R. J. Two-dimensional Dual-Phase-Lag thermal behavior in single-/multi-layer structures using CESE method. *International Journal of Heat and Mass Transfer* **2009**, *52*, 239–249.

(121)   Lim, Y. I.; Jorgensen, S. B. A fast and accurate numerical method for solving simulated moving bed (SMB) chromatographic separation problems. *Chemical Engineering Science* **2004**, *59*, 1931–1947.

(122)   Lim, Y. I.; Lee, J.; Bhatia, S. K.; Lim, Y. S.; Han, C. Improvement of para-Xylene SMB process performance on an industrial scale. *Industrial & Engineering Chemistry Research* **2010**, *49*, 3316–3327.

(123)   Ward, J. D.; Yu, C. C. Population balance modeling in Simulink: PCSS. *Chemical Engineering Science* **2008**, *32*, 2233–2242.

(124)   Noor, S.; Qamar, S. The space time CE/SE method for solving one-dimensional batch crystallization model with fines dissolution. *Chinese Journal of Chemical Engineering* **2015**, *23*, 337–341.

(125)   Nocedal, J.; Wright, S. J., *Numerical Optimization*; Springer: 2006.

(126)   Bard, Y., *Nonlinear Parameter Estimation*; Academic Press: 1974.

(127)   Rawlings, J. B.; Miller, S. M.; Witkowski, W. R. Model identification and control of solution crystallization processes: A review. *Industrial & Engineering Chemistry Research* **1993**, *32*, 1275–1296.

(128)   Abu Bakar, M. R.; Nagy, Z. K.; Saleemi, A. N.; Rielly, C. D. The impact of direct nucleation control on crystal size distribution in pharmaceutical crystallization processes. *Crystal Growth & Design* **2009**, *9*, 1378–1384.

(129)   Mitchell, N. A.; Óciardhá, C. T.; Frawley, P. J. Estimation of the growth kinetics for the cooling crystallisation of paracetamol and ethanol solutions. *Journal of Crystal Growth* **2011**, *328*, 39–49.

172

(130)   Amagliani, L.; O'Regan, J.; Kelly, A. L.; O'Mahony, J. A. Physical and flow properties of rice protein powders. *Journal of Food Engineering* **2016**, *190*, 1–9.

(131)   Anjaneyulu, P.; Khakhar, D. V. Rheology of a gas-fluidized bed. *Powder Technology* **1995**, *83*, 29–34.

(132)   Liu, L. X.; Marziano, I.; Bentham, A. C.; Litster, J. D.; White, E. T.; Howes, T. Effect of particle properties on the flowability of ibuprofen powders. *International Journal of Pharmaceutics* **2008**, *362*, 109–117.

(133)   Glor, M. Ignition hazard due to static electricity in particulate processes. *Powder Technology* **2003**, *135-136*, 223–233.

(134)   Perkett, M. R.; Hagana, M. F. Using Markov state models to study self-assembly. *Journal of Chemical Physics* **2014**, *140*.

(135)   Shukla, D.; Hernández, C. X.; Weber, J. K.; Pande, V. S. Markov state models provide insights into dynamic modulation of protein function. *Accounts of Chemical Research* **2015**, *48*, 414–422.

(136)   Tang, X.; Bevan, M. A.; Grover, M. A. The construction and application of Markov state models for colloidal self-assembly process control. *Molecular Systems Design and Engineering* **2017**, *2*, 78–88.

(137)   Kim, Y.; Dean, K.; Kawajiri, Y.; Rousseau, R. W.; Grover, M. A. Unification of an empirical and a physically-based approach to crystallization monitoring. *Proceedings of the American Control Conference* **2018**, *2018-June*, 5106–5112.

(138)   Grant, M.; Boyd, S. *Recent Advances in Learning and Control*, Blondel, V., Boyd, S., Kimura, H., Eds.; Lecture Notes in Control and Information Sciences; Springer-Verlag Limited: 2008, pp 95–110.

(139)   Grant, M.; Boyd, S. CVX: Matlab Software for Disciplined Convex Programming, version 2.1, http://cvxr.com/cvx, 2014.

(140)   Bursal, H. F.; Hu, C. S. Application of a Cell-Mapping Method to Optimal-Control Problems. *International Journal of Control* **1989**, *49*, 1505–1522.

(141)   Sun, J. Q. Control of Nonlinear Dynamic Systems with the Cell Mapping Method. *Advances in Intelligent Systems and Computing* **2013**, *175*, 3–18.

(142)   Efroymson, M. A. *Mathematical Methods for Digital Computers*, Ralston, A., Wilf, H. S., Eds.; John Wiley, New York: 1960.

(143) Faraway, J. J., *Linear Models with R, Second Edition*; Chapman & Hall/CRC Texts in Statistical Science; Taylor & Francis: 2014.

(144) Rasamoelina, A. D.; Adjailia, F.; Sincak, P. A Review of Activation Function for Artificial Neural Network. *SAMI 2020 - IEEE 18th World Symposium on Applied Machine Intelligence and Informatics, Proceedings* **2020**, 281–286.

(145) Lee, D. H.; Kim, Y. T.; Lee, S. R. Shallow landslide susceptibility models based on artificial neural networks considering the factor selection method and various non-linear activation functions. *Remote Sensing* **2020**, *12*, 1994.

(146) Mathworks® Choose a Multilayer Neural Network Training Function https://www.mathworks.com/help/deeplearning/ug/choose-a-multilayer-neural-network-training-function.html, (accessed 02/20/2021).

(147) Hagan, M. T.; Menhaj, M. B. Training Feedforward Networks with the Marquardt Algorithm. *IEEE Transactions on Neural Networks* **1994**, *5*, 989–993.

(148) Akaike, H. A New Look at the Statistical Model Identification. *IEEE Transactions on Automatic Control* **1974**, *19*, 716–723.

(149) Schwarz, G. Estimating the Dimension of a Model. *Annals of Statistics* **1978**, *6*, 461–464.

(150) Cavanaugh, J. E. Unifying the derivations for the Akaike and corrected Akaike information criteria. *Statistics and Probability Letters* **1997**, *33*, 201–208.

(151) Panchal, G.; Ganatra, A.; Kosta, Y. P.; Panchal, D. Searching Most Efficient Neural Network Architecture Using Akaike's Information Criterion (AIC). *International Journal of Computer Applications* **2010**, *1*, 54–57.

(152) D'Emilio, A.; Aiello, R.; Consoli, S.; Vanella, D.; Iovino, M. Artificial neural networks for predicting the water retention curve of sicilian agricultural soils. *Water* **2018**, *10*.

(153) Kim, H. J.; Jang, B. S.; Park, C. K.; Bae, Y. H. Fatigue analysis of floating wind turbine support structure applying modified stress transfer function by artificial neural network. *Ocean Engineering* **2018**, *149*, 113–126.

(154) Escobar, C. A.; Morales-Menendez, R. Process-monitoring-for-quality - A model selection criterion for shallow neural networks. *Annual Conference of the PHM Society* **2019**, *11*.

(155) Rosen, R.; Von Wichert, G.; Lo, G.; Bettenhausen, K. D. About the importance of autonomy and digital twins for the future of manufacturing. *IFAC-PapersOnLine* **2015**, *28*, 567–572.

(156) Downs, J. J.; Vogel, E. F. A plant-wide industrial process control problem. *Computers and Chemical Engineering* **1993**, *17*, 245–255.

(157) Bathelt, A.; Ricker, N. L.; Jelali, M. Revision of the Tennessee eastman process model. *IFAC-PapersOnLine* **2015**, *28*, 309–314.

(158) He, R.; Chen, G.; Dong, C.; Sun, S.; Shen, X. Data-driven digital twin technology for optimized control in process systems. *ISA Transactions* **2019**, *95*, 221–234.

(159) Min, Q.; Lu, Y.; Liu, Z.; Su, C.; Wang, B. Machine Learning based Digital Twin Framework for Production Optimization in Petrochemical Industry. *International Journal of Information Management* **2019**, *49*, 502–519.

(160) Uhlenbrock, L.; Jensch, C.; Tegtmeier, M.; Strube, J. Digital Twin for Extraction Process Design and Operation. *Processes* **2020**, *8*, 866.

(161) Portela, R. M. C.; Varsakelis, C.; Richelle, A.; Giannelos, N.; Pence, J.; Dessoy, S.; von Stosch, M. When Is an In Silico Representation a Digital Twin? A Biopharmaceutical Industry Approach to the Digital Twin Concept. *Advanced Biochemical Engineering Biotechnology* **2020**.

(162) Lopez, P. C.; Udugama, I. A.; Thomsen, S. T.; Roslander, C.; Junicke, H.; Mauricio-Iglesias, M.; Gernaey, K. V. Towards a digital twin: a hybrid data-driven and mechanistic digital shadow to forecast the evolution of lignocellulosic fermentation. *Biofuels, Bioproducts and Biorefining* **2020**, *14*, 1046–1060.

(163) Chang, S.-C. Courant number insensitive CE/SE schemes. *AIAA paper* **2002**, 2002–3890.

(164) Hiraoka, S.; Kamei, N.; Kato, Y.; Tada, Y.; Cheon, H.; Yamaguchi, T. Power Correlation for Pitched Blade Paddle Impeller in Agitated Vessels With and Without Baffles. *KAGAKU KOGAKU RONBUNSHU* **1997**, *23*, 969–975.

(165) Paul, E. L.; Atiemo-Obeng, V. A.; Kresta, S. M., *Handbook of Industrial Mixing: Science and Practice*; Wiley: 2004.